UNIVERSIDADE DE LISBOA

INSTITUTO SUPERIOR TÉCNICO

Probing the Epoch of Reionization with Intensity Mapping of Molecular and Atomic Lines

Marta Bruno Silva

Supervisor: Doctor Mário Gonçalo Rodrigues dos Santos
CO-Supervisor: Doctor Asantha Roshan Cooray

Thesis approved in public session to obtain the PhD Degree in **Physics**
Jury final classification: **Pass with Distinction**

Jury

Chairperson: Chairman of the IST Scientific Board
Members of the Commitee:
Doctor Benoit Semelin
Doctor Ana Maria Vergueiro Monteiro Cidade Mourão
Doctor Jonathan Robin Pritchard
Doctor Mário Gonçalo Rodrigues dos Santos

2014

UNIVERSIDADE DE LISBOA

INSTITUTO SUPERIOR TÉCNICO

Probing the Epoch of Reionization with Intensity Mapping of Molecular and Atomic Lines

Marta Bruno Silva

Supervisor: Doctor Mário Gonçalo Rodrigues dos Santos

CO-Supervisor: Doctor Asantha Roshan Cooray

Thesis approved in public session to obtain the PhD Degree in **Physics**

Jury final classification: **Pass with Distinction**

Jury

Chairperson: Chairman of the IST Scientific Board

Members of the Commitee:

Doctor Benoit Semelin, Full Professor at LERMA, Observatoire de Paris, Université Pierre et Marie Curie, França

Doctor Ana Maria Vergueiro Monteiro Cidade Mourão, Associate Professor at Instituto Superior Técnico, Universidade de Lisboa

Doctor Jonathan Robin Pritchard, Lecturer, Imperial College London, UK

Doctor Mário Gonçalo Rodrigues dos Santos, Invited Assistant Professor at Instituto Superior Técnico, Universidade de Lisboa

Funding Institutions:

Fundação para a Ciência e Tecnologia, REF: SFRH/BD/51373/2011

2014

Desvendando a Época da Reionização usando Mapas de Intensidade de Linhas Atómicas e Moleculares

Marta Bruno Silva
Doutoramento em Física

Orientador: Mário Gonçalo Rodrigues dos Santos
Co-Orientador: Asantha Roshan Cooray

Resumo

A Época da Reionização é uma das menos conhecidas fases da evolução do nosso Universo, ela assinala o nascimento das primeiras estrelas e a consequente ionização do hidrogénio no meio intergalactico. Este processo é difícil de se caracterizar com experiências para observar galáxias individualmente uma vez que a maioria das galáxias responsáveis pela reionização são demasiado pouco luminosas para serem detectadas directamente. Observações da linha de 21cm do hidrogénio no meio intergaláctico foram propostas como uma alternativa para estudar esta época e várias experiências estão agora a tentar medir o sinal. Esta tese explora ainda mais este método e expande o ao uso de mapeamento a três dimensões da intensidade de outras linhas de transição típicas de várias fases do gás em galáxias. O trabalho aqui apresentado inclui modelos detalhados para simular mapas de intensidade das linhas de 21cm, CO, CII e Lya, tendo em conta os processos astrofísicos envolvidos na emissão das linhas. Estudos de contaminação extragaláctica são apresentados para cada linha e várias configurações experimentais foram analisadas. Também é demonstrado como mapas de intensidade podem ser usados para determinar as condições astrofísicas nos meios interestelar e intergaláctico, para constranger modelos de formação galáctica e até mesmo para constranger o modelo cosmológico.

Palavras-chave: Reionizaçao, mapas de intensidade, linhas de emissão, estrelas, matéria escura, halos, radiação, contaminantes, diagramas de luminosidade, espectros de potência

Probing the Epoch of Reionization with Intensity Mapping of Molecular and Atomic Lines

Abstract

The Epoch of Reionization is one of the last unknown phases in the evolution of our Universe, signaling the birth of the first stars and the consequent ionization of the hydrogen in the intergalactic medium. The process is hard to be characterized by galaxy surveys since most galaxies responsible for reionization are too faint to be directly observed. Observations of the hydrogen 21cm line from the intergalactic medium have been proposed as an alternative to probe this epoch and several experiments are now trying to measure the signal. This thesis further explores this approach and expands it to the use of three-dimensional intensity mapping of other transition lines typically connected to emission from several gas phases in galaxies. The work presented includes detailed models to simulate the intensity mapping signals from the 21cm, CO, CII and Lya lines, taking into account the astrophysical processes involved in the lines emission. Foreground contamination studies are presented for each line and several experimental setups are analysed. It is also shown how intensity maps can be used to determine the astrophysical conditions in the interstellar and in the intergalactic medium, to constrain galaxy formation models and even to probe the cosmological model.

Key-words: Reionization, intensity maps, emission lines, stars, dark matter, halos; radiation, foregrounds, luminosity functions, power spectra

Acknowledgements

Em primeiro lugar eu gostava de agradecer ao meu orientador Mário Santos por tudo o que aprendi com ele durante todos os anos em que trabalhamos juntos, por me ter motivado a trabalhar em investigação e por me ter inspirado a não me concentrar só num tema mas a tentar aprender um pouco de tudo.

Gostaria também de agradecer ao meu co-orientador Asantha Cooray pelas suas ideias de projectos e por me abrir horizontes.

Agradeço ao Yan Gong por me ter sempre recebido bem na UCI e pelas boas conversas durante a preparaçao dos artigos.

Agradeço ás muitas pessoas que passaram pelo CENTRA por todas as distracções, discussões e pelo apoio e companheirismo: Jordi, Helvi, Vitor, Andrea, Mariam, Jorge, Paolo, Dário, Mark, Terrence, Jan, Nino, Sayan, Stefano, Caio, Raphael, Vincenzo, Hirotada, Ketron, Lluis, Steven, Isabella, Richard, Masato, Nami, Ryuichi e Prado.

Um agradecimento especial ao Jordi, o meu inesquecivel companheiro de escritório por 5 anos, por me toda a paciência que teve a ouvir me falar de trabalho e outros assuntos, por todo o apoio e pelas dicas que me deu para preparar esta tese.

Obrigada aos professores Jorge Dias de Deus, Ana Mourão e Sande Lemos pelo bom acolhimento no CENTRA, aos informáticos Sérgio e Manuel pela paciência para resolverem os problemas do costume e à Dulce por toda a ajuda com as burocracias que eu tento evitar a todo o custo.

Obrigada também aos meus pais Júlia e José, aos meus irmãos Pedro, Rute e Sara e a todos os amigos de fora do centra pelo apoio, pela paciência para me aturarem e por toda a confiança que em mim depositam.

A frase seguinte resume o que sinto por vocês: “O valor das coisas não está no tempo que elas duram, mas na intensidade com que acontecem. Por isso existem momentos inesquecíveis, coisas inexplicáveis e pessoas incomparáveis.

List of Publications

Publications included in this Thesis:

Probing Reionization with Intensity Mapping of Molecular and Fine-Structure Lines (Paper I)
Gong Y., Cooray A., **Silva M. B.**, Santos M. G. and Lubin P.
The Astrophysical Journal, 705, 135-14 (2009)
arXiv:0909.1971

Intensity mapping of the CII fine structure line during the Epoch of Reionization (Paper II)
Gong Y., Cooray A., **Silva M. B.**, Santos M. G., Bock J., Bradford C. and Zemcov M.
The Astrophysical Journal, 745, 49 (2012)
arXiv:1107.3553

The OH line contamination of 21 cm intensity fluctuation measurements for z=1 4 (Paper III)
Gong Y., **Silva M. B.**, Chen X., Cooray A., Santos M. G., Bock J., Bradford C. and Zemcov M.
ApJL, 740, 1 (2011)
arXiv:1108.0947

Intensity Mapping of Lyman-alpha emission during the Epoch of Reionization (Paper IV)
Silva M. B., Santos M. G., Gong Y., Cooray A. and Bock, J.
The Astrophysical Journal, 763:132, 16pp (2013)
arXiv:1205.1493

Foreground contamination in Lyman-alpha intensity mapping during the Epoch of Reionization (Paper V)
Gong Y., **Silva M. B.**, Cooray A. and Santos M. G.
The Astrophysical Journal, 785:1, 72 (2012)
arXiv:1312.2035

Prospects for detecting CII emission during the Epoch of Reionization (Paper VI)
Silva M. B., Santos M. G., Cooray A. and Gong Y.
To be submitted to The Astrophysical Journal

Other works related with this Thesis:

Santos, M.G., Ferramacho, L., **Silva, M.B.**, Amblard A., and Cooray A.,
Fast and Large Volume Simulations of the 21 cm Signal from the Reionization and pre-Reionization Epochs
Monthly Notices of the Royal Astronomical Society, 406, 2421 (2010) arXiv:0911.2219

Yahya, S., **Marta S.**, Santos M., Okouma, P., Maartens R. and Basset B.
Dark energy measurements with SKA HI galaxy surveys.
Submitted to Mon. Not. R. Astron. Soc.

Silva, M.B., Santos, M.G., Pritchard, J.R., Cen, R. and Cooray, A.
Probing the first galaxies with the Square Kilometer Array
Astronomy & Astrophysics, Volume 527, id.A93, 13 pp., (2011) arXiv:1009.0950

Silva, M.B., Santos, M.G., Pritchard, J.R., Cen, R. and Cooray, A.
Probing the Very First Galaxies with the SKA.
In Joint European and National Astronomy Meeting (JENAM)/18th Annual Meeting of the European-Astronomical-Society/20th Annual Portuguese Meeting of Astronomy and Astrophysics/Symposium 7 - Square Kilometre Array (SKA), Astrophysics and Space Science Proceedings, pages 101−116. SPRINGER, January 2012.

Staniszewski, Z., Bock, J., Bradford. M., Brevik, J., Cooray, A., Gong, Y., Hailey-Dunsheath, S., O'Brient, R., Santos, M., Shirokoff, E., **Silva, M.** and Zemcov, M.
The tomographic Ionized-Carbon Mapping Experiment (TIME) CII Imaging Spectrometer
Astrophysics and Space Science Proceedings, pages 101−116. SPRINGER, May 2014.

Contents

1 Introduction

Characterizing galaxies and stars properties and evolution is a major stepping stone in the study of our Universe. There is a large variety of types of galaxies, with their different characteristics mainly set by the galaxies formation mechanisms, time of formation and age. The key to the modeling of the cosmological and astrophysical processes responsible for galaxies formation and their subsequent evolution lies in the study of the first galaxies, which were formed during the Epoch of Reionization (EoR), at a redshift $z > 6$. The EoR is a crucial stage in the history of galaxy and structure formation as it marks the ionization of the hydrogen gas in the intergalactic medium (IGM), by radiation from the first galaxies. This last major phase transition of the gas state affected the subsequent formation of bound structures and the astrophysical processes in galaxies and in the IGM. Therefore modeling the process of hydrogen reionization is essential to the study of the high redshift Universe. Currently, there are enough observations up to a redshift of $z \sim 6$, to prove that galaxies properties suffered a large evolution through time. We know that the stellar mass density evolved rapidly from $z \sim 3$ to $z \sim 1$ and that the Universe star formation rate density peaked at $z \sim 2.5$, however it is still not clear what forces drove this evolution. Due to sensitivity limitations of galaxy surveys our knowledge of galaxies properties decreases as we go to higher redshifts and so we need alternative ways to probe the first galaxies.

In this thesis I propose to use three dimensional line intensity mapping to probe the very first galaxies and to help constraining the hydrogen reionization process. This new technique promises to be very valuable to the study of the reionization process, given that intensity mapping avoids the sensitivity limitations of galaxy surveys by measuring the integrated emission of a line, at low resolution, without resolving its sources. Therefore, intensity mapping experiments will collect even the radiation from the IGM and from the relatively faint sources which are thought to be the main responsible for the reionization of hydrogen. The work shown in this thesis is centered in the planning of observational three dimensional intensity mapping experiments that aim at measuring the intensity and spatial fluctuations of the 21cm, CO(1-0), the CII, the OH and the Lyman alpha transition lines. Intensity mapping of the hydrogen 21cm line has previously been thought as a direct probe of the IGM state during the EoR and the first 21cm intensity mapping experiments are already in operation. In order to complete and confirm 21cm line observations, here we also

propose the use of the same technique in the analysis of emission lines characteristic of galaxies, emitted during the last stages of the EoR, in order to directly probe the sources of the reionization process. These studies involve the modeling of the mechanisms of line emission and the estimation of the lines intensity and spatial fluctuations using semi-numerical simulations in order to include all the astrophysics involved in the processes of line emission. Also, a thorough study of the foregrounds contaminating the observational intensity maps according to different experimental setups were made for each line. Intensity maps of several lines from the same epoch can be used to probe the different gas phases and therefore can help determining the astrophysical conditions in the interstellar and in the intergalactic medium. Given that these maps provide a tomographic view of Universe containing the spatial distribution and time evolution of the radiative emission sources, we explored how we can use them to constrain galaxy formation models and even probe the cosmological model. The final step of the studies here presented, was the analysis of the possibility of using of cross correlations between maps of different lines as a potential extra astrophysical probe and as a foreground removal mechanism.

The introduction to the subject of probing the high redshift Epoch of Reionization with three dimensional mapping of transition lines, starts with a basic description of the current cosmological model which is used to place the Epoch of Reionization in the context of Universe formation and evolution, see Section 1.1. The current knowledge about the Epoch of Reionization is presented afterwards in Section 1.2. In Section 1.3 the most direct probe of the reionization process, the neutral hydrogen 21cm line is described in detail. The potential of 3-dimensional line intensity mapping as a cosmological probe is approached in the Section 1.4. Section 1.5 describes the modeling details behind simulating emission of the 21cm, CO(1-0), CII, Lyman alpha and OH lines and the current observational constrains in the emission of these lines. In Section 1.6 the Simfast21 code which was used to perform the intensity mapping simulations shown in this thesis is presented. In Section 1.7 the foregrounds in intensity maps are described for each line. The advantages and disadvantages of building intensity mapping experiments as well as a description of intensity mapping experiments currently in planning or in operation is discussed in Section 1.8.

1.1 The first stages of the Universe formation

The high redshift Epoch of Reionization marks a fundamental stage in the process of the Universe evolution from the Big Bang till the high complexity of structures we see today. In order to understand the importance of reionization we first need to take a quick look to the first steps of the formation of the Universe as predicted by the standard cosmological model.

The Universe is thought to be approximately 13.7 billion years. When it was only about $10^{-43}s < t < 10^{-30}s$ old and composed by only vacuum energy it suffer a period of exponential expansion known as inflation which is responsible for the flatness, large scale homogeneity and isotropy we see today [1] [2]. During inflation tiny perturbations appeared in the field which latter gave origin to the density fluctuations responsible for the clumpiness of the Universe. As inflation ended the potential energy of the vacuum was converted into kinetic energy as matter and radiation were formed [3]. The post-inflation Universe was therefore composed by a very hot and dense plasma of matter and radiation. The thermal energy of this plasma was higher than the Coulomb energy and as a result electrons and protons could not bound and so electrons were free to scatter photons which resulted in an extremely small photon mean free path making the plasma opaque to electromagnetic radiation. At this time overdensities had grown considerably

originating gravitational forces which were counterbalanced by radiation pressure due to the photons being coupled to the baryons by Thomson scattering. The competition between these two forces gave origin to spherical pressure waves of the baryon-photon plasma around dark matter, similar to acoustic waves.

As the Universe expanded it cooled enough that neutral hydrogen could be formed and only a small fraction of the electrons remained free, this is known as the Recombination Epoch. Shortly after recombination photons decoupled from matter and became free to travel through the Universe forming what we now know as the Cosmic Microwave Background (CMB), this occured when the Universe was almost 400,000 years old (corresponding to a redshift of $z \sim 1100$). The CMB photons carry information about the temperature and matter fluctuations in the primordial plasma right before the decoupling [4] [5]. Also, while travelling in space the CMB photons suffer interactions with the matter and radiation in its path which slightly alters their spectrum. During decoupling, while the radiation pressure fainted the spherical waves of baryons stalled. The velocity during the release from photon drag became imprinted as density excesses in the matter density fluctuations. The scales of the overdensities depend on the plasma baryon and photon densities and so the signature left by baryon acoustic oscillations in the matter power spectra can be used as a cosmological probe.

The period between the decoupling of radiation and the formation of the first stars and galaxies is known as the dark ages and is characterized by the absence of sources of light in the Universe. During this period the matter fluctuations grew so much that the more overdense regions ended up suffering gravitational collapse and forming the first large scale bound structures, known as dark matter halos. The first stars, galaxies and quasars were formed in these halos, bringing light again to the Universe at about 13.5 billion years ago when the Universe was $\sim$180 million years old ($z \sim 20$). As the number of light sources increased their radiation ionized the hydrogen gas in its surroundings and with time the ionized regions grew and merged until more that 99% of the hydrogen in the Universe was ionized at z$\sim$6-8, this is known as the hydrogen reionization process.

1.2 The Epoch of Reionization

The term Epoch of Reionization is used to refer to the period during which the hydrogen in the Intergalactic Medium (IGM) was ionized by UV and X-ray radiation from the first stars and galaxies ever formed. This epoch was marked by complex cosmological and astrophysical events such as the formation of the large scale structures in the Universe, the birth and evolution of light sources and a phase transformation in the gas in the Universe, which all together are responsible for the evolution of the Universe into what we observe today.

If we define the EoR as the time between which the fraction of neutral hydrogen in the IGM changed from less than 1% to more than 99% then the reionization process occurred roughly from z$\sim$20-15 to z$\sim$8-6 [6] [7]. Most details of how this process occurred are still poorly known, even the timeline of hydrogen reionization is very uncertain, especially because the two main observational constraints of the EoR suggest that it ended at somewhat different times. Also, as the characteristics of light sources evolved, there may have been intercalated times dominated by processes of reionization and recombination [8].

Before reionization started the first light sources heated the gas in and outside galaxies but were not numerous enough to ionize a meaningful fraction of the IGM. As the number of stars increased their UV radiation ionized the gas in its surroundings producing spherical, homogeneously ion-

ized regions, while their X-ray radiation heated and partly ionized the IGM regions further away from galaxies producing an inhomogeneous reionization. Which regions were ionized first, if the underdense regions in the cold IGM (which are easier to ionize), or the overdense regions close to galaxies (but where there are strong columns of neutral hydrogen which act as sinks of radiation) is still not completely known. As ionized regions grew and merged, the mean free path of UV photons quickly increased, which would indicate that the reionization process should accelerate. However, the evolution of the mean IGM ionized fraction is also dependent on the density and temperature of the gas left to ionize and on whether the feedback effect caused by ionized regions on galaxies evolution had a large impact on the ionizing power of galaxies. Also, recombinations in previously ionized regions might cause the formation of filaments of neutral gas to appear, which would decrease the average ionizing filling factor of these regions. Since the hydrogen recombination time is large, for an increase of the number of neutral hydrogen atoms in ionized regions to be meaningful, there would have to be a decrease in the ionizing photon background caused by evolution of the properties of ionizing sources. Eventually, the hydrogen in the IGM became fully ionized, marking the end of the EoR and from then on neutral hydrogen is basically restricted to shielded regions inside galaxies.

The main problem for modeling reionization is to characterize the properties and evolution of the reionization sources and sinks accurately enough so that theoretical models and observations agree with each other. A standard model for the process of hydrogen reionization is still not well established since there are not enough observations to fully support a given model, see Section 1.2.4.

1.2.1 Sources and sinks of ionizing radiation

The several sources of ionizing radiation include: stellar emission, quasars, mini-quasars, supernovae explosions, structure formation and even maybe dark matter decays/annihilations.

The relative importance of quasars and stellar emission for the ionizing photon budget can be probed with a rough estimation of the number of ionizing photons necessary to complete reionization, obtained assuming that it takes one ionizing photon per hydrogen atom. High energy photons emitted mainly by quasars can ionize several hydrogen atoms each, while stellar photons can normally ionize at most one hydrogen atom. Figure 1.1, shows reasonable constraints on the contribution from stars in galaxies and from quasars to the completion of the reionization process. From this figure we can conclude that quasars appeared too late to make a large impact on the evolution of the IGM ionized fraction, although they should still be taken into account particularly for late reionization models.

Mini-quasars might have been produced from the remnants of the first stellar population, and therefore provide a source of ionizing radiation during the EoR. However, the amount of mini-quasars is constrained by the soft X-ray background to be too small to make a relevant contribution to the reionization of hydrogen [10] [11][12]. Supernovae explosions can also be a relevant source for hydrogen reionization, since the ionizing photons generated during these events are likely to have escape fractions much higher than the usual values [13]. Thermal emission due to gas shock heated during cosmic structure formation [14], or fast accretion shocks in particular during the formation of massive halos ($M \simeq 10^{10.5} M_{\odot}$) are extra sources of ionizing photons, which may show to be non-negligible to the reionization of hydrogen, although this is still a subject in discussion [15] [16]. Nevertheless, even if structure formation does not contribute much for the ionizing photon budget it will certainly heat the IGM and therefore contribute to reionization by decreasing

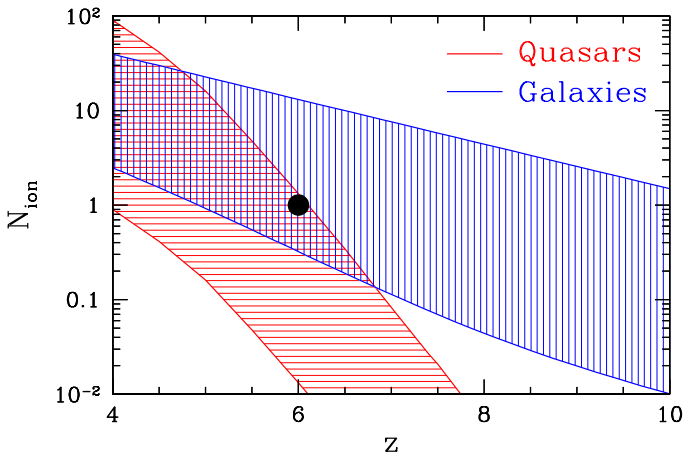

Figure 1.1: Most likely ranges for the number of ionizations per hydrogen atom from quasars (red) and galaxies (blue) based in observational luminosity functions. The lower bound for quasars assumes only the high luminosity quasars which are currently observationally detected while the upper bound is obtained by multiplying the lower bound by one hundred in order to include the contribution from lower luminosity quasars. The lower and upper bound for galaxies were obtained by assuming an ionizing photon escape fraction of 2% and 20% respectively. Note that currently higher values for the escape fraction of ionizing photons from galaxies are considered possible. The black dot corresponds to the minimum conditions to terminate reionization at z = 6. Figure taken from Trac & al. (2007) [9].

the hydrogen recombination rate. Heating and ionizations by dark matter decays/annihilations is possible, yet it will only be relevant for reionization in the case of considering some strange form of dark matter particle since the impact of a more normal candidate such as a WIMP (Weakly Interacting Massive Particle) is considerably small [17].

Taking into consideration all of the possible sources of ionizing photons previously described it is clear that the main sources of hydrogen reionization were stars. There is however the need to characterize the two populations of stars involved in the reionization of hydrogen: POP III stars and POP II stars. The first population of stars, known as POP III stars, were formed from pristine primordial gas uncontaminated by metals. These stars were solely composed by hydrogen, helium and small traces of lithium and beryllium, but they produced heavier metals which were expelled into the IGM and therefore the second population of stars, POP II stars, already had a small percentage of metals which affected their properties and evolution. Population III stars are thought to have been very massive and of having a very high emissivity, and so despite their small number density they should have been able to ionize a large part of the hydrogen in the Universe. It is however difficult to analyse the properties of these stars, since they can no longer be observed either because they were all very massive and already died or because their outer layers were later contaminated by metals and these stars are now wrongly classified as POP II stars. Population II stars are likely to have been important during a large part of the hydrogen reionization process and their properties are considerably better known than those of the first population of stars. Since POP II stars are considerably less powerful than POP III stars, during the transition between these two populations, there might have been a small period of time when the ionizing photon background and even maybe the IGM ionized fraction decreased instead of increasing.

There exist reasonable models of stellar mass functions for each stellar population, although setting the mass limits especially in POP III stars is still debated. Usually a Salpeter mass function with an upper limit of 100 to 150 $M_\odot$ is used for POP II stars, while a more top-heavy formula such as a Larson or a Kroupa stellar mass function with an upper limit of 150 to 300 $M_\odot$ is used for POP III stars. Stellar lifetimes and ionizing emissivities based in non thermodynamic equilibrium models for the two stellar populations can also be found in several publications [18] [19] [20], although, these predictions are likely to be highly dependent of the stellar type. Also, using average values in reionization simulations will not take into account that these quantities are correlated with other parameters relevant for the study of reionization such as the ionizing photon escape fraction.

1.2.2 Probes of the Epoch of Reionization

Current observational probes of the Reionization Epoch include the Lyα Gunn-Peterson opacity, the electron scattering optical depth measured in CMB experiments, the UV Background intensity, redshift evolution of Lyman Limit systems, the IGM temperature evolution, the IGM metallicity, the cosmic star formation history, high-z galaxy counts and the Near Infrared Background. In the near future intensity mapping of emission lines will also be used to probe the EoR.

The number of EoR probes might be high, however the constrains they put in the reionization process are very modest. As an example, the main current observational probes of the reionization process only weakly constrain its timeline. The optical depth to reionization measured by CMB experiments like the WMAP [21] and the Planck [22] missions gives an overall measure of the number density of free electrons, which according to its current better value of ($\tau > 0.075$) sets the instantaneous reionization process to a redshift as high as $z \sim 11$. If we assume that the ionized fraction of gas increased continuously, this value would indicate an early reionization history with the Universe being fully ionized at $z = 8$ or at most at $z = 7$. Early reionization histories are however contradicted, first by observations of an absorption feature in the spectra of high redshift quasars which indicates meaningful evolution of the IGM ionized fraction from $z \sim 7 - 6$, and also in the last few years by observations of Lyman alpha emitters and Lyman alpha drop outs which show an evolution in these signals consistent with an evolution of the IGM ionized fraction (x_i) of up to 0.5 from $z \sim 7 - 6$, in this way delaying the end of hydrogen reionization to $z = 6$. The constraints in the reionization timeline due to observations of quasars and galaxies spectra is statistically limited given the small number of observations and it is still uncertain if the absorption of Lyman alpha photons by neutral hydrogen near these sources is the result of a large evolution in the IGM ionized fraction between z $\sim 7 - 6$ or if it can be explained in an alternative way such as a more modest evolution of the ionizing background as suggested by Mesinger et al. (2014) [23]. Which basically means that either the ionized regions had not yet time to fully cover the IGM, or that due to a decrease in the ionizing background the rate of recombinations temporarily dominated over the rate of ionizations, and so the percentage of neutral hydrogen gas inside ionized regions increased. Several other explanations are given for the evolution of galaxies spectra, some of which do not imply a high evolution in the IGM ionized fraction (see Section 1.5.4 for alternative explanations), and so for now it is more reasonable to assume an evolution in the IGM ionized fraction $x_i \leqq 0.1$ from $z \sim 7 - 6$ in order to insure that reionization models are compatible with the current constraints in the optical depth to scattering by free electrons.

Galaxy surveys can only probe the end of the EoR and as the redshift increases they are limited to observe only the high end of the galaxies luminosity function, whereas the galaxies thought to

be responsible for reionization have more modest masses. This is a big problem, since for example the star formation rate density (SFRD) constrained from current observational luminosity functions (LFs) is slightly too small to explain how all of the hydrogen in the Universe was ionized at $z > 6$, which seems to indicate that the low end of the galaxies luminosity function is being underestimated. Nevertheless, galaxy surveys are essential to characterize galaxy formation mechanisms and the astrophysical conditions of the gas in the ISM. They are also needed to clarify how the environment conditions affected the processes of star formation and to probe other astrophysical parameters essential to the study of high redshift galaxies. Large galaxy datasets can also be used to probe the dark matter halos mass function, the galaxy bias, the non linear component of the matter density field, and others. Observations of the infrared background can be used to probe the EoR since part of this radiation is the result of redshifted photons emitted in the UV at $\mathrm{z} > 6$, and so these observations can impose upper limits in the overall ionizing photons emission at high redshifts.

These are however indirect probes of the reionization process, and in many cases the measurements are still uncertain and so they cannot provide strong constraints to the modeling of the EoR. Therefore, there is a pressing need for a more direct probe of the high redshift Universe, such as intensity maps of spectral lines. Till now there are still no available observational intensity maps of any line emitted during the EoR, however the first intensity mapping experiments that will directly probe this epoch by detecting 21cm line emission: (LOFAR [24], MWA [25] PAPER [26] and GMRT [27]) are operating and we soon expect the first detection of the signal.

By making three dimensional maps of the 21cm line at several redshift steps, observational 21cm experiments will allow to directly measure the evolution of IGM ionized fraction, the size and shape of ionized regions and the neutral fraction in ionized regions. A statistical analysis of these maps will also probe the non linear dark matter density power spectra and give extra insight on the evolution of the properties of sources and sinks of ionizing photons. The intensity mapping technique was first thought for the 21cm line, but it can also be applied to other lines, such as the CO, the CII and the Lyman alpha lines and therefore it can be used to probe the different phases of the gas at high redshift. Intensity mapping of several emission lines greatly increases the potential of these experiments to properly characterize galaxies and the ISM and IGM gas properties, at least during the end of the EoR.

1.2.3 Why probing the Epoch of Reionization with Intensity Maps

Several studies of the EoR agree that most of the ionizing radiation responsible for the hydrogen reionization process was originated in relatively low mass galaxies. Therefore, given the intrinsic limitations of photometric and spectroscopic galaxy surveys these experiments will not be able to detect and characterize the sources of reionization. The intensity mapping technique has the advantage of measuring the overall intensity and spatial fluctuations of a spectral line from a given redshift, with a low resolution, and so it will detect radiation originated even from the more faint galaxies and from the IGM. Intensity maps of emission lines originated from galaxies, such as the CO and the CII lines, can be used to detect and characterize the first galaxies, while intensity maps of lines emitted mainly from the IGM, such as the 21cm line from neutral hydrogen, can be used to characterize the IGM gas properties as well as to measure the morphology, evolution and spatial fluctuations of the ionization field. The 21cm line has two characteristics which make it a particular promising probe for the study of the EoR, first this is an hydrogen line and so it was abundant even in the beginning of the EoR and second the 21cm line emitted from the EoR and

the Pre-EoR will be observed in the radio band at such a large wavelength that no other relevant emission line will contaminate its observations. There will nevertheless be contamination to 21cm intensity maps originated in continuum emission from galaxies. Just the contamination from our galaxy will be orders of magnitude higher than the 21cm signal [28].

The effects caused in the power spectra of spectral lines by the several astrophysical quantities which contribute to their intensity will be very difficult to disentangle, just with intensity maps of one line. Therefore intensity mapping of two ore more lines will be very important to successfully constrain astrophysical quantities. In particular, at the end of the EoR the intensity mapping technique can be applied to the hydrogen 21cm, CO(1-0), CII and Ly-α lines discussed in Section 1.5. With intensity mapping of these lines we can constrain several astrophysical quantities such as the temperature of the ISM and of the IGM, the SFRD, the escape fraction of ionizing photons and Lyman alpha photons, the metallicity of the ISM, the clumping of the IGM and others [29] [30] [31]. Observational intensity maps of several lines can also be cross correlated with each other or with galaxy maps in order to obtain a statistical measurement free of foregrounds.

The statistical power spectra of spectral lines, obtained from intensity maps, can also provide constraints to several cosmological parameters since the fluctuations in the intensity of a line are correlated with the underlying dark matter density fluctuations. General advantages and disadvantages of the intensity mapping technique will be discussed in detail in Section 1.8.

1.2.4 A standard model for Reionization

Constructing a standard model for the EoR means basically to establish what was the timeline of the hydrogen reionization process, to characterize the ionizing photon sources and sinks and to determine what was the size, morphology and evolution rate of ionized regions during the EoR.

As was already referred in Section 1.2.2 the timeline for reionization is still poorly known. The beginning of reionization is dependent on the characteristics and abundance of POP III stars at very high redshifts and so there is a pressing need to better characterize this stellar population. There are observational constraints of the end of the EoR, however different observations seem to point at reionization terminating at fairly different times. Therefore, the modeling of the EoR should be made using a physically based description for the reionization sources while ensuring that the final predictions are compatible with reionization ending at $z \geq 6$. In practice, this can be made by including evolving POP II and POP III stars as sources of ionizing radiation as well as using a proper description of reionization sinks, although taking into account feedback from ionized regions is also recommended [32].

The improved constraints in the evolution of the IGM ionized fraction, which will hopefully soon be obtained, will help to distinguish between different reionization models since they can be used to differentiate between models with top heavy or normal mass functions, to determine if reionization occurred in two phases or all at once and even to confirm whether low density regions were ionized before dense regions and therefore to distinguish between inside-out, outside in and filament-last models [33]. The signatures of different reionization models in the evolution of the IGM ionized fraction and in the shape of the power spectra of spectral emission or absorption lines, should therefore be identified with numerical and semi-numerical simulations and implemented in codes, which can be used to interpret the data obtained by intensity mapping experiments.

1.3 The neutral hydrogen 21cm line

The 21cm line corresponds to the energy released or absorbed during a forbidden transition in neutral hydrogen. The number of these transitions, and therefore the quantity of neutral hydrogen, can be measured as a temperature off-set against the temperature of the CMB. When radiation from the CMB crosses a path of neutral hydrogen the change in the radiation energy and temperature caused by 21cm transitions referred to as brightness temperature fluctuations is given by:

$$\delta T_{\rm b}(\nu) = \frac{T_S - T_{\rm CMB}(z)}{1+z}(1 - e^{-\tau_\nu}) \tag{1.1}$$

where $T_{\rm S}$ is the excitation temperature of the 21cm transition, usually referred to as the spin temperature and τ_ν is the 21cm optical depth of the diffuse IGM gas expanding uniformly with the Hubble flow, given by:

$$\begin{aligned} \tau_\nu &= \frac{3}{32\pi}\frac{h_p c^3 A_{10}}{k_{\rm B} T_{\rm S} \nu_0^2}\frac{x_{\rm HI} n_{\rm H}}{(1+z)(dv_\parallel/dr_\parallel)} \\ &\approx 0.0092(1+\delta)(1+z)^{3/2}\frac{x_{\rm HI}}{T_{\rm S}}\left[\frac{H(z)/(1+z)}{dv_\parallel/dr_\parallel}\right], \end{aligned}$$

where $A_{10} = 2.85 \times 10^{-15} s^{-1}$ is the spontaneous decay rate of the 21cm transition, $x_{\rm HI}$ is the neutral fraction of hydrogen, $k_{\rm B}$ is the Boltzmann constant, $h_{\rm p}$ is the Planck constant, ν is the rest frequency of the 21cm line, $(1+\delta)$ is the fractional overdensity of baryons and $dv_\parallel/dr_\parallel$ is the gradient of the proper velocity along the line of sight which includes both the Hubble expansion and the peculiar velocity.

From equations 1.1 and 1.2 it follows that brightness temperature fluctuations along the line of sight are given by:

$$\delta T_{\rm b}(\nu) \approx \frac{T_{\rm S} - T_{\rm CMB}}{1+z}\tau_{\nu_0} \approx 9 x_{\rm HI}(1+\delta)(1+z)^{1/2}\left[\frac{1 - T_{\rm CMB}}{T_{\rm S}}\right]\left[\frac{H(z)/(1+z)}{dv_{||}/dr_{||}}\right]. \tag{1.2}$$

1.3.1 Spin Temperature

The spin temperature of the 21cm transition of neutral hydrogen is regulated by three competing processes: absorption or emission of CMB photons, collisions with other hydrogen atoms, free electrons and protons and scattering of Lyman alpha photons. The first process drives $T_{\rm S}$ into the $T_{\rm CMB}$ while the second and third processes drive $T_{\rm S}$ into the gas kinetic temperature ($T_{\rm K}$). Since the relevant scales for these processes are much shorter than the expansion time equilibrium is a very good approximation. The spin temperature will therefore have a value between $T_{\rm CMB}$ and $T_{\rm K}$ depending on the coupling coefficients for collisions ($x_{\rm c}$) and scattering of Lyman alpha photons (x_α) according to the relation:

$$T_{\rm S}^{-1} = \frac{T_{\rm CMB}^{-1} + x_{\rm c} T_{\rm K}^{-1} + x_\alpha T_{\rm K}^{-1}}{1 + x_{\rm c} + x_\alpha}. \tag{1.3}$$

The radiative coupling coefficient is caused by the Wouthuysen-Field mechanism which is ba-

sically the redistribution of the electrons between the hyperfine states in neutral hydrogen due to absorption and re-emission of Lyman alpha photons and so it depends on the Lyman alpha emissivity. The collisional coupling coefficient depends on the number densities of the intervenients (hydrogen atoms and electrons), as well as in their kinetic energy which is set by the CMB and the gas temperatures. Collisional coupling is mainly important for high redshifts (typically $z \simeq 25$) where the density is high, while radiative coupling can be important till a redshift as low as ($z \lesssim 10$) depending on the SFRD evolution and on the galaxies spectral emission.

1.3.2 IGM ionized fraction evolution

One of the main results from 21cm experiments will be measuring the IGM ionized fraction which can be used to probe astrophysical properties of galaxies and their evolution. Current constraints in the evolution of the ionization field from CMB surveys, indicate that there should be a considerable part of the Universe ionized at $z \sim 11$, while other observational constraints impose reionization to end the later at $z \sim 7 - 6$. A detailed study of the evolution of the IGM ionized fraction should take into account all of the sources of ionizing photons and include also a detailed description of its sinks however given the uncertainy of the contribution from most ionizing photon sources it is reasonable to discuss the evolution of the IGM ionized fraction by only considering ionizing photons originated in stellar emission and by using a simplified estimation of the rate of recombinations in the IGM.

The evolution of the average IGM ionized fraction is balanced by the number density rate of ionizations ($\dot{n}_{\rm ion}$) and the number density rate of recombinations ($\dot{n}_{\rm rec}$) as:

$$\frac{\delta x_i}{\delta t} = \frac{\dot{n}_{\rm ion} - \dot{n}_{\rm rec}}{n_{\rm H}} \cong \frac{A_{\rm He}}{n_{\rm H}} \int_{M_{\rm min}}^{M_{\rm max}} dM \frac{dn}{dM}\, SFR\, Q_{\rm ion}\, f_{\rm esc} - \alpha_{\rm rec} C n_{\rm e} n_{\rm HII}, \tag{1.4}$$

where $n_{\rm H}$ is the number density of hydrogen atoms and the number density of ionizing photons emitted by each dark matter halo that escape into the IGM depends on the halo SFR, on the number of ionizing photons emitted per solar mass in SFR ($Q_{\rm ion}$), on a correction factor which accounts for helium ionizations ($A_{\rm He}$), on the halo mass function and on the average escape fraction of ionizing photons ($f_{\rm esc}^{\rm UV}$). The number rate of recombinations is a function of the local values of the ionized hydrogen gas clumping factor in the IGM ($C \equiv \langle n_{\rm HII}^2 \rangle / \langle n_{\rm HII} \rangle^2$), of the average free electron number density (n_e) and of the temperature dependent comoving recombination coefficient which is given by:

$$\alpha_{\rm rec} = (2.6 - 4.2) \times 10^{-13} \left(T_{\rm K}/10^4 K\right)^{-0.7}\ {\rm cm^3 s^{-1}}, \tag{1.5}$$

where the value 2.6 is appropriate for recombinations distributed uniformly in the IGM while the factor 4.2 is appropriate for recombinations in very dense partly neutral gas (Lyman limit systems). Equation 1.4 can be used to obtain an estimate of the evolution of the IGM ionized fraction or to study the evolution of an ionized region around a single source, however it cannot be so easily applied in a scenario with merging of ionized regions or with feedback. Also, the time scale of recombinations ($t_{\rm rec} = \alpha_{\rm rec} n_{\rm HII}[1 + {\rm Y}/4{\rm X}]$, where the mass fraction of hydrogen is ${\rm X} = 0.75$ and the mass fraction of helium is ${\rm Y} = 0.25$ [9]) should introduce a correction factor in the effective number of recombinations in the case of integrating equation 1.5 in small periods of time.

1.3.3 The 21cm signal from the pre-Reionization Epoch

The pre-Reionization Epoch ($30 \gtrsim z \gtrsim 20$) is characterized by the very first population of stars, emitting enough radiation to ionize only its immediately surroundings and so during this time there is no detectable growth of ionized regions [34]. This period can only be probed with observations of the 21cm line from hydrogen emitted/absorbed in galaxies. The properties of the first light sources and their capability of heating/ionizing the surrounding gas set the spin temperature of the 21cm transition somewhere between the CMB and the gas temperature. The 21cm line is observed against the CMB radiation and so it will not be observed if $T_{\rm S}$ is strongly coupled to $T_{\rm CMB}$ and it will be observed in emission or in absorption depending on weather $T_{\rm S}$ is above or below $T_{\rm CMB}$. The evolution of the 21cm line intensity and spatial fluctuations in this period was therefore highly dependent on the timeline of the heating and ionization processes.

Depending on the model used, the 21cm line intensity evolution may show an absorption feature between ($25 \gtrsim z \gtrsim 20$) which can help to constrain the spin temperature contribution to 21cm signal fluctuations. This feature is usually predicted by reionization models which assume a halo ionizing efficiency linearly dependent on the halo mass. Using more realistic prescriptions for the halos ionizing emissivity can result in a higher heating of the IGM during the pre-EoR causing a shift of 21cm signal absorption feature to higher redshifts or even completely erasing it. Also, just by adding a higher variability to the ionizing power of each halo, the power spectra of the 21cm line would change considerably compared to what is usually predicted. These effects are particularly important for the planning of the 21cm Dark Ages Radio Explorer experiment (DARE) [35], which proposes to measure the frequencies and slopes of the 21-cm sky-averaged spectrum and to the second generation Square Kilometer Array (SKA) [36], which proposes to make intensity mapping measurements of the 21cm line from the pre-EoR.

Disentangling the astrophysical and cosmological contributions to the 21cm signal power spectra is a difficult challenge. However, at $z > 20$, there is a possibility to do it by assuming an expansion of the 21cm signal fluctuations till a low order and than separating the power spectra in its angular components [37] [38]. At lower redshifts higher order contributions to the 21cm line will become increasingly important and this separation might no longer be possible.

1.3.4 Evolution of brightness temperature fluctuations

During the dark ages all the gas in the Universe was neutral and the spin temperature of the 21cm transition was coupled to the CMB temperature and so the 21cm signal from this period cannot be detected against the CMB. When the first galaxies appeared, in the Pre-EoR, they emitted photons between the Lyman limit and the Lyman alpha frequencies which redshift into the Lyman alpha line in the IGM coupling the spin temperature of the 21cm line to the gas temperature. At this point we expect the 21cm signal to be seen in absorption with its fluctuations dominated by Lyman alpha fluctuations [39]. Somewhat latter stellar X-rays heated the IGM gas locally which produced large inhomogeneities in the gas temperature. At this point, collisional and radiative coupling deviated the spin temperature from the CMB temperature towards the gas temperature. The fluctuations in the 21cm signal during the pre-EoR period were therefore dominated by fluctuations in the spin temperature. With time the light sources increased in number and mass and the reionization process started with the ionization of hydrogen in the IGM around galaxies, at $z < 20$. During the EoR, the contribution from spin temperature fluctuations to the 21cm signal began to saturate and so the 21cm signal become dominated by fluctuations in the IGM neutral fraction and in

the density. At this time the 21 cm signal can be seen in emission against the CMB. After the end of the EoR ($z \sim 8-6$), the 21cm signal became restricted to emission from galaxies and so brightness temperature fluctuations became dominated by matter density fluctuations and by the number density of galaxies containing HI. Also, peculiar velocities cause fluctuations in the observed 21cm signal, especially during the end of the EoR. The timeline of these events is highly discussed and depends on the several yet unknowns of the EoR, therefore in order to model the evolution of the 21cm signal it is important to properly model the mechanisms that drive the spin temperature and the IGM ionized fraction using realistic models for the reionization sources.

The time evolution of matter density fluctuations is mainly a result of the growth of overdense regions, and so at large scales it translates to a reasonably well known linear increase in the amplitude of fluctuations, however at small scales there is also a non linear component to the fluctuations and so even when the 21cm signal fluctuations are dominated by the contribution from matter density, both the shape and the amplitude of its power spectra will suffer time evolution.

1.3.5 The 21cm signal power spectra

The 21cm signal power spectra will soon be observationally obtained and therefore it is important to analyse the individual contributions to this statistical measurement. The power spectra of 21cm fluctuations is defined as $P_{21}(\mathbf{k}]) = \langle|\delta_{\mathrm{T}_{21}}(\mathbf{k})|^2\rangle$ where $\delta_{\mathrm{T}_{21}}$ are the fractional fluctuations in the 21cm temperature. To a first order approximation the fluctuations in the temperature of the 21cm signal (also known as brightness temperature fluctuations) are given by:

$$\delta_{\mathrm{T}_{21}} = \beta_{\mathrm{b}}\delta_{\mathrm{b}} + \beta_{x_{\mathrm{HI}}}\delta_{x_{\mathrm{HI}}} + \beta_{\alpha}\delta_{\alpha} + \beta_{\mathrm{T_K}}\delta_{\mathrm{T_K}} - \delta_{\partial \mathrm{v}}, \tag{1.6}$$

where we are taking into account fluctuations in the baryon density (b), the neutral fraction of hydrogen in the IGM (x_{HI}), the Lyman alpha coupling coefficient (α), the gas temperature ($\mathrm{T_K}$), and the line-of-sight peculiar velocity gradient (∂v) [40].

Before the reionization process started, $\delta_{\mathrm{T}_{21}}$ was dominated by fluctuations in $\mathrm{T_K}$. As the ionization of hydrogen in the IGM was initiated $\delta_{\mathrm{T}_{21}}$ become dominated by the evolution of x_{HI} and δ_b, and so the shape of the 21cm signal power spectra was set by the relative contribution from these two sources. At the end of Epoch of Reionization ($\mathrm{z} \lesssim 8$), ∂v became increasingly strong causing line of sight distortions in the observed angular power spectrum, which can be used to separate the 21-cm signal contributions according to their angular dependence [37] [38]. In the post Reionization Epoch $\delta_{\mathrm{T}_{21}}$ become dominated by fluctuations in the amount of neutral hydrogen in galaxies

Additional contributions to the observed 21cm signal power spectra during the EoR include for example distortions caused by weak gravitational lensing due to very large-scale structures. These distortions increase the three-dimensional 21cm power spectra mainly at scales ($\mathrm{k} > 1\mathrm{hMpc}^{-1}$) [41].

1.3.6 The 21cm signal from galaxies

The EoR is characterized by the ionization of hydrogen in the IGM however there is also neutral hydrogen in galaxies emitting in the 21cm line. During the pre-EoR, the first light sources began heating the IGM but were not enough to efficiently ionize it, and so the 21cm signal from this epoch can only be detected in and around galaxies where the coupling of the 21cm line spin temperature to the gas temperature was higher. As ionized regions grew around galaxies during the Epoch of

Reionization the situation changed and the 21cm signal intensity and fluctuations become strongly dominated by emission from the IGM while in comparison the 21cm signal from galaxies become negligible. When the reionization process ended, there was no more 21cm emission from the IGM and so the emission in this line become restricted to emission from galaxies.

The intensity of the 21cm signal from the pre-EoR depends mainly in the amount of radiation emitted by light sources which was responsible and so it can be estimated from the galaxies overall ionizing power. In the post-EoR the 21cm signal intensity and spatial fluctuations is proportional to the neutral hydrogen (HI) gas content of galaxies and therefore can be obtained from the HI density ($\rho_{\rm HI} = m_{\rm HI}\rho_c$ where ρ_c critical density) using:

$$\bar{T}_{\rm b}^{\rm G} = C(z)\frac{\rho_{\rm HI}}{X_H\rho_b}({\rm mK}), \tag{1.7}$$

where $\mathrm{C(z)} \sim 23(1+\mathrm{z})^{1/2}$ is independent of the location in the sky but depends slightly on the cosmology and scales with redshift. The HI mass density can be estimated assuming that it scales with halo mass and than integrating the HI mass in each galaxy over the halo mass function using:

$$\rho_{\rm HI} = \int_{M_{\rm min}}^{M_{\rm max}} dM \frac{dn}{dM} M_{\rm HI}(M), \tag{1.8}$$

where $M_{\rm max}$ and $M_{\rm min}$ are the maximum and minimum masses of halos and dn/dM is the halo mass function. In reality the HI mass in each galaxy depends not only on its mass, but also on its angular momentum and formation history as has been shown observationally using galaxies surveys and simulated using physical prescriptions (such as was done by Obreschkow et al. (2009) [42] using the galaxies in the DeLucia & Blaizot (2007) simulated catalog [43]). The intensity of 21cm emission from galaxies can also be obtained from the matter density fluctuations using:

$$T_b^{\rm G}(\mathbf{x}) = \bar{T}_b^{\rm G}(\mathbf{x})\left[1 + b_{\rm HI}\right]\delta(\mathbf{x}), \tag{1.9}$$

where the HI bias with halo mass ($b_{\rm HI}$) is a crucial parameter for the planning of 21cm experiments, which has only been properly constrained by observations at $\mathrm{z} < 1$.

In right panel of figure 1.2 we can observe the prediction of the HI bias evolution with redshift for several cuts in flux obtained using the Obreschkow et al. (2009) [42] simulated galaxies catalog. This figure shows how galaxy surveys, which are intrinsically flux limited, will have difficulties at measuring the overall HI bias at $z > 1$. The increase in bias with flux cut observed in this figure is a result of the HI emission being dominated by increasingly larger galaxies and the increase in bias with redshift indicates that the average HI content of a galaxy with a given mass increases with redshift as expected. The clustering power spectra of 21cm emission by galaxies is given by:

$$P_{\rm HI}^{\rm G}(z,k) = \left[\bar{T}_b^{\rm G}(\mathbf{x})\right]^2 b_{\rm HI}^2 P(z,k), \tag{1.10}$$

and the shot noise due to the discretization of galaxies is given by:

$$P_{\rm HI}^{\rm shot}(z) = \int_{M_{\rm min}}^{M_{\rm max}} dm \frac{dn}{dm}\left[c(z)\frac{M_{\rm HI}}{X_{\rm H}\rho_{\rm b}}\right]^2. \tag{1.11}$$

The total galaxies power spectra is a sum of the two components:

$$P_{\rm HI}^{\rm tot}(z) = P_{\rm HI}^{\rm cross}(z) + P_{\rm HI}^{\rm shot}(z) \tag{1.12}$$

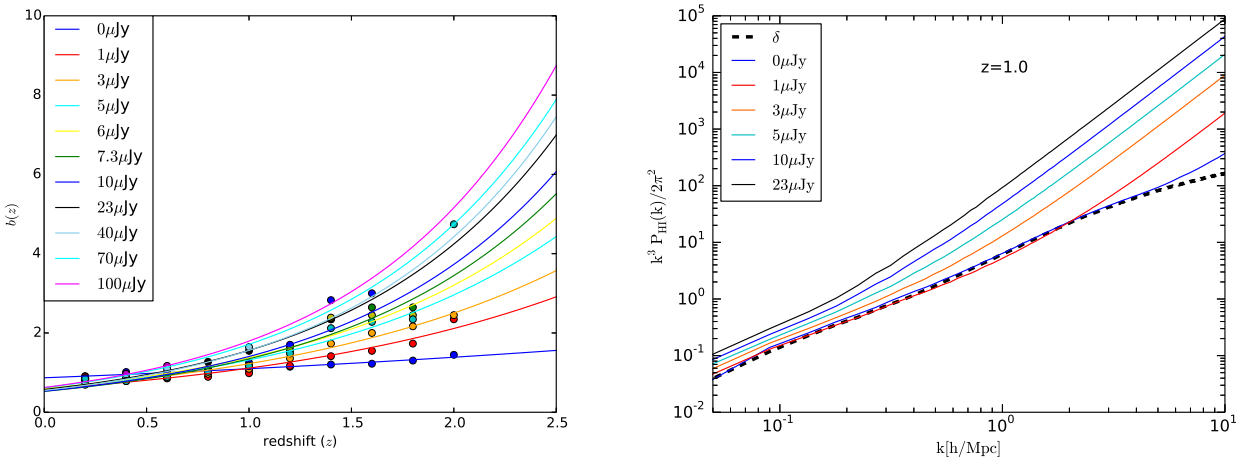

Figure 1.2: Left panel: HI bias obtained with the HI masses in the [42] galaxies catalog according with different lower cuts in HI flux (figure taken from Yahya et al. in prep.). Right panel: Dimensionless HI galaxy power spectrum for different sensitivities at z=1 (solid lines). Black dashed line shows the dark matter power spectrum from CAMB at z=1.

In left panel of figure 1.2, the HI power spectra at $z = 1$ for several flux cuts is presented, together with the matter power spectra. The increase in the fluctuations amplitude for higher fluxes is a result of the sources in the sample having an average higher mass and the shot noise contribution is increasing due to the number of sources being decreasing.

The post reionization 21cm signal can be used to probe cosmology by measuring the increase in power at the scale of the first Baryon Acoustic Oscillations peak which can later be used to constrain the dark energy equation of state, see Section 1.4.3.

1.4 Intensity mapping as a cosmological probe

The cosmological and astrophysical potential of studying the EoR is directly linked to the EoR model, the tracer used to probe the evolution of the ionization field and to the technology available to construct reionization experiments.

Both the matter density fluctuations and the growth of bound structures are a result of the constituents of the primordial plasma, their spatial perturbations and their physical properties. The locations of the sources of reionization and the evolution of the ionization field are correlated respectively to the peaks and to the fluctuations in the density field. The power spectra of the intensity of a line, which can be obtained from intensity maps, will trace the fluctuation in the matter power spectra and so it can be used to probe cosmological parameters and the conditions in the early universe. Probing cosmology with intensity maps requires a considerable level of accuracy in the extraction of the matter power spectra from these maps. Therefore, there are scales, redshifts and emission lines which optimize the probability of constraining cosmology with intensity maps from the EoR. As an example, for the 21cm signal, the best redshifts to probe cosmology are when the matter fluctuations contribution to the power spectra dominates over the ionization fraction contribution, because otherwise it will be difficult to disentangle these two contributions, given that the second and third order terms to the 21cm signal power spectra will

be too high to ignore. This corresponds to either the pre-EoR, to the end of the EoR when the 21cm signal is easier to measure, or to the post-Reionization Epoch when the 21cm signal is only be emitted from galaxies. The best scales to probe cosmology with intensity mapping of emission lines are usually around $k \sim 1\mathrm{hMpc}^{-1}$, or even less if we consider an experiment with a large field of view like the SKA, since for very high scales the statistics is low and for lower scales the experimental errors are high. Also, on very large scales the light cone effect will increase the power spectra intensity making it very difficult to accurately constrain any parameter unless this effect is accounted for [44]. Cosmic variance and shot noise due to galaxy discretization will however add complication to the cosmological analysis of power spectra extracted from intensity maps.

From the other lines discussed in this thesis the CO(1-0) line is the most promising to probe cosmology since it is emitted only from molecular gas in galaxies and so it is easier to interpret the CO power spectra in terms of its cosmological and astrophysical components.

1.4.1 The matter power spectrum

Under the standard inflationary model, the primordial fluctuations have a power spectra shape given by $P(k) = Ak^{\mathrm{n}-1}$, where n in close to 1 and A is observationally constrain by CMB observations to be $A^{1/2} \sim 2.45 \times 10^{-9}$ at k= $0.02\mathrm{Mpc}^{-1}$. As perturbations grow the large scale power spectra evolves as the square of the growth factor and this evolution is termed linear evolution. At small scales there is a non-linear gravitational growth of perturbations and so besides the linear increase in amplitude there is also an extra increase in power towards low scales which changes the shape of the power spectra.

We can probe the matter power spectra with signals which are biased to density fluctuations, such as the intensity fluctuations in maps of the 21cm line or of other transition lines. Locally, the emission of these lines will also depend on several astrophysical quantities, however at large enough scales the fluctuations in their intensity should only be proportional to matter density fluctuations. Three dimensional intensity maps of transition lines can be observationally obtained by intensity mapping experiments and so we can expect to be able to probe the matter power spectra from the power spectra of these lines. The study of the evolution on the non-linear power spectrum can be used to reject inflation models, warm dark matter models and neutrinos [45] [46] [47].

1.4.2 Dark matter particle models

Recent studies of indirect methods of dark matter detection have considered using signatures of dark stars and of dark matter decay/annihilations in the CMB or in the 21cm signal during the EoR. Dark stars are basically stars mainly fuelled by annihilations of dark matter particles, which might have been formed in the Pre-EoR and in the beginning of the EoR. The existence of dark matter in the first population of stars would facilitate the initial baryonic collapse and the cooling and contract of baryons during star formation, which would increase the gravitational potential of the star attracting even more dark matter. The result of dark matter powering a star would be the size and the luminosity of the stars increasing to very high values. A large amount of dark stars could influence the history of reionization by increasing the heating and ionizations at high redshifts. However, even if these stars exist it will be difficult to distinguish their effects in the IGM from the effects caused by normal POP III stars with a high ionizing efficiency or with a very heavy stellar initial mass function [48]. Nevertheless, it was noted that the strong luminosity of very powerful dark stars could potential affect the ionization of the stars surroundings by changing

the morphology of the ionized regions and so they produce a signature in the power spectra of the 21cm line at very high redshifts which can be detected with an experiment like the SKA [49]. The contribution of dark stars to hydrogen reionization would also increase the optical depth to scattering by free electrons which can be used to rule out the more extreme dark stars scenarios where more than 90% of the star forming baryons are in dark stars and dark stars with lifetimes higher than 250 Myr (calculation made with WMAP7 constraints Schleicher et al. 2009) [49].

Heating and ionizations by dark matter particles is a more likely scenario and would affect the 21cm intensity evolution during the Pre-EoR by heating the gas in an earlier phase compared to the case where is only considered stellar heating. This extra heating and ionizations would also alter the power spectra of 21cm line fluctuations even in later times during the EoR [50]. The effect of dark matter decay/annihilations in 21cm line observables is however highly dependent on the properties of the dark matter particles. Therefore, a detectable effect would require a reasonable candidate for the dark matter particle, such as a WIMP, but with properties very close to the current values not yet excluded by experiments such as a $3 \times 10^{-26}\mathrm{cm}^3\mathrm{s}^{-1}$ cross section and a $30\mathrm{GeV}$ mass [51] or some strange form of dark matter particle.

1.4.3 Baryon acoustic oscillations

Baryon acoustic oscillations can be used as standard rulers to measure distances and so it can be used as a cosmological probe. In the primordial plasma right before decoupling the spherical shells of baryons and photons around dark matter propagated outwards as acoustic waves with a velocity of $c_\mathrm{s} = c/(3 + 3R_\mathrm{s})^{1/2}$ where the radius of the spherical shells is set by the baryonic and radiative densities as $R_\mathrm{s} \equiv 3\rho_\mathrm{b}/4\rho_\gamma \propto \Omega_\mathrm{b}/(1 + z)$ (where c is the light velocity, ρ_b is the baryonic matter density, ρ_r is the radiation density and Ω_b is the baryonic matter density relatively to the critical density). After decoupling the power spectra of baryonic matter fluctuations has an excess at a scale correspondent to R_s, and since dark matter and baryonic matter interact through gravitational attraction, dark matter also preferentially clumps at the R_s scale. The correlation scale of BAO is $\sim 105\mathrm{h}^{-1}$ and so the first BAO peak can be observed at $k \sim 0.06\mathrm{hMpc}^{-1}$. The first BAO peak can be detected in the 21cm power spectra during the end of the EoR however at this scale the contribution from the fluctuations in the IGM ionized fraction will reduce the accuracy at which this measurement can be made. In the post reionization epoch the correlation between the 21cm signal and the matter power spectra will be strong however non linearities in the power spectra might shift the BAO scale, also contamination from other emission lines such as OH lines might become important [52].

Measuring the BAO peaks with the CMB can tell us about deviations in the homogeneity of the primordial plasma, and therefore it can be used to probe non-gaussianity from inflation. Also, measuring the excess in the matter power spectra at the first BAO peak with galaxy surveys or with intensity mapping of lines can be used to measure the angular diameter distance and the Hubble parameter and therefore to probe the expansion of the Universe, which is linked to the dark energy equation of state, the growth factor and the curvature of the Universe.

1.4.4 Non-Gaussianity

Inflation models predict the formation of small fluctuations in the matter distribution which should be originated following an almost gaussian distribution. Deviations from gaussianity are characteristic of each inflation model and therefore observational detections of non-gaussianity can help

to probe the physics in the early Universe and the process of inflation.

The scale dependent bias, introduced by primordial non-gaussianity (PNG) in the relation between galaxies distribution at large scales and the underlying dark matter distribution can be probed with CMB experiments, with galaxy surveys like the LSST[53], Euclid[54], eRosita[55] (through large scale structure distribution, galaxy number counts, weak lensing power spectrum and bispectrum) or with intensity mapping of high redshift emission lines. On large scales, the power spectra of emission lines obtained from intensity mapping experiments follows the matter power spectra and so it can in principle be used to probe non gaussianity. The 21cm line from neutral hydrogen is the most promising line to probe non-gaussianity since it can be probed at high redshifts and at very large scales where the effect of non-gaussianity in the power spectra should be larger.

1.4.5 Weak lensing

Gravitational lensing by cosmological large structure will increase the 21cm observed power spectrum by order 1% on scales $\mathrm{k} < 0.1\mathrm{hMpc}^{-1}$, and by considerable more at $\mathrm{k} > 1\mathrm{hMpc}^{-1}$, and so this signature might be possible to detect with high-resolution observations by a low-frequency radio experiment as powerful as the SKA [41]. Besides, the extra contribution for the 21 power spectra from weak lensing can also be observed in tomographic maps of the 21cm line, and therefore be used to complement optical weak lensing observations given that intensity maps provide more accurate redshift information for the lensed structures than current methods.

1.5 Modeling and simulating emission lines for intensity mapping calculations

A considerable part of the original work shown in this thesis is the modeling of the overall emission in the 21cm, CO(1-0), CII, Lyman alpha and OH lines, originated both in galaxies and in the IGM. There are previous prescriptions for modeling galaxy emission in some of these lines but in most cases these models were made using observations of local galaxies and so they are not appropriate to describe the emission of high redshift sources. Also, the intensity mapping technique requires the model of all the sources of emission in galaxies and in the IGM while previous models are mostly adequate to describe high luminosity galaxies.

The prediction of the intensity and spatial fluctuations of a line, such as it will be measured by intensity mapping experiments, can be made using theoretical calculations, however since it is sometimes impossible to include all of the complexity involved in the process of emission of a line in a theoretical calculation the approximations made can be rude and lead to at least 10-20% errors in the estimations. As an example, it is impossible to include in a theoretical calculation the effect caused in the power spectra of a line by the variability of luminosity in galaxies with the same mass. Numerical simulations can be used for these calculations, however it is difficult to build numerical simulations with sizes large enough compared with the volumes observed by intensity mapping experiments, and these codes cannot be easily modified to account for different models of emission. Also, including foregrounds or testing foreground removal techniques would require extensive post processing of the output of numerical simulations. Semi-numerical simulations are an easy and practical solution for planning intensity mapping experiments since they can be used to simulate large sky volumes with several different input parameters and can be adapted to include foreground contamination.

Therefore, in this section I will approach the modeling and simulating of emission lines at high redshift taking into account that these modeling is appropriate to implement in semi-numerical simulations and to use for the planning of intensity mapping experiments.

1.5.1 Modeling and Simulating 21cm emission during the EoR

Modeling the 21cm line from the EoR requires first modeling matter density fluctuations, and the formation of bound structures due to the collapse of overdense regions, and than populating the dark matter halos with appropriate sources of ionizing photons. The ionizing emissivity of these sources, the fraction of ionizing photons which will successfully escape galaxies into the IGM and the properties of the IGM gas such as its clumping and temperature are essential to establish the evolution of the reionization process, the morphology of ionized regions (HII regions or HII bubbles) and the merging of HII regions. Additional complications such as feedback and recombining systems (or Lyman limit systems) can delay the process of hydrogen reionization [56] [57] [58], by respectively suppressing star formation in low-mass halos and consuming a large amount of ionizing radiation. Most of these parameters and processes are not well constrained either by simulations or observations, and so there are a large set of models who attempt at describing the process of hydrogen reionization which cannot yet be discarded. These models will however be constrained in the near future with the help of simulations, which can be used to determine what signatures each model leaves in intensity maps of lines emitted during the EoR.

In order to discuss the modeling of the 21cm line we first need to describe current constraints in key parameters of the EoR, such as the IGM ionized fraction, the SFR of galaxies and the ionizing photons escape fraction. The 21cm signal can than be estimated from equation 1.2 and its spatial fluctuation can be obtained using simulations as will be discussed in Section 1.6.

Modeling the IGM ionized fraction evolution

Given the large number of uncertain parameters and the large range of scales involved, a proper implementation of sources and sinks of ionizing photons in simulations of the EoR is not always possible, and so it is usual to use a simple parameter set to a constant value in order to account for the ionizing power of halos and also for recombinations. This is not a physical parameter since it accounts for several parameters which vary with the properties of the host dark matter halo and evolve with redshift, and so the ionizing efficiency parameter value is simply adjusted in order for the reionization timeline to be compatible with current observational constraints, especially with the optical depth to reionization. With the soon arrival of the first data from 21cm experiments the use of a single parameter is no longer enough and so it is advisable to estimate the evolution of ionized regions using the physical quantities present in equation 1.4. Recently, there have been in simulation codes that used to use the ionizing efficiency parameter and so for example, now the semi-numerical code Simfast21 [59][31] was updated in order to include the possibility of estimating the galaxies ionizing power based in physical properties of galaxies, available in detailed simulated galaxy catalogs, and the 21cmFast code [60] was update by adding a sub-grid in the cells of the simulation in order to make an improved estimation of the sinks of ionizing photons.

As is implicit in equation 1.4 the amount of UV emission from stars available for ionizing the IGM depends on a large set of astrophysical parameters. Some of these parameters have been relatively well modeled with detailed simulations, calibrated with the few available observations, although for some parameters such as the SFR and the escape fraction of ionizing photons, there

is still no consensus about what should be the range of possible values.

Modeling the escape fraction of ionizing photons

Ionizing photons which do not escape a galaxy are either absorbed by the dust in the galaxy or consumed in ionizing the ISM gas. For reionization sources, the metallicity and therefore the dust content is low, and so the UV photons that do not escape the galaxy can be assumed to be spent in ionizing hydrogen and helium.

The difficulty in constraining the ionizing photons escape fraction lies in its complex dependence on the galaxy mass, redshift, evolution history, morphology, composition, emission spectra and gas density distribution. Most of the properties of the ISM of high redshift sources are also not well constrained, and therefore it is challenging to accurately estimate $f_{\rm esc}^{\rm UV}$ even with numerical simulations. Current observations of the escape fraction of UV photons (available for low redshift galaxies) predict very small values ($f_{\rm esc}^{\rm UV} \sim 1 - 10\%$) for this parameter. The low redshift constraints in $f_{\rm esc}^{\rm UV}$ are however not valid for galaxies during the EoR, given that the properties of high redshift galaxies are very different, and likely to allow much higher values for $f_{\rm esc}^{\rm UV}$. The precise determination of $f_{\rm esc}^{\rm UV}$ is one of the major goals of future observations of high-redshift galaxies at $z \geq 7$. This parameter can be measured from deep imaging observations or can be estimated from the equivalent widths of the hydrogen and helium Balmer lines. At high redshifts the abundance of low mass galaxies (which are thought to be the main responsible for hydrogen reionization), with high SFRs, should lead to high escape fractions such as the $20 - 30\%$ to 60% now indicated by Lyman alpha and UV luminosity functions [61] [62].

The ionizing photon escape fraction dependence on the galaxy mass and SFR as a function of redshift, has been estimated using simulations that make several assumptions about the ionizing power of galaxies and the absorption of radiation in the ISM, however for the redshifts ($z \sim 20-6$) and the halo mass range relevant for reionization ($10^8 - 10^{13}{\rm M}_\odot$), there are no simulations that cover the full parameter space, and the ones that exist do not completely agree with each other [64] [65] [66] [67] [68]. The currents constraints in $f_{\rm esc}^{\rm UV}$ that cover more of the parameter space relevant for reionization, were obtained by Razoumov & Sommer-Larsen (2010) [63], which estimated $f_{\rm esc}^{\rm UV}$of star forming galaxies in the redshift range $z \sim 10 - 4$ and in the halo mass range $10^{7.8} - 10^{11.5}{\rm M}_\odot$ using numerical simulations. Although, their simulations do not have the resolution necessary to resolve most star forming regions and capture the small clumps in the ISM, and so their escape fractions might be overestimated. Figure 1.3 was taken from the Razoumov & Sommer-Larsen (2010) study [63], and illustrates the dispersion of the $f_{\rm esc}^{\rm UV}$ versus halo mass relation. Other relevant studies for the determination of $f_{\rm esc}^{\rm UV}$ relevant for reionization studies have included in their simulations: super novae explosions, minihalos and runaway OB stars [69].

For the modeling of the reionization process it is reasonable to assume that for higher redshifts the escape fraction of ionizing photons will continue to increase since the dust content in galaxies will be increasingly small, and the ratio between SFR and halo mass will increase, which will result in a higher efficiency for the escape of UV photons.

Modeling the SFR in galaxies

The SFR is one of the most important parameters in intensity mapping models since it is correlated with most of the galaxy properties, and because it is a quantity which can relatively easily be obtained by observational experiments.

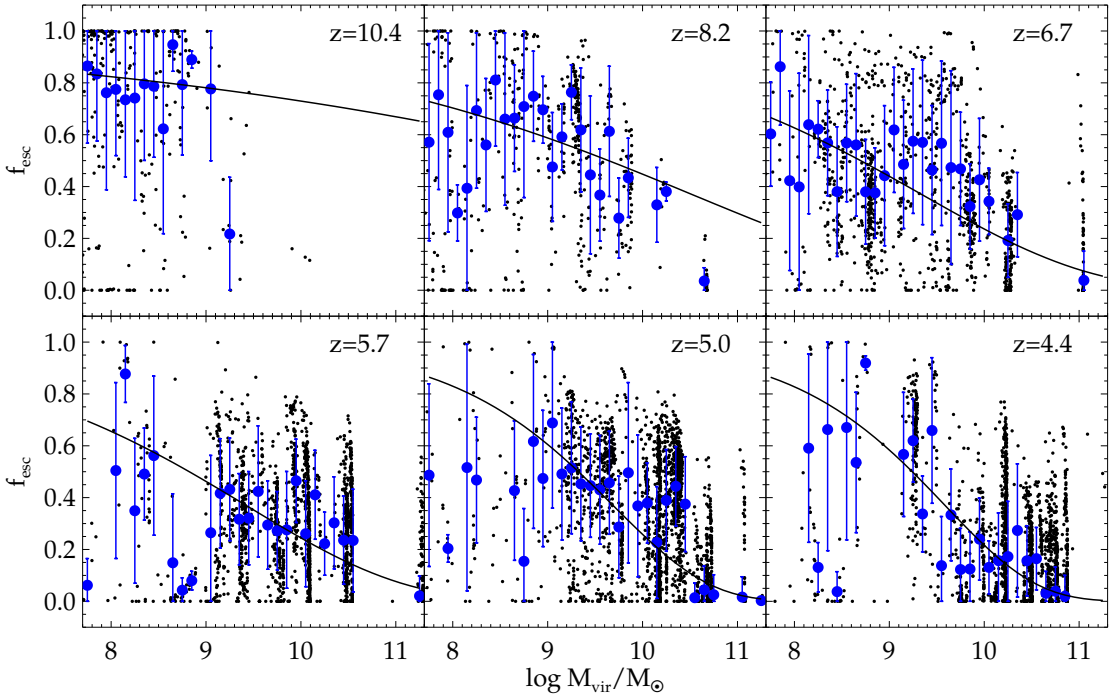

Figure 1.3: Escape fractions of UV photons from star-forming regions (black dots) versus mass of the host halo at six redshifts. The blue circles and the error bars show $f_{\rm esc}^{\rm UV}$ averaged inside each mass bin. The error bars correspond to the 1 sigma deviations. The black lines are fits to the average relation. Figure taken from [63]

Intensity mapping calculations require the modeling of the SFR in all types of galaxies, or at least in the galaxies mainly responsible for the signal we want to study, and since the intensity mapping technique measures the overall intensity from several sources it is very useful to relate the SFR of galaxies with the halo mass so that we can use a theoretical halo mass function to estimate the SFRD. A dark matter halo can contain more than one galaxy especially if its mass is high, which is more relevant for low redshifts, however the halo SFR is usually dominate by the SFR in one main galaxy. The number of secondary or satellite galaxies in a halo of a given mass can be estimated using the theoretical formulas in Cooray and Sheth (2002) [70]. The SFR of a galaxy depends on its age, mass, formation history, available fuel, metallicity and other properties and so a relation between SFR and halo mass and redshift is possible although there is expected a large fluctuation in this relation. Observationally, the SFR is obtained indirectly by detecting emission from a galaxy in a given emission line or spectral range, which can be originated from the stellar continuum emission or from emission in the ISM, and so there is a reasonably uncertainty in this measurement which reflects in the observational SFR halo mass relation. At low halo masses and high redshifts the uncertainy in the relation is particularly high since these galaxies are more difficult to observe and so the statistics is poor.

Currently the best constraints in the SFR halo mass relation made using simulations and observations are presented in figure 1.4. Extrapolating these estimates for the low mass end and for the galaxies present during the EoR is not trivial and therefore, a good alternative is to use the SFR halo mass relation from simulations such as the DeLucia et Blaizot (2007)[43] and the Guo

et al. (2011) [71] galaxy catalogs, which were obtained by post processing with semi-analytical models of galaxy formation, respectively the Millennium [72] and the Millennium II [72] dark matter simulations. These catalogs contain all the redshift and mass range relevant for reionization studies, and at low redshifts are roughly consistent with the relations shown in figure 1.4, and with the overall evolution of the SFR versus halo mass relation with redshift.

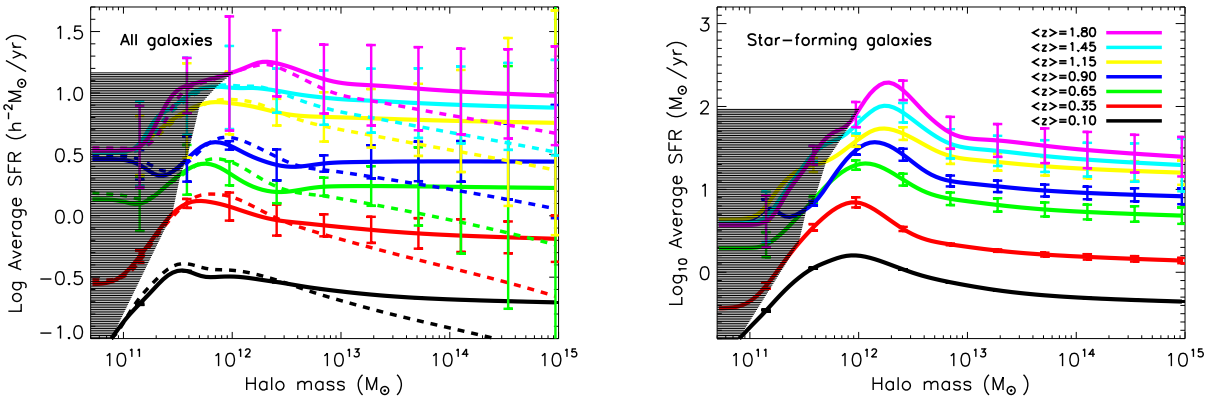

Figure 1.4: Left: Average SFR as a function of halo mass. The solid/dashed lines correspond to the SFR halo mass relation derived assuming that the SFR at fixed stellar mass is independent of halo mass and the dashed lines assume a distribution of SFR values at fixed stellar mass according to the halo mass. The hatched regions indicate the halo mass range where the relation showed is poorly constrained Right: Similar to the left panel but for star-forming galaxies only. Since the SFR distribution at a given stellar mass, for star-forming galaxies, is independent of environment and so of halo mass, in this figure only one line is plotted for each redshift. Figures taken from [73]

The overall SFR halo mass evolution derived from simulations can be used to estimate the SFRD, and can be compared with direct observational constraints of this quantity or with indirect constraints derived from the reionization timeline. In particular, the current optical depth to reionization, implies a SFRD higher than what is currently observed at $z \sim 8-6$ which can be explained by the SFRD at these redshifts being underestimated, since we are only probing the high end of the luminosity function or by the galaxies at higher redshifts being even more intense than what is currently predicted or by the poor modeling of the high redshift escape fraction of ionizing photons. Note that the optical depth to reionization is only sensible to the product of the SFRD and the SFR averaged escape fraction of ionizing photons $\left(f_{\rm esc}^{\rm UV}\right)$.

1.5.2 Modeling and Simulating CO emission during the EoR

Intensity mapping of the CO(1-0) line can be used to characterize the properties of molecular clouds (the sites of star formation) in high redshift galaxies, during the end of the EoR. It can also be used as a probe of the distribution of large structure in the Universe.

Carbon is one of the most common metals produced by stars, and so there is already a reasonable amount of carbon in the interstellar medium during the end of the Epoch of Reionization. Carbon monoxide (CO) is the second most abundant molecule in the galaxies gas after H_2, and it can be easily excited in collisions (especially collisions with H_2), and emit radiation in several

lines. The rate of CO excitations, and therefore of emission in its several rotational transitions, is directly linked to the amount of H_2, to the clumping of the gas and to the gas temperature, which are set by the CMB temperature and by radiative feedback from star bursts and active galactic nuclei. Rotational transitions in molecular carbon produce emission at frequencies multiples of the CO(J=1-0) transition, which has a rest frequency of 115.271 GHz. The CO(1-0) transition is however the most likely transition and so the easiest one to detect at high redshifts.

There is usually used a fixed value (X), to convert between H_2 mass and CO(1-0) luminosity, which is based in the intrinsic relation between SFR and molecular mass, however this approximation is not valid for all types of galaxies since the value of X is a function of several ISM gas properties such as: its pressure, its dynamics and metallicity. For most normal galaxies this conversion is still useful at least until we have better observational constraints. A recent prediction of the H_2 mass function and the CO(1-0) luminosity is shown in figure 1.5.

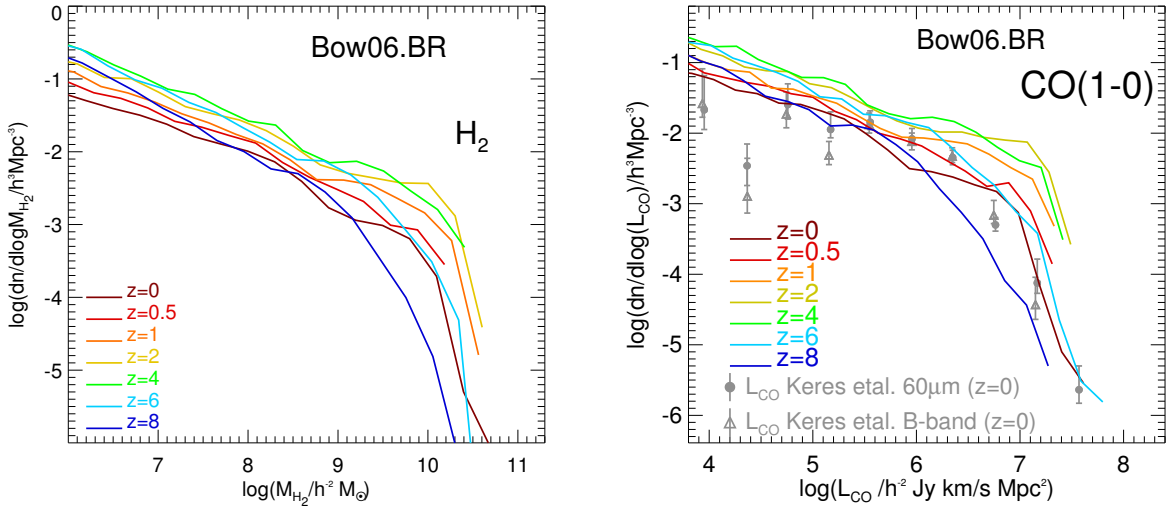

Figure 1.5: H_2 mass function (left panel) and CO(1-0) LF (right panel), at several redshifts, using the Bower & Benson (2006) model (Bow06.BR) [74], characterized by using a Kennicutt IMF and including AGN heating as a feedback mechanism. The CO(1-0) luminosities were obtained from the H_2 mass function with fixed conversion factors of X = 3.5 for quiescent star formation and X = 0.5 for burst star formation. Also shown, are the CO(1-0) LFs estimated at z = 0 by Keres et al. (2003)[75], which were used to normalize the CO(1-0) luminosity prescription in Obreschkow et al. (2009) [76]. Figures taken from Lagos et al. (2011) [77].

Using a detailed prescription for the emission of CO by molecular carbon, Obreschkow et al. (2009) [76] post processed the galaxies in the DeLucia et al. (2007)[43] simulated galaxy catalog first by separating the cold gas component in atomic and molecular gas, and than by estimating the CO fluxes individually, for every galaxy in the catalog [42] [76]. The Obreschkow et al. (2009) galaxies catalog is publicly available and has for each galaxy the mass of the dark matter halo which contains the galaxy, and the CO fluxes of all its rotational transitions. This catalog is available for all of the redshifts useful for the study of the EoR. In this catalog, the relative emission from different CO transition, was obtained by assuming local thermodynamic equilibrium, which has shown to be a good fit to the luminosities of several different types of galaxies. Note that the galaxies in this catalog where simulated based in a WMAP1 cosmology and so there should be a small scaling in the galaxies properties compared to a cosmology like the one obtained by WMAP7

however if the intensity is estimated with a WMAP7 cosmology the final result should be a good estimation.

Other, studies of CO emission using simulations and observations are compiled in the recent review of cool gas in galaxies by Carilli and Walters (2013) [78]. From these studies, the one by Lagos et al. (2012) [79] used a similar semi-analytical method to the one used by Obreschkow et al. (2009), but with an improved galaxy formation model to separate the HI from the H_2 phases of the gas and used a PDR code (Photon Dominated Region code) to model the various CO rotation transitions. Nevertheless, both these models were scaled to fit the CO(1-0) luminosity function in Keres et al. (2003) [75]. A completely independent method based on observations was developed by Sargent et al. (2013) [80][81] which separated the contributions of main sequence and starburst galaxies and used IR LFs appropriate for each galaxy population to predict the CO(1-0) luminosity function. Also Sargent et al. used a metallicity dependent relation to estimate the evolution of the CO(1-0) versus H_2 mass relation which is similar to the previously obtained relations by Geach & Papadopoulos (2012) [82] and Carilli & Blain (2002) [83]. These studies are however centered in emission of the CO(1-0) line and although in some publications, including in the Carilli & Walters (2013) review, there are some observational ratios between CO(1-0) emission and higher CO transitions, these ratios are obtained from a non significant statistical sample and are biased towards properties of high luminosity galaxies. Soon, due to observations with the Atacama Large Millimeter/submillimeter Array (ALMA) telescope, there will be a lot better constraints in CO emission at higher redshifts, but this experiment will not go as far as to detect CO emission from low mass galaxies during the EoR and so intensity mapping of CO transition lines is still needed to study these galaxies.

The intensity of the CO rotation lines are easier to estimate by using a CO luminosity parameterized as a function of halo mass and redshift, which can be done since CO emission is connected to the mass in H_2 which is related to galaxy mass. The intensity of the CO lines can be estimated by integrating the luminosity over the halo mass as:

$$\bar{I}_{\rm CO} = \int_{M_{\rm min}}^{\infty} dM \frac{dn}{dM}(z, M) \frac{L_{\rm CO}(z, M)}{4\pi D_{\rm L}^2} y(z) D_{\rm A}^2, \tag{1.13}$$

where dn/dM is the halo mass function [84], $D_{\rm L}$ is the luminosity distance, $D_{\rm A}$ is the comoving angular diameter distance, $y(z) = d\chi/d\nu$ converts from distance to observed frequency and the minimum mass of halos emitting in the CO line, can be assumed to match the minimum dark matter halos that can host galaxies, which would be $M_{\rm min} = 10^8 {\rm M}_\odot/{\rm h}$, or can be set to a higher value (to be consistent with the mass scale of atomic Hydrogen cooling or a virial temperature of 10^4K [85]).

1.5.3 Modeling and Simulating CII emission during the EoR

Carbon is a very abundant element and since it can be ionized by radiation with energy above 11.26eV, which is less than the ionization energy of hydrogen, it can be found in several phases of the galaxy gas. Ionized carbon has a fine structure transition of the 2^P level with an equivalent temperature of 91K, and so it can be easily excited by collisions with hydrogen or free electrons and protons in regions where the free electrons number density $(n_{\rm e})$, and the neutral hydrogen number density $(n_{\rm H})$, follow the relation $(n_e/n_{\rm H} \gtrsim 10^{-3})$, resulting in emission of the CII $157\mu m$ line [86]. The CII line of typical star forming galaxies accounts for 0.1% to 1% of their bolometric luminosities. The CII fine structure line is therefore an efficient cooling mechanism which can

be emitted from photodissociation regions (PDRs), ionized regions and also from the boundary of CO-dark molecular clouds. From galaxy observations of CII emission and other important cooling lines, which are characteristic of either PDRs of ionized regions, we now know that most CII emission is originated in PDRs. Although, in some extreme conditions ionized regions can account for up to 30 or even 50% of the total CII emission. The best explanation for why there is not much CII emission in ionized regions compared to their large carbon content, is that in this medium most of the carbon is shielded from ionizing radiation by strong columns of hydrogen gas. Both in PDRs and in HII regions CII emission is correlated with the galaxy SFR, and so the total CII emission from several sources in a relatively large volume can be estimated with some accuracy from the SFR in these galaxies.

Current observational constraints in the CII versus SFR relation present in figure 1.6, show clearly that there is a correlation between CII emission and SFR in galaxies. The dispersion in this relation is smaller than the dispersion in the same relation for most emission lines and the SFR. The strength of the relation between CII emission and SFR can be easily understood in the case of CII emission originated in PDRs since carbon in this medium is ionized by FUV radiation (the amount of CII in PDRs is proportional to the FUV flux and inversely proportional to the hydrogen number density) and so number density of CII atoms should be proportional to the stellar spectral emission in this band. The relation between CII emission and SFR in ionized regions is based in the size of ionized regions being proportional to the stellar UV radiation and so there is an indirect relation between the amount of ionized carbon in these regions and the SFR.

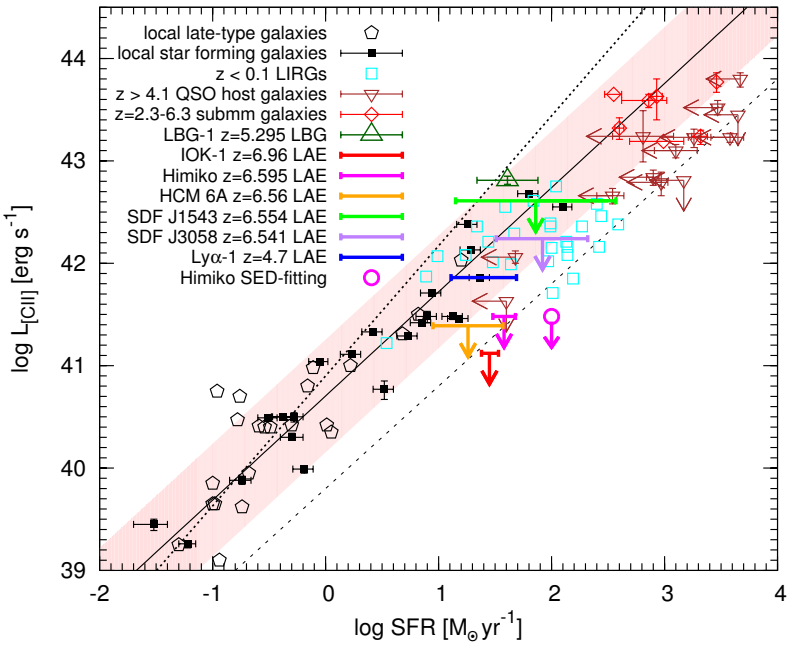

Figure 1.6: Observations of CII emission from local to high redshift galaxies. The arrows indicate upper limits in the CII luminosity of very high redshift galaxies. The best fit to the CII SFR relation from local late type galaxies is shown by the dotted line. The solid line and the shadow region indicate the best fit and the two sigma scatter of local star forming galaxies and the dashed line is the best fit to galaxies with far infrared luminosities above $10^{12}L_{\odot}$. (For references see the original publication of this figure in [87]).

There are several measurements of CII emission at low redshifts which indicate that the relation between CII emission and SFR is likely to decrease for very massive galaxies such as LIRGs (Luminous Infrared Galaxies) and ULIRGs (Ultra Luminous Infrared Galaxies). The few existent observations of CII emission at high redshift also show this tendency. The decrease in CII emission with infrared luminosity $(L_{\rm IR})$ and high dust temperatures is now confirmed, although the causes are not well confirmed. The main arguments to explain this deficit are saturation of the CII line due to high density of neutral gas, self absorption, ionization of dust grains in environments with a high far-UV field compared to the gas density or high dust-to-gas opacity due to an increase of the average ionization state of the gas. Extinction and self absorption, cannot on their own explain the total deficit observed since they would imply respectively extinction ratios in the band $400 - 1000\mu m$ which are not detected in observations of other lines and extremely large column densities of the gas [88].

For intensity mapping studies the CII line can be parameterized by assuming that it is proportional to the SFR in galaxies, although the choice of the relation between CII luminosity and SFR to be used for estimating the overall CII emission during the EoR, should be made using observational data but taking into account that the available observations target high luminosity galaxies which account for only a small fraction of the overall CII intensity. The intensity of CII emission can be estimated from the CII luminosity in a similar way to the one used for the CO intensity, see equation 1.13. The SFR of galaxies can be related to the halo mass and the intensity of CII emission can be estimated by integrating the CII luminosity times the halo mass function over the halo mass. In simulations there can also be assigned scatter to the CII luminosity versus halo mass relation using the scatter in the SFR versus halo mass relation of by attributing scatter to the CII versus SFR relation.

1.5.4 Modeling and Simulating Lyman alpha emission during the EoR

The Lyman alpha line corresponds to a transition between the first and the second levels in hydrogen atoms. Lyman alpha photons are emitted with a rest frequency of $\nu_0 = 2.47 \times 10^{15}{\rm Hz}$ which corresponds to an energy release of $10.2{\rm eV}$ (more than one million times more energetic than the hydrogen 21cm line), and so Lyman alpha emission during the Epoch of Reionization is now observed at the near infrared.

Lyman alpha line emission is originated in galaxies and in the IGM due to excitations or during hydrogen recombinations. Intensity maps of the Lyman alpha will however be also sensible to continuum emission, and so observations will collect photons originated in stellar continuum and in continuum emission from the ISM which includes free-free, free-bound and two photon emission.

In galaxies, Lyman alpha emission is originated in continuum stellar emission, recombinations, collisions and gas cooling during structure collapse, while in the IGM Lyman alpha emission is originated in scatter of Lyman-n photons and also in recombinations and collisions. Since Lyman alpha is a very strong line its emission from galaxies has been highly studied using galaxy surveys till a redshift of $z \sim 8$. Interpreting Lyman alpha emission at the high redshifts of the EoR is however not an easy task, since current surveys can only probe the high end of the Lyman alpha luminosity function and also because Lyman alpha photons are scattered by neutral hydrogen. Therefore, observations of Lyman alpha emission from galaxies will strongly depend on the transmission of Lyman alpha photons in galaxies and in the IGM which is still not well modeled and constrained. From theoretical studies and observations of low redshift galaxies, we know that the intrinsic Lyman alpha emission from galaxies is dominated by emission from recombinations

which is given by:

$$L^{\rm Gal}_{{\rm Ly}\alpha,{\rm int}} \sim 0.67 E_{Ly\alpha}(1 - f^{\rm UV}_{\rm esc})\dot{N}_{\rm ion}(1 - f_{\rm dust}), \tag{1.14}$$

where the factor 0.67 is the probability of a Lyman alpha photon being emitted during an hydrogen recombination, $f^{\rm UV}_{\rm esc}$ is the ionizing photons escape fraction, $f_{\rm dust}$ is the fraction of Lyman alpha photons absorbed by the dust in the galaxy and $\dot{N}_{\rm ion} = Q_{\rm ion} \times SFR$ is the number rate of emitted ionizing photons, which can be obtained by the product of the average number of ionizing photons emitted per solar mass in star formation $Q_{\rm ion}$ and by the galaxy SFR. Collisional excitation of the Lyman alpha line in galaxies will be highly dependent on the stellar spectral emission, and so it will only be relevant for very strong luminosity sources, which are extremely rare especially during the EoR. Lyman alpha emission is also a cooling mechanism of gas, which has been shock heated during infall into potential wells. This fact is important for the modeling of galaxy formation but the overall Lyman alpha emission originated in this process is quite small compared to the other processes of Lyman alpha emission in galaxies.

Scattering of Lyman-n photons in the IGM is important for the coupling of the 21cm spin temperature to the gas temperature in the Pre-EoR, and to the overall heating of the IGM, however the contribution of this source of Lyman alpha photons is quite small compared to other sources in the IGM during the end of the EoR. The UV and X-ray energy which escapes the galaxy gets distributed in the IGM in ionizations, direct excitation (followed by photon emission) and heating of the gas. Lyman alpha emission is then emitted during hydrogen recombinations and as a cooling mechanism of the hydrogen gas. Both recombination and collisional Lyman alpha emission are dependent on the temperature, clumping and ionization state of the IGM. Recombination Lyman alpha emission in the IGM is highly dominated by ionized regions, since it depends on the product of the number density of free electrons and ionized hydrogen atoms and it also depends mildly on the temperature. In ionized regions there is an elevated heating of the gas, but efficient cooling by several emission lines sets the temperature to about $(1-2) \times 10^4$K. The rate of collisional Lyman alpha emission depends roughly on the product of neutral hydrogen atoms and free electrons and so during the EoR it is mainly originated in ionization fronts. The intensity of Lyman alpha emission due to collisional excitations is highly dependent on the temperature of the IGM since it changes by about three orders of magnitude in the temperature range of $(1-2) \times 10^4$K. As a result, although recombination Lyman alpha emission is fairly easy to estimate at a fixed IGM ionized fraction, collisional/excitational Lyman alpha emission in the IGM is a function of local values of the IGM ionized fraction and temperature and so it is dependent on details of the process of reionization such as the clumping, morphology and time evolution of ionized regions, also at the boundaries of ionized regions the temperature is not even close to equilibrium and so a proper estimation of this emission requires very high resolution simulations of the expansion of ionization fronts and other reionization constraints which are still fairly unknown.

Nevertheless, a rough theoretical estimation of Lyman alpha emission during the end of the EoR suggests that the intensity of this emission is dominated by galaxies over emission from the IGM and by recombinations over collisions. Assuming that Lyman alpha is dominated by emission from galaxies and from the ionized bubbles around galaxies than the cross correlation between Lyman alpha and 21cm emission will be negative at large scales and sensible to the average size of ionized regions. In the case where ionized regions are very large and/or Lyman alpha emission from the IGM becomes comparable or higher than emission from galaxies, the cross correlation power spectra between Lyman alpha emission and HI emission will be more unstable and can no

longer be directly used to constrain the size of ionized regions.

Most of the contributions to Lyman alpha emission are directly related to the galaxies SFR and to the IGM ionized fraction, and so they can roughly be estimated with these two parameters. Simulations of Lyman alpha emission are mainly needed to predict the power spectra of Lyman alpha emission and to properly correlate Lyman alpha and 21cm intensity maps.

Current observation of Lyman alpha emission

Observations of Lyman alpha emission in a line of sight will dependent on the transmissivity of Lyman alpha photons ($T_{Ly\alpha} = L^{\rm Gal}_{\rm Ly\alpha,obs}/L^{\rm Gal}_{\rm Ly\alpha,int}$, where $L^{\rm Gal}_{\rm Ly\alpha,obs}$ is the observed Lyman alpha luminosity from galaxies) in the IGM which is set by the flux of Lyman alpha photons, the neutral fraction content of the IGM and by the conditions of neutral hydrogen clouds such as their column densities, morphology and temperature.

After the end of the EoR the neutral gas content in the IGM is very small and so $T_{Ly\alpha} \sim 1$, however, as we go to higher redshifts there can be sheets of neutral hydrogen in the IGM in the direction of the observer, which will cause the Lyman alpha photons to be absorbed and re-emitted by neutral atoms in a different direction and so only a small fraction or even none of the Lyman alpha flux will be observed. This transmission coefficient is very difficult to estimate given the uncertainties in the neutral gas content at high redshifts. However, if we assume that there is no evolution of the intrinsic Lyman alpha luminosity from galaxies in a given redshift range than the observed difference in the Lyman alpha luminosity functions should constrain this transmissivity. Also, observations in nearby wavelengths can be used to probe a galaxy intrinsic Lyman alpha luminosity which can be directly compared with the observed Lyman alpha luminosity. Current constraints in Lyman alpha luminosity functions at redshifts 5.7, 6.6 and 7 can be observed in figure 1.7 taken from Ota et al (2010) [89].

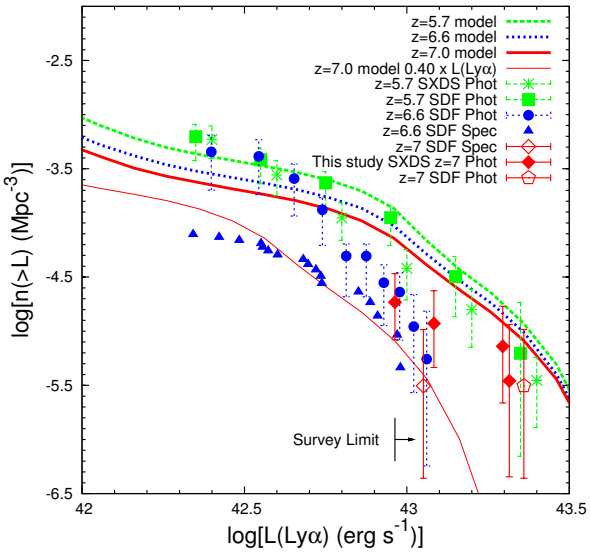

Figure 1.7: Lyman alpha LFs at $z = 5.7$ in the Subaru Deep Field (SDF) [90] and in the Subaru/XMM-Newton Deep Survey (SXDS) [91], at $z = 6.6$ in the SXDS [92] and at $z = 7$ in the SDF [93] (Figure taken from [89]).

The observed evolution in the Lyman alpha luminosity function at $z \sim 7 - 6$ can be an indi-

cator of evolution of the IGM ionized fraction, but can also be due to evolution of the galaxies responsible for the Lyman alpha emission, or due to the evolution of the IGM conditions. Different alternatives to the Lyman alpha luminosity function evolution include but are not restricted to:

1. An increase of available gas to fuel SFR at high redshifts which might result in an increase in the opacity of the infalling gas.

2. A higher escape fraction of ionizing photons due to evolution of galaxies properties which would result in a lower $L^{\rm Gal}_{{\rm Ly}\alpha,{\rm int}}$.

3. From $\mathrm{z} = 5.7$ to $\mathrm{z} = 6.7$ the density of the universe increases by up to 50% which implies a 30% decrease in the transmission of Lyman alpha photons in the IGM, although these value is still not completely confirmed.

4. A decrease in the photon-ionizing background, which would cause an increase in the number of Lyman limit systems without requiring a high evolution in the IGM ionized fraction.

5. An evolution of the IGM ionized fraction of up to 0.5 for $\mathrm{z} \lesssim 7$.

For a more detailed discussion of alternatives to explain the evolution of Lyman alpha photons luminosity functions, see for example Dijkstra (2014)[94]. Note that Lyman alpha emission in some galaxies at $\mathrm{z} \lesssim 5.7$ also suffers some scatter, and that observations are still statistically limited, and so for now Lyman alpha observations cannot put any strong constrains in the timeline of the reionization process.

Intensity maps of Lyman alpha emission during the EoR will not be much affected by the Lyman alpha transmission coefficient. However, the contribution for these maps originated in Lyman alpha emission from the IGM will be a powerful probe of the IGM ionization state and can help explain the observations of Lyman alpha emitters by galaxy surveys. Also, the cross correlation power spectra between the 21cm and the Lyman alpha lines will be sensible to the size of ionized regions and therefore will be a good indirect probe of the IGM ionized fraction.

1.5.5 Modeling and Simulating OH emission

Intensity maps of the 21cm line, emitted during the EoR, will not suffer much contamination from other emission lines, however at lower redshifts after the end of the reionization process, the metallicity of the gas is much higher and so there can be considerable contamination of 21cm line intensity maps by hydroxyl (OH) emission from slightly higher redshifts. A proper study of the overall intensity of OH emission from masers is therefore essential to estimate this contamination. The term masers stands for **m**icrowave **a**mplification by **s**timulated **e**mission of **r**adiation, and so it is used to refer to regions in galaxies, whose particular properties cause amplification of otherwise faint lines.

There are four OH 18cm lines, two main lines with 1665/1667 MHz and two much more faint satellite lines with 1612/1720 MHz. OH emission in most galaxies is comparable to what would be expected from gas emitting as a black body, and so these 18cm lines are not usually strong. However, in the ISM of some galaxies OH radiation is highly amplified (by a factor of more than ~ 1010) due to a process of inversion of level populations and it becomes easily detectable. Strong OH emission by masers was discovered in 1965, and was soon the object of interest of the astronomical community given its potential as an astrophysical probe. Masers tend to exist

in locations difficult to observe in the visible, and so they are a valuable probe of the conditions of dense gas in the ISM of protostars located in star forming regions and in late type stars that have lost their mass into circumstellar space. OH emission can be found in star-forming regions and in M stars, but it is primarily observed in galaxies experiencing a merger driven burst of star formation, high luminosity OH emitters are located in LIRGS and ULIRGS and so can be detected by observing these galaxies. Intensity maps of the OH 18cm lines are dominated by emission of strong sources, and so estimating this emission requires determining what are the number densities of LIRGS and ULIRGS, how many of these galaxies can potential hold a maser, and to model the OH luminosity of a maser as a function of the mass of the dark matter halo which contains it. LIRGs and ULIRGS are characterized by having IR luminosities above respectively $10^{11}\mathrm{L}_{\odot}$ and $10^{12}\mathrm{L}_{\odot}$, and so their number can be estimated by taking advantage of the empirical relation between IR luminosity and SFR [95] [96]:

$$L_{\mathrm{IR}} = 5.8 \times 10^{9}\mathrm{SFR}\,[\mathrm{M}_{\odot}]\,, \tag{1.15}$$

and by correlating the SFR with the host dark matter halo. The fraction of LIRGS and ULIRGS which contain a maser is close to 0.2 as estimated by Darling and Giovanelli (2002) [97] using a more than 300 sample of candidates observed with the Arecibo OH megamaser survey. Masers give origin to high dust temperatures and so they are more likely to be found in warmer FIR galaxies. In galaxy samples this translates into a correlation between the presence of a maser and the galaxy spectral shape in the far infrared.

Using more than one hundred galaxies Darling and Giovanelli were also able to establish a relation between IR luminosity and OH luminosity (L_{OH}), after correcting for the Malmquist bias (which consists in the correlation between OH and infrared luminosity with distance that affects flux limited surveys). This relation is physically based in the fact that OH masers are being radiatively pumped by FIR radiation, however it is nor linear since the source of stimulated emission is the radio continuum, which is also proportional to FIR emission and so would imply a relation $L_{\mathrm{OH}} \propto L_{\mathrm{FIR}}^{\gamma}$ with $\gamma = 2$. In the case than the maser gets saturated than the correlation between OH luminosity and FIR emission will be characterized by $1 < \gamma < 2$. The best current estimate for this parameter is $\gamma \sim 1.2$ obtained by Darling and Giovanelli (2002) [97].

1.6 Simulating Reionization

The use of large simulations is nowadays essential in order to probe the high redshift Universe astrophysical and cosmological properties. Simulations are necessary to achieve an accurate picture of the evolution of the Universe by completing and helping to interpret theoretical models and observational data. With simulations we can probe the effect of astrophysical and cosmological models in the evolution of small and large scale structures and also analyse physical processes in galaxies and in the IGM in detail. Simulations, also play a crucial role in the planning of observational experiments since they are essential to estimate the necessary parameters and sensitivities for an experimental to be able to detect an astrophysical or cosmological signature.

There are two main types of simulations which are useful at different stages of the analysis of the reionization process: numerical and semi-numerical simulations.

Semi-Numerical codes - Semi-numerical simulations are very fast and easily adaptable, which makes them particularly appropriate for analysing a large set of galaxy formation models and

astrophysical/cosmological parameters. These codes can be used to simulate large volumes and so are appropriate to help planning observations. Also, the large datasets obtained by observational experiments require fast methods to do a primary analysis of the data which are only on the reach of this type of experiments. Nevertheless, semi-numerical codes can only handle simple situations, need to use input parameters constrained from observations and numerical simulations, and even then should be compared with the output from numerical simulations whenever its possible to insure the validity of the several approximations used.

As example of this type of simulations we have the Simfast21 [59] and the 21cmFAST [60] codes, which can be used to simulate intensity maps of the 21cm line and are publicly available. In particular the Simfast21 code was recently adapted to generate simulations of the 21cm signal from the Epoch of Reionization using galaxy catalogs generated from more detailed numerical simulations and the 21cmFAST code was adapted to model in detail sinks of reionization by adding a sub grid to the code.

Numerical codes - Numerical simulations are becoming more and more complex and can include in detail a large variety of physical and chemical processes. These simulations allow a proper determination in a self-consistent way of several parameters essential to model the conditions in galaxies and in the IGM, and so numerical codes are useful to do a deep analysis of reionization models, and therefore to improve constraints in astrophysical and cosmological parameters. However, since numerical codes are slow and expensive they should preferably be used to test the models previously selected using semi-numerical codes and observational data.

Current simulations have shown an increasing success in the modeling of astrophysical processes, and in the interpretation of observational data, however the large variety and complexity of the processes involved in the reionization of hydrogen in the IGM, and the huge data sets, which will be available in the near future due to intensity mapping experiments, requires more and better simulations. It is therefore essential, to improve and to create new numerical and semi-numerical codes taking into account the more pressing needs of observational experiments.

The Simfast21 code

The Simfast21 code is a semi-numerical modeling tool, originally designed to simulate 3-dimensional intensity maps of the 21cm line during the Epoch of Reionization and later extended to also simulate intensity maps of other emission lines.

The code is divided in several modules so that it can easily be corrected, improved and updated. There is also, the option of running the code at once after the input parameters are set. The large number of input parameters which can be adjusted prior to running the code make it easy to test the effect of several astrophysical and cosmological parameters in the history of reionization and in the reionization observables. The output of the Simfast21 code is similar to what we can expect to obtain from observational experiments, and so this code is an important tool for the planning of intensity mapping experiments, and for the scientific interpretation of observational intensity maps.

The simulation produces three dimensional boxes with a length L and a total number of cells N^3 set by the user. The basic structure of the code was made to follow the following steps:

1. A realization of a linear density field is generated at redshift $z = 0$. The density fluctuations for each cell of the simulation are generated following a gaussian random distribution, with

statistical properties defined by the matter density power spectra, which can be read by the code in an input file (obtained for example using the Code for Anisotropies in the Microwave Background [98]) or can be generated by the Simfast21 code itself using the power spectrum formulas from Eisenstein & Hu [99], set by the relevant cosmological parameters in the input file.

2. Dark matter halos are obtained from the linear density field at several redshifts, where the density field for $z > 0$, is simply derived from the density fluctuations at $z = 0$, by multiplying them by the linear growth factor.
The halos can be found using two prescriptions based in the excursion set formalism. In the first prescription the algorithm uses spheres with decreasing radius and finds the halos by determining if there is enough mass in a sphere centered at a given pixel of the simulation for there to be a dark matter halo centered at that pixel, according to the Sheth & Tormen (1999) [84] collapse criterium, which is based in standard Press-Schechter theory [100]. This method can only be used to find halos down to a radius defined by the resolution of the box. The second prescription tests for independently for every cell of the simulation, what is the probability of it containing a halo or more with a given radius, for decreasingly small radius. The number of halos with a given radius contained in each cell is obtained from a random poisson distribution, with an average given by the theoretical number of halos expected at that cell, which is given by the halo mass function times a factor of $(1 + \delta)$, where δ is the fractional matter overdensity in the cell (this means that the halos are sampled directly from the density field). This second method has the advantage of being able to find halos below the mass resolution of the simulation box. The obtained halos output is made in a collapsed matter box and/or in a halo catalogs.

3. A velocity field is obtained from the density field, so that it can later be used to calculate the effect of peculiar velocities in the 21cm signal or in the implementation of non linear corrections in the density and collapse mass boxes.

4. There is an optional module, which can be used to obtain first order non linear corrections to the density fields and to the dark matter halos, using the Zel'Dovich approximation.

5. In the initial version of the Simfast21 code, star formation rate density boxes were obtained from the halo catalogs assuming that a fixed fraction of the increase in collapsed mass in a cell between two redshifts, was used in producing stars. The new version of the Simfast21 code uses parameterizations of the SFR versus halo mass obtained from the simulated galaxy catalogs from DeLucia et Blaizot (2007)[43] and Guo et al.(2011) [71], for respectively high halo masses and low halo masses, to independently assign a SFR to each halo of the catalog, according to its mass and redshift. A SFRD box can than easily be obtained from the halo catalogs.

6. The ionization field is generated from the density field and from the halo catalogs. In the initial version of the Simfast21 code, the ionized regions where found using the excursion set formalism with the ionizing power of each halo derived from its mass using a fixed ionizing efficiency parameter, which accounted for hydrogen ionizations and reionizations and was set to a given value so that the code reproduced a reionization history compatible with the output of numerical simulations. This module was updated to attribute a physically based ionizing power to each halo and to add recombinations to each halo using equation 1.4,

together with astrophysical parameters based either in recent detailed simulations and/or in observational results. In this new method recombinations were implemented in the code assuming that the ionized gas was at a temperature of 10^4K.
In the Simfast21 code, there is also and optional module to estimate the optical depth to reionization from the ionization field, which can be used to insure that the resulting 21cm intensity maps are compatible with observational constraints.

7. For the simulation of intensity maps of the 21cm line, the Simfast21 code has additional modules to estimate the coupling of the 21cm line to the gas temperature due to radiative and collisional emission. These extra modules calculate these corrections to the 21cm line fluctuations using the previously simulated dark matter density field, dark matter halos, star formation rate density and ionized boxes, for more details see [59].

8. The final 21cm intensity maps are obtained using equation 1.2.

9. In order to obtain intensity maps of other lines, the Simfast21 code has now the option to add several properties from the DeLucia et Blaizot (2007)[43], the Guo et al.(2011) [71] and the Obreschkow et al. (2009) [76] simulated galaxy catalogs to the halo catalogs generated with the Simfast21 code. These new halo catalogs, can than be used to generate intensity maps of several lines, following the prescriptions described in Section 1.5.

10. The Simfast21 code was also improved by adding extra modules which can be used to produce mock observational cones (three dimensional boxes with two angular directions and a frequency direction) with the intensity a transition line, similar to what we can obtain from intensity mapping experiments. These modules use as an input the previously described halo catalogs. Also, there is a module to cut a slice of the mock observational cones and reconstruct an intensity map of a transition line with three spatial dimensions which is useful to scientifically analyse the 3-dimensional intensity maps. The extra modules included in the Simfast21 code can easily be used to estimate line contamination in observational maps and to simulate foreground removal techniques.

Other modules can be added to the Simfast21 code, and the base code can be altered to test different astrophysical and cosmological parameters as well as to use different parameterizations for important quantities such as the SFR of halos, the ionizing photons escape fraction and others.

1.7 Foregrounds in Intensity Mapping

Intensity maps will suffer foreground contamination from continuum and line emission, from galactic and extragalactic origin, and will also be sensible to experimental errors and systematics. Continuum contamination is usually removed from intensity maps by taking advantage of the smooth evolution in frequency of this emission compared to the evolution of an emission line [101]. Ideally, continuum emission can be fitted by a polynomial function and removed from observational maps, however this process will originate subtracting errors which can be relevant in the case of confusion of the continuum emission as it enters our galaxy. Line contamination is mainly a problem in the case of there being strong emission lines from lower redshifts which fall in the observing frequency band. Usualy fluctuations in the intensity of foreground emission lines can be efficiently decreased by a few orders of magnitude, in observational maps, just by masking the map

pixels were emission from a few high luminosity galaxies is observed. There are three main issues to take into account in order for the masking technique to be successfully applied: the intensity of the foreground lines has to be properly estimated, the percentage of pixels to mask should not be higher than 30%, and there has to be a feasible way to detect the contaminant galaxies either by detecting them in the contaminant line or by using a good tracer of the line easier to detect observationally. In the case that the masking of a contaminating line is not possible there remains the possibility to cross correlate the target emission line with other emission lines, since different lines are usually affected by uncorrelated foregrounds and so the cross correlation power spectra would provide a statistical measurement of the product of the fluctuations of the two lines free of foregrounds. The possibility of cross correlating intensity maps with cosmic microwave background radiation can also be considered as an additional way of avoiding foregrounds in some lines such as the 21cm transition [102]. Also, in the uncommon case that two emission lines from the same galaxy are detected in the observational maps there is the possibility to probe their intensity and location using statistical methods, such as in the case of observations in the range $200 - 300\mathrm{GHz}$ frequency window where the CO(3-2) and CO(4-3) lines from redshift $z \sim 0.63$ are observed at respectively $212\mathrm{GHz}$ and $283\mathrm{GHz}$.

Experimental errors will impose lower limits in the intensity of the signal we are trying to detect, but they can in principle be well characterized with a careful analysis of the experimental setup and with observational tests. Systematics are a problem in every experiment and are impossible to completely estimate, however some systematic errors can be detected with the use of different statistical methods of analysis.

The degree of continuum and line contamination is particularly for each emission line and so these issues will now be independently discussed for the 21cm, CO(1-0), CII and Lyman alpha lines.

1.7.1 Foregrounds in 21cm Intensity Maps

Intensity maps of the 21cm line will be contaminated by galactic and extragalactic foregrounds orders of magnitude higher than the signal, plus distortion of the signal from the ionosphere, and basic radio frequency interference (RFIs). As a reference the intensities involved at 150MHz are of $\sim 5\mathrm{mK}$ for the EoR signal, $2\mathrm{K}$ for the foregrounds and $\sim 50\mathrm{mK}$ for 400 hours of total observing with an experiment like LOFAR [103]. Most galactic and extragalactic foregrounds can be removed taking advantage of their smooth evolution in frequency [104], although there might be some problems due to ionospheric distortions. In addition, there will be complications due to the instrumental response and noise as well as from the treatment of the signal which includes: calibration, inversion and extraction of the signal. Dealing with calibration issues, requires self calibrating the instrument or using bright point sources or satellites for absolute calibration which makes it a very time consuming process.

Even if we are successful with the cleaning of the signal and calibrating issues, the final 21cm maps will inevitable contain the signal, residual foregrounds, subtraction errors, noise and systematics. The noise might ruin the possibility of detecting the 21cm signal along one line of sight, but the overall 21cm signal can still be detected with some statistical methods such as first characterizing the general properties of the noise and then considering the 21cm signal as the extra source of variance. Position errors in the sky-model for bright sources ($\gtrsim 1\mathrm{Jy}$) will be the main source of subtraction errors and so it is essential to detect this sources with an accuracy of the order of 0.1 arcsec [105].

In the end systematic errors are likely to become one of the biggest issues in 21cm intensity maps. Although there are some ways to deal with these errors by using several statistical methods to avoid them, there will still be necessary to compare the signal with simulation outputs in order to identify possible inconsistencies in the observations. Nevertheless, there is likely to be some errors in the final prediction of the 21cm signal intensity and power spectra and so the scales of the fluctuation less likely to be affected by systematics will be the ones preferably used to constrain reionization models [106]. The extraction of cosmological signatures from the 21cm signal power spectra will also have big problems with systematics, which will decrease the sensitivity at which they can be detected [107].

1.7.2 Foregrounds in CO(1-0) Intensity Maps

Intensity maps of the CO(1-0) line will suffer contamination from continuum emission and from other lines from higher or lower redshifts, which are observed in the same frequency band. The continuum foregrounds in CO maps are spectrally smooth compared to the frequency evolution of this emission line and therefore they can in principle be fitted and removed from observations. Contamination from CO emission from higher transitions is likely to be negligible since for example the CO(1-0) line at redshifts $(6-8)$ would be contaminated by the CO(2-1) line from redshifts $(13-17)$, where the amount of molecular carbon should be extremely low. The most significant contamination to the CO(1-0) intensity maps during the EoR will be emission from HCN (hydrogen cyanide) molecules and radio recombination lines, but these are faint compared to the CO emission [108].

Most of the foregrounds affecting CO observations are similar to the ones contaminating 21cm observations however given the relative intensities of the signals and foregrounds this issue will be a lot less problematic for CO intensity mapping.

1.7.3 Foregrounds in CII Intensity Maps

The ionized carbon $\lambda = 157\mu m$ line, emitted from a redshift of $z \sim 8.5-5.5$, will be observed in the frequency range 200 to $300\mathrm{GHz}$. Intensity maps of CII emission in this frequency band will suffer contamination by continuum and line foregrounds. The continuum contamination in CII maps will be originated in emission from stars, dust emission, free-free, free-bound and two photon emission, however the overall intensity from these processes will be at least 2-3 orders of magnitude below the predicted CII signal and so in principle it will not be necessary to clean these foregrounds.

Line emission contamination is more problematic to CII intensity mapping during the EoR, since at these observational frequencies the intensity maps will be contaminated by emission from several infrared lines, namely the $[\mathrm{OI}]145\mu\mathrm{m}$, the $[\mathrm{NII}]122\mu\mathrm{m}$, the $[\mathrm{NII}]205\mu\mathrm{m}$ and the CO rotation lines from transitions $\mathrm{CO}(2-1)$ and higher. The $[\mathrm{OI}]145\mu\mathrm{m}$ and the $[\mathrm{NII}]205\mu\mathrm{m}$ lines are emitted from PDRs and the $[\mathrm{NII}]122\mu\mathrm{m}$ line is emitted from HII regions and so the SFR is a good tracer of their emission such as in the CII case. The fraction of FIR emission in each of these lines depends on the galaxy properties but rough estimates can be obtained from several references, namely from: Graciá-Carpio et al. (2011) [109], Brauher et al. (2008)[110], Ferkinhoff et al.(2011) [111] and Zhao et al.(2013) [55] for respectively the [OI]$145\mu m$, the [NII]$122\mu m$ and the [NII]$205\mu m$ line. Using the relations in these studies plus a SFR versus halo mass relation as a function of redshift such as the one which can be obtained from the DeLucia et al.(2007) [43]

simulated galaxies catalog, the luminosity of these lines can be estimated for a galaxy or a dark matter halo as a function of its mass and redshift. Since intensity mapping calculations involve large volumes, with several galaxies per pixel of observation, average luminosities are a good enough approximation. Therefore, the intensity of these foreground lines in the observing band of $200 - 300\mathrm{GHz}$ can be estimated by integrating their luminosities times a theoretical halo mass function over the halo mass. By using these estimates, the total resulting contamination will have an intensity of less than $100\mathrm{Jysr}^{-1}$. With the maximum contribution originating in the [NII]$205\mu m$ line at redshifts $z \sim 3.9 - 6.3$. The contamination power spectra of these lines is smaller than the most reasonable estimations for the CII line power spectra.

The CO lines are emitted from molecular gas and their luminosities depend on several characteristics of the gas and so their emission should be carefully estimated. As previously discussed in Section 1.5.2, observations of CO luminosities mostly target the CO(1-0) line, and observational constraints of the ratios between higher CO transitions are restricted to low redshift galaxies with very high luminosities, and so they cannot impose constrains in the ratios of CO emission in normal galaxies at high redshifts. The ratios between different CO transitions can also be estimated using hydrodynamical simulations, however the computational cost of this type of simulations does not allow to study the wide range of galaxy types necessary to establish statistical properties, such as the relations between CO emission and infrared luminosity [79], and so the use of phenomenological models in semi-analytical codes is more appropriate for intensity mapping studies [112][79].

Currently the most complete simulation of CO emission from several transitions available for high redshifts was obtained by Obreschkow et al. (2009) [112], who post processed the galaxies in the DeLucia et al. (2007) [43] simulated catalog and attribute them first HI and H_2 masses and than used a prescription to associate to each galaxy CO(1-0) luminosities according to their H_2 mass, metallicity, and SFR. The passage from CO(1-0) luminosity to higher transitions was made by assuming that the gas was in thermal equilibrium and using empirical relations calibrated with local observations. More recent studies found that the prescription used by Obreschkow et al. (2009) [112] to separate the cold gas in galaxies in atomic and molecular gas was overestimating the molecular content in galaxies for $z > 2$ and that the prescription used by the same author to obtain CO luminosities was underestimating the ratios between the CO luminosities of the CO(1-0) line and higher transitions [77] [79]. The contamination of CO emission in CII maps can also be estimated with observational LFs as described in Section 1.5.2, however given the uncertainty of the passage from CO(1-0) luminosity to higher transitions it will not be a very reliable estimate.

Given the high degree of contamination by line emission in CII intensity maps it is necessary to remove from observations the contamination from at least the stronger foregrounds. Since the majority of the line contamination will be originated from galaxies with high CO luminosity at redshifts a lot smaller than the CII line sources it is possible to use independent experiments to target these foreground galaxies, find their positions and estimate their intensities so that they can be removed from observations. Since in some cases it might not be possible to directly detect the CO emission from the contaminating galaxies, it is possible to use a tracer of these lines such as the SFR or the apparent magnitudes in a given filter to find them. If we could estimate the contamination by each galaxy with a high accuracy we could in principle remove their intensity from the observational maps, however since such an accuracy is usually not possible and the contamination by foregrounds is higher than the signal we are trying to probe the subtracting errors would be to big. The alternative in these cases is simply to find the position of the contaminant galaxies with a higher flux and put to zero the observational pixels where one of these galaxies is found, this

technique is known as masking foregrounds.

As an alternative for avoiding foregrounds in CII intensity maps, there is the possibility to cross correlate maps of two of the foreground lines at the same redshift or to cross correlate one of the foreground lines with HI 21cm line maps. These cross correlations could be used to properly probe the intensity and fluctuations of the foreground lines and even in same cases to subtract part of the foreground signal from the intensity maps.

1.7.4 Foregrounds in Lyman-alpha Intensity Maps

Intensity maps of Lyman alpha emission during the EoR will be contaminated by transition lines from lower redshifts such as the 6563Å Hα, the 5007Å [OIII] and the 3727Å [OII] lines. The foreground lines which will contaminate Lyman alpha intensity maps at $z \sim 7$ will be emitted at $z \sim 0.5$ for Hα, $z \sim 0.9$ for [OIII] and $z \sim 1.6$ for [OII].

The referred emission lines are all used as tracers of SFR and so they can be estimated both from the galaxy SFR and from observational luminosity functions. Relations between these lines luminosities and the SFR appropriate for the redshift range in study, can be found in Kennicut (2008) [113] for Hα and [OII] and in Ly et al. (2007) [114] for [OIII]. In these publications the SFR versus Hα line luminosity relation is physically based, while the relations for [OII] and [OIII] are based in observations of low redshift galaxies. The advantage of using these relations instead of directly using luminosity functions is that we get better estimates of the contribution of low intensity galaxies since LF methods do not properly account for these galaxies. Luminosity functions for Hα, [OIII] and [OII] can be found in publications such as Ly et al. (2007) [114], Drake et al. [115] and in Gunawardhana et al. (2013) [116] for the $\mathrm{H}\alpha$ line. The conjugation of these studies indicates a meaningful redshift evolution of the lines LFs, especialy at the low luminosity end compared to the high luminosity end. Also, these studies show that the high luminosity constraints are dependent on the experimental setup with observations of larger volumes resulting in shallower slopes.

As a result of these uncertainties, the power spectra of the lines will have an uncertainty ranging from one order of magnitude for Hα to about half an order of magnitude for [OII], at the relevant redshifts. The contamination power spectra of these three lines, scaled to the redshift of the Lyman alpha line, is likely to slightly exceed the Lyman alpha power spectra and so the masking technique should be applied to reduce the contribution from foreground galaxies in Lyman alpha observational maps. A masking of up to 30% of the observational pixels should be enough to remove the foreground without affect much the observational signal. Note that masking the right pixels requires precision in the determination of the positions of the foreground galaxies, which should be taken into consideration in the choice of the experimental setup necessary to target these galaxies.

1.8 Intensity mapping experiments

Intensity mapping experiments collect all radiation from a relatively large angular area and frequency band but with a low resolution, and so without resolving the sources of emission. The flux observed by a intensity mapping experiment is converted into a three dimensional map according only with the angular direction from where it is originated and with its observed frequency. These experiments are set to detect frequencies in a band $[f_{\mathrm{min}}, f_{\mathrm{max}}]$, correspondent to the ob-

served frequency of an emission line with rest frequency f_0 emitted from the redshift interval $z_{\min} = f_0/f_{\max} - 1$ to $z_{\max} = f_0/f_{\min} - 1$. In this way all the radiation emitted at redshift z by the emission line from galaxies and/or from the IGM will be included in the map. However, radiation from continuum emission and from other lines emitted at different redshifts, which are observed in the same frequency band will contaminate the intensity maps.

Observational intensity maps are defined by two angular coordinates indicating the area on the sky and by a frequency coordinate which can be translated into a redshift coordinate for a given line. In the direction of the frequency coordinate there will be redshift evolution of the signal and so the observational power spectra of a line emitted at redshift z will deviate from the intrinsic power spectra of the line at large scales. Intensity mapping experiments have several advantages over other experiments and in particular over galaxy surveys such as:

1. This type of experiments captures radiation from even the more faint stars, which is essential for the study of the Epoch of Radiation.

2. Intensity mapping is possible at high redshifts for which galaxy surveys can only detect the bright end of the galaxy luminosity function, and so it is the only type of experiment which can characterize the astrophysical properties of the main population of high redshift stars.

3. The intensity mapping technique can be used to study the IGM astrophysical properties.

4. The three dimensional structure of intensity maps can be used to probe large structure formation and evolution and in the case of the 21cm line to probe the morphology of ionized regions.

5. The power spectra obtain from intensity maps gives a strong statistic measure of how sources of radiation are distributed over space and can therefore be used for example in the case of the 21cm line to study the sizes and spatial distribution of ionized regions.

6. Also, intensity mapping of different lines emitted from the same redshift and the same region in space can be cross correlated with the advantage that the cross correlation power spectra will not be affected by most foregrounds since the lines will be observed at different frequencies and therefore their foregrounds will be uncorrelated.

There are also three main problems which affect intensity mapping experiments such as:

1. The intensity of some lines is quite small and so intensity mapping at very high redshift is mainly possible with hydrogen and carbon emission lines.

2. The astrophysical and cosmological interpretation of the information contained in intensity maps is highly depended on the use of simulations to model the signals and disentangle the different contributions.

3. Intensity maps suffer contamination from several sources of foregrounds which can be difficult or even impossible to identify and remove.

1.8.1 21cm line Intensity mapping

LOFAR: From the currently available 21cm experiments LOFAR will be particularly good in measuring the 21 intensity and power spectra at redshifts ($z \sim 6$ to $z \sim 11.5$). This experiment has good chances of making the first positive detection of the 21cm line from the EoR. Currently the LOFAR high band antenna (HBA) array operating in the frequency range 115 MHz to 163 MHz is processing the first available data and dealing calibration and noise issues [117].

MWA:The Murchison Widefield Array is a SKA precursor located in Western Australia at the location of the planned Square Kilometre Array. This telescope operates around 80 to 300 MHz with an arcmin resolution and proposes to characterize the ionizing photon sources responsible for reionization and to measure the global evolution of the 21cm signal from $6 \lesssim z \lesssim 10$. This experiment will be sensible to the 21cm power spectra for neutral fractions below 0.8 at the scale $k \sim 0.1$ [118].

PAPER: The Precision Array for Probing the Epoch of Reionization (PAPER) is a low frequency radio interferometer designed to measure 21cm emission at redshifts $z \sim 7 - 12$ (100-200MHz band). It is an array of 32 antennas in South Africa but it is being expanded to a 128 array. This experiment proposes to put upper limits in the 21cm signal intensity and spectral fluctuations as well as serve as a pathfinder to the SKA.

So far this experiment achieved a $(41\mathrm{mK})^2$ upper limit in the 21cm spectra at a redshift of $z = 7.7$ and a scale of $k = 0.27\mathrm{hMpc}^{-1}$. Observations made by the PAPER experiment also served to exclude cold reionization scenarios, which means that they showed to a good confidence level that the neutral IGM at this period was already heated probably by X-rays sources such as X-ray binaries and mini quasars [119]. A positive detection of the 21cm signal during the Epoch of Reionization is however unlikely to be in the reach of this experiment given that it has a small collecting area and so it has big problems at dealing with foregrounds the 21cm signal foregrounds.

SKA: The Low frequencies aperture array antennas from the square kilometre array will be located in Australia and they will operate at least in the frequency range 50 MHz to 350 GHz which corresponds to observations of the 21cm line from redshifts up to a redshift of 19.4 or even more. Which will cover at least the Epoch of Reionization. If constructed a second phase of the SKA will reach lower frequencies and probe the Pre-Reionization Epoch. The SKA will be constructed in two phases the first of is planned to be finished at 2019 and it the second one should be finalized at 2024 [120].

GMR: The Giant Metrewave Radio Telescope experiment consists in 30 parabolic dishes of 45m diameter spread over distances of up to 25 Km in Pune, India. This antenna measures emission observed around 50MHz, 153MHz, 233MHz, 325MHz, 610MHz and 1420MHz which corresponds to the 21cm line from respectively the redshifts $z \sim 27.6$, $z \sim 8.4$, $z \sim 5.1$, $z \sim 3.4$, $z \sim 1.3$ and $z \sim 6 \times 10^{-3}$. The best current EoR constraints obtained with this experiment consist in upper limits at $z \sim 8.4$ of $(70\mathrm{mK})^2$ at $k = 0.65\mathrm{hMpc}^{-1}$ and of $(248\mathrm{mK})^2$ at $k = 0.5\mathrm{hMpc}^{-1}$ [121].

1.8.2 Intensity mapping of the CO(1-0) and CII lines

Emission of the CO(1-0) and CII lines can now be studied with galaxy surveys till the redshifts of the end of EoR, with experiments like the ALMA (Atacama Large Millimeter/submillimeter Array) and EVLA (Expanded Very Large Array) for CO and ALMA, CARMA (Combined Array for Research in Millimeter-wave Astronomy) and the PdBI (Plateau de Bure Interferometer) for CII. Intensity mapping experiments of these lines at high redshifts do not yet exist, although they

have been proposed by several authors [122] [123] [124] [29] [30] and are now being planned by several groups. Examples of proposed experiments are given below.

SPICA: The Space Infrared Telescope for Cosmology and Astrophysics is a 3.5 meter space-borne infrared telescope which should be launched in 2017, and can in principle be used to carry a high performance spectrometer designed to detect emission from transitions CO(1-0) and CO(2-1) at $z \sim 6$[125].

TIME: The Tomographic Ionized-Carbon Mapping Experiment proposes to map CII emission in the redshift range $z \sim 8.5 - 5.5$, using 32 independent single-beam, single-polarization spectrometers, each covering a $200 - 300\mathrm{GHz}$ frequency band. Each spectometer will have 57 bolometers and the total survey will cover a 1.3 deg $\times$ 0.5 arcmin area with a frequency resolution of 2GHz times 0.5^2 arcmin^2.

The TIME group proposes to complement the CII experiment with the use of current galaxy surveys to detect the CO emitting galaxies from lower redshifts, which will contaminate CII intensity maps. The possibility to construct an experiment especially to detect CO emission, from several transitions, originated from galaxies with redshifts below six, is also being considered.

1.8.3 Intensity mapping of the Lyman alpha line

During the EoR a significant fraction of $(\sim 5 - 40\%)$ of the bolometric luminosity of star forming galaxies was emitted in the Lyman alpha line. Most of this emission was scattered by neutral hydrogen around the galaxy, which makes the line of sight signal very weak and difficult to be observed by galaxy surveys.

However, intensity mapping of this line has the potential of probing most of the Lyman alpha emission by not resolving its sources of emission and by detecting emission in very large volumes. Even though Lyman alpha emission might be observed at slightly different directions/frequencies compared to the position of the sources of Lyman alpha photons, this will not be a problem since with intensity maps we can still probe average properties of the sources of emission. Lyman alpha intensity mapping experiments during the EoR still do not exist, but they have been suggested in several publications [126][127][128] and are now in a proposal phase.

2
Summaries of the publications

In this Chapter are shown brief summaries of the publications included in this thesis. The complete original publications are shown in the Appendix.

During this PhD the main works the PhD candidate collaborated in resulted in six publications: Paper I, Paper II, Paper III, Paper IV, Paper V and Paper VI, which constitute the core of this thesis.

Publications Paper I, Paper II, Paper IV, Paper V and Paper VI show three dimensional intensity mapping estimations of lines emitted during the high redshift Epoch of Reionization, while publication Paper III shows a intensity mapping estimation of a line emitted in the post-Epoch of Reionization. In a overall view of these publications, they contain calculations of the intensity and spatial fluctuations of high redshift emission lines, which were based in a careful analysis of the astrophysical mechanisms responsible for the radiation emission, in the use several simulations in order to properly model the signals in the constant use and/or comparison of the results obtained with the available observational data.

Following the regulations of the IST PhD program, the contribution of the PhD candidate to the publications is specified here.

In all the referred publications the candidate performed the necessary computations related with handling simulated or observational databases, made or altered all the simulation codes necessary for these studies, ran all the codes and analysed most of the simulated data. Note that in order to develop the simulations necessary for publications Paper IV and Paper VI the candidate had to make fundamental improvements to the Simfast21 Reionization code.

The candidate participated in the extensive research of the available observational and simulated data used in all of the publications present in this thesis, and in the establishment of the relations between these data and the intensity of the relevant emission lines. Also, the candidate was responsible for most of the foreground studies in publications Paper IV and Paper VI and contributed for the remaining foreground studies.

The candidate wrote most of publications Paper IV and Paper VI, made all of the figures in these publications, contributed to the writting of publications Paper I, Paper II, Paper III and Paper V and made some of the figures in these publications. The final interpretations of the results obtained was done by the candidate together with other authors.

2.1 Probing Reionization with Intensity Mapping of Molecular and Fine-Structure Lines (Paper I)

Gong Y., Cooray A., **Silva M. B.**, Santos M. G. and Lubin P.
The Astrophysical Journal, 705, 135-14 (2009)
arXiv:0909.1971

In Paper I we studied the potential of intensity mapping of the ^{12}CO(J=1-0) line at redshifts ($z \sim 6-8$), to constrain the Epoch of Reionization. The CO lines are tracers of molecular gas, which is associated with star forming regions, and therefore can be used to probe properties of the galaxies responsible for the process of hydrogen reionization. Since, there are no observations of the CO(1-0) transition at such high redshifts we theoretically estimated the intensity of the this line using the simulated galaxies catalog from Obreschkow et al. (2010) [112]. This catalogs contains CO(1-0) fluxes, for galaxies in the redshift range relevant for this study, however it only contains galaxies belonging to dark matter halos with high masses, therefore we used the properties from the galaxies in these catalogs to establish parameterizations of the CO luminosity as a function of halo mass and extrapolated it into lower halo masses. The intensity of the CO line could then be estimated by integrating the CO flux of a halo, times the theoretical halo mass function, over the mass range of the halos capable of emitting in the CO line.

Dark matter halos are formed by gravitational collapse of overdense regions, and so the fluctuation in the intensity of lines emitted from these halos, such as the CO(1-0) line, will be strongly biased with the underling matter density fluctuations. Based in Press-Schechter halo theory, we used the parameterized relation between CO(1-0) luminosity and halo mass to estimated an average CO(1-0) bias with the matter density of $b_{\rm CO} = 6$. Theoretically, it is expected that the spatial fluctuations in the CO(1-0) intensity follow the fluctuations in dark matter with a normalization given by the product of the bias and the intensity previously estimated. We used this assumption to calculate the clustering component of the CO power spectra and added shot noise to this power spectra, in order to account for the discretization of galaxies.

We took our predictions of the CO(1-0) power spectra and tested the possibility of using a CO interferometer, similar to the ones used 21cm experiments, to measure and map CO emission. We concluded that during the end of the EoR, at $z \sim 8-6$, the CO(1-0) line can be observed by the proposed experiment with a mean brightness temperature of about 0.5μK and rms fluctuations of $\sim 0.1\mu$K at the scales 1 to 10 Mpc. We made a mistake in the units conversion during this calculation and so the expected intensities should be one order of magnitude lower than the ones referred, however the experiment proposed is still possible.

We used theoretical formulas to estimated the 21cm line intensity from galaxies and from the IGM at the same redshifts. In our calculations we simplified the estimation of the 21cm intensity from the IGM by assuming that the spin temperature contribution to the 21cm intensity was already saturated and by ignoring the contribution from peculiar velocities. We set the HI fraction to be equal to 0.3 and 0.7 at $z = 7$ and $z = 8$ respectively, following the estimations from the Mao et al. (2008) [37]) simulation.

The 21cm intensity from galaxies was theoretically estimated using HI masses obtained from the properties of the halos in the Obreschkow et al. (2010) [112] galaxies catalog. In figure 2.1 we show the parametrizations we made, with the simulated galaxies catalog, for the CO(1-0) luminosity and for the HI mass as a function of halo mass. The power spectra of the hydrogen 21cm line emission was also estimated by assuming that HI fluctuations were proportional to fluctuations

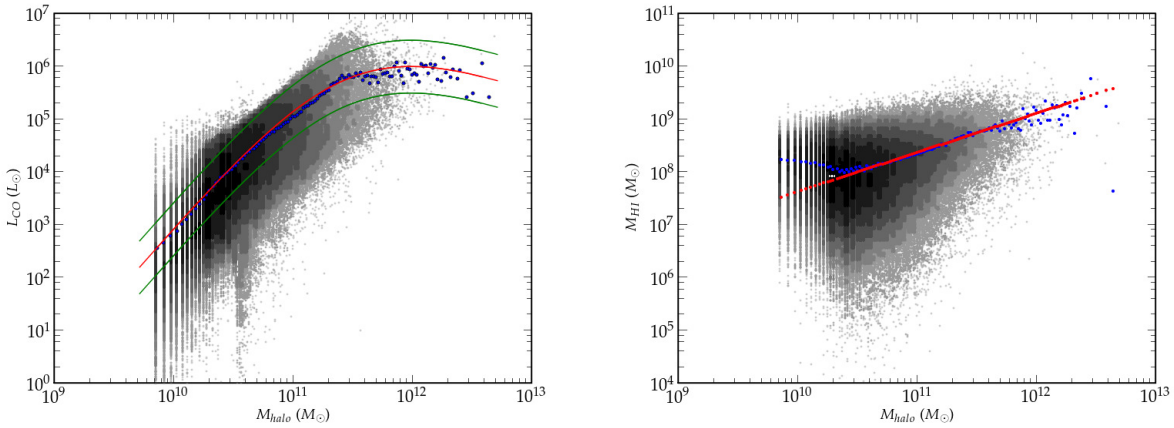

Figure 2.1: *Left*: The $L_{\rm CO}(1-0)$ versus halo mass relation as a function of the halo mass at $z = 7$. The lines shows the mean relation (thick center line) and the $\pm 1\sigma$ relations (thin lines), given the scatter. The dots show the mean of the scatter when binned to 150 logarithmic intervals in halo mass. *Right:* The relation between neutral hydrogen mass content in individual galaxies versus the halo mass at $z = 7$.

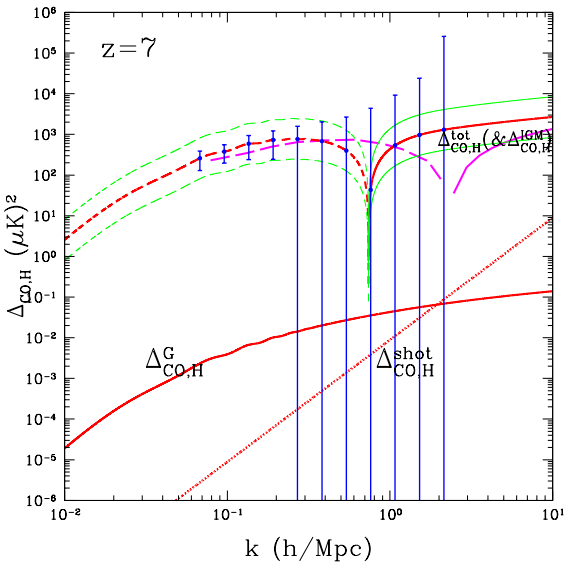

Figure 2.2: Dimensionless cross power spectrum (red line) and shot noise power spectrum (red dotted line) for the CO(1-0) line and 21cm line at z = 7. The blue solid lines show the error using the LOFAR setup to observe the 21cm line. The green dashed line correspond to the 68.3% C.L. (1σ). The long-dashed magenta line is the results from the simulation of 21cm in Santos et al. (2010)[38] for comparison.

in the dark matter density, plus a shot noise contribution in the HI fluctuations from galaxies. We theoretically cross correlated the CO(1-0) and the HI lines in this way obtaining a statistical measure of the intensity of the two lines free of foregrounds. As is shown in figure 2.2, the cross correlation power spectra for the 21cm line from the IGM and of the CO(1-0) line is positive at small scales since they both follow density fluctuations, but it is negative at large scales since they

are emitted in separate phases of the gas. The cross correlation turnover scale is proportional to the IGM ionized fraction and to the size of ionized regions. The cross correlation between the 21cm line from galaxies and the CO(1-0) line is always positive since both these lines are emitted from the same regions. From the intensity of the cross correlation power spectra of these lines we concluded that it is possible to built a interferometer to measure CO(1-0) emission in the region of the sky observed by LOFAR, and than estimate the cross correlation of the two lines, especially at scales close to $0.1\mathrm{Mpc/h}$, see figure 2.2.

2.2 Intensity mapping of the [CII] fine structure line during the Epoch of Reionization (Paper II)

Gong Y., Cooray A., **Silva M. B.**, Santos M. G., Bock J., Bradford C. and Zemcov M.
The Astrophysical Journal, 745, 49 (2012)
arXiv:1107.3553

In Paper II we used the ionized carbon fine structure line emitted at $157.7\mu m$ to trace the dense gas emission at $z = 6 - 8$, and therefore to probe the Epoch of Reionization.

We took into account all the astrophysical processes relevant for CII emission, which includes spontaneous, stimulated and collisional emission and estimated the intensity and spatial fluctuations of CII emission from galaxies and from the IGM using analytic calculations and using simulations. We started by estimating the theoretical intensity formula for CII intensity, which we found to be mainly dependent in the number density of CII ions $(n_{\rm CII})$ and in the spin temperature of the transition, which we estimated for both the IGM and the galaxies ISM. In galaxies we assumed that the spin temperature could be ignored since it was much higher than the transition temperature, which was higher than the CMB temperature and so it was saturated. The $n_{\rm CII}$ from galaxies was calculated analytically and using simulated data. The $n_{\rm CII}$ from the diffuse IGM was calculated only theoretically, since that was enough to see that the intensity from this gas component was negligible. For the analytic galaxies calculation we assumed that the metallicity in galaxies evolved with redshift as $({\rm Z/Z_\odot} = 10^{-0.4z})$, that the metals fraction in carbon was similar to the one found in the sun and that a fraction of 0.01 of the carbon in galaxies was in hot dense environments and therefore emitting in the CII line. For the analytic calculation in the IGM we assumed that the metallicity $(Z_{\rm IGM})$ was only 10^{-2} times the metallicity from galaxies and that $n_{\rm CII} = Z_{\rm IGM}\bar{n}_b$ where $\bar{n}_b$ is just the baryon number density.

The simulated CII emission from galaxies was modeled using a $n_{\rm CII}$ derived from galaxy properties contained in the Obreschkow et al. (2010) galaxies catalog [112]. In this calculation we assumed that all the carbon in the hot gas component available in the galaxies catalog was ionized and emitting in the CII line. We also considered the possibility that a small fraction of the cold gas was actually warm and emitting in the CII line. The evolution of the number density of atoms emitting in the CII line predicted by these calculations is shown in left panel of figure 2.3. We simulated intensity maps of CII emission by altering and adding modules to the Simfast21 code [59]. The output CII intensities are shown in right panel of figure 2.3.

A variety of CO transitions at lower redshifts will contaminate CII observations, since the lines will be observed at the same frequencies. We used the CO luminosity formula from Visbal & Loeb (2010) [122] (which was calibrated based in the ratios of the galaxy M82 for the SFR and the luminosity in each of the CO lines), to estimate the contamination power spectra of CO emission. This contamination power spectra corresponds to the distortion caused by CO intensity fluctuations at z' in the CII power spectra at z, where $(1+z') = (1+z)\left(\nu_{\rm CO(J\rightarrow J-1)}/\nu_{\rm CII}\right)$, $\nu_{\rm CO(J\rightarrow J-1)}$ is the rest frequency of the $\rm CO(J \rightarrow J-1)$ transition and $\nu_{\rm CII}$ is the rest frequency of the CII line. We found that the higher contamination by CO was originated in emission by very massive galaxies and that the degree of contamination by CO lines from transitions (2-1) to (6-5) in the CII power spectra, was only about 2% to 30% of the CII power spectra. Since the degree of contamination is small, the main CO emitting galaxies can be easily detected by galaxy surveys and the observational pixels of the CII intensity maps, where the CO emission is detected, can be masked without erasing CII fluctuations.

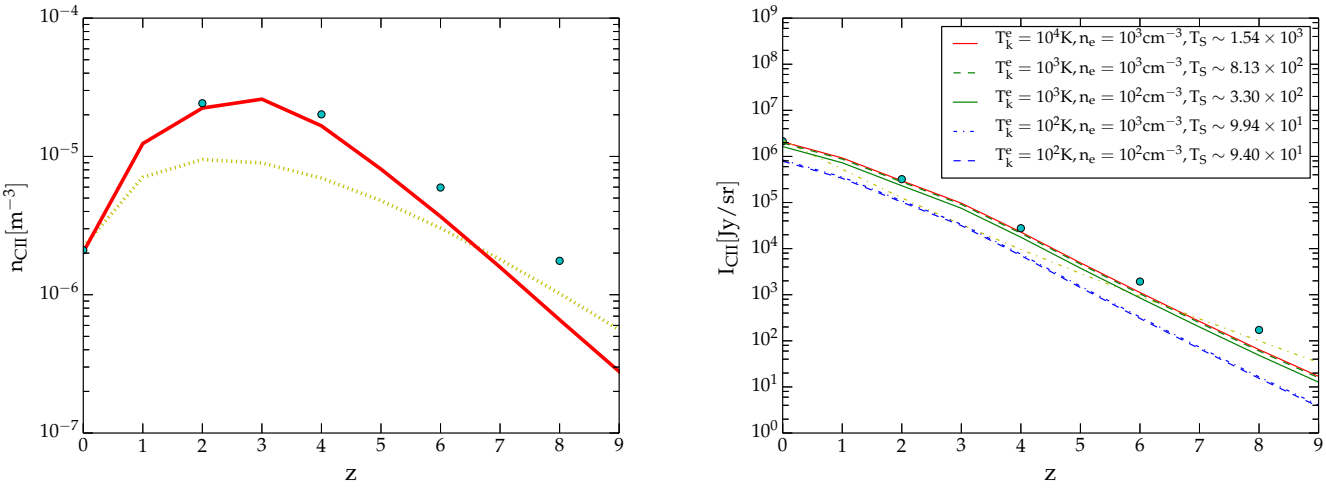

Figure 2.3: Left panel: The CII proper number density as a function of redshift. The red solid line is derived from our simulation with just hot gas contributing to $L_{\rm CII}$, the yellow dotted line is our analytic result, and the blue spots are obtained from the simulation using both the hot gas and the warm gas (10% of the cold gas in the galaxies). Right panel: Intensity of the [CII] emission line obtained using the galaxy properties from the De Lucia & Blaizot (2007) [43] simulation at several different redshifts. Our analytic result is shown in the yellow dotted line whereas the blue spots were obtained from the simulation with the hot and warm gas contributing to the CII luminosity, these intensities were calculated with $n_{\rm e} = 10,000{\rm cm}^3$ and that the electronic temperature was 10^4 K. The other lines were obtained from the simulation, assuming that only the hot gas contributes to the CII luminosity.

Based in these results, we outlined three potential CII intensity mapping experiments using different size aperture telescopes outfitted with a bolometer array spectrometer, which should be capable to map the CII intensity fluctuations at redshifts $z \sim 6$ to 8

We also proposed to cross correlate maps of the CII line and of the HI 21cm line, emitted from the IGM, by using two independent 21cm and CII experiments observing overlapping regions in the sky at redshifts 6, 7 and 8. For the HI intensity calculation we assumed mean neutral hydrogen fractions of 0.05, 0.35 and 0.62 at redshifts 6, 7 and 8 respectively, wher the neutral hydrogen ($x_{\rm HI} = 1 - x_i$) values were obtained from a HI simulation made with the Simfast21 code. The cross correlation power spectra between the CII and HI lines can be observed in left panel of figure 2.4, plotted together with error bars from the HI 21cm line assuming a 21cm experiment with a similar setup to the SKA. This plot shows that according to the models used it is possible to constrain the fluctuations in these two lines for large scales at redshifts $z \sim 6 - 7$. The HI and the CII lines are anti-correlated at large scales since they are originated in gas contained in the IGM or in galaxies, respectively. At small scales the two lines are correlated since both these lines are positively biased with the underlying matter density fluctuations. The cross correlation power spectra between HI and CII emission is given by $P_{\rm CII,HI} \propto 4/3(1-\bar{x}_i)P_{\delta\delta} - \bar{x}_i P_{\delta_x \delta}$, where $P_{\delta\delta}$ is the matter density power spectra and $P_{\delta_x \delta}$ is the cross power spectra between density fluctuations and the ionization field. This relation predicts the discontinuity in the cross correlation power spectra to mark the point when the matter density auto correlation stops dominating the cross correlation.

In left panel of figure 2.4 we show the cross correlation coefficient between CII and HI emission

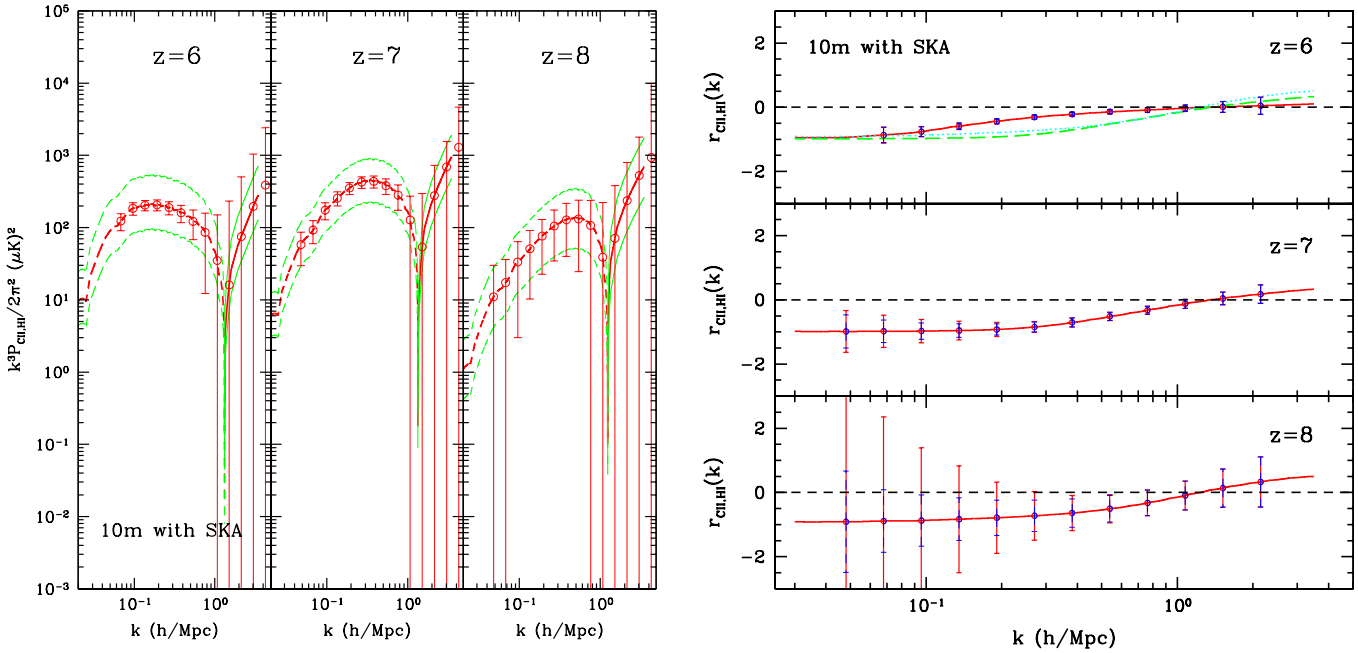

Figure 2.4: Left panel: The cross power spectrum of the CII line and the 21cm emission line from the IGM at $z = 6$, $z = 7$ and $z = 8$. The red dashed lines denote the negative correlations while the red solid lines denote positive correlations. The 1σ errors are also shown in thin green lines. Right panel: The cross-correlation coefficient (r) of the CII and 21cm emission at $z = 6$, $z = 7$ and $z = 8$. The error bars in r are shown in the red solid lines and the error contribution from 21cm emission is shown with the blue dashed bars. The extra lines in the top panel, which correspond to $r_{\rm CII,HI}(k)$ at $z = 7$ (green dashed) and $z = 8$ (cyan dotted), are shown to denote the evolution of the ionized regions size at these redshifts relative to $z = 6$. As expected, the average ionized regions size is greater at $z = 6$ than at $z = 7$ and 8. Both plots assume a submillimeter survey with a 10m aperture for the CII line and a setup similar to SKA for 21-cm measurements.

at $z = 6$, $z = 7$ and $z = 8$, defined as $r_{\rm CII,HI}(k) = P_{\rm CII,HI}(k)/\sqrt{P_{\rm CII}(k)P_{\rm HI}(k)}$. The scale at which $r_{\rm CII,HI}(k)$ rises up from -1 towards zero reflects the typical size of ionized bubbles and so it increases for lower redshifts, as is shown in figure 2.4.

2.3 The OH line contamination of 21 cm intensity fluctuation measurements for z=1 4. (Paper III)

Gong Y., **Silva M. B.**, Chen X., Cooray A., Santos M. G., Bock J., Bradford C. and Zemcov M.
ApJL, 740, 1 (2011)
arXiv:1108.0947

In Paper III we discuss the contamination of 21cm intensity maps in the post-Reionization Epoch, originated in 18 cm OH lines emitted by masers. More specifically, we determined the contamination of 21cm line intensity maps at $z_{HI} = 1, 2$ and 3 by OH 18cm lines from respectively $z = 1.38, 2.42$ and 3.57, using semi numerical simulations to estimate the intensity and spatial fluctuations of the signal and of the foreground lines. Emission in the OH line by masers will trace star forming regions obscured by dust and so intensity maps of these lines can be very useful to probe the evolution of the star formation rate density. The final objective of this study was to determine if it is possible to constrain the dark matter density fluctuations from their contribution to hydrogen 21cm intensity maps at $z \sim 1 - 3$, despite contamination issues by OH emission.

OH masers and megamasers are rare as they are only found in the luminous infrared galaxies (LIRGs with $L_{IR} > 10^{11} L_{\odot}$) and in ultra-luminous infrared galaxies (ULIRGs with $L_{IR} > 10^{12}\ L_{\odot}$), however the emission by this molecule can be a strong contaminant in 21cm observations since the intensity of these lines is strongly amplified [97]. We used observational constraints and simulations to determine what fraction of the dark matter halos contained LIRGs or ULIRGS, which of this subset of galaxies hosted an OH megamaser, and how the OH luminosity of a halo can be related to its mass. Based in previous observational studies we assumed that only a fraction f_{IR}, of the halos above $10^{11} M_{\odot}$ contains LIRGs or ULIRGs, where $f_{IR} \sim 1$ for halos with masses above $10^{12} M_{\odot}$ and decays very fast for lower halo masses. We also assumed that only a fraction $f_{OH} = 0.2$ of the LIRGs and ULIRGs hosted OH megamasers [97].

Following the most recent observational constraints available, the OH luminosity of a galaxy scales with its SFR (see middle panel of figure 2.5), and although there is a reasonable dispersion in this relation, for the large volumes and low resolutions involved in intensity mapping studies it is reasonable to assume that the total OH emission will follow the average of this relation, since the estimates are being made with a large number of galaxies. The final link to estimate the OH intensity at the relevant redshifts is the SFR versus halo mass relation, which we estimated using the properties of the galaxies in the DeLucia et Blaizot (2007)[43] simulated catalog, see left panel of figure 2.5.

The intensity of a line can be theoretically estimated by integrating the line's luminosity density times the dark matter halos mass function over the halos mass. Using this assumption we theoretically estimated the OH intensity to be between 1 and 16 μK, in the relevant redshift range. With the OH luminosity versus halo mass relation we also estimated the OH bias with dark matter density fluctuations and finally its spatial fluctuations. The resulting bias and OH intensity equivalent temperature are shown in left panel of figure 2.6.

At low redshifts the hydrogen in the IGM is fully ionized and so the remaining neutral hydrogen is restricted to galaxies. Using the HI masses in galaxies in the Obreschkow et al. [112] simulated catalog obtained by post processing the galaxies in the DeLucia et Blaizot (2007) catalog we parameterized the HI mass as a function of halo mass (see: left panel of figure 2.5) and estimated the HI density by integrating the HI mass times a theoretical halo mass function over the halo mass. We confirmed that the resulting HI density was compatible with recent observational constraints.

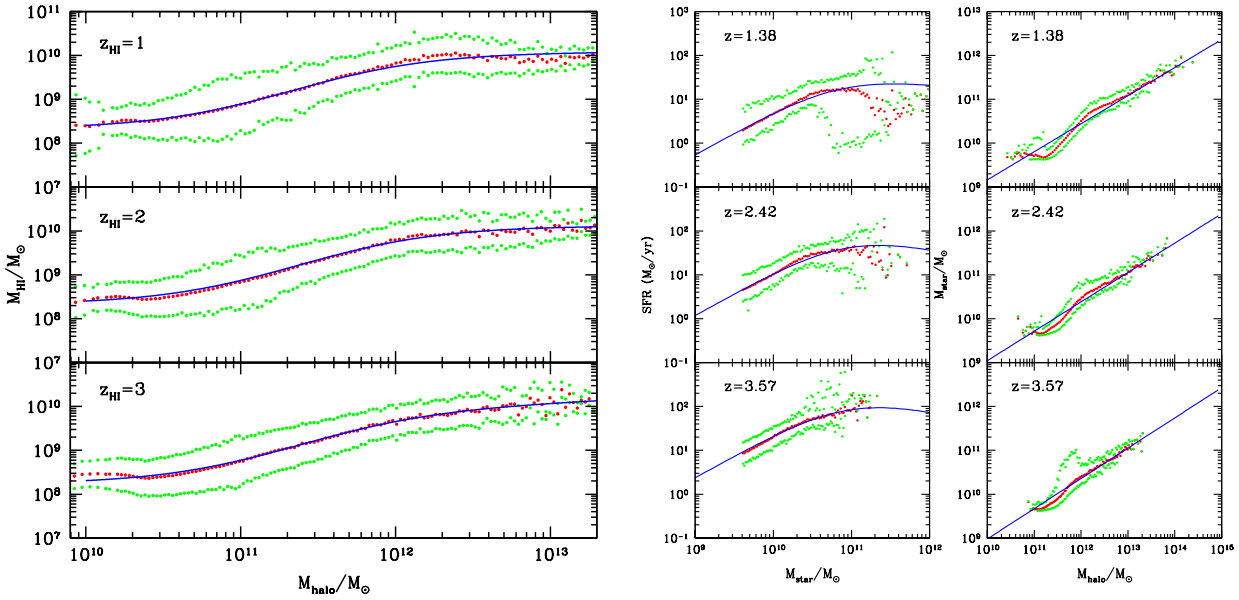

Figure 2.5: Right panel: the $M_{\rm HI}$-$M_{\rm halo}$ relation from the simulation. Left panel: the SFR vs. the stellar mass $(M_\star)$ and $M_\star$ vs. $M_{\rm halo}$. The relations in both panels were derived from the DeLucia et al. (2007) [43] galaxy catalog. The red dots are the mean value and the green dots show the 1σ error from the simulation. The best fits are shown in the blue solid lines.

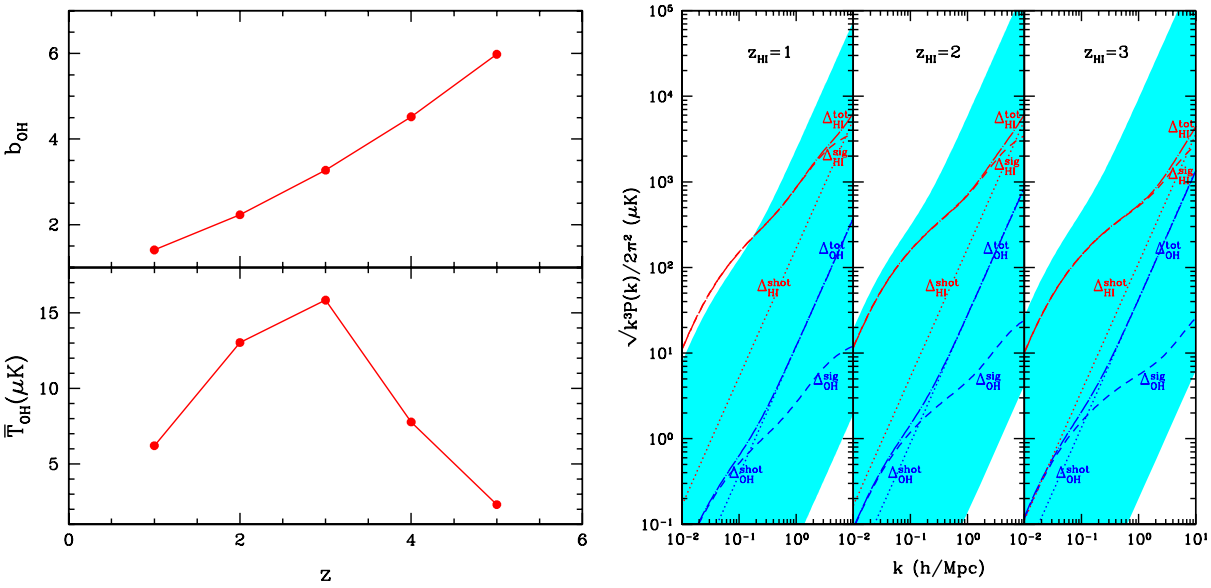

Figure 2.6: Left panel: OH megamaser clustering bias and the mean OH brightness temperature at z=1, 2, 3, 4 and 5. Right panel: The rms intensity fluctuations for OHM megamasers and 21-cm emission. The blue dashed, dotted and dash-dotted lines correspond to the OH megamaser signal, shot-noise and total power spectrum. The uncertainty of the OH emission is shown in the cyan region, which was estimated using the uncertainty in the OH luminosity versus infrared luminosity relation. The red lines correspond to the 21-cm power spectrum.

The brightness temperature intensity and fluctuation due to HI emission from galaxies was then estimated using the usual theoretical formulas.

The contamination by OH emission in 21cm line observations, according to the uncertainty in OH emission, can be observed in right panel of figure 2.6. Depending on the relation between OH luminosity and infrared luminosity the contamination by OH in the 21cm power spectrum can be high, however for our most likely estimation the contamination levels will not be too problematic. With this study we estimated that at the scale of the first BAO peak (about $k = 0.075\mathrm{h/Mpc}$), the OH rms fluctuations are about 0.03%, 0.07% and 0.11% of the 21 cm rms fluctuations at $z_{\mathrm{HI}} = 1$, 2 and 3 respectively. We also note that higher redshifts the OH contamination will become even smaller, while the 21cm signal will become stronger, and so OH contamination in 21cm intensity maps will not be an important issue at higher redshifts.

2.4 Intensity Mapping of Lyman-alpha emission during the Epoch of Reionization (Paper IV)

Silva M. B., Santos M. G., Gong Y., Cooray A. and Bock, J.
The Astrophysical Journal, 763:132, 16pp (2013)
arXiv:1205.1493

In our previous publications we found that intensity mapping of transition lines emitted from hot ionized gas or from molecular gas, during the end of the EoR, were good astrophysical and cosmological probes and that the cross correlation between maps of these lines and of the 21 cm line was a viable way to probe the EoR. In this work we apply the same methodology to study the possibility to develop an intensity mapping experiment targeting Lyman-alpha emission during the same period.

Lyman alpha is emitted by hydrogen gas due to several processes both in galaxies and in the IGM, and so to properly estimate its intensity of emission and spatial fluctuations we consider Lyman alpha emission due to: recombinations, collisions, continuum emission from galaxies, cooling of gas heating shock heated during structure formation and scattering of Lyman alpha photons in the IGM.

The objective of making these intensity maps is to study the Lyman alpha signal from "line emission" and so the continuum contribution from galaxies originated in stellar, free-free, free-bound and two photon emission will only confuse the Lyman alpha signal, fortunately with our study we were able to shown that the continuum contribution, at the relevant redshifts for this study, is several orders below the total signal. Contributions to Lyman alpha line emission from galaxies originated in recombinations, collisions and cooling of gas during structure formation can be calculated from the galaxies SFR, cold gas mass, ionizing photons emissivity and escape fractions of ionizing and Lyman alpha photons, using the previously obtained theoretical and simulated relations in Gould & Weinberg [129] and in Fardal et al. (2001) [130]. To estimate the different Lyman alpha luminosities we used the SFR and cold baryonic mass versus halo mass relations parameterized from data in simulated galaxy catalogs [43], [71] and [112] and the best available constraints from simulations and observations for the other parameters [18][63] [131]. Given the uncertainty in the parameters relevant for the estimation of Lyman alpha emission we also considered two extra models of the SFR versus halo mass relation, set to be more compatible with current constraints of the EoR timeline. Since, there are a few observational galaxy luminosity functions of high redshift Lyman alpha emitters, we compared our predictions with these constraints and concluded that they were compatible considering the uncertainty in the transmission of Lyman alpha photons in the IGM, which decreases the observed Lyman alpha luminosities compared to the intrinsic Lyman alpha luminosities, where the intrinsic values are the relevant quantities for intensity mapping experiments.

The Lyman alpha emissivity from the IGM depends on local values of the gas ionized fraction, temperature and density and so it requires simulations to be properly calculated. Therefore, we altered the Simfast21 code [59] so that it generated intensity maps of Lyman alpha emission in the IGM including the contribution from recombinations and collision in ionized regions and from recombinations, collisions and scattering of Lyman-n photons (originally emitted from galaxies) in the cold IGM. The main alteration to the code was to improve the hydrogen ionization module by substituting the ionizing efficiency constant parameter by a proper astrophysically based estimation of the number of ionizations and recombinations in a ionized region. The use of simulations

allowed us to make an improved estimation of the number density of Lyman alpha emission due to recombinations in ionized regions. However, even with the improvements made the Simfast21 code could not be used to estimate Lyman alpha emission outside of ionized regions originated in recombinations or excitations (which is not very problematic issue since the emission in this medium should be negligible), and could not properly simulate Lyman alpha emission due to collisional excitations in ionized regions. The number of excitations of Lyman alpha emission in the IGM was therefore only roughly estimated in these simulations given the high resolution required to model such a emission. We were however able to put theoretical limits in the intensity of Lyman alpha excitation emission in the IGM and our study was able to show that Lyman alpha emission in this medium should be dominated by recombinations and not by collisional excitations, see figure 2.7.

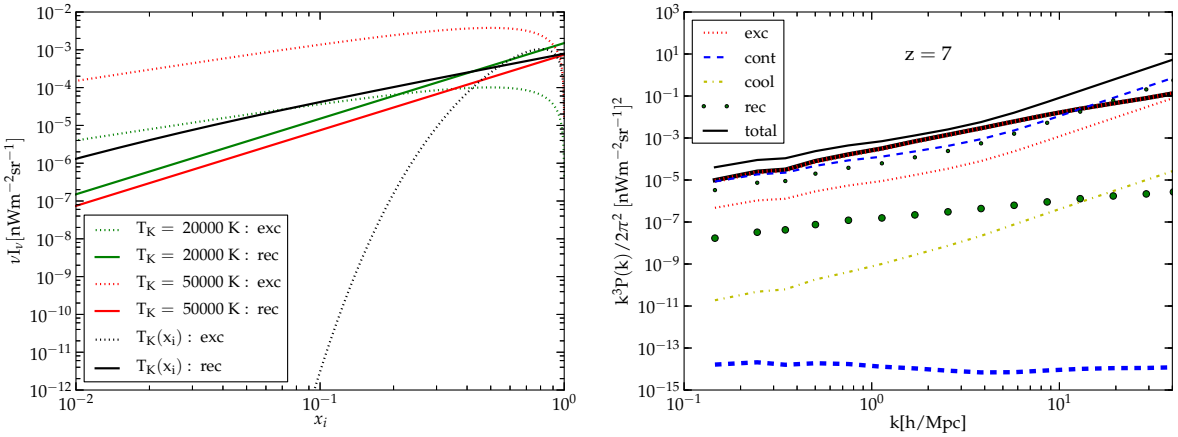

Figure 2.7: Left panel: Intensity of Lyman-alpha emission at redshift 7 due to recombinations and excitations in the IGM as a function of the hydrogen ionized fraction. Black lines uses a gas temperature dependent on the IGM ionized fraction. The green and red lines assume a constant gas temperature of 20.000K and 50.000K respectively. Right panel: Power spectrum of Lyman alpha surface brightness from galaxies (thin lines) and from the IGM (thick lines) at redshift 7. The shown contributions to the Lyman alpha flux are from: excitations and collisions, recombinations, continuum emission inside the Lyman alpha width (from galaxies), scattering of Lyman$-n$ photons (from the IGM), cooling emission in galaxies and total emission.

Using our simulations we estimated the power spectrum of the several contributions to Lyman alpha surface brightness as is shown in right panel of figure 2.7. According to our calculations at a redshift of z $\sim$ 7, Lyman alpha emission from galaxies should dominate over Lyman alpha emission from the IGM. The predicted contamination of Lyman alpha intensity maps by Hα emission lines emitted from lower redshift galaxies is also plotted in right panel of figure 2.8, before and after a cleaning procedure being applied to the observational maps in order to show that the Lyman alpha signal can be successfully extracted from observational intensity maps.

Since both the 21cm and the Lyman alpha lines trace neutral hydrogen these two lines are expected to be strongly correlated, and so with the Simfast21 code we generated intensity maps of 21cm emission from neutral hydrogen and cross correlated them with the Lyman alpha intensity maps. The cross correlation between these two lines is free of most foregrounds that affect each

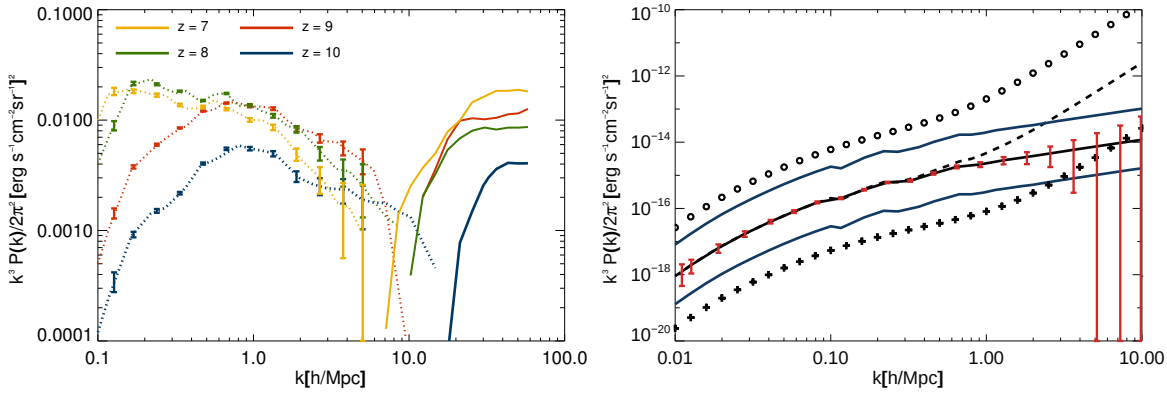

Figure 2.8: Left panel: Cross correlation power spectrum between Lyman alpha emission and the 21cm signal for redshifts 7, 8, 9 and 10. Dotted lines indicate a negative correlation and solid lines indicate a positive correlation. Right panel: Lyman alpha clustering power spectrum at $z = 7$. Black solid line shows the clustering power spectrum for our lower SFR model while the dashed line includes the shot noise. Red vertical bars show the error. The lower blue solid line shows the clustering power spectrum for a high SFR model while the top blue solid line shows the same for a low SFR model with the same reionization history and optical depth (from WMAP) but multiplied by 9 taking into account the upper bounds of uncertainties involved. Circles show the expected Hα contamination power spectrum originated from emission of galaxies at $z = 0.5$ and crosses gives the expected Hα signal after galaxies with a Hα luminosity $> 1.0 \times 10^{40}$ erg s^{-1} being removed. The error bars in the figures were obtained using a space based experiment for the Lyman alpha measurements and an experiment like SKA phase two for the 21cm signal measurements.

line and can therefore be very valuable in confirming 21cm signal observations. The correlation is negative for large scales, as a result of Lyman alpha emission being mainly originated around galaxies in opposite to the 21 cm line which is mainly originated from the cold IGM. In the cross correlation power spectra, the scale of the discontinuity is proportional to the IGM ionized fraction and to the size of ionized bubbles and can therefore be used to constrain these quantities, see left panel in figure 2.8.

2.5 Foreground contamination in Lyman-alpha intensity mapping during the Epoch of Reionization (Paper V)

Gong Y., **Silva M. B.**, Cooray A. and Santos M. G.
The Astrophysical Journal, 785:1, 72 (2012)
arXiv:1312.2035

In this publication we completed the study presented in publication Paper IV, by making an improved and more complete calculating of the contamination by foreground emission lines in Lyman alpha intensity maps at z $\sim$ 7.

In this study we made use of both SFRs and luminosity functions (LFs) to estimate the intensity and power spectra of the three foreground emission lines: Hα at $z \sim 0.5$, [OIII] at $z \sim 0.9$ and [OII] at $z \sim 1.6$, that will dominate the contamination in Lyman alpha intensity maps at z $\sim$ 7. For the Lyman alpha intensity calculation we used the formulas deduced in publication Paper IV and estimated the Lyman alpha luminosity using one of the SFR versus halo mass relation presented in the same publication, since this relation has shown to be in good agreement with observational constraints from the EoR. The luminosities of the foreground lines are good tracers of the SFR in galaxies and so we estimated the intensity of these lines at the relevant redshifts using observational fits of the lines luminosity as a function of SFR. There is however a 30% to 50% uncertainty in the relations between line luminosity and SFR due to the different types of galaxies, which we used to estimate the upper and lower bound of the emission. We used a SFR halo mass relation parameterized using the galaxies in the Guo et al.(2011) [71] simulated galaxies catalog, a SFR relation obtained from a observational SFRD and four observational LFs to estimate the theoretical intensity of the contaminant lines. The resulting intensities can be observed in figure 2.9.

In order to estimate the contamination of these lines in the Lyman alpha power spectra we had to project the contaminants power spectra to the redshift of the Lyman alpha line, which basically

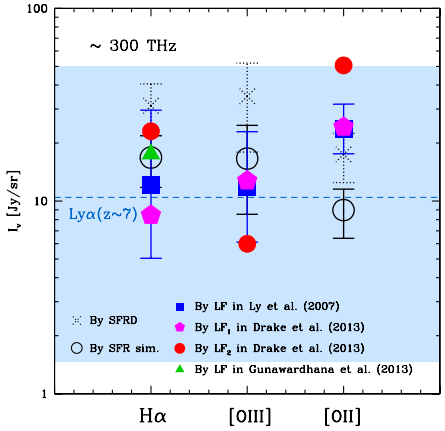

Figure 2.9: Mean intensity of Hα, [OIII] and [OII] using both SFR and LF methods around $z = 0.5$, $z = 0.9$ and $z = 1.6$. The dashed line denotes the mean intensity of Lyman alpha emission at $z \sim 7$ with the uncertainties showed by the shaded region. The results from these two methods are basically consistent with each other. The mean intensities of the Hα, [OII] and [OIII] are generally higher than the central value of the Lyman alpha emission mean intensity, which can provide considerable contamination on Lyman alpha intensity maps.

resulted in a shift of the original power spectra to higher scales and an increase in the amplitude. We found the contamination from these lines to be very high, and so we estimated that we should mask pixels with contamination by sources with a flux above 1.4×10^{-20} W/m^2 in order to decrease the contamination power spectra by a factor of ~ 100. This flux cut corresponds only to the masking of 3% of the pixels in the proposed experiment and allows the detection of the Lyman alpha power spectra at least around $k \sim 0.1$, where the shot noise in the contaminants power spectra is small, see figure 2.10.

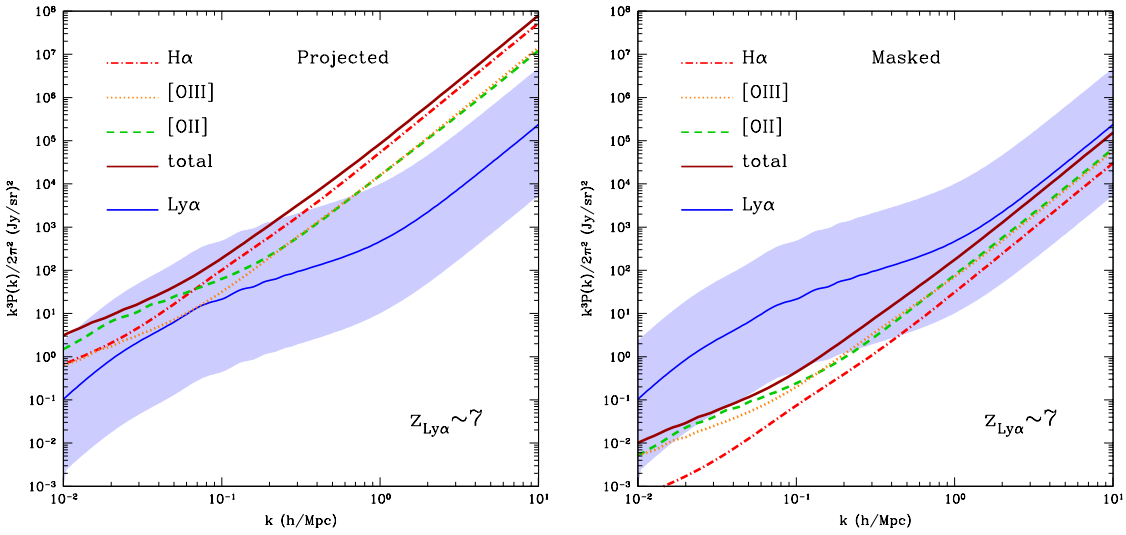

Figure 2.10: Left Panel: Comparison between the total power spectrum of the Lyman alpha at $z \sim 7$ to that of the projected power spectra of the Hα at $z = 0.5$, [OIII] at $z = 0.9$ and [OII] at $z = 1.6$ lines. The uncertainty of the Lyman alpha power spectrum is shown by the shaded region. Right Panel: The power spectra of the Hα, [OII] and [OIII] emission lines masked and projected. The deep red line denotes the total foreground power spectrum after the masking.

The 1.4×10^{-20} W/m^2 flux cut corresponds to line luminosities of: $L_{\mathrm{H}\alpha} \simeq 3.5 \times 10^6$ L$_\odot$, $L_{[\mathrm{OII}]} \simeq 6.3 \times 10^7$ L$_\odot$ and $L_{[\mathrm{OIII}]} \simeq 1.5 \times 10^7$ L$_\odot$. Since these luminosity cuts are close to the lower luminosity limit used to estimate the intensities and power spectra (which was chosen based in the lower limits in the available LFs), the validity of our masking results is dependent of the luminosity of lower luminosity galaxies. These galaxies correspond to the faint-end slopes of the LFs and so their luminosities is poorly constrained by observational data. Note that given the masking percentage estimated being very low it is theoretically possible to mask deeper in luminosity, however we would need to detect the foreground galaxies with a very sensitive experiment targeting a strong SFR tracer.

2.6 Prospects for detecting CII emission during the Epoch of Reionization (Paper VI)

Silva M. B., Santos M.G., Cooray A. and Gong Y.,
To be submitted to The Astrophysical Journal

In Paper VI we improved the ionized carbon intensity calculations presented in publication Paper II and properly estimated all the line and continuum emission foregrounds which will contaminate intensity mapping observations of this line at the observed frequencies of 200 to 300 GHz ($z \sim 8.5 - 5.5$).

Given new observational constraints from galaxy surveys we concluded that the majority of CII emission is originated from photodissociation regions (PDRs) and not from ionized regions as was assumed in publication Paper II. The explanation for the low CII emission from ionized regions is simply that most carbon in these regions is highly shielded from radiation by dense hydrogen columns. Therefore, instead of just using theoretical calculations we estimated the CII luminosity using four models for the CII luminosity versus SFR relation all based in observations of galaxies from medium to high redshifts. The resulting average CII intensity is of approximately $90 - 600 \mathrm{Jysr}^{-1}$ in the 200-300GHz frequency range, where the range of values depends on the CII luminosity model. The connection between CII emission from PDRs and SFR is originated in the carbon being ionized by UV radiation and in CII emission being powered by FUV radiation [132]. While, the connection between CII emission and SFR in ionized regions is based in the size of the ionized region, being proportional to the SFR. We also theoretically estimated the maximum possible CII intensity arising from ionized regions using the relations obtained in publication Paper II, but using an improved parameterization for the mass in metals as a function of halo mass, which is based in two simulated galaxy catalogs. The resulting upper limit for the intensity of CII emission arising from ionized regions is of $\sim 1 \times 10^3 \mathrm{Jysr}^{-1}$ in the 200-300GHz frequency range.

CII intensity maps in the frequency range in study will be highly contaminated by continuum and line foregrounds. Here we used theoretical relations, simulations and observations to estimate the continuum contamination originated in emission from: stars, dust, free-free, free-bound and two photon emission in the ISM, which we found to be of the order of $10^{-1} \mathrm{Jysr}^{-1}$ and therefore a lot lower than the predicted CII signal. Line emission contamination is more problematic to CII intensity mapping during the EoR, since at the relevant observational frequencies, the observational maps will be contaminated by emission from several infrared lines, namely the $[\mathrm{OI}]145\mu\mathrm{m}$, the $[\mathrm{NII}]122\mu\mathrm{m}$, the $[\mathrm{NII}]205\mu\mathrm{m}$ and the CO rotation lines from transitions $\mathrm{CO}(2-1)$ and higher. The $[\mathrm{OI}]145\mu\mathrm{m}$ and the $[\mathrm{NII}]205\mu\mathrm{m}$ lines are emitted from PDRs and the $[\mathrm{NII}]122\mu\mathrm{m}$ line is emitted from HII regions and so we used the SFR as a tracer of their emission such as in the CII case and determined their total intensity to be around $7 \times 10^1 \mathrm{Jysr}^{-1}$.

The CO lines are emitted from molecular gas and their luminosities depend on several characteristics of the gas and so we carefully estimated the intensity of CO emission using two independent methods. We first estimated CO emission using the CO fluxes from the galaxies in the Obreschkow et al. (2009) simulated catalog [112] and than we confirmed our predictions with a CO intensity and power spectra estimated with observational IR luminosity functions and observational relations between the different CO transitions. We found the contamination power spectra of CO emission in CII intensity maps to be very high (up to one or two orders of magnitude above the CII power spectra) and so we estimated the flux cuts necessary to decrease the CO contamination up to two orders of magnitude.

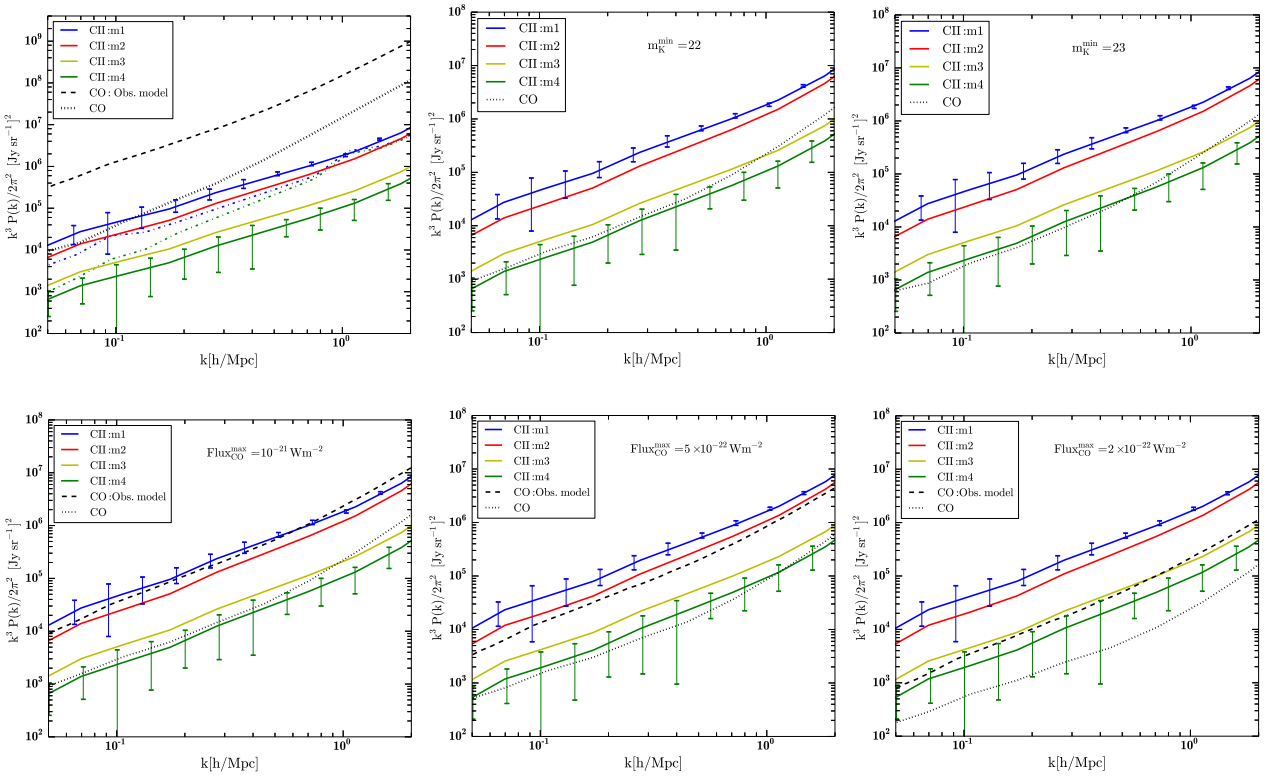

Figure 2.11: Power spectra of CII emission for four parameterizations of LCII vs SFR (solid lines) and power spectra of CO contamination (dotted lines) observed in a frequency range of 37GHz centered at $\mathrm{F_{obs}} \approx 250\mathrm{GHz}$. Upper, left panel corresponds to the total CII power spectra and CO contamination power spectra. The middle and right upper panels assume only CO sources with AB relative magnitudes in the K band above $\mathrm{m_K} = 22$ and $\mathrm{m_K} = 23$ respectively. Lower panels assume only CO sources with Fluxes below $10^{-21}\mathrm{Wm}^{-2}$ (left panel), $5 \times 10^{-22}\mathrm{Wm}^{-2}$ (middle panel) and $2 \times 10^{-22}\mathrm{Wm}^{-2}$ (right panel). Also shown in the lower panels are dashed lines of the theoretical CO emission, with the same flux cuts, estimated using the observationally based method.

Since the flux cuts in CO emission impose the masking of relatively low luminosity galaxies it might not be possible to observationally target CO emission in all of the necessary galaxies, and

Flux/$\mathrm{m_K}$ cuts	CII-low Masking %	CII-high Masking %
$\mathrm{F_{CO}} > 1 \times 10^{-21}[\mathrm{Wm}^{-2}]$	7.70	1.59
$\mathrm{F_{CO}} > 5 \times 10^{-22}[\mathrm{Wm}^{-2}]$	12.99	9.30
$\mathrm{F_{CO}} > 2 \times 10^{-22}[\mathrm{Wm}^{-2}]$	23.31	9.31
$\mathrm{m_K} < 22$	6.23	1.28
$\mathrm{m_K} < 23$	13.76	2.92

Table 2.1: Masking percentages for an observation in a frequency range of 200 to 300GHz made with a pixel resolution of $8.4 \times 10^{-3}\mathrm{deg}^2$ times 0.4GHz or 2GHz for CII-low and CII-high respectively.

so we also proposed to use a CO probe such as AB magnitudes in the K filter ($\mathrm{m_K}$) to detect the contaminant galaxies. The effect of the CO flux cuts and of the cuts in $\mathrm{m_K}$ emission in the contamination power spectra can be observed in figure 2.11, also the masking percentages correspondent to these cuts are presented in table 2.1. As an alternative or in order to complement the masking technique applied to the CO intensity maps, we also proposed to use cross correlation of intensity maps of CO lines to help to measure and to clean foregrounds in CII intensity maps. Finally, we cross correlated CII intensity maps and HI intensity maps at redshift 7 in order to probe if this cross correlation is strong enough to be detected and if it can be used to help constraining the 21cm line intensity during the Epoch of Reionization. We found that the cross correlation between CII and HI emission to be highly dependent on the scale observed and therefore its detection is dependent on the experimental uncertainty at each scale.

3
Conclusions

Properly characterizing the properties of stars and galaxies in the Universe requires a clear understanding of their formation mechanisms and of the forces which drive their evolution. This can only be completely understood with the study of the first light sources which were formed at very high redshifts during the Epoch of Reionization. Given the intrinsic limitations of galaxy surveys, as we go to higher redshifts they become only sensible to the galaxies high luminosity end, which are very rare at high redshift and so are not good representatives of the main galaxy population. In order to characterize global properties of the first galaxies such as the star formation rate density we need an alternative observational method, sensible to more modest luminosity galaxies. The current best alternative to study global properties of the high redshift Universe is using the intensity mapping technique, which measures large scale intensity fluctuations of transition lines characteristic of the different gas phases in galaxies and in the IGM, and therefore can provide a more complete picture of the Universe astrophysical properties.

The work shown in this thesis is centered in the study of the astrophysical and cosmological potential of making line intensity mapping observations of several transition lines towards the end of the Epoch of Reionization and was developed in a way to be useful for the planning of future intensity mapping experiments. The choice of studying the 21cm, the CO(1-0), the CII, the Lyman alpha, was made taking into consideration if the line intensities was high enough to be detected with reasonable experiments, what foregrounds will affect their intensity maps and what intensity mapping of these lines can tell us about the conditions of the Universe during Reionization. Since these lines were emitted during a major transition in the state of the gas in the Universe, these studies frequently addressed the hydrogen reionization process and included discussions about how intensity mapping of these lines can help to put constraints on this process. In the near future, we will finally be able to access a direct signal of the EoR due to 21cm line intensity mapping experiments. However, on its own it will be very difficult to extract from the 21cm signal intensity and spatial fluctuations, all of the precious astrophysical and cosmological information it contains. Also, the foregrounds that will contaminate intensity maps of the 21cm line will be extremelly strong and so the "clean" observational maps will suffer from several types of errors which are impossible to fully quantify.

In this thesis we tackled this problem by suggesting the use of intensity mapping of several lines emitted during the end of the EoR as independent probes of the high redshift Universe. In this thesis we describe the advantages of using the intensity mapping technique over other observational probes of the EoR, and point out how with this technique we can detect emission from even the more faint sources, which includes the galaxies mainly responsible for the reionization process. We also show how intensity maps of the several lines discussed in this thesis will trace neutral gas (the 21cm line), ionized recombining gas (the Lyman alpha line), ionized gas (the CII line) and molecular gas (the CO lines) and so they can serve as probes of several properties of the ISM and the IGM gas. Our studies show that observational intensity maps of these lines can be used to characterize the reionization process by determining the sources and sinks of ionizing photons as well as the morphology of the ionization field and the evolution of the IGM ionized fraction. We described how the power spectra of emission lines, obtained from intensity maps, can be used to probe large scale structure formation and evolution and can maybe even be used to constrain cosmological parameters, the matter power spectrum, dark matter particle models, dark energy and non-gaussianity. We showed that observational intensity maps of the CO, CII and Lyman alpha lines can be used to cross correlate with the 21cm line and therefore to provid a statistical measurement of the product of the two lines free of contamination. Moreover, since different emission lines are dependent on overlaping sets of parameters by performing intensity mapping of two or more lines during the same period, we will be able to put a lot stronger constraints in several key astrophysical and cosmological parameters. In this thesis, the study of OH line emission was motivated by this line being an important contaminant in HI intensity maps at the post-EoR, however the study presented can also be used as a motivation to the use of intensity maps of OH emission as a probe of the conditions of star forming regions at relatively high redshifts, which includes the period when the SFRD peaks and so it is relevant for several astrophysical studies.

Observational intensity maps will be highly contaminated by several galactic and extragalactic foregrounds and will also be sensible to experimental errors. Therefore, in Section 1.7 and in the several publications in appendix A we discussed the contaminants which will affect the lines in study and how to estimate them and remove them from observations. In particular, we pointed out how continuum foregrounds should be removed taking into account their smooth evolution in frequency compared to the emission line, that contamination from other emission lines should be removed by masking the contaminated pixels of the observational maps and that if these procedures are not enough to extract the signal than the cross correlation between two lines can be used to probe the signals taking advantage that the foregrounds in each of the lines are usually uncorrelated.

The main results and conclusions obtained during this thesis, for the CO(1-0), CII, Lyman alpha and OH lines, will now be described.

The CO(1-0) line is only emitted from one gas phase (molecular gas), and its intensity can be connected to the metallicity and to the molecular gas mass in the ISM. Intensity maps of this line have no important line contaminants and will suffer a lot less continuum contamination than 21cm line maps and so the CO(1-0) line would be the best candidate to cross correlate with the 21cm line, except for its relatively low intensity. The main problem with intensity mapping of the CO(1-0) line, is that during the end of the EoR the intensity of this line is somewhat low $I_{\rm CO}(z=7) \sim (1-7) \times 10^{-8}{\rm K}$, and so it requires a very sensitive intensity mapping experiment to detect this line intensity fluctuations. As a reference, the rms fluctuation in CO emission should be in the range $(1-3) \times 10^{-2} \mu{\rm K}$ at a scale of ${\rm k} = 0.1{\rm h}^{-1}{\rm Mpc}$ and a redshift of $z = 7$.

The CII line is emitted in different gas phases and depends on the metallicity of the galaxy, in

the intensity of the emitted UV and X-ray radiation as well as in the clumping of the gas. Predicting its intensity is not easy and its maps will suffer important contamination from emission lines at lower redshifts. However, according to our study the chances of removing these contaminants by masking them is good and it will allow to at least measure the evolution of the CII intensity during the end of the EoR, from intensity maps. CII emission is expected to have an intensity of $I_{\rm CII} \sim (9-60)\mathrm{Jysr}^{-1}$ in the redshift range $z \sim 8.5-5.5$, where the uncertainty is dependent on the evolution of CII emission of a galaxy with a given SFR for high redshifts. The rms fluctuations of CII emission are expected to be in the range $(5-20)\times 10^{1}\mathrm{Jysr}^{-1}$, at a scale of $\mathrm{k} = 0.1\mathrm{h}^{-1}\mathrm{Mpc}$ and a redshift of $z = 6.5$. This line is strong enough to be a good candidate to cross correlate with HI emission.

The Lyman alpha line is a very difficult line to model since it is emitted both from galaxies and from the IGM, and also because its emission depends on the ionization state of the IGM and so its intensity and spatial fluctuations at high redshifts are strongly correlated with the reionization process. Our best constraints for the intensity of Lyman alpha emission indicate that it will be in the range: $I_{\mathrm{Ly}\alpha}(z=7) \sim (5-20)\times 10^{-2}\mathrm{Jysr}^{-1}$. The rms fluctuations of Lyman alpha emission are expected to be in the range $(1-10)\mathrm{Jysr}^{-1}$, at a scale of $\mathrm{k} = 0.1\mathrm{h}^{-1}\mathrm{Mpc}$ and a redshift of $z = 7$. This line will also be contaminated by lower emission lines, but according to our study cleaning Lyman alpha intensity maps by masking its line contaminants is a reasonable possibility. The big advantage of cross correlating Lyman alpha and 21cm line maps is that the Lyman alpha line is emitted from ionized recombining gas and the 21cm line is emitted from neutral gas, and so during the EoR these two lines will be correlated and uncorrelated at different scales. Also, the scale of the transition in the cross correlation will be proportional to the size of ionized regions, and so it can be used as a statistical probe of the evolution of the ionization field.

The 18cm OH lines intensity can only be estimated with a reasonable uncertainty given the small number of OH masers detected and the variation of the relation between OH emission and the galaxies FIR continuum. We estimated the intensity of OH emission to be around 1 to $16\mu\mathrm{K}$ for $z \sim 1-5$, and that the contamination of OH rms fluctuation should not be above 10% of the fluctuations of the HI 21cm line at $z \sim 1-3$, therefore the contamination by OH lines can be efficiently removed from 21cm line intensity maps.

As a final remark, all of the subjects approached in this thesis and the results obtained are essential to the planning of intensity mapping experiments targeting the high redshift Universe and are also an important step in the interpretation of future observational intensity maps.

Bibliography

[1] R. Kallosh. Deformation, non-commutativity and the cosmological constant problem. *ArXiv High Energy Physics - Theory e-prints*, May 2004.

[2] S. Hollands and R. M. Wald. Essay: An Alternative to Inflation. *General Relativity and Gravitation*, 34:2043–2055, December 2002.

[3] B. Spokoiny. Deflationary Universe scenario. *Physics Letters B*, 315:40–45, September 1993.

[4] J. Butterfield. On Under-determination in cosmology. *ArXiv e-prints*, June 2014.

[5] S. Zaroubi. Probing the Epoch of Reionization with Low Frequency Arrays. *ArXiv e-prints*, February 2010.

[6] A. Natarajan and N. Yoshida. The Dark Ages of the Universe and Hydrogen Reionization. *ArXiv e-prints*, April 2014.

[7] S. Zaroubi. The Epoch of Reionization. In T. Wiklind, B. Mobasher, and V. Bromm, editors, *Astrophysics and Space Science Library*, volume 396 of *Astrophysics and Space Science Library*, page 45, 2013.

[8] R. Cen. The Universe Was Reionized Twice. *Astrophys. J.*, 591:12–37, July 2003.

[9] H. Trac and R. Cen. Radiative Transfer Simulations of Cosmic Reionization. I. Methodology and Initial Results. *Astrophys. J.*, 671:1–13, December 2007.

[10] P. Madau, M. J. Rees, M. Volonteri, F. Haardt, and S. P. Oh. Early Reionization by Miniquasars. *Astrophys. J.*, 604:484–494, April 2004.

[11] R. Salvaterra, F. Haardt, and A. Ferrara. Cosmic backgrounds from miniquasars. *Mon. Not. Roy. Astron. Soc.*, 362:L50–L54, September 2005.

[12] M. Dijkstra. On the contribution of (mini)quasars to reionization. *New Astron. Rev.*, 50:204–207, March 2006.

[13] J. L. Johnson and S. Khochfar. The Contribution of Supernovae to Cosmic Reionization. *Astrophys. J.*, 743:126, December 2011.

[14] F. Miniati, A. Ferrara, S. D. M. White, and S. Bianchi. Ultraviolet background radiation from cosmic structure formation. *Mon. Not. Roy. Astron. Soc.*, 348:964–976, March 2004.

[15] J. S. B. Wyithe, J. Mould, and A. Loeb. The Shocking Truth: The Small Contribution to Hydrogen Reionization from Gravitational Infall. *Astrophys. J.*, 743:173, December 2011.

[16] M. A. Dopita, L. M. Krauss, R. S. Sutherland, C. Kobayashi, and C. H. Lineweaver. Reionizing the universe without stars. *Astrophys. Spa. Sci.*, 335:345–352, October 2011.

[17] T. Sekiguchi and H. Tashiro. Constraining warm dark matter with 21 cm line fluctuations due to minihalos. *ArXiv e-prints*, January 2014.

[18] D. Schaerer. On the properties of massive Population III stars and metal-free stellar populations. *Astron. Astrophys.*, 382:28–42, January 2002.

[19] M. Shull, A. Harness, M. Trenti, and B. Smith. Critical Star-Formation Rates for Reionization: Full Reionization occurs at z = 7. *ArXiv e-prints*, August 2011.

[20] A. Cooray, Y. Gong, J. Smidt, and M. G. Santos. The Near-infrared Background Intensity and Anisotropies during the Epoch of Reionization. *Astrophys. J.*, 756:92, September 2012.

[21] E. Komatsu, K. M. Smith, J. Dunkley, C. L. Bennett, B. Gold, G. Hinshaw, N. Jarosik, D. Larson, M. R. Nolta, L. Page, D. N. Spergel, M. Halpern, R. S. Hill, A. Kogut, M. Limon, S. S. Meyer, N. Odegard, G. S. Tucker, J. L. Weiland, E. Wollack, and E. L. Wright. Seven-year Wilkinson Microwave Anisotropy Probe (WMAP) Observations: Cosmological Interpretation. *Astrophys. J. Suppl*, 192:18, February 2011.

[22] Planck Collaboration, P. A. R. Ade, N. Aghanim, C. Armitage-Caplan, M. Arnaud, M. Ashdown, F. Atrio-Barandela, J. Aumont, C. Baccigalupi, A. J. Banday, and et al. Planck 2013 results. XVI. Cosmological parameters. *ArXiv e-prints*, March 2013.

[23] A. Mesinger, A. Aykutalp, E. Vanzella, L. Pentericci, A. Ferrara, and M. Dijkstra. Can the intergalactic medium cause a rapid drop in Lyman alpha emission at z=6? *ArXiv e-prints*, June 2014.

[24] H. J. A. Rottgering, R. Braun, P. D. Barthel, M. P. van Haarlem, G. K. Miley, R. Morganti, I. Snellen, H. Falcke, A. G. de Bruyn, R. B. Stappers, W. H. W. M. Boland, H. R. Butcher, E. J. de Geus, L. Koopmans, R. Fender, J. Kuijpers, R. T. Schilizzi, C. Vogt, R. A. M. J. Wijers, M. Wise, W. N. Brouw, J. P. Hamaker, J. E. Noordam, T. Oosterloo, L. Bahren, M. A. Brentjens, S. J. Wijnholds, J. D. Bregman, W. A. van Cappellen, A. W. Gunst, G. W. Kant, J. Reitsma, K. van der Schaaf, and C. M. de Vos. LOFAR - Opening up a new window on the Universe. *ArXiv Astrophysics e-prints*, October 2006.

[25] S. J. Tingay, R. Goeke, J. D. Bowman, D. Emrich, S. M. Ord, D. A. Mitchell, M. F. Morales, T. Booler, B. Crosse, R. B. Wayth, C. J. Lonsdale, S. Tremblay, D. Pallot, T. Colegate, A. Wicenec, N. Kudryavtseva, W. Arcus, D. Barnes, G. Bernardi, F. Briggs, S. Burns, J. D. Bunton, R. J. Cappallo, B. E. Corey, A. Deshpande, L. Desouza, B. M. Gaensler, L. J. Greenhill, P. J. Hall, B. J. Hazelton, D. Herne, J. N. Hewitt, M. Johnston-Hollitt, D. L. Kaplan, J. C. Kasper, B. B. Kincaid, R. Koenig, E. Kratzenberg, M. J. Lynch, B. Mckinley, S. R. Mcwhirter, E. Morgan, D. Oberoi, J. Pathikulangara, T. Prabu, R. A. Remillard, A. E. E. Rogers, A. Roshi, J. E. Salah, R. J. Sault, N. Udaya-Shankar, F. Schlagenhaufer, K. S. Srivani, J. Stevens, R. Subrahmanyan, M. Waterson, R. L. Webster, A. R. Whitney,

A. Williams, C. L. Williams, and J. S. B. Wyithe. The Murchison Widefield Array: The Square Kilometre Array Precursor at Low Radio Frequencies. *Pub. Astron. Soc. Australia*, 30:7, January 2013.

[26] A. Liu and M. Tegmark. How well can we measure and understand foregrounds with 21-cm experiments? *Mon. Not. Roy. Astron. Soc.*, 419:3491–3504, February 2012.

[27] G. Paciga, T.-C. Chang, Y. Gupta, R. Nityanada, J. Odegova, U.-L. Pen, J. B. Peterson, J. Roy, and K. Sigurdson. The GMRT Epoch of Reionization experiment: a new upper limit on the neutral hydrogen power spectrum at z$\sim$ 8.6. *Mon. Not. Roy. Astron. Soc.*, 413:1174–1183, May 2011.

[28] S. Zaroubi, A. G. de Bruyn, G. Harker, R. M. Thomas, P. Labropolous, V. Jelić, L. V. E. Koopmans, M. A. Brentjens, G. Bernardi, B. Ciardi, S. Daiboo, S. Kazemi, O. Martinez-Rubi, G. Mellema, A. R. Offringa, V. N. Pandey, J. Schaye, V. Veligatla, H. Vedantham, and S. Yatawatta. Imaging neutral hydrogen on large scales during the Epoch of Reionization with LOFAR. *Mon. Not. Roy. Astron. Soc.*, 425:2964–2973, October 2012.

[29] Y. Gong, A. Cooray, M. B. Silva, M. G. Santos, and P. Lubin. Probing Reionization with Intensity Mapping of Molecular and Fine-structure Lines. *Astrophys. J. Lett.*, 728:L46, February 2011.

[30] Y. Gong, A. Cooray, M. Silva, M. G. Santos, J. Bock, C. M. Bradford, and M. Zemcov. Intensity Mapping of the [C II] Fine Structure Line during the Epoch of Reionization. *Astrophys. J.*, 745:49, January 2012.

[31] M. Silva, M. G. Santos, Y. Gong, and A. Cooray. Intensity Mapping of Lyman-alpha Emission During the Epoch of Reionization. *ArXiv e-prints*, May 2012.

[32] K. Hasegawa and B. Semelin. The impacts of ultraviolet radiation feedback on galaxies during the epoch of reionization. *Mon. Not. Roy. Astron. Soc.*, 428:154–166, January 2013.

[33] C. A. Watkinson and J. R. Pritchard. Distinguishing models of reionization using future radio observations of 21-cm 1-point statistics. *ArXiv e-prints*, December 2013.

[34] N. Y. Gnedin and P. A. Shaver. Redshifted 21 Centimeter Emission from the Pre-Reionization Era. I. Mean Signal and Linear Fluctuations. *Astrophys. J.*, 608:611–621, June 2004.

[35] J. O. Burns, J. Lazio, S. Bale, J. Bowman, R. Bradley, C. Carilli, S. Furlanetto, G. Harker, A. Loeb, and J. Pritchard. Probing the first stars and black holes in the early Universe with the Dark Ages Radio Explorer (DARE). *Advances in Space Research*, 49:433–450, February 2012.

[36] C. L. Carilli, S. Furlanetto, F. Briggs, M. Jarvis, S. Rawlings, and H. Falcke. Probing the dark ages with the Square Kilometer Array. *New Astron. Rev.*, 48:1029–1038, December 2004.

[37] Y. Mao, M. Tegmark, M. McQuinn, M. Zaldarriaga, and O. Zahn. How accurately can 21cm tomography constrain cosmology? *Phys. Rev. D*, 78(2):023529, July 2008.

[38] M. G. Santos, M. B. Silva, J. R. Pritchard, R. Cen, and A. Cooray. Probing the first galaxies with the Square Kilometer Array. *Astron. Astrophys.*, 527:A93, March 2011.

[39] B. Semelin, F. Combes, and S. Baek. Lyman-alpha radiative transfer during the epoch of reionization: contribution to 21-cm signal fluctuations. *Astron. Astrophys.*, 474:365–374, November 2007.

[40] J. R. Pritchard and A. Loeb. 21 cm cosmology in the 21st century. *Reports on Progress in Physics*, 75(8):086901, August 2012.

[41] K. S. Mandel and M. Zaldarriaga. Weak Gravitational Lensing of High-Redshift 21 cm Power Spectra. *Astrophys. J.*, 647:719–736, August 2006.

[42] D. Obreschkow, D. Croton, G. De Lucia, S. Khochfar, and S. Rawlings. Simulation of the Cosmic Evolution of Atomic and Molecular Hydrogen in Galaxies. *Astrophys. J.*, 698:1467–1484, June 2009.

[43] G. De Lucia and J. Blaizot. The hierarchical formation of the brightest cluster galaxies. *Mon. Not. Roy. Astron. Soc.*, 375:2–14, February 2007.

[44] K. Zawada, B. Semelin, P. Vonlanthen, S. Baek, and Y. Revaz. Light-cone anisotropy in the 21 cm signal from the epoch of reionization. *Mon. Not. Roy. Astron. Soc.*, 439:1615–1627, April 2014.

[45] S. Joudaki, O. Doré, L. Ferramacho, M. Kaplinghat, and M. G. Santos. Primordial Non-Gaussianity from the 21 cm Power Spectrum during the Epoch of Reionization. *Physical Review Letters*, 107(13):131304, September 2011.

[46] M. Viel, K. Markovič, M. Baldi, and J. Weller. The non-linear matter power spectrum in warm dark matter cosmologies. *Mon. Not. Roy. Astron. Soc.*, 421:50–62, March 2012.

[47] S. Bird, M. Viel, and M. G. Haehnelt. Massive neutrinos and the non-linear matter power spectrum. *Mon. Not. Roy. Astron. Soc.*, 420:2551–2561, March 2012.

[48] P. Scott, A. Venkatesan, E. Roebber, P. Gondolo, E. Pierpaoli, and G. Holder. Impacts of Dark Stars on Reionization and Signatures in the Cosmic Microwave Background. *Astrophys. J.*, 742:129, December 2011.

[49] D. R. G. Schleicher, R. Banerjee, and R. S. Klessen. Dark stars: Implications and constraints from cosmic reionization and extragalactic background radiation. *Phys. Rev. D*, 79(4):043510, February 2009.

[50] M. Valdés, C. Evoli, A. Mesinger, A. Ferrara, and N. Yoshida. The nature of dark matter from the global high-redshift H I 21 cm signal. *Mon. Not. Roy. Astron. Soc.*, 429:1705–1716, February 2013.

[51] S. Ando and E. Komatsu. Constraints on the annihilation cross section of dark matter particles from anisotropies in the diffuse gamma-ray background measured with Fermi-LAT. *Phys. Rev. D*, 87(12):123539, June 2013.

[52] Y. Gong, X. Chen, M. Silva, A. Cooray, and M. G. Santos. The OH Line Contamination of 21 cm Intensity Fluctuation Measurements for z = 1-4. *Astrophys. J. Lett.*, 740:L20, October 2011.

[53] LSST Dark Energy Science Collaboration. Large Synoptic Survey Telescope: Dark Energy Science Collaboration. *ArXiv e-prints*, November 2012.

[54] J. Amiaux, R. Scaramella, Y. Mellier, B. Altieri, C. Burigana, A. Da Silva, P. Gomez, J. Hoar, R. Laureijs, E. Maiorano, D. Magalhães Oliveira, F. Renk, G. Saavedra Criado, I. Tereno, J. L. Auguères, J. Brinchmann, M. Cropper, L. Duvet, A. Ealet, P. Franzetti, B. Garilli, P. Gondoin, L. Guzzo, H. Hoekstra, R. Holmes, K. Jahnke, T. Kitching, M. Meneghetti, W. Percival, and S. Warren. Euclid mission: building of a reference survey. In *Society of Photo-Optical Instrumentation Engineers (SPIE) Conference Series*, volume 8442 of *Society of Photo-Optical Instrumentation Engineers (SPIE) Conference Series*, September 2012.

[55] Y. Zhao, N. Lu, C. K. Xu, Y. Gao, S. Lord, J. Howell, K. G. Isaak, V. Charmandaris, T. Diaz-Santos, P. Appleton, A. Evans, K. Iwasawa, J. Leech, J. Mazzarella, A. O. Petric, D. B. Sanders, B. Schulz, J. Surace, and P. P. van der Werf. A Herschel Survey of the [N II] 205 μm Line in Local Luminous Infrared Galaxies: The [N II] 205 μm Emission as a Star Formation Rate Indicator. *Astrophys. J. Lett.*, 765:L13, March 2013.

[56] C. M. Simpson, G. L. Bryan, K. V. Johnston, B. D. Smith, M.-M. Mac Low, S. Sharma, and J. Tumlinson. The effect of feedback and reionization on star formation in low-mass dwarf galaxy haloes. *Mon. Not. Roy. Astron. Soc.*, 432:1989–2011, July 2013.

[57] S. Wyithe and A. Loeb. A suppressed contribution of low mass galaxies to reionization due to supernova feedback. *ArXiv e-prints*, September 2012.

[58] E. Sobacchi and A. Mesinger. Inhomogeneous recombinations during cosmic reionization. *Mon. Not. Roy. Astron. Soc.*, 440:1662–1673, May 2014.

[59] M. G. Santos, L. Ferramacho, M. B. Silva, A. Amblard, and A. Cooray. Fast large volume simulations of the 21-cm signal from the reionization and pre-reionization epochs. *Mon. Not. Roy. Astron. Soc.*, 406:2421–2432, August 2010.

[60] A. Mesinger, S. Furlanetto, and R. Cen. 21CMFAST: a fast, seminumerical simulation of the high-redshift 21-cm signal. *Mon. Not. Roy. Astron. Soc.*, 411:955–972, February 2011.

[61] Y. Ono, M. Ouchi, K. Shimasaku, J. Dunlop, D. Farrah, R. McLure, and S. Okamura. Stellar Populations of Lyα Emitters at z ˜ 6-7: Constraints on the Escape Fraction of Ionizing Photons from Galaxy Building Blocks. *Astrophys. J.*, 724:1524–1535, December 2010.

[62] R. J. Bouwens, G. D. Illingworth, P. A. Oesch, M. Trenti, M. Stiavelli, C. M. Carollo, M. Franx, P. G. van Dokkum, I. Labbé, and D. Magee. Very Blue UV-Continuum Slope β of Low Luminosity z ˜ 7 Galaxies from WFC3/IR: Evidence for Extremely Low Metallicities? *Astrophys. J. Lett.*, 708:L69–L73, January 2010.

[63] A. O. Razoumov and J. Sommer-Larsen. Ionizing Radiation from z = 4-10 Galaxies. *Astrophys. J.*, 710:1239–1246, February 2010.

[64] A. Fernández-Soto, K. M. Lanzetta, and H.-W. Chen. Mission: impossible (escape from the Lyman limit). *Mon. Not. Roy. Astron. Soc.*, 342:1215–1221, July 2003.

[65] B. Siana, H. I. Teplitz, J. Colbert, H. C. Ferguson, M. Dickinson, T. M. Brown, C. J. Conselice, D. F. de Mello, J. P. Gardner, M. Giavalisco, and F. Menanteau. New Constraints on the Lyman Continuum Escape Fraction at z˜1.3. *Astrophys. J.*, 668:62–73, October 2007.

[66] N. Y. Gnedin, A. V. Kravtsov, and H.-W. Chen. Escape of Ionizing Radiation from High-Redshift Galaxies. *Astrophys. J.*, 672:765–775, January 2008.

[67] J. H. Wise and R. Cen. Ionizing Photon Escape Fractions From High-Redshift Dwarf Galaxies. *Astrophys. J.*, 693:984–999, March 2009.

[68] F. Haardt and P. Madau. Radiative Transfer in a Clumpy Universe. IV. New Synthesis Models of the Cosmic UV/X-Ray Background. *Astrophys. J.*, 746:125, February 2012.

[69] T. Kimm and R. Cen. Escape Fraction of Ionizing Photons during Reionization: Effects due to Supernova Feedback and Runaway OB Stars. *Astrophys. J.*, 788:121, June 2014.

[70] A. Cooray and R. Sheth. Halo models of large scale structure. *Phys. Rep.*, 372:1–129, December 2002.

[71] Q. Guo, S. White, M. Boylan-Kolchin, G. De Lucia, G. Kauffmann, G. Lemson, C. Li, V. Springel, and S. Weinmann. From dwarf spheroidals to cD galaxies: simulating the galaxy population in a ΛCDM cosmology. *Mon. Not. Roy. Astron. Soc.*, 413:101–131, May 2011.

[72] V. Springel, S. D. M. White, A. Jenkins, C. S. Frenk, N. Yoshida, L. Gao, J. Navarro, R. Thacker, D. Croton, J. Helly, J. A. Peacock, S. Cole, P. Thomas, H. Couchman, A. Evrard, J. Colberg, and F. Pearce. Simulations of the formation, evolution and clustering of galaxies and quasars. *Nature*, 435:629–636, June 2005.

[73] L. Wang, D. Farrah, S. J. Oliver, A. Amblard, M. Béthermin, J. Bock, A. Conley, A. Cooray, M. Halpern, S. Heinis, E. Ibar, O. Ilbert, R. J. Ivison, G. Marsden, I. G. Roseboom, M. Rowan-Robinson, B. Schulz, A. J. Smith, M. Viero, and M. Zemcov. Connecting stellar mass and star-formation rate to dark matter halo mass out to z $\sim$ 2. *Mon. Not. Roy. Astron. Soc.*, 431:648–661, May 2013.

[74] R. G. Bower, A. J. Benson, R. Malbon, J. C. Helly, C. S. Frenk, C. M. Baugh, S. Cole, and C. G. Lacey. Breaking the hierarchy of galaxy formation. *Mon. Not. Roy. Astron. Soc.*, 370:645–655, August 2006.

[75] D. Keres, M. S. Yun, and J. S. Young. CO Luminosity Functions for Far-Infrared- and B-Band-selected Galaxies and the First Estimate for Ω_{HI}+H_2. *Astrophys. J.*, 582:659–667, January 2003.

[76] D. Obreschkow, I. Heywood, H.-R. Klöckner, and S. Rawlings. A Heuristic Prediction of the Cosmic Evolution of the Co-luminosity Functions. *Astrophys. J.*, 702:1321–1335, September 2009.

[77] C. D. P. Lagos, C. M. Baugh, C. G. Lacey, A. J. Benson, H.-S. Kim, and C. Power. Cosmic evolution of the atomic and molecular gas contents of galaxies. *Mon. Not. Roy. Astron. Soc.*, 418:1649–1667, December 2011.

[78] C. L. Carilli and F. Walter. Cool Gas in High-Redshift Galaxies. *Ann.Rev.Astron.Astrophys*, 51:105–161, August 2013.

[79] C. d. P. Lagos, E. Bayet, C. M. Baugh, C. G. Lacey, T. A. Bell, N. Fanidakis, and J. E. Geach. Predictions for the CO emission of galaxies from a coupled simulation of galaxy formation and photon-dominated regions. *Mon. Not. Roy. Astron. Soc.*, 426:2142–2165, November 2012.

[80] M. T. Sargent, M. Béthermin, E. Daddi, and D. Elbaz. The Contribution of Starbursts and Normal Galaxies to Infrared Luminosity Functions at z $\lesssim$ 2. *Astrophys. J. Lett.*, 747:L31, March 2012.

[81] M. T. Sargent, E. Daddi, M. Béthermin, H. Aussel, G. Magdis, H. S. Hwang, S. Juneau, D. Elbaz, and E. da Cunha. Regularity underlying complexity: a redshift-independent description of the continuous variation of galaxy-scale molecular gas properties in the mass-star formation rate plane. *ArXiv e-prints*, March 2013.

[82] J. E. Geach and P. P. Papadopoulos. Molecular and Atomic Line Surveys of Galaxies. I. The Dense, Star-Forming Gas Phase as a Beacon. *Astrophys. J.*, 757:156, October 2012.

[83] C. L. Carilli and A. W. Blain. Centimeter Searches for Molecular Line Emission from High-Redshift Galaxies. *Astrophys. J.*, 569:605–610, April 2002.

[84] R. K. Sheth and G. Tormen. Large-scale bias and the peak background split. *Mon. Not. Roy. Astron. Soc.*, 308:119–126, September 1999.

[85] A. Loeb and R. Barkana. The Reionization of the Universe by the First Stars and Quasars. *Ann.Rev.Astron.Astrophys*, 39:19–66, 2001.

[86] T. Díaz-Santos, L. Armus, V. Charmandaris, S. Stierwalt, E. J. Murphy, S. Haan, H. Inami, S. Malhotra, R. Meijerink, G. Stacey, A. O. Petric, A. S. Evans, S. Veilleux, P. P. van der Werf, S. Lord, N. Lu, J. H. Howell, P. Appleton, J. M. Mazzarella, J. A. Surace, C. K. Xu, B. Schulz, D. B. Sanders, C. Bridge, B. H. P. Chan, D. T. Frayer, K. Iwasawa, J. Melbourne, and E. Sturm. Explaining the [C II]157.7 μm Deficit in Luminous Infrared Galaxies-First Results from a Herschel/PACS Study of the GOALS Sample. *Astrophys. J.*, 774:68, September 2013.

[87] K. Ota, F. Walter, K. Ohta, B. Hatsukade, C. L. Carilli, E. da Cunha, J. González-López, R. Decarli, J. A. Hodge, H. Nagai, E. Egami, L. Jiang, M. Iye, N. Kashikawa, D. A. Riechers, F. Bertoldi, P. Cox, R. Neri, and A. Weiss. ALMA Observation of 158 micron [CII] Line and Dust Continuum of a z=7 Normally Star-forming Galaxy in the Epoch of Reionization. *ArXiv e-prints*, May 2014.

[88] S. Malhotra, G. Helou, G. Stacey, D. Hollenbach, S. Lord, C. A. Beichman, H. Dinerstein, D. A. Hunter, K. Y. Lo, N. Y. Lu, R. H. Rubin, N. Silbermann, H. A. Thronson, Jr., and M. W. Werner. Infrared Space Observatory Measurements of [C II] Line Variations in Galaxies. *Astrophys. J. Lett.*, 491:L27–L30, December 1997.

[89] K. Ota, M. Iye, N. Kashikawa, K. Shimasaku, M. Ouchi, T. Totani, M. A. R. Kobayashi, M. Nagashima, A. Harayama, N. Kodaka, T. Morokuma, H. Furusawa, A. Tajitsu, and T. Hattori. Lyα Emitters at z = 7 in the Subaru/XMM-Newton Deep Survey Field: Photometric Candidates and Luminosity Functions. *Astrophys. J.*, 722:803–811, October 2010.

[90] K. Shimasaku, N. Kashikawa, M. Doi, C. Ly, M. A. Malkan, Y. Matsuda, M. Ouchi, T. Hayashino, M. Iye, K. Motohara, T. Murayama, T. Nagao, K. Ohta, S. Okamura, T. Sasaki, Y. Shioya, and Y. Taniguchi. Lyα Emitters at z = 5.7 in the Subaru Deep Field. *Pub. Astron. Soc. Japan*, 58:313–334, April 2006.

[91] M. Ouchi, K. Shimasaku, M. Akiyama, C. Simpson, T. Saito, Y. Ueda, H. Furusawa, K. Sekiguchi, T. Yamada, T. Kodama, N. Kashikawa, S. Okamura, M. Iye, T. Takata, M. Yoshida, and M. Yoshida. The Subaru/XMM-Newton Deep Survey (SXDS). IV. Evolution of Lyα Emitters from z=3.1 to 5.7 in the 1 deg^2 Field: Luminosity Functions and AGN. *Astrophys. J. Suppl*, 176:301–330, June 2008.

[92] N. Kashikawa, K. Shimasaku, M. A. Malkan, M. Doi, Y. Matsuda, M. Ouchi, Y. Taniguchi, C. Ly, T. Nagao, M. Iye, K. Motohara, T. Murayama, K. Murozono, K. Nariai, K. Ohta, S. Okamura, T. Sasaki, Y. Shioya, and M. Umemura. The End of the Reionization Epoch Probed by Lyα Emitters at z = 6.5 in the Subaru Deep Field. *Astrophys. J.*, 648:7–22, September 2006.

[93] K. Ota, M. Iye, N. Kashikawa, K. Shimasaku, M. Kobayashi, T. Totani, M. Nagashima, T. Morokuma, H. Furusawa, T. Hattori, Y. Matsuda, T. Hashimoto, and M. Ouchi. Reionization and Galaxy Evolution Probed by z = 7 Lyα Emitters. *Astrophys. J.*, 677:12–26, April 2008.

[94] M. Dijkstra. Lyman Alpha Emitting Galaxies as a Probe of Reionization. *ArXiv e-prints*, June 2014.

[95] B. Magnelli, D. Elbaz, R. R. Chary, M. Dickinson, D. Le Borgne, D. T. Frayer, and C. N. A. Willmer. Evolution of the dusty infrared luminosity function from z = 0 to z = 2.3 using observations from Spitzer. *Astron. Astrophys.*, 528:A35, April 2011.

[96] A. G. Tekola, P. Väisänen, and A. Berlind. The environments of local luminous infrared galaxies: star formation rates increase with density. *Mon. Not. Roy. Astron. Soc.*, 419:1176–1186, January 2012.

[97] J. Darling and R. Giovanelli. A Search for OH Megamasers at z>0.1. III. The Complete Survey. *Astronom. J.*, 124:100–126, July 2002.

[98] A. Lewis, A. Challinor, and A. Lasenby. Efficient Computation of Cosmic Microwave Background Anisotropies in Closed Friedmann-Robertson-Walker Models. *Astrophys. J.*, 538:473–476, August 2000.

[99] D. J. Eisenstein and W. Hu. Power Spectra for Cold Dark Matter and Its Variants. *Astrophys. J.*, 511:5–15, January 1999.

[100] W. H. Press and P. Schechter. Formation of Galaxies and Clusters of Galaxies by Self-Similar Gravitational Condensation. *Astrophys. J.*, 187:425–438, February 1974.

[101] A. Liu, J. R. Pritchard, M. Tegmark, and A. Loeb. Global 21 cm signal experiments: A designer's guide. *Phys. Rev. D*, 87(4):043002, February 2013.

[102] H. Tashiro, N. Aghanim, M. Langer, M. Douspis, S. Zaroubi, and V. Jelic. Detectability of the 21-cm CMB cross-correlation from the epoch of reionization. *Mon. Not. Roy. Astron. Soc.*, 402:2617–2625, March 2010.

[103] V. Jelić, S. Zaroubi, P. Labropoulos, R. M. Thomas, G. Bernardi, M. A. Brentjens, A. G. de Bruyn, B. Ciardi, G. Harker, L. V. E. Koopmans, V. N. Pandey, J. Schaye, and S. Yatawatta. Foreground simulations for the LOFAR-epoch of reionization experiment. *Mon. Not. Roy. Astron. Soc.*, 389:1319–1335, September 2008.

[104] X. Wang, M. Tegmark, M. G. Santos, and L. Knox. 21 cm Tomography with Foregrounds. *Astrophys. J.*, 650:529–537, October 2006.

[105] A. Datta, J. D. Bowman, and C. L. Carilli. Bright Source Subtraction Requirements for Redshifted 21 cm Measurements. *Astrophys. J.*, 724:526–538, November 2010.

[106] G. Harker, S. Zaroubi, G. Bernardi, M. A. Brentjens, A. G. de Bruyn, B. Ciardi, V. Jelić, L. V. E. Koopmans, P. Labropoulos, G. Mellema, A. Offringa, V. N. Pandey, A. H. Pawlik, J. Schaye, R. M. Thomas, and S. Yatawatta. Power spectrum extraction for redshifted 21-cm Epoch of Reionization experiments: the LOFAR case. *Mon. Not. Roy. Astron. Soc.*, 405:2492–2504, July 2010.

[107] L. Wolz, F. B. Abdalla, C. Blake, J. R. Shaw, E. Chapman, and S. Rawlings. The effect of foreground subtraction on cosmological measurements from intensity mapping. *Mon. Not. Roy. Astron. Soc.*, 441:3271–3283, July 2014.

[108] A. Lidz, S. R. Furlanetto, S. P. Oh, J. Aguirre, T.-C. Chang, O. Doré, and J. R. Pritchard. Intensity Mapping with Carbon Monoxide Emission Lines and the Redshifted 21 cm Line. *Astrophys. J.*, 741:70, November 2011.

[109] J. Graciá-Carpio, E. Sturm, S. Hailey-Dunsheath, J. Fischer, A. Contursi, A. Poglitsch, R. Genzel, E. González-Alfonso, A. Sternberg, A. Verma, N. Christopher, R. Davies, H. Feuchtgruber, J. A. de Jong, D. Lutz, and L. J. Tacconi. Far-infrared Line Deficits in Galaxies with Extreme L_{FIR}/M_{H_{2}} Ratios. *Astrophys. J. Lett.*, 728:L7, February 2011.

[110] J. R. Brauher, D. A. Dale, and G. Helou. A Compendium of Far-Infrared Line and Continuum Emission for 227 Galaxies Observed by the Infrared Space Observatory. *Astrophys. J. Suppl*, 178:280–301, October 2008.

[111] C. Ferkinhoff, D. Brisbin, T. Nikola, S. C. Parshley, G. J. Stacey, T. G. Phillips, E. Falgarone, D. J. Benford, J. G. Staguhn, and C. E. Tucker. First Detections of the [N II] 122 μm Line at High Redshift: Demonstrating the Utility of the Line for Studying Galaxies in the Early Universe. *Astrophys. J. Lett.*, 740:L29, October 2011.

[112] D. Obreschkow, H.-R. Klöckner, I. Heywood, F. Levrier, and S. Rawlings. A Virtual Sky with Extragalactic H I and CO Lines for the Square Kilometre Array and the Atacama Large Millimeter/Submillimeter Array. *Astrophys. J.*, 703:1890–1903, October 2009.

[113] R. C. Kennicutt, Jr. The Global Schmidt Law in Star-forming Galaxies. *Astrophys. J.*, 498:541, May 1998.

[114] C. Ly, M. A. Malkan, N. Kashikawa, K. Shimasaku, M. Doi, T. Nagao, M. Iye, T. Kodama, T. Morokuma, and K. Motohara. The Luminosity Function and Star Formation Rate between Redshifts of 0.07 and 1.47 for Narrowband Emitters in the Subaru Deep Field. *Astrophys. J.*, 657:738–759, March 2007.

[115] A. B. Drake, C. Simpson, C. A. Collins, P. A. James, I. K. Baldry, M. Ouchi, M. J. Jarvis, D. G. Bonfield, Y. Ono, P. N. Best, G. B. Dalton, J. S. Dunlop, R. J. McLure, and D. J. B. Smith. Evolution of star formation in the UKIDSS Ultra Deep Survey field - I. Luminosity functions and cosmic star formation rate out to z = 1.6. *Mon. Not. Roy. Astron. Soc.*, 433:796–811, July 2013.

[116] M. L. P. Gunawardhana, A. M. Hopkins, J. Bland-Hawthorn, S. Brough, R. Sharp, J. Loveday, E. Taylor, D. H. Jones, M. A. Lara-López, A. E. Bauer, M. Colless, M. Owers, I. K. Baldry, A. R. López-Sánchez, C. Foster, S. Bamford, M. J. I. Brown, S. P. Driver, M. J. Drinkwater, J. Liske, M. Meyer, P. Norberg, A. S. G. Robotham, J. H. Y. Ching, M. E. Cluver, S. Croom, L. Kelvin, M. Prescott, O. Steele, D. Thomas, and L. Wang. Galaxy And Mass Assembly: evolution of the Hα luminosity function and star formation rate density up to z $\lesssim$ 0.35. *Mon. Not. Roy. Astron. Soc.*, 433:2764–2789, August 2013.

[117] S. Yatawatta, A. G. de Bruyn, M. A. Brentjens, P. Labropoulos, V. N. Pandey, S. Kazemi, S. Zaroubi, L. V. E. Koopmans, A. R. Offringa, V. Jelić, O. Martinez Rubi, V. Veligatla, S. J. Wijnholds, W. N. Brouw, G. Bernardi, B. Ciardi, S. Daiboo, G. Harker, G. Mellema, J. Schaye, R. Thomas, H. Vedantham, E. Chapman, F. B. Abdalla, A. Alexov, J. Anderson, I. M. Avruch, F. Batejat, M. E. Bell, M. R. Bell, M. Bentum, P. Best, A. Bonafede, J. Bregman, F. Breitling, R. H. van de Brink, J. W. Broderick, M. Brüggen, J. Conway, F. de Gasperin, E. de Geus, S. Duscha, H. Falcke, R. A. Fallows, C. Ferrari, W. Frieswijk, M. A. Garrett, J. M. Griessmeier, A. W. Gunst, T. E. Hassall, J. W. T. Hessels, M. Hoeft, M. Iacobelli, E. Juette, A. Karastergiou, V. I. Kondratiev, M. Kramer, M. Kuniyoshi, G. Kuper, J. van Leeuwen, P. Maat, G. Mann, J. P. McKean, M. Mevius, J. D. Mol, H. Munk, R. Nijboer, J. E. Noordam, M. J. Norden, E. Orru, H. Paas, M. Pandey-Pommier, R. Pizzo, A. G. Polatidis, W. Reich, H. J. A. Röttgering, J. Sluman, O. Smirnov, B. Stappers, M. Steinmetz, M. Tagger, Y. Tang, C. Tasse, S. ter Veen, R. Vermeulen, R. J. van Weeren, M. Wise, O. Wucknitz, and P. Zarka. Initial deep LOFAR observations of epoch of reionization windows. I. The north celestial pole. *Astron. Astrophys.*, 550:A136, February 2013.

[118] J. D. Bowman, I. Cairns, D. L. Kaplan, T. Murphy, D. Oberoi, L. Staveley-Smith, W. Arcus, D. G. Barnes, G. Bernardi, F. H. Briggs, S. Brown, J. D. Bunton, A. J. Burgasser, R. J. Cappallo, S. Chatterjee, B. E. Corey, A. Coster, A. Deshpande, L. deSouza, D. Emrich, P. Erickson, R. F. Goeke, B. M. Gaensler, L. J. Greenhill, L. Harvey-Smith, B. J. Hazelton, D. Herne, J. N. Hewitt, M. Johnston-Hollitt, J. C. Kasper, B. B. Kincaid, R. Koenig, E. Kratzenberg, C. J. Lonsdale, M. J. Lynch, L. D. Matthews, S. R. McWhirter, D. A. Mitchell, M. F. Morales, E. H. Morgan, S. M. Ord, J. Pathikulangara, T. Prabu, R. A. Remillard, T. Robishaw, A. E. E. Rogers, A. A. Roshi, J. E. Salah, R. J. Sault, N. U. Shankar, K. S. Srivani, J. B. Stevens, R. Subrahmanyan, S. J. Tingay, R. B. Wayth, M. Waterson,

R. L. Webster, A. R. Whitney, A. J. Williams, C. L. Williams, and J. S. B. Wyithe. Science with the Murchison Widefield Array. *Pub. Astron. Soc. Australia*, 30:31, April 2013.

[119] A. R. Parsons, A. Liu, J. E. Aguirre, Z. S. Ali, R. F. Bradley, C. L. Carilli, D. R. DeBoer, M. R. Dexter, N. E. Gugliucci, D. C. Jacobs, P. Klima, D. H. E. MacMahon, J. R. Manley, D. F. Moore, J. C. Pober, I. I. Stefan, and W. P. Walbrugh. New Limits on 21 cm Epoch of Reionization from PAPER-32 Consistent with an X-Ray Heated Intergalactic Medium at z = 7.7. *Astrophys. J.*, 788:106, June 2014.

[120] F. Aharonian, T. G. Arshakian, B. Allen, R. Banerjee, R. Beck, W. Becker, D. J. Bomans, D. Breitschwerdt, M. Brüggen, A. Brunthaler, B. Catinella, D. Champion, B. Ciardi, R. Crocker, M. A. de Avillez, R. J. Dettmar, D. Engels, T. Enßlin, H. Enke, T. Fieseler, L. Gizon, E. Hackmann, B. Hartmann, C. Henkel, M. Hoeft, L. Iapichino, D. Innes, C. James, J. Jasche, D. Jones, V. Kagramanova, G. Kauffmann, E. Keane, J. Kerp, H.-R. Klöckner, K. Kokkotas, M. Kramer, M. Krause, M. Krause, N. Krupp, J. Kunz, C. Lämmerzahl, K. J. Lee, M. List, K. Liu, A. Lobanov, G. Mann, A. Merloni, E. Middelberg, J. Niemeyer, A. Noutsos, V. Perlick, W. Reich, P. Richter, A. Roy, A. Saintonge, G. Schäfer, J. Schaffner-Bielich, E. Schinnerer, D. Schleicher, P. Schneider, D. J. Schwarz, A. Sedrakian, A. Sesana, V. Smolčić, S. Solanki, R. Tuffs, M. Vetter, E. Weber, J. Weller, N. Wex, O. Wucknitz, and M. Zwaan. Pathway to the Square Kilometre Array - The German White Paper -. *ArXiv e-prints*, January 2013.

[121] G. Paciga, J. G. Albert, K. Bandura, T.-C. Chang, Y. Gupta, C. Hirata, J. Odegova, U.-L. Pen, J. B. Peterson, J. Roy, J. R. Shaw, K. Sigurdson, and T. Voytek. A simulation-calibrated limit on the H I power spectrum from the GMRT Epoch of Reionization experiment. *Mon. Not. Roy. Astron. Soc.*, 433:639–647, July 2013.

[122] E. Visbal and A. Loeb. Measuring the 3D clustering of undetected galaxies through cross correlation of their cumulative flux fluctuations from multiple spectral lines. *J. Cosm. Astropart. Phys.*, 11:16, November 2010.

[123] M. Righi, C. Hernández-Monteagudo, and R. A. Sunyaev. Carbon monoxide line emission as a CMB foreground: tomography of the star-forming universe with different spectral resolutions. *Astron. Astrophys.*, 489:489–504, October 2008.

[124] C. L. Carilli. Intensity Mapping of Molecular Gas During Cosmic Reionization. *Astrophys. J. Lett.*, 730:L30, April 2011.

[125] E. Visbal, H. Trac, and A. Loeb. Demonstrating the feasibility of line intensity mapping using mock data of galaxy clustering from simulations. *J. Cosm. Astropart. Phys.*, 8:10, August 2011.

[126] J. B. Peterson and E. Suarez. Intensity Mapping with the 21-cm and Lyman Alpha Lines. *ArXiv e-prints*, June 2012.

[127] M. B. Silva, M. G. Santos, Y. Gong, A. Cooray, and J. Bock. Intensity Mapping of Lyα Emission during the Epoch of Reionization. *Astrophys. J.*, 763:132, February 2013.

[128] A. R. Pullen, O. Doré, and J. Bock. Intensity Mapping across Cosmic Times with the Lyα Line. *Astrophys. J.*, 786:111, May 2014.

[129] A. Gould and D. H. Weinberg. Imaging the Forest of Lyman Limit Systems. *Astrophys. J.*, 468:462, September 1996.

[130] M. A. Fardal, N. Katz, J. P. Gardner, L. Hernquist, D. H. Weinberg, and R. Davé. Cooling Radiation and the Lyα Luminosity of Forming Galaxies. *Astrophys. J.*, 562:605–617, December 2001.

[131] M. Hayes, D. Schaerer, G. Östlin, J. M. Mas-Hesse, H. Atek, and D. Kunth. On the Redshift Evolution of the Lyα Escape Fraction and the Dust Content of Galaxies. *Astrophys. J.*, 730:8, March 2011.

[132] I. de Looze, M. Baes, G. J. Bendo, L. Cortese, and J. Fritz. The reliability of [C II] as an indicator of the star formation rate. *Mon. Not. Roy. Astron. Soc.*, 416:2712–2724, October 2011.

A

Appendix: Publications

A.1 Paper I

Probing Reionization with Intensity Mapping of Molecular and Fine Structure Lines

Gong Y., Cooray A., **Silva M. B.**, Santos M. G. and Lubin P.
The Astrophysical Journal Letters, 728, L46 (2011)
arXiv:1101.2892

The Astrophysical Journal Letters, 728:L46 (5pp), 2011 February 20 doi:10.1088/2041-8205/728/2/L46

PROBING REIONIZATION WITH INTENSITY MAPPING OF MOLECULAR AND FINE-STRUCTURE LINES

Yan Gong[1], Asantha Cooray[1], Marta B. Silva[2], Mario G. Santos[2], and Phillip Lubin[3]
[1] Department of Physics & Astronomy, University of California, Irvine, CA 92697, USA
[2] CENTRA, Instituto Superior Téecnico, Lisboa 1049-001, Portugal
[3] Department of Physics & Astronomy, University of California, Santa Barbara, CA, USA
Received 2010 December 22; accepted 2011 January 18; published 2011 February 2

ABSTRACT

We propose observations of the molecular gas distribution during the era of reionization. At $z \sim 6$–8, the ^{12}CO($J = 1$–0) line intensity results in a mean brightness temperature of about 0.5 μK with an rms fluctuation of 0.1 μK at 1–10 Mpc spatial scales, corresponding to 30 arcminute angular scales. This intensity fluctuations can be mapped with an interferometer, similar to existing and planned 21 cm background experiments, but operating at ∼12–17 GHz. We discuss the feasibility of detecting the cross-correlation between H I and CO molecular gas since such a cross-correlation has the advantage that it will be independent of systematics and most foregrounds in each of the 21 cm and CO(1–0) line experiments. Additional instruments tuned to higher-order transitions of the CO molecule or an instrument operating with high spectral resolution at millimeter wavelengths targeting 158 μm C II could further improve the reionization studies with molecular gas. The combined 21 cm and CO line observations has the potential to establish the relative distribution of gas in the intergalactic medium and molecular gas that are clumped in individual first-light galaxies that are closely connected to the formation of massive stars in these galaxies.

Key words: cosmology: theory – diffuse radiation – galaxies: starburst – radio lines: galaxies

Online-only material: color figures

1. INTRODUCTION

Recently there has been a great deal of interest in the evolution of the intergalactic medium (IGM) at high redshifts ($z > 6$) and specifically the reionization history of the universe. Most of this interest is sparked by existing multi-wavelength observations that suggest a complex reionization history, with a strong possibility for an extended and highly inhomogeneous period of reionization. Observations of the 21 cm spin-flip line of neutral hydrogen are currently considered to be one of the most promising probes of the epoch of reionization (e.g., Madau et al. 1997; Loeb & Zaldarriaga 2004; Gnedin & Shaver 2004). Given the line emission, leading to a frequency selection for observations, the 21 cm data provide a tomographic view of the reionization (Santos et al. 2005; Furlanetto et al. 2004). It is also a useful cosmological probe (Mao et al. 2008; Santos & Cooray 2006; McQuinn et al. 2006; Bowman et al. 2007).

Here, we propose spectral line intensity mapping associated with molecular gas during the era of reionization as an additional probe during the formation of first-light galaxies. In particular, we study the $J = 1$ to 0 transition of the ^{12}CO (carbon monoxide), which has a rest wavelength of 2.61 mm. Our suggestion extends the initial work on this topic by Righi et al. (2008; see also Basu et al. 2004). Instead of the angular power spectrum, which is dominated by cosmic microwave background (CMB) anisotropies at tens of arcminute scales, we propose spectral line intensity mapping leading to the three-dimensional power spectrum (see also Visbal & Loeb 2010). An additional probe of reionization is useful since the first-generation 21 cm experiments are expected to be noise dominated and the observations could, in principle, be affected by various systematics and residual foregrounds. A second probe of the reionization epoch providing three-dimensional information can be cross-correlated with the 21 cm spectral line measurements to improve the overall understanding of reionization.

In terms of potential spectral lines of interest, the line intensity of the $J = 1$–0 transition of ^{12}CO has been used as a way to establish the gas mass of star-forming galaxies both at low (e.g., Downes & Solomon 1998) and medium (e.g., Greve et al. 2005) redshifts. Individual CO line observations now exist out to $z = 5.3$ (e.g., Riechers et al. 2010), which is significant given that the highest 21 cm line emission from a galaxy currently measured is at z of 0.24 (Lah et al. 2007; see Chang et al. 2010 for 21 cm intensity variations of the kind we propose at $z \sim 0.9$). In addition to the CO lines, we also find that the fine-structure C II line, with observations in the millimeter range of the spectrum, could be a strong probe of reionization.

This Letter is organized as follows: in the next section, we outline the calculation related to the strength of the expected signal from reionization, Section 3 presents results related to a potential CO brightness temperature fluctuation experiment that targets the 1–0 transition, and Section 4 discusses the cross-correlation with the 21 cm background.

2. THE CO(1–0) SIGNAL

For a galaxy at a given redshift, the CO(1–0) luminosity is taken to be related to the H_2 content and the metallicity of the gas (Obreschkow et al. 2009a). A key input here is the relation between CO(1–0) luminosity, L_{CO}, and the halo mass. While such a relation is expected, it also has a large scatter coming from differences in the gas content, at a fixed halo mass, due to variations in the halo ages at a fixed mass; the gas in older halos is more likely to be depleted more than the younger ones with older halos containing more stars. However, for sufficiently large volumes, we will be averaging over many galaxies so that the mean relation and its scatter can be quantified. This is similar to the luminosity–halo mass relation for optical light, which has allowed statistics such as the conditional luminosity functions to be constructed and improve the halo modeling beyond the simple halo occupation number

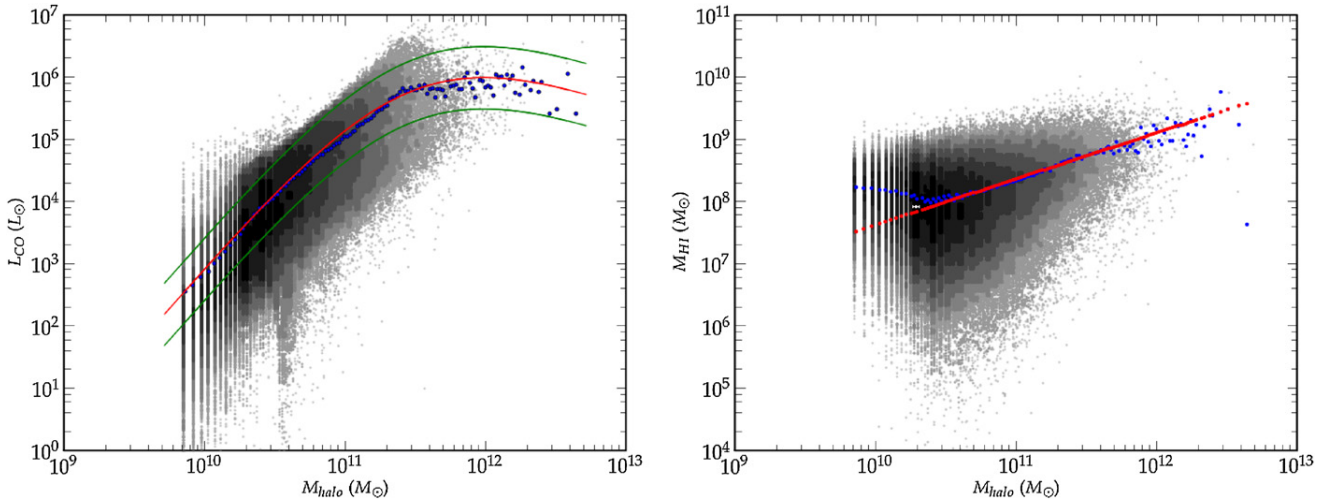

Figure 1. Left: the $L_{\rm CO}(M_{\rm halo})$ relation for CO(1–0) luminosity as a function of the halo mass $M_{\rm halo}$ at $z = 7$. The lines show the mean relation (thick center line) and $\pm 1\sigma$ relation (thin lines) given the scatter (see text for details). The dots show the mean of the scatter when binned to 150 logarithmic intervals in halo mass. Right: the relation neutral hydrogen mass content in individual galaxies $M_{\rm H\,I}$ vs. the halo mass $M_{\rm halo}$ at $z = 7$.

(A color version of this figure is available in the online journal.)

(e.g., Yang et al. 2004; Cooray & Milosavljevic 2005b; Cooray 2006).

Here we make use of the numerical simulations of Obreschkow et al. (2009c) that are available as part of the SKA Simulated Skies Web site.[4] This simulation is based on the galaxy catalog from De Lucia & Blaizot (2007), which post-processed the Millennium dark matter simulation with semi-analytical models of galaxy formation. It captures the gas astrophysics, especially HI and H_2, and allows for the cosmic evolution of these two phases of the cold hydrogen gas (see Obreschkow et al. 2009a, 2009b for details). They also constructed a virtual sky field with H I and CO line luminosities for each of the galaxies, calculated from a combination of the neutral and molecular hydrogen gas masses and the metallicity of each galaxy. Using the online tools we made a query with a four-degree observing cone containing more than 5×10^5 galaxies at each of $z = 7$.

The $L_{\rm CO}(M)$ from every halo at $z \sim 7$ from this simulation is shown in the left panel of Figure 1 with the shade of gray darker in the regions where the halo density is higher. Typically we find one galaxy per halo at these redshifts. The lines show the result of averaging the total $L_{\rm CO}$ from the halos for each of 150 logarithmic bins of halo mass. Motivated by parameterization of optical luminosity and halo mass (Cooray & Milosavljevic 2005a), we use a relation of the form $L_{\rm CO}(M) = L_0(M/M_c)^b(1 + M/M_c)^{-d}$ to describe the mean relation and determine the four free parameters A, b, c and d. At $z = 6, 7$, and 8, these parameters take the values of $L_0 = 4.3 \times 10^6, 6.2 \times 10^6, 4.0 \times 10^6\, L_\odot$, $b = 2.4, 2.6, 2.8$, $M_c = 3.5 \times 10^{11}, 3.0 \times 10^{11}, 2.0 \times 10^{11}\, M_\odot$, and $d = 2.8, 3.4, 3.3$, respectively.

Using the above relation between $L_{\rm CO}$ and halo mass M as a function of redshift, we can write the mean intensity of the CO(1–0) line as

$$\bar{I}_{\rm CO} = \int_{M_{\rm min}}^{\infty} dM \frac{dn}{dM}(z, M) \frac{L_{\rm CO}(z, M)}{4\pi D_{\rm L}^2} y(z) D_{\rm A}^2, \qquad (1)$$

where we take $M_{\rm min} = 10^8 (M_\odot/h)$ as the minimum mass of the dark matter halos that can host galaxies (to be consistent with mass scale of atomic hydrogen cooling or a virial temperature of 10^4 K; Loeb & Barkana 2001), dn/dM is the halo mass function (Sheth & Tormen 1999), D_L is the luminosity distance, and $D_{\rm A}$ is the comoving angular diameter distance. In above $y(z) = d\chi/d\nu = \lambda_{\rm CO}(1+z)^2/H(z)$, where χ is the comoving distance, ν is the observed frequency, $\lambda_{\rm CO} = 2.6$ mm is the rest-frame wavelength of the CO(1–0) line.

The signal is expected to contain spatial variations around the average intensity due to Poisson fluctuations in the number of halos (shot noise) and correlations with the underlying dark matter density field which will enhance the fluctuations by a factor of $(1 + b(z, M)\delta)$, with δ being the density contrast of this dark matter field. The intensity of the CO(1–0) line can be written as a function of the spatial location $I_{\rm CO}(\mathbf{x}) = \bar{I}_{\rm CO}[1 + b_{\rm CO}\delta(\mathbf{x})]$ with bias $b_{\rm CO}$ given by

$$b_{\rm CO}(z) = \frac{\int_{M_{\rm min}}^{\infty} dM \frac{dn}{dM} L_{\rm CO} b(z, M)}{\int_{M_{\rm min}}^{\infty} dM \frac{dn}{dM} L_{\rm CO}}, \qquad (2)$$

where $b(z,M)$ is the halo bias (Sheth & Tormen 1999).

In Figure 2, we show both the mean signal and the halo bias as a function of the redshift during reionization. For simplicity, we have converted the mean intensity of the signal to Rayleigh–Jeans brightness temperature. At $z \sim 6$, the signal is at the level of 0.2 to 1.5 μK, with the large range coming from the scatter in the $L_{\rm CO}(M)$ relation.

Since the mean intensity is challenging to measure as it requires absolute measurements, we discuss the feasibility of measuring anisotropies of the CO line intensity. The total power spectrum of the CO(1–0) line involves two contributions, the clustering term and the shot noise. Following the mean intensity and bias given above, the clustering power spectrum is

$$P_{\rm CO}^{\rm clus}(z, k) = \bar{T}_{\rm CO}^2 b_{\rm CO}^2 P_{\delta\delta}(z, k). \qquad (3)$$

Here $\bar{T}_{\rm CO}$ is the mean temperature of CO line, $P_{\delta\delta} = P_{\rm lin}(z, k)$ where $P_{\rm lin}$ is the linear power spectrum of the dark matter. The shot-noise power spectrum, due to discretization of the

[4] http://s-cubed.physics.ox.ac.uk

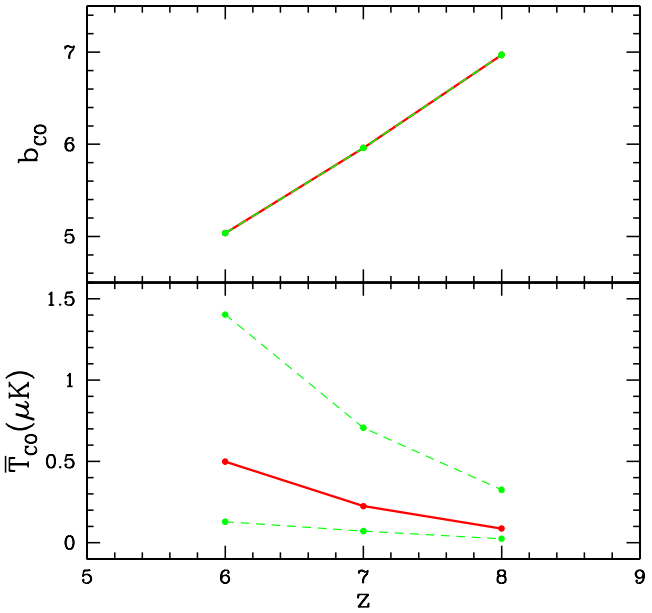

Figure 2. Bias and brightness temperature of CO line for $z = 6$, 7, and 8. The 68.3% CL (1σ) are also shown in green dashed lines. The bias has no additional uncertainty as the uncertainty in $L_{\rm CO}(M)$ relation is a change in the overall amplitude at a given mass and not a shape change (see Equation (2)).

(A color version of this figure is available in the online journal.)

galaxies, is

$$P_{\rm CO}^{\rm shot}(z) = \int_{M_{\rm min}}^{\infty} dM \frac{dn}{dM} \left(\frac{L_{\rm CO}}{4\pi D_{\rm L}^2} y D_{\rm A}^2 \right)^2. \quad (4)$$

3. CROSS POWER SPECTRUM OF CO LINE AND 21 cm EMISSION

In order to calculate the expected strength of the correlation between 21 cm and CO line intensities, we briefly discuss the brightness temperature variations in the 21 cm signal. We consider two signals, the usual signal coming from neutral gas in the IGM that is not directly correlated with molecular gas in galaxies, and the remaining neutral gas in individual galaxies. During the era of reionization, the 21 cm brightness temperature fluctuations are expected to be dominated by the IGM. At lower redshifts, while the IGM signal is zero, a small 21 cm contribution still remains due to the neutral gas in individual galaxies.

The difference of the spatially averaged brightness temperature of 21 cm emission in the IGM and the CMB temperature at redshift z (Mao et al. 2008) is

$$\bar{T}_{\rm b}^{\rm IGM} = c(z)\bar{x}_{\rm H} \left(\frac{\bar{T}_{\rm s} - T_{\rm CMB}}{\bar{T}_{\rm s}} \right) ({\rm mK}). \quad (5)$$

Here $\bar{x}_{\rm H}$ is the mean neutral hydrogen fraction, which we assume $\bar{x}_{\rm H} \equiv 1 - \bar{x}_{\rm i}$ where $\bar{x}_{\rm i}$ is the mean ionized fraction, and we set $\bar{x}_{\rm H} = 0.3$ and 0.7 at $z = 7$ and 8, respectively (Mao et al. 2008). The $\bar{T}_{\rm s}$ is the averaged spin temperature of the IGM, and we assume $\bar{T}_{\rm s} \gg T_{\rm CMB}$ here. The parameter $c(z)$ (defined in Santos et al. 2008) is

$$c(z) = 23 \left(\frac{0.7}{h} \right) \left(\frac{\Omega_{\rm b} h^2}{0.02} \right) \left(\frac{0.15}{\Omega_{\rm m} h^2} \frac{1+z}{10} \right)^{1/2} ({\rm mK}), \quad (6)$$

where $\Omega_{\rm b}$ is the baryon density parameter.

We obtain the power spectrum of the 21 cm fluctuations in the IGM using the fitting formula of Mao et al. (2008) at several redshifts during reionization. For comparison we also consider the reionization simulations of Santos et al. (2010). These simulations have a smaller bubble size on average than the models of Mao et al. (2008). As we will discuss later, while the two models we consider give rise to the same 21 cm power spectrum, they differ significantly in terms of the cross-correlation of CO and 21 cm brightness temperature fluctuations.

Similar to the IGM calculation the mean brightness temperature of 21 cm emission from the galaxies can be calculated through

$$\bar{T}_{\rm b}^{\rm G} = c(z) \frac{\rho_{\rm H}(z)}{X \rho_{\rm b}(z)} ({\rm mK}), \quad (7)$$

where $X = 0.76$ is the hydrogen mass fraction, $\rho_{\rm b}(z) = \Omega_{\rm b}(1+z)^3 \rho_{\rm c}$ is the baryon density at z, and $\rho_{\rm c} = 2.7752 \times 10^{11}\, M_\odot\, h^{-1}$ (Mpc h^{-1})$^{-3}$.

We assume that the total hydrogen mass in a given pixel of the experiment only depends on the halo mass so that the hydrogen mass density $\rho_{\rm H}$ is given by $\rho_{\rm H} = \int_{M_{\rm min}}^{\infty} dM \frac{dn}{dM} M_{\rm H\,I}(M)$. To obtain $M_{\rm HI}(M)$ we used the same procedure as before, querying the simulation from Obreschkow et al. (2009c) and adding the $M_{\rm H\,I}$ from the galaxies in each halo. The resulting scatter plot is shown in the right panel of Figure 1 together with the average in each mass bin (blue dots). The red line shows a fitting function to the average values using $M_{\rm H\,I} = 10^{A \times \log_{10}(M) + B}$, where M is the halo mass, $A = 0.75$, 0.74, and 0.75, and $B = 0.17$, 0.23, and 0.07 for $z = 6$, 7, and 8, respectively.

Following the description related to the CO line intensity, the mean 21 cm brightness temperature is taken to have spatial variations $T_{\rm b}^{\rm G}(\mathbf{x}) = \bar{T}_{\rm b}^{\rm G}(1 + b_{\rm H}\delta(\mathbf{x}))$, where $b_{\rm H}$ is the bias of galaxies containing neutral hydrogen,

$$b_{\rm H}(z) = \frac{\int_{M_{\rm min}}^{\infty} dM \frac{dn}{dM} M_{\rm H} b(z, M)}{\rho_{\rm H}}. \quad (8)$$

The clustering power spectrum of the 21 cm emission from galaxies is then $P_{\rm H}^{\rm G}(z,k) = (\bar{T}_{\rm b}^{\rm G})^2 b_{\rm H}^2 P_{\delta\delta}(z,k)$. Again, the shot-noise power spectrum for 21 cm emission is

$$P_{\rm H}^{\rm shot}(z) = \int_{M_{\rm min}}^{\infty} dM \frac{dn}{dM} \left(c(z) \frac{M_{\rm H}}{X \rho_{\rm b}(z)} \right)^2. \quad (9)$$

The total power spectrum of 21 cm emission follows from a sum of shot noise and clustering terms (see the middle panel in Figure 3).

The cross power spectrum between 21 cm and CO line intensities is $P_{\rm CO,H}^{\rm tot} = P_{\rm CO,H}^{\rm IGM} + P_{\rm CO,H}^{\rm G} + P_{\rm CO,H}^{\rm shot}$, where we again separate the contribution from neutral hydrogen in the IGM and neutral hydrogen remaining in individual galaxies. Based on the discussion related to 21 cm fluctuations, the cross power spectrum of the CO line and 21 cm emission in the IGM is

$$P_{\rm CO,H}^{\rm IGM}(z,k) = \bar{T}_{\rm CO} b_{\rm CO} c(z) [(1 - \bar{x}_{\rm i}) P_{\delta\delta} - \bar{x}_{\rm i} P_{\delta_x \delta}], \quad (10)$$

where $P_{\delta_x \delta}(z,k)$ is the cross power spectrum for the ionized fraction and the dark matter. The IGM gas is correlated with CO lines as they both trace the same underlying dark matter density field.

The cross power spectrum of the CO line and 21 cm emission in individual galaxies is

$$P_{\rm CO,H}^{\rm G}(z,k) = \bar{T}_{\rm CO} \bar{T}_{\rm b}^{\rm G} b_{\rm CO} b_{\rm H} P_{\delta\delta}(z,k), \quad (11)$$

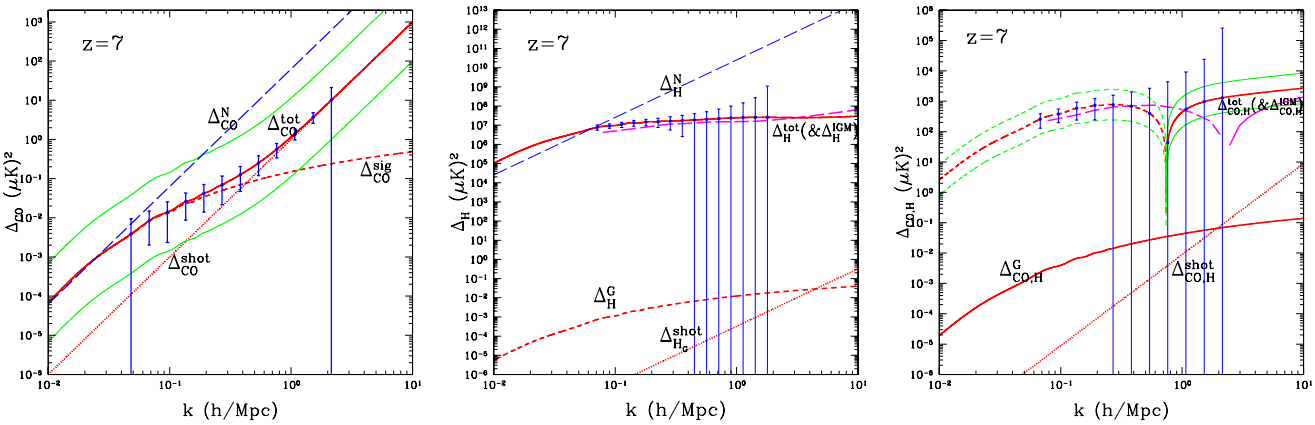

Figure 3. Left panel: the dimensionless auto power spectrum and the shot-noise power spectrum for CO line at $z = 7$. The 68.3% CL (1σ) is shown in green thin lines. Middle panel: the dimensionless auto power spectrum and the shot-noise power spectrum for 21 cm emission at $z = 7$. The auto and shot-noise power spectrum of the galaxies Δ^G_H and $\Delta^{shot}_{H_G}$ are so small compared with Δ^{IGM}_H that Δ^{tot}_H is dominated by Δ^{IGM}_H. The blue lines with error bars make use of noise power spectrum (shown by the blue dashed line) corresponding to the design of LOFAR. Right panel: the dimensionless cross power spectrum and shot-noise power spectrum for CO line and 21 cm emission at $z = 7$. The blue solid line is the error from LOFAR. The 68.3% CL (1σ) is shown in red thin lines. The long-dashed magenta lines in the middle and right panels are the results from the simulation of 21 cm in Santos et al. (2010) for comparison.

(A color version of this figure is available in the online journal.)

while the shot-noise power spectrum of the CO line and 21 cm emission in the galaxies is

$$P^{shot}_{CO,H}(z) = \int_{M_{min}}^{\infty} dM \frac{dn}{dM} \frac{L_{CO}}{4\pi D_L^2} y D_A^2 c(z) \frac{M_H}{X\rho_b(z)}. \quad (12)$$

4. DISCUSSION

In Figure 3, left panel, we show the brightness temperature power spectrum for the CO line at $z = 7$, while in the middle panel we show the 21 cm brightness temperature fluctuations at the same redshift and in the right panel, we show the cross-correlation between the two. In the case of 21 cm fluctuations, the solid lines show the prediction based on the models of Mao et al. (2008), while in dashed lines we show the prediction from the semi-numerical simulation of Santos et al. (2010).

To discuss the possibility of measuring the CO signal and the CO–21 cm cross-correlation, we make use of a calculation similar to the one used in 21 cm interferometers. Following Santos et al. (2010), the noise power spectrum P_N for a given experimental "pixel" in Fourier space is given by $P_N(k,\theta) = D_A^2 y(\lambda^4 T_{sys}^2)/[A_e^2 t_0 n\,(D_A k \sin(\theta)/2\pi)]$, where A_e is the collecting area of one element of the interferometer (which could be a station), t_0 is the total observation time, and the function $n()$ captures the baseline density distribution on the plane perpendicular to the line of sight, assuming already it is rotationally invariant (k is the moduli of the wave mode $\mathbf{k}$, and θ is the angle between $\mathbf{k}$ and the line of sight). Typically, this baseline distribution will be more concentrated around the core but for interferometers with high filling factors we can make the simplification that the distribution is constant so that the required function for above is $n() = \lambda^2 N_a^2/\pi D_{max}^2$, with N_a as the number of elements of the interferometer and D_{max} the maximum baseline of the distribution. Note that the error in the measured power spectrum at a given $\mathbf{k}$ is just $(P_S + P_N)/\sqrt{(N_m)}$, where P_S is the signal power spectrum and N_m is the number of modes contributing to a given binned measurement. In order to count the number of these modes, we consider a grid in k space with a resolution given by $(2\pi)^3/(\mathrm{yr}^2 \cdot \mathrm{FoV} \cdot \mathrm{B})$, which is set by the volume of the experiment (B is the bandwidth used in the analysis and FoV is the field of view).

Typically, we will be interested on linear scales ($k < 1.0\,h\,\mathrm{Mpc}^{-1}$) corresponding to a few arcminutes. Given the frequencies involved, the need for large FoV and high sensitivity to μK brightness temperature fluctuations leads to an experimental setup that involves a total collecting area $A_{tot} = 385$ m^2, bandwidth $B = 1$ GHz with spectral resolution $\delta\nu = 30$ MHz, and interferometer spacings between 0.7 and 25 m. The number of elements is 1000 with each having a receiver with system temperature of 20 K. In the left panel of Figure 3, we assume a total integration time of 3000 hr when calculating the noise power spectrum. For 21 cm noise calculations we make use of a setup similar to LOFAR, though we note that our calculations are not too different from an experiment like Murchison Widefield Array. For experimental parameters related to LOFAR, we refer the reader to Harker et al. (2010). The values (at 150 MHz) are $A_{tot} = 5 \times 10^4$ m^2, $T_{sys} = 490$ K (instrument noise temperature), FoV $= 25$ deg^2, bandwidth of 8 MHz with $\delta\nu = 0.5$ MHz, and $D_{max} = 2000$ m. We take $T_{int} = 1000$ hr.

For the proposed experimental setup, the brightness temperature fluctuations can be detected with a cumulative signal-to-noise ratio that leads to more than 40σ confidence. However, CO(1–0) mapping could be impacted by foregrounds, including spectral lines associated with other molecules. In the case of other transitions of the CO lines, the contamination for CO(1–0) measurements at $z \sim 6$ to 8 is likely to be minimal; the CO(2–1) line for example must originate from $z \sim 13$ to 17. The most significant contaminations will likely come from molecular transitions that have rest wavelengths longward of the CO(1–0) line and thus coming from lower redshifts. To avoid such contaminations and to improve the overall study of reionization, we suggest a cross-correlation between 21 cm brightness temperature fluctuations and the CO intensities.

For the cross-correlation, we assume that observations will be conducted in overlapping areas on the sky by both the CO and 21 cm experiment. This is a necessary feature of cross-correlation study leading to some coordination between two experiments. We reduce both data sets to a common, and a lower resolution, cube in frequency, and count the total number of common modes contributing to a given bin in k space using

the same method for noise calculation as before for each of the experiments. Note that the error in a given pixel in k space can be written as $\sqrt{(P_{\rm CO,H}^2 + P_{\rm CO} P_{\rm H})/N_m}$, where N_m is the number of modes. In Figure 3, right panel, we show the cross-correlation power spectrum at $z = 7$ and the expected binned errors by using LOFAR and the CO experiment with parameters outlined above. The overall uncertainties are dominated by the 21 cm observations. For reference, we also show the prediction of the model by Mao et al. (2008) and from the numerical simulation of Santos et al. (2010). While the two give a similar 21 cm fluctuation power spectrum, they differ significantly in terms of the cross-correlation with the CO emission. The difference is primarily related to the average scale of the reionized bubble sizes, and we find that the cross-correlation such as the one we propose here is more sensitive to astrophysics during reionization than with 21 cm data alone.

While our calculation and results are related to the CO(1–0) transition, our method can be extended to other transitions and other molecules as well as long as a correction is made for the ratio of line intensity between higher J-transitions of CO and the 1–0 line. Existing observations, at low to moderate redshifts, suggest a value of about 0.6 for $J = 2$ to 1 luminosity when compared to 1–0 luminosity. The 2–1 observations will be over the frequency range of 25.5 to 32 GHz for $z \sim 6$ to 8.

The fine-structure C II line has been detected in several of the high-z galaxies and existing studies indicate that $L_{\rm C\,II}/L_{\rm CO} \sim 4100$. With a rest wavelength at 158 μm, observations are required over the frequency range of 210 to 270 GHz (1.1 to 1.4 mm). The rms fluctuations are expected to be at the level of 10^2 to 10^3 Jy sr^{-1} at $z \sim 7$ to 8 at tens of arcminute angular scales. To probe reionization fluctuations associated with the C II line, observations must be carried out in small frequency intervals of 50 MHz with instruments providing angular resolution of order ten arcminutes with survey areas of order a few tens square degrees. In a future paper we hope to return to the scientific case of a potential C II experiment, since such an observation can probe multiple redshifts with both C II and high-J CO lines.

We thank participants of the Kavli Institute for Space Studies' (KISS) Billion Years workshop for helpful discussions. This work was supported by NSF CAREER AST-0645427 at UCI. M.G.S. and M.B.S. acknowledge support from FCT-Portugal under grant PTDC/FIS/100170/2008.

REFERENCES

Basu, K., Hernandez-Monteagudo, C., & Sunyaev, R. A. 2004, A&A, 416, 447
Bowman, J., Morales, M. F., & Hewitt, J. N. 2007, ApJ, 661, 1
Chang, T.-C., Pen, U.-L., Bandura, K., & Peterson, J. B. 2010, Nature, 466, 463
Cooray, A. 2006, MNRAS, 365, 842
Cooray, A., & Milosavljevic, M. 2005a, ApJ, 627, 85
Cooray, A., & Milosavljevic, M. 2005b, ApJ, 627, 89
De Lucia, G., & Blaizot, J. 2007, MNRAS, 375, 2
Downes, D., & Solomon, P. M. 1998, ApJ, 507, 615
Furlanetto, S. R., Zaldarriaga, M., & Hernquist, L. 2004, ApJ, 613, 16
Gnedin, N. Y., & Shaver, P. A. 2004, ApJ, 608, 611
Greve, T. R., et al. 2005, MNRAS, 359, 1165
Harker, et al. 2010, MNRAS, 405, 2492
Lah, P., et al. 2007, MNRAS, 376, 1357
Loeb, A., & Barkana, R. 2001, ARA&A, 39, 19
Loeb, A., & Zaldarriaga, M. 2004, Phys. Rev. Lett., 92, 211301
Madau, P., Meiksin, A., & Rees, M. J. 1997, ApJ, 475, 429
Mao, Y., Tegmark, M., McQuinn, M., Zaldarriaga, M., & Zahn, O. 2008, Phys. Rev. D, 78, 023529
McQuinn, M., Zahn, O., Zaldarriaga, M., Hernquist, L., & Furlanetto, S. R. 2006, ApJ, 653, 815
Obreschkow, D., Croton, D., De Lucia, G., Khochfar, S., & Rawlings, S. 2009a, ApJ, 698, 1467
Obreschkow, D., Heywood, I., Klockner, H.-R., & Rawlings, S. 2009b, ApJ, 702, 1321
Obreschkow, D., Klockner, H.-R., Heywood, I., Levrier, F., & Rawlings, S. 2009c, ApJ, 703, 1890
Riechers, D. A., et al. 2010, ApJ, 720, L131
Righi, M., Hernandez-Monteagudo, C., & Sunyaev, R. A. 2008, A&A, 2, 489
Santos, M. G., Amblard, A., Pritchard, J., Trac, H., Cen, R., & Cooray, A. 2008, ApJ, 689, 1
Santos, M. G., & Cooray, A. 2006, Phys. Rev. D, 74, 083517
Santos, M. G., Cooray, A., & Knox, L. 2005, ApJ, 625, 575
Santos, M. G., Silva, M. B., Pritchard, J. R., Cen, R., & Cooray, A. 2010, A&A, in press (arXiv:1009.0950)
Sheth, R. K., & Tormen, G. 1999, MNRAS, 308, 119
Visbal, E., & Loeb, A. 2010, J. Cosmol. Astropart. Phys., JCAP11(2010)016
Yang, X., Mo, H. J., Jing, Y. P., van den Bosch, F. C., & Chu, Y. 2004, MNRAS, 350, 1153

A.2 Paper II

INTENSITY MAPPING OF THE [Cii] FINE STRUCTURE LINE DURING THE EPOCH OF REIONIZATION

Gong Y., Cooray A., **Silva M. B.**, Santos M. G., Bock J., Bradford C. and Zemcov M.
The Astrophysical Journal, 745, 49 (2012)
arXiv:1107.3553

The Astrophysical Journal, 745:49 (16pp), 2012 January 20 doi:10.1088/0004-637X/745/1/49

INTENSITY MAPPING OF THE [C II] FINE STRUCTURE LINE DURING THE EPOCH OF REIONIZATION

Yan Gong[1], Asantha Cooray[1], Marta Silva[2], Mario G. Santos[2], James Bock[3,4], C. Matt Bradford[3,4], and Michael Zemcov[3,4]
[1] Department of Physics & Astronomy, University of California, Irvine, CA 92697, USA
[2] CENTRA, Instituto Superior Técnico, Technical University of Lisbon, Lisboa 1049-001, Portugal
[3] California Institute of Technology, 1200 E. California Blvd., Pasadena, CA 91125, USA
[4] Jet Propulsion Laboratory, 4800 Oak Grove Drive, Pasadena, CA 91109, USA
Received 2011 July 18; accepted 2011 October 20; published 2011 December 28

ABSTRACT

The atomic C II fine-structure line is one of the brightest lines in a typical star-forming galaxy spectrum with a luminosity ∼0.1%–1% of the bolometric luminosity. It is potentially a reliable tracer of the dense gas distribution at high redshifts and could provide an additional probe to the era of reionization. By taking into account the spontaneous, stimulated, and collisional emission of the C II line, we calculate the spin temperature and the mean intensity as a function of the redshift. When averaged over a cosmologically large volume, we find that the C II emission from ionized carbon in individual galaxies is larger than the signal generated by carbon in the intergalactic medium. Assuming that the C II luminosity is proportional to the carbon mass in dark matter halos, we also compute the power spectrum of the C II line intensity at various redshifts. In order to avoid the contamination from CO rotational lines at low redshift when targeting a C II survey at high redshifts, we propose the cross-correlation of C II and 21 cm line emission from high redshifts. To explore the detectability of the C II signal from reionization, we also evaluate the expected errors on the C II power spectrum and C II-21 cm cross power spectrum based on the design of the future millimeter surveys. We note that the C II-21 cm cross power spectrum contains interesting features that capture physics during reionization, including the ionized bubble sizes and the mean ionization fraction, which are challenging to measure from 21 cm data alone. We propose an instrumental concept for the reionization C II experiment targeting the frequency range of ∼200–300 GHz with 1, 3, and 10 m apertures and a bolometric spectrometer array with 64 independent spectral pixels with about 20,000 bolometers.

Key words: cosmology: theory – diffuse radiation – intergalactic medium – large-scale structure of universe

Online-only material: color figures

1. INTRODUCTION

Carbon is one of the most abundant elements in the universe and it is singly ionized (C II) at 11.26 eV, an ionization energy that is less than that of the hydrogen. With a splitting of the fine-structure level at 91 K C II is easily excited resulting in a line emission at 157.7 μm through the $^2P_{3/2} \rightarrow ^2P_{1/2}$ transition. It is now well established that this line provides a major cooling mechanism for the neutral interstellar medium (ISM; Dalgarno & McCray 1972; Tielens & Hollenbach 1985; Wolfire et al. 1995; Lehner et al. 2004). It is present in multiple phases of the ISM in the Galaxy (Wright et al. 1991) including the most diffuse regions (Bock et al. 1993) and the line emission has been detected from the photodissociation regions (PDRs) of star-forming galaxies (Boselli et al. 2002; De Looze et al. 2011; Nagamine et al. 2006; Stacey et al. 2010) and, in some cases, even in $z > 6$ Sloan quasars (Walter et al. 2009).

The C II line is generally the brightest emission line in star-forming galaxy spectra and contributes to about 0.1%–1% of the total far-infrared (FIR) luminosity (Crawford et al. 1985; Stacey et al. 1991). Since carbon is naturally produced in stars, C II emission is then expected to be a good tracer of the gas distribution in galaxies. Even if the angular resolution to resolve the C II emission from individual galaxies is not available, the brightness variations of the C II line intensity can be used to map the underlying distribution of galaxies and dark matter (Basu et al. 2004; Visbal & Loeb 2010; Gong et al. 2011).

Here we propose C II intensity mapping as an alternative avenue to probe the era of reionization, including the transition from primordial galaxies with PopIII stars alone to star formation in the second generation of galaxies with an ISM polluted by metals. C II intensity mapping complements attempts to study reionization with low-frequency radio experiments that probes the 21 cm spin-flip line from neutral hydrogen. While those experiments are sensitive to the neutral gas distribution dominated by the intergalactic medium (IGM), C II will probe the onset of star formation and metal production in $z \sim 6$–8 galaxies.

Recently it has also been proposed to use rotational lines of CO molecule to probe reionization (e.g., Gong et al. 2011; Carilli 2011; Lidz et al. 2011). CO studies have the advantage that redshift identification is facilitated by multiple J transition lines, while with C II some confusion could result in the line identification with other atomic fine-structure and molecular lines at sub-mm and mm wavelengths. In comparison, and based on limited observational data, C II emission is expected to be brighter in low mass galaxies, compared to the case of CO luminosity. It is unclear if the galaxies present during reionization are analogous to low-redshift dwarf galaxies or the local ultra-luminous infrared galaxy population. At high redshifts, we expect most of the carbon to be in C II rather than CO, since the high-redshift galaxies may not host significant dust columns required to shield CO from dissociating UV photos. Given that a CO experiment to study reionization will involve an experiment at mid radio frequencies of 15–30 GHz, while C II will involve high frequencies, the two methods will be affected by different systematics and foregrounds. Thus, a combined approach involving multiple probes of reionization, 21 cm, CO, and C II, would provide the best avenue to study the $z > 6$ universe.

In this paper we present an analytical calculation to predict the C II intensity as a function of the redshift by considering spontaneous, stimulated and collisional emission processes (Suginohara et al. 1999; Basu et al. 2004). This intensity changes the brightness spectrum of the cosmic microwave background (CMB) at the frequency corresponding to the C II line (Basu et al. 2004). In this paper, we focus on the C II flux from individual galaxies where the matter density is high and the collisional emission is the dominant process. As a check on our analytical calculations, we also consider results derived from numerical simulations to establish the C II intensity. The two approaches are generally consistent. We then consider the measurement of the C II intensity fluctuations resulting from the clustering of the galaxy distribution and sources that are present during and toward the end of reionization at $z \sim 6$–8.

Experimentally, there are several challenges that one must overcome before the C II intensity fluctuations from high redshifts can be reliably established. First, higher J transitions of CO from dense molecular gas at lower redshifts contaminate the C II line intensity measurements. In particular, one must account for all of CO(2-1) to CO(13-12) emission lines from individual narrow redshift ranges in the foreground between 0 and 6 when probing C II fluctuations at $z > 6$. To the extent to which a variety of existing predictions on the CO intensity can be trusted (Gong et al. 2011; Lidz et al. 2011; Carilli 2011), we generally find that the contamination is mostly below the level of the C II signal. Extending previous studies (Basu et al. 2004; Visbal & Loeb 2010; Gong et al. 2011; Lidz et al. 2011), we propose the cross-correlation of C II line intensity mapping and 21 cm fluctuations as a way to improve studies related to the epoch of reionization. To evaluate the detectability of the C II signal, we calculate the errors on the C II power spectra and C II-21 cm cross-correlation, respectively, based on the design of potential (sub-)millimeter surveys for the C II emission. For 21 cm, we consider the first-generation experiment LOw Frequency ARray[5] (LOFAR) survey as well as the improvement expected from a second-generation experiment like the low-frequency extension to the Square Kilometer Array (SKA).

The paper is organized as follows: in the next section, we derive the formulas to calculate the spin temperature of the C II line in the ISM of galaxies and the IGM. In Section 3, we calculate the mean C II intensity analytically and compare it with results derived from a simulation. We show the C II power spectrum in Section 4. In Section 5, we discuss the low-redshift contamination from CO emission lines for C II intensity mapping at $z > 6$ and in Section 6 we propose a cross-correlation between C II and 21 cm line intensity measurements over the overlapping redshift ranges as a way to both distinguish the C II signal from the CO emission and to improve overall constraints on reionization physics. In Section 7 we outline the experimental parameters of a C II spectral mapping experiment designed to probe $z \sim 6$–8 C II intensity fluctuations and discuss the detectability of the C II power spectrum and the C II and 21 cm cross-correlation when combined with LOFAR and SKA. We conclude with a summary of our results in Section 8. Throughout this paper, we assume the flat ΛCDM model with $\Omega_m = 0.27$, $\Omega_b = 0.046$, $\sigma_8 = 0.81$, $n_s = 0.96$, and $h = 0.71$ (Komatsu et al. 2011).

[5] http://www.lofar.org/

2. THE DERIVATION OF THE SPIN TEMPERATURE OF THE C II EMISSION

The C II line intensity can be generated from carbon present in both the ISM of individual galaxies and the diffuse IGM in between galaxies. In the ISM of galaxies, C II is expected to be in thermodynamic equilibrium with resonant scattering emission off of CMB photons and the collisional emission induced by gas in the galaxy. If the number density of gas particles $n_{\rm gas}$ is greater than a critical value $n_{\rm cr}$, the collisional excitation and de-excitation rate would exceed that of the radiative (spontaneous and stimulated) processes.

Since the ionization potential of carbon is 11.26 eV, below 13.6 eV of hydrogen ionization, the surrounding gas of C II ions can be either neutral hydrogen or electrons. However, because the critical number density of electrons to trigger collisional excitation $n_{\rm e}^{\rm cr}$ is less than 100 cm^{-3} while the critical number density of neutral hydrogen for collisional excitation $n_{\rm H}^{\rm cr}$ is about 10^3 to 10^4 cm^{-3} (Malhotra et al. 2001), the electrons can collide with C II ions more frequently than with H I, especially in ionized gas (Lehner et al. 2004; Suginohara et al. 1999). For simplicity and not losing generality, we assume that the ISM is mostly ionized in individual galaxies. Then the C II line emission would mainly be excited by electrons in the ISM (Suginohara et al. 1999).

On the other hand, in the diffuse IGM in between galaxies C II line emission will be mainly due to radiative processes such as spontaneous emission, stimulated emission due to collisions with CMB photons, and an UV pumping effect similar to the Ly-α coupling for the 21 cm emission (Wouthuysen 1952; Field 1958; Hernandez-Monteagudo et al. 2006). We will focus on the C II emission from the ISM of galaxies first and then consider the signal from the IGM. The latter is found to be negligible.

2.1. The C II Spin Temperature in the ISM of Galaxies

In the ISM of galaxies, the ratio of thermal equilibrium population of the upper level $^2P_{3/2}$ and lower level $^2P_{1/2}$ of C II fine structure line can be found by solving the statistical balance equation

$$\frac{n_{\rm u}}{n_{\rm l}} = \frac{B_{\rm lu} I_\nu + n_{\rm e} C_{\rm lu}}{B_{\rm ul} I_\nu + A_{\rm ul} + n_{\rm e} C_{\rm ul}} \equiv \frac{g_{\rm u}}{g_{\rm l}} \exp\left[-T_{\star,{\rm ul}}/T_{S,{\rm ul}}\right]. \quad (1)$$

Here $A_{\rm ul} = 2.36 \times 10^{-6}$ s^{-1} is the spontaneous emission Einstein coefficient (Suginohara et al. 1999), $B_{\rm ul}$ and $B_{\rm lu}$ are the stimulated emission and absorption coefficients, respectively, $I_\nu \equiv B[T_{\rm CMB}(z)]$ is the intensity of CMB at $\nu_{\rm ul}$, $n_{\rm e}$ is the number density of electrons, and $C_{\rm lu}$ and $C_{\rm ul}$ are the excitation and de-excitation collisional rates (in cm^3 s^{-1}), respectively. Note that the UV pumping effect is neglected here and, as we discuss later, it should not affect the result unless the UV intensity inside the galaxy ($I_{\rm UV}^{\rm gal}$) is higher than 10^{-15} erg s^{-1} cm^{-2} Hz^{-1} sr^{-1}, which is about 10^6 times greater than the UV background (Giallongo et al. 1997; Haiman et al. 2000). We note that even if the radiative coupling from UV pumping made a small contribution to the spin temperature it would be in the same direction as the collisional coupling since the UV color temperature follows the gas temperature.

The second line of Equation (1) defines the excitation or spin temperature $T_{S,{\rm ul}}$ of the C II line. The statistical weights are $g_{\rm u} = 4$ and $g_{\rm l} = 2$, and $T_{\star,{\rm ul}} \equiv h\nu_{\rm ul}/k_B \simeq 91$ K is the equivalent temperature of the level transition. The excitation collisional rate $C_{\rm lu}$ can be written as (Spitzer 1978; Osterbrock

1989; Tayal 2008)

$$C_{\rm lu} = \frac{8.629\times10^{-6}}{g_{\rm l}\sqrt{T_{\rm k}^{\rm e}}}\gamma_{\rm lu}(T_{\rm k}^{\rm e})\exp\left(\frac{-T_{\star,\rm lu}}{T_{\rm k}^{\rm e}}\right), \quad (2)$$

where $T_{\rm k}^{\rm e}$ is kinetic temperature of the electron and $\gamma_{\rm lu}$ is the effective collision strength, a dimensionless quantity.

To derive the spin temperature T_S, we can use Einstein relations $g_{\rm l}B_{\rm lu} = g_{\rm u}B_{\rm ul}$ and $A_{\rm ul} = (2h\nu^3/c^2)B_{\rm ul}$ to convert both stimulated emission coefficient $B_{\rm ul}$ and absorption coefficient $B_{\rm lu}$ in terms of the spontaneous emission coefficient $A_{\rm ul}$. Also, using the collisional balance relation

$$\frac{C_{\rm lu}}{C_{\rm ul}} = \frac{g_{\rm u}}{g_{\rm l}}\exp\left[-T_{\star,\rm ul}/T_{\rm k}^{\rm e}\right], \quad (3)$$

we can finally write

$$\frac{T_{\star,\rm ul}}{T_{S,\rm ul}} = \log\left\{\frac{A_{\rm ul}\left[1+(I_\nu c^2/2h\nu^3)_{\nu_{\rm ul}}\right]+n_{\rm e}C_{\rm ul}}{A_{\rm ul}\left(I_\nu c^2/2h\nu^3\right)_{\nu_{\rm ul}}+n_{\rm e}C_{\rm ul}\exp\left(-T_{\star,\rm ul}/T_{\rm k}^{\rm e}\right)}\right\}. \quad (4)$$

Note that the de-excitation collisional rate $C_{\rm ul}$ is dependent on the $T_{\rm k}^{\rm e}$, and using Equations (2) and (3), we can calculate the de-excitation collisional rate $C_{\rm ul}$ for a fixed value of the electron kinetic temperature. Here we adopt the values of $\gamma_{\rm lu}$ which are calculated by the R-matrix in Keenan et al. (1986), and they find $\gamma_{\rm lu} = 1.58$, 1.60, and 2.11 at $T_{\rm k}^{\rm e} = 10^2$, 10^3, and 10^4 K, respectively. Putting all values together, we find $C_{\rm ul} = 3.41\times10^{-7}$, 1.09×10^{-7}, and 4.55×10^{-8} cm^3 s^{-1} for $T_{\rm k}^{\rm e} = 10^2$, 10^3, and 10^4 K, respectively. This is well consistent with the de-excitation rate of 4.6×10^{-8} cm^3 s^{-1} at 10^4 K given in Basu et al. (2004).

The deviation of the C II spin temperature $T_{S,\rm ul}$ relative to $T_{\rm CMB}$ as a function of redshift for the electron-dominated ISM of galaxies is shown in Figure 1. We choose several values of the electron kinetic temperature $T_{\rm k}^{\rm e}$ and the number density $n_{\rm e}$ to plot the spin temperature T_S as a function of the redshift. We note that although the mean number density of electrons $n_{\rm e}^{\rm mean}$ can be very small ($<10^{-2}$ cm^{-3}) in a halo, the significant C II emission in galaxies comes from dense gas clumps which have a much higher n_e (Suginohara et al. 1999). Due to gas clumping the local $n_{\rm e}$ can be much greater than $n_{\rm e}^{\rm cr}$ even though $n_{\rm e}^{\rm mean} < n_{\rm e}^{\rm cr}$. Thus we choose to assume several high $n_{\rm e}$ values in our plots, but also show the case with two low values of $n_{\rm e} = 1$ and 10 cm^{-3}. These values are less than $n_{\rm e}^{\rm cr}$. We find the T_S is almost constant and always greater than $T_{\rm CMB}$ for $0 < z < 10$ in all these cases. In Equation (4), it is easy to find that the T_S depends on the relative strength of the radiative (spontaneous and stimulated) and collisional processes. If the spontaneous and stimulated emission are dominant, we have $T_S \sim T_{\rm CMB}$, while $T_S \sim T_{\rm k}^{\rm e}$ if collisions are dominant. Given a fixed number density $n_{\rm e}$, the only variable that depends on redshift z in Equation (4) is $I_\nu(z)$, but the spin temperature is not strongly sensitive to it. This implies that the collisional process is dominant in the ISM of galaxies when compared to the resonant scattering off of CMB photons. As we discuss next, this result is not true for the emission of the C II line in the diffuse IGM (Basu et al. 2004), where T_S is much smaller and varies with redshift similar to $T_{\rm CMB}$.

2.2. The C II Spin Temperature in the Diffuse IGM

In the IGM, the collisional process becomes unimportant since the number density of electrons and other elements are much smaller than in dense regions within the ISM of galaxies (Basu et al. 2004). Also, the spontaneous emission and the stimulated absorption and emission by the CMB photons are considerable. We will also take into account UV pumping that can enhance C II emission. This effect is similar to the Wouthuysen–Field effect for the 21 cm line (Wouthuysen 1952; Field 1958; Hernandez-Monteagudo et al. 2006) and, to the extent we are aware of, has not been discussed in the literature previously.

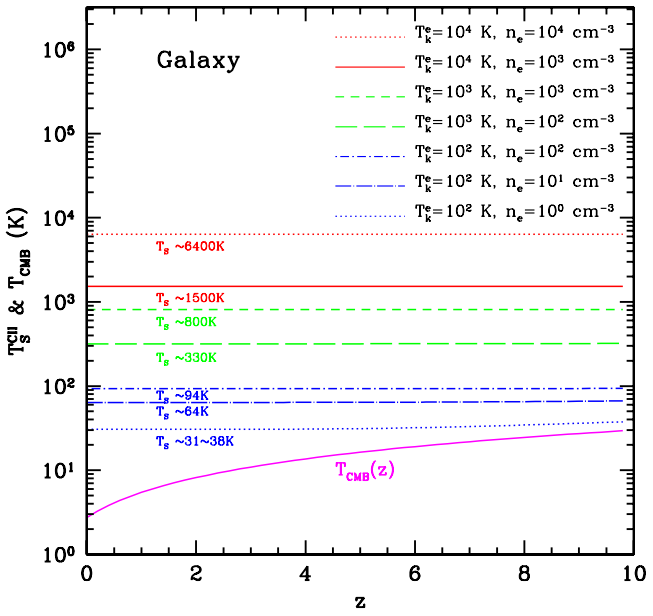

Figure 1. C II spin temperature $T_S^{\rm C\,II}$ and the $T_{\rm CMB}$ in the ISM of galaxies as a function of the redshift. To capture different ISM conditions within a large sample of galaxies we select several pairs of the electron kinetic temperature $T_{\rm k}^{\rm e}$ and the number density $n_{\rm e}$ for this calculation. We find that the C II spin temperature is almost constant with redshift, which indicates that the collisional process is dominant in the ISM of galaxies when compared to the radiative processes.

(A color version of this figure is available in the online journal.)

At high redshifts the soft UV background at 1330 Å generated by the first galaxies and quasars can pump the C II ions from the energy level $2s^22p\ ^2P_{1/2}$ to $2s2p^2\ ^2D_{3/2}$ at 1334.53 Å and $2s^22p\ ^2P_{3/2}$ to $2s2p^2\ ^2D_{3/2}$ at 1335.66 Å. Then this pumping effect can lead to the C II fine-structure transitions $^2D_{3/2} \rightarrow ^2P_{3/2} \rightarrow ^2P_{1/2}$, which would mix the levels of the C II line at 157.74 μm. The UV de-excitation and excitation rates are given by (Field 1958)

$$P_{\rm ul}^{\rm UV} = \frac{g_{\rm k}}{g_{\rm u}}\frac{A_{\rm kl}}{\sum_{\rm n}A_{\rm kn}}A_{\rm ku}\left(\frac{c^2I_\nu^{\rm UV}}{2h\nu^3}\right)_{\nu_{\rm ku}} \quad (5)$$

and

$$P_{\rm lu}^{\rm UV} = \frac{g_{\rm k}}{g_{\rm l}}\frac{A_{\rm ku}}{\sum_{\rm n}A_{\rm kn}}A_{\rm kl}\left(\frac{c^2I_\nu^{\rm UV}}{2h\nu^3}\right)_{\nu_{\rm kl}}, \quad (6)$$

where "k" stands for the level $^2D_{3/2}$, $g_{\rm k} = 4$, $A_{\rm kl} = 2.41\times10^8$ s^{-1} and $A_{\rm ku} = 4.76\times10^7$ s^{-1} are the Einstein coefficients of $^2D_{3/2} \rightarrow ^2P_{1/2}$ and $^2D_{3/2} \rightarrow ^2P_{3/2}$, respectively (see the NIST Web site[6]), and $\sum_{\rm n}A_{\rm kn} = A_{\rm kl} + A_{\rm ku}$. Also, it is helpful to define the UV color temperature $T_{\rm UV,ul}$ in terms of the ratio of

[6] http://physics.nist.gov/PhysRefData/ASD/lines_form.html

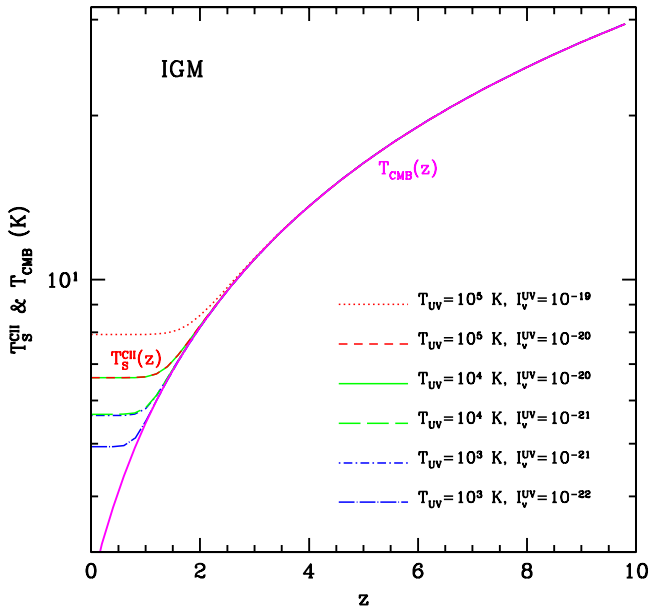

Figure 2. C II spin temperature $T_S^{\rm CII}$ and $T_{\rm CMB}$ in the diffuse IGM as a function of the redshift. We select several pairs of the UV color temperature $T_{\rm UV}$ and the UV background intensity $I_\nu^{\rm UV}$ for this calculation. We find that the spin temperature is close to $T_{\rm CMB}$ at high redshifts ($z > 2$).
(A color version of this figure is available in the online journal.)

the UV de-excitation and excitation rates

$$\frac{P_{\rm lu}^{\rm UV}}{P_{\rm ul}^{\rm UV}} = \frac{g_{\rm u}}{g_{\rm l}} \exp\left[-T_{\star,{\rm ul}}/T_{\rm UV,ul}\right]. \quad (7)$$

Then, following a similar derivation as to the case of spin temperature in the ISM of galaxies, we find that the C II spin temperature in the diffuse IGM is

$$\frac{T_{\star,{\rm ul}}}{T_{S,{\rm ul}}} = \log\left\{\frac{A_{\rm ul}\left[1+\left(I_\nu c^2/2h\nu^3\right)_{\nu_{\rm ul}}\right]+P_{\rm ul}^{\rm UV}}{A_{\rm ul}(I_\nu c^2/2h\nu^3)_{\nu_{\rm ul}}+P_{\rm ul}^{\rm UV}\exp(-T_{\star,{\rm ul}}/T_{\rm UV})}\right\}. \quad (8)$$

In Figure 2, we show the departure of T_S from $T_{\rm CMB}$ as a function of the redshift. We see that the $T_S^{\rm IGM}$ does not change if $T_{\rm UV} > 10^3$ K when fixing $I_\nu^{\rm UV}$, and it is close to $T_{\rm CMB}$ at high redshifts ($z > 2$). Together with Equation (8) this implies that $A_{\rm ul} \gg P_{\rm ul}^{\rm UV}$, i.e., the spontaneous and stimulated emission are much greater than the UV pumping effect at high redshifts. By comparing Figure 2 with Figure 1, we can see that the C II spin temperature in the ISM of galaxies is much larger than that of the diffuse IGM, and $T_S^{\rm IGM}$ is quite close to $T_{\rm CMB}$ at high redshift while $T_S^{\rm gal}$ is larger than $T_{\rm CMB}$.

3. THE CALCULATION OF THE C II MEAN INTENSITY

To establish the overall intensity of the C II line emission, we calculate the distortion of the CMB spectrum ΔI_ν and take into account the mean intensity of the C II line emitted by the ISM galaxies and the IGM. Considering the spontaneous, stimulated emission, and absorption, and the expansion of the universe, we write the radiative transfer equation as

$$\frac{dI_\nu(z)}{ds} = j_\nu(z) - \alpha_\nu(z)I_\nu - 3\frac{H(z)}{c}I_\nu, \quad (9)$$

where ds is the line element along the line of sight, and $H(z)$ is the Hubble parameter. The spontaneous emission and absorption coefficients are

$$j_\nu(z) = \frac{h\nu_{\rm ul}}{4\pi} n_{\rm u}(z) A_{\rm ul}\phi(\nu)$$

and

$$\alpha_\nu(z) = \frac{h\nu_{\rm ul}}{4\pi}\phi(\nu)(n_{\rm l}B_{\rm lu} - n_{\rm u}B_{\rm ul}),$$

respectively, where $\phi(\nu)$ is the line profile function which can be set as delta function $\phi(\nu') = \delta(\nu' - \nu)$ if the thermal broadening or velocity is much smaller than the frequency resolution (Suginohara et al. 1999; Basu et al. 2004). Integrating Equation (9) along the line of sight then gives

$$\Delta I_\nu = \int \frac{j_\nu(z) - \alpha_\nu(z)I_\nu}{(1+z)^3} ds = \int \frac{j_\nu(z) - \alpha_\nu(z)I_\nu}{H(z)(1+z)^4} c dz. \quad (10)$$

Using the relation of the line profile and the redshift $\phi(\nu') = \phi[\nu_0(1+z')] = [(1+z)/\nu]\delta(z'-z)$ we can obtain the integrated intensity of the C II emission lines at z as

$$\Delta I_\nu = \frac{hc}{4\pi H(z)(1+z)^3} A_{\rm ul}\, f_{\rm CII}^{\rm grd} n_{\rm CII}(z) \frac{g_{\rm u}}{g_{\rm l}} \exp(-T_{\star,{\rm ul}}/T_{S,{\rm ul}}) \times \left[1 - \frac{\exp(T_{\star,{\rm ul}}/T_{S,{\rm ul}}) - 1}{(2h\nu^3/c^2 I_\nu)_{\nu_{\rm ul}}}\right], \quad (11)$$

where $f_{\rm CII}^{\rm grd}$ is the fraction of C II ions at the ground level $^2P_{1/2}$. If $T_S \gg T_\star (> T_{\rm CMB})$, which is the usual case in the galaxies, then $\exp(\pm T_{\star,{\rm ul}}/T_{S,{\rm ul}}) \sim 1$, and we can find

$$\Delta I_\nu = \frac{hc}{4\pi H(z)(1+z)^3} \frac{g_{\rm u}}{g_{\rm l}} A_{\rm ul}\, f_{\rm CII}^{\rm grd} n_{\rm CII}(z). \quad (12)$$

If T_S is much larger than $T_{\star,{\rm ul}}$ (e.g., the cases in galaxies), $f_{\rm CII}^{\rm grd} \simeq 1/3$ is a good approximation, and when $T_S \ll T_{\star,{\rm ul}}$ we can set $f_{\rm CII}^{\rm grd} \simeq 1$ (e.g., the case of the IGM). The $n_{\rm CII}(z)$ is the number density of the C II ions at z, which has to be carefully estimated for both the galaxy and IGM cases.

To calculate the C II intensity, we now need an estimate of the number density of the C II ions. For the IGM case, it is easy to calculate if we know the metallicity evolution and the average baryonic density as a function of z. However, for the ISM of galaxies, we also have to find the fraction of the C II ions which exceed the critical density to trigger the dominant collisional emission. In the next section, we will first evaluate the $n_{\rm CII}$ theoretically for both the ISM and IGM cases, and then calculate $n_{\rm CII}$ using data from a simulation and compare it to the analytical result as a check on the consistency. We also provide an order of magnitude estimate on the $z \sim 6$–8 C II mean intensity using scaling relations such as those involving star formation rate (SFR) and the total far-IR luminosity of galaxies.

3.1. The Analytic Estimation

We start by writing

$$n_{\rm CII}(z) = f_{\rm CII}(z) Z_{\rm C} \bar{n}_{\rm gas}(z), \quad (13)$$

where $Z_{\rm C} = X_{\rm C} Z_\odot^{\rm C}$, $Z_\odot^{\rm C} = 3.7 \times 10^{-4}$ is the solar carbon abundance (Basu et al. 2004), and we assume $X_{\rm C} = 1$ in the

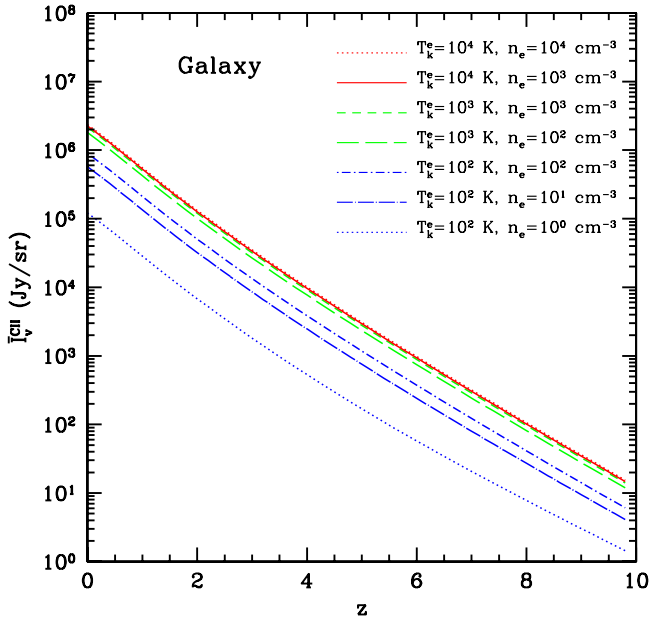

Figure 3. Mean intensity of C II emission line from the ISM gas in galaxies as a function of the redshift. We find that the electron collisional emission saturates when $n_e \gtrsim 10^2$ cm^{-3} and $T_k^e \gtrsim 10^3$ K.

(A color version of this figure is available in the online journal.)

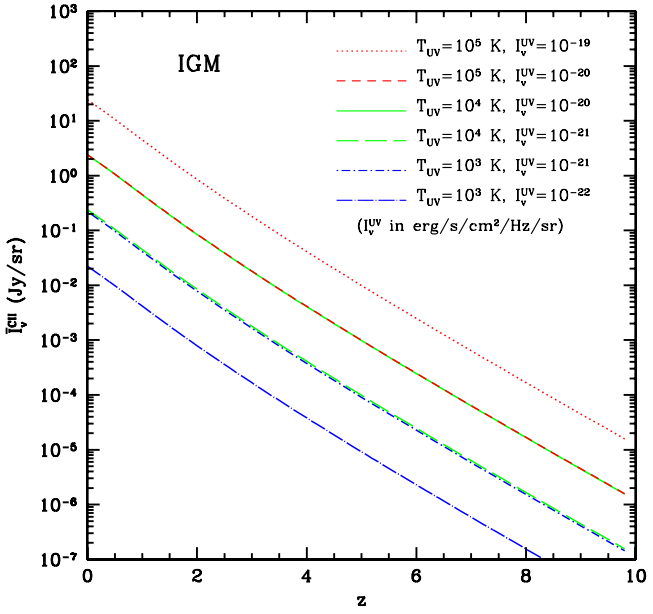

Figure 4. Mean intensity of C II emission line from carbon in the IGM as a function of the redshift. The intensity here is much smaller than that of ISM in galaxies since the spin temperature is close to the CMB temperature and the gas density is much lower than galaxy ISM.

(A color version of this figure is available in the online journal.)

galaxy and $X_C = 10^{-2}$ in the IGM (Savaglio 1997; Aguirre & Schaye 2005; Kramer et al. 2010). The $f_{CII}(z) = Z/Z_\odot(z)$ is the global metallicity at different redshift, and we use an approximated relation $Z/Z_\odot(z) = 10^{-0.4z}$ in our calculation, which assumes that the present mean metallicity of the universe is equal to the solar metallicity (note that this assumption may overestimate the metallicity at low redshifts) and the carbon atoms are totally ionized to be C II. This relation is consistent with the observational data from the damped Ly-α absorbers (DLAs) metallicity measurements, which covers the redshift range from 0.09 to 3.9 (Kulkarni et al. 2005), and also matches a previous theoretical estimation (Pei et al. 1995, 1999; Malaney & Chaboyer 1996).

The $\bar{n}_{gas}(z)$ in Equation (13) is the mean number density of the gas, which, for the IGM case, is just the baryon density, $\bar{n}_b(z) = 2 \times 10^{-7}(1+z)^3$ cm^{-3}. For the ISM of galaxies, we use $\bar{n}_{gas}(z) = f_{gas}^{hot} f_{gas}^{cr} \bar{n}_b(z)$, where f_{gas}^{cr} is the fraction of the gas that is present in dense environments of the ISM and satisfies $n_{gas} \gtrsim n_{cr}$ (Suginohara et al. 1999). The value of f_{gas}^{cr} depends on the gas clumping within the ISM of galaxies and the Jeans mass (Fukugita & Kawasaki 1994; Suginohara et al. 1999). We find f_{gas}^{cr} is about 0.1 at $z = 6$ and decreases slowly at higher redshifts in our simulation (Santos et al. 2010). For simplicity, we just take $f_{gas}^{cr} = 0.1$ to be the case for all galaxies independent of the redshift. As is clear, this parameter is the least uncertain of the calculation we present here. Observations with Atacama Large Millimeter/submillimeter Array (ALMA) and other facilities of *Herschel* galaxy samples will eventually narrow down this value.

The fraction of the "hot" gas ($T > 10^3$ K) in halos f_{gas}^{hot} is also included here, since the main contribution of C II emission comes from the gas with $T > 10^3$ K (see Figure 3). We find the fraction is around 0.3 and remains constant from $z = 8$ to 6 in the De Lucia catalog (De Lucia & Blaizot 2007), which is used to derive the C II number density from the simulation in the next subsection. As we are computing the mean intensity expected in a cosmological survey, $\bar{n}_{gas}$ is the number density for galaxies in a large space volume instead of one individual galaxy and thus we can still use $\bar{n}_b$ for the ISM of galaxies.

In Figure 3, we plot an analytical estimate of intensity of C II emission line from the ISM of galaxies as a function of redshift. We select the same pairs of T_k^e and n_e as in the Figure 1. We see that the intensity is practically independent of the electron number density and the temperature when $n_e > 10^2$ cm^{-3} and $T_k^e > 10^3$ K, e.g., the signal is only seen in emission and is essentially proportional to the C II density (see Equation (12)). Even for $n_e = 1$ and 10 cm^{-3} which is less than the n_e^{cr}, we still find a significant intensity for the C II emission from the ISM of galaxies.

In Figure 4, we show the same for carbon in the diffuse IGM. We find the I_ν^{CII} from the IGM is much smaller than that from galaxies, and $I_{CII}^{gal}/I_{CII}^{IGM} \gtrsim 10^4$ for all cases we consider at all redshifts. This is because the C II spin temperature and the C II abundance in the ISM of galaxies are much larger than that in the diffuse IGM. Thus the C II emission from IGM can be safely neglected, and hereafter we will just take into account the C II emission from the ISM of galaxies when discussing intensity fluctuations.

Note the line intensity measurements of individual galaxies are generally described with PDR models using the number density and the UV intensity within the ISM, instead of number density and temperature as we use here (Malhotra et al. 2001). We depart from the PDR modeling approach as we are considering global models that are appropriate for cosmological observations and are not attempting to model the properties of line emission from individual galaxies. It is likely that future work will need to improve our model by making use of a more accurate description of the stellar mass function and the star formation history of each of the galaxies in a large cosmological simulation by performing calculations to determine T_e given the UV intensity field dominated by the massive, bright stars. When making predictions related to the C II intensity power

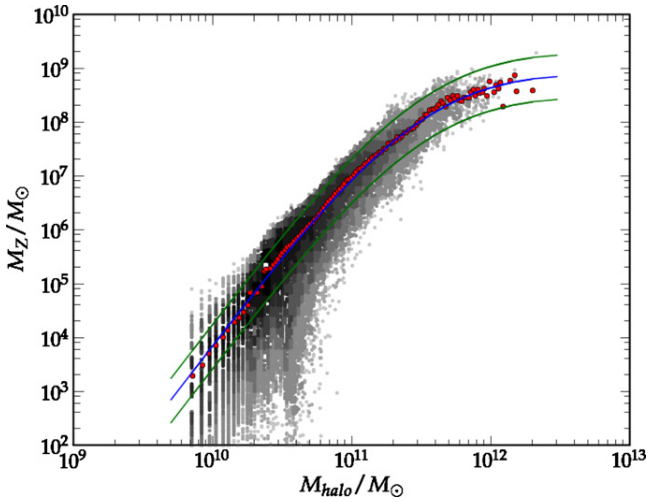

Figure 5. Mass in metals M_Z as a function of the halo mass M at $z = 8$. The solid lines show the mean relation (blue center line) and $\pm 1\sigma$ relation (green lines). The red dots denote the mean value of the scattering (gray region) when binned to 150 logarithmic intervals in halo mass.

(A color version of this figure is available in the online journal.)

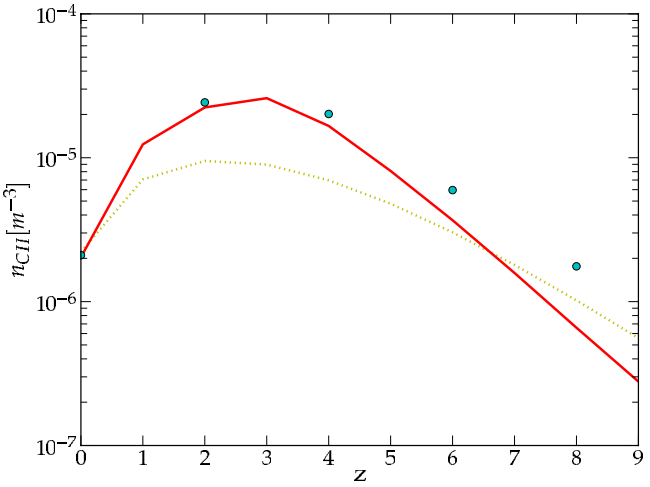

Figure 6. C II proper number density as a function of redshift. The red solid line is derived from our simulation with just hot gas contributing to $L_{\rm C\,II}$, the yellow dotted line is our analytic result, and the blue spots are obtained from the simulation using both the hot gas and the warm gas (10% of the cold gas in the galaxies; see the text for details).

(A color version of this figure is available in the online journal.)

spectrum (Section 4), we take as default values $T_{\rm e} = 1000$ K and $n_{\rm e} = 100$ cm^{-3}. These values are fully consistent with the findings of Malhotra et al. (2001), where they find for 60 normal star-forming galaxies, the values of $T \sim 225$ to 1400 K and $n \sim 10^2$ to 10^4 cm^{-3}.

3.2. Intensity Estimated from Numerical Simulations

Since the evolution of the metallicity and the critical fraction of the gas $f_{\rm gas}^{\rm cr}$ are hard to estimate, the number density of the C II ions $n_{\rm C\,II}$ is not well determined analytically for the case involving C II emission from the ISM of galaxies. So we use results derived from a numerical simulation to check the analytical estimation. To do this we first derive the expected C II mass, $M_{\rm C\,II}$, in a halo with mass M at a given redshift. Then, by integrating over all possible halo masses in a given volume, we estimate the C II mass for that same volume.

To find $M_{\rm C\,II}(z)$ with simulations, we make use of the galaxy catalog from De Lucia & Blaizot (2007). This catalog is obtained by post-processing the Millennium dark matter simulation with semi-analytical models of galaxy formation (Springel et al. 2005), and has the metal content in each of four different components: stars, cold gas, hot gas, and an ejected component. In this calculation we will assume that the C II emission comes from the hot gas component which has a temperature of about 10^5–10^7 K. However, according to Obreschkow et al. (2009a), some of the gas in galactic disks which is considered as cold gas ($T \approx 10^2$–10^3 K) in the De Lucia catalog should actually be warm ($T \approx 10^4$ K) and ionized. So we will also consider the case where 10% of this cold gas from the De Lucia & Blaizot (2007) simulation is recategorized as warm and thus contribute to the C II luminosity.

In Figure 5 we plot the mass in metals M_Z as a function of the halo mass M for the hot gas only case. There is some scatter, specially at the low mass end, but note that if the experimental volume is large enough, we will be observing a large number density of galaxies such that the total M_Z should approach the average. The average relation between M_Z and halo mass M can be parameterized in the form $M_Z(M) = M_0(M/M_c)^b(1 + M/M_c)^{-d}$. At $z = 6$, $z = 7$, and $z = 8$, these parameters take the values $M_0 = 1.1 \times 10^9$, 1.0×10^9, and 1.6×10^9, $M_c = 3.5 \times 10^{11}$, 3.5×10^{11}, and 3.7×10^{11}, $b = 3.6$, 3.4, and 3.4, and $d = 3.25$, 3.1, and 3.6, respectively.

At high ISM temperatures with $T > 100$ K we assume carbon is ionized, so we have $M_{\rm C\,II} = f_\odot^C M_Z$ where $f_\odot^C = 0.21$ is the carbon fraction of the mass in metals in the Sun (Arnett 1996). By taking into account the expected number of halos, we can obtain $n_{\rm C\,II}$ as

$$n_{\rm C\,II}^{\rm sim}(z) = \int_{M_{\rm min}}^{M_{\rm max}} dM \frac{dn}{dM} \frac{M_{\rm C\,II}(M, z)}{m_{\rm c}}, \qquad (14)$$

where m_c is the atomic carbon mass, M is the halo mass and dn/dM is the halo mass function (Sheth & Tormen 1999). The integration is made from $M_{\rm min} = 10^8\ M_\odot\ h^{-1}$ to $M_{\rm max} = 10^{13}\ M_\odot\ h^{-1}$, and $M_{\rm min}$ is the minimum mass of the dark matter halo that can host galaxies. Note that the result is insensitive to the exact value of $M_{\rm max}$ since halos with $M > 10^{13}$ are rare due to the exponential term in the halo mass function. From the previous section we can safely assume that the spin temperature is saturated (e.g., the C II is only seen in emission) so that we now have all the ingredients to calculate the signal using the simulation values.

In Figure 6, we show the number density of the C II ions $n_{\rm C\,II}^{\rm sim}(z)$ using the simulation result. We find our analytic result (black dashed line) is well consistent with that derived from the simulation especially at high redshift. The departure at low redshift in our analytical calculation is reasonable since the hot gas fraction $f_{\rm gas}^{\rm hot}$ should be higher at low redshifts because of the higher SFR.

Assuming that only the hot gas component of De Lucia & Blaizot (2007) contribute to the C II line luminosity, $L_{\rm C\,II}$, our two calculational methods differ by a factor of a few; however, after adding the warm component, the analytical result of the previous section match the numerical values at $z > 6$ where we are especially interested. The difference is again the same for the mean intensity of the C II emission shown in Figure 7. Again, we find that the C II emission saturates when $n_{\rm e} \gtrsim 10^2$ cm^{-3} and $T_{\rm k}^{\rm e} \gtrsim 10^3$ K. For higher values, C II intensity is almost independent of $n_{\rm e}$ and $T_{\rm k}^{\rm e}$.

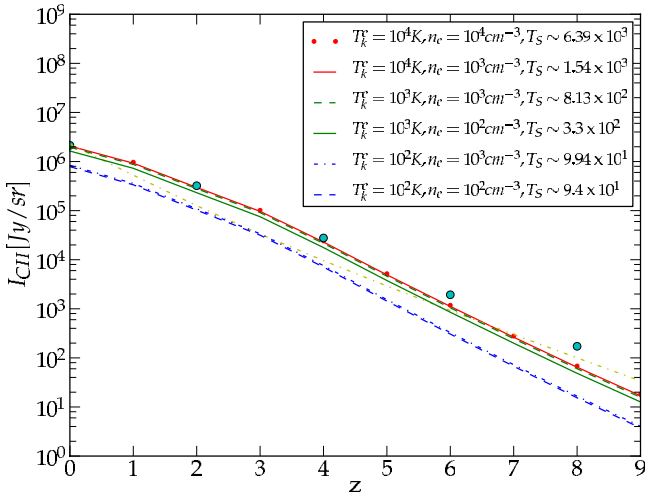

Figure 7. Mean intensity of C II emission line from the outputs obtained from the De Lucia & Blaizot (2007) simulation at several different redshifts. The yellow dotted line is our analytic result, and the blue spots are obtained from the simulation with the hot and warm gas contributing to the $L_{\rm C\,II}$. The yellow line and the blue spot were calculated with $n_{\rm e} = 10^3$ cm^{-3} and $T_{\rm k}^{\rm e} = 10^4$ K. The other lines are derived from the simulation assuming that only the hot gas contributes to the $L_{\rm C\,II}$.

(A color version of this figure is available in the online journal.)

3.3. Intensity Estimated from Observed Scaling Relations

At $z \sim 7$, our calculations involving either analytical or through De Lucia & Blaizot (2007) simulations suggest a mean intensity of about 100–500 Jy sr^{-1} with a preferred value around 200 Jy sr^{-1}. We can use an approach based on observed scaling relations, similar to the approach used by Carilli (2011) to estimate the mean CO(1-0) intensity during reionization, to estimate the mean C II intensity. We begin with the SFR from $z \sim 6$ to 8. While estimates exist in the literature from Lyman break galaxy (LBG) dropouts (Bouwens et al. 2008), such estimates only allow a lower estimate of the SFR as the luminosity functions are limited to the bright-end of galaxies and the slope at the low-end is largely unknown and could be steeper than indicated by existing measurements. An independent estimate of the SFR during reionization involves the use of gamma-ray bursts (GRBs) (Kistler et al. 2009). Together, LBG and GRB SFRs lead to a range of 0.01 to 0.1 $M_\odot$ yr^{-1} Mpc^{-3} at $z \sim 7$.

We can convert this SFR to the C II luminosity of $\sim 3 \times 10^{40}$ to $\sim 3 \times 10^{41}$ erg s^{-1} using the observed scaling relation of De Looze et al. (2011) for low-redshift galaxies when averaging over 100 Mpc^3 volumes. We also get a result consistent with this estimate when converting the SFR to total integrated FIR luminosity and then assuming that 10^{-2} to 10^{-3} of the $L_{\rm FIR}$ appears in C II Stacey et al. (2010), again consistent with $z \sim 2$ redshift galaxy samples. Once again we note that our estimate is uncertain if either the SFR to C II luminosity calibration evolves with redshift or the C II to FIR luminosity ratio evolves with redshift. The above range with an order of magnitude uncertainty in the SFR, and subject to uncertain evolution in observed scaling relations from $z \sim 2$ to 7, corresponds to an intensity of 40–400 Jy sr^{-1} at $z \sim 7$. This range is consistent with our independent estimate, but could be improved in the near future with C II and continuum measurements of high-redshift galaxy samples with ALMA.

4. THE C II INTENSITY POWER SPECTRUM

The C II intensity we have calculated is just the mean intensity, so in this section we will discuss spatial variations in the intensity and consider the power spectrum of the C II emission line as a measure of it. This power spectrum captures the underlying matter distribution and if C II line intensity fluctuations can be mapped at $z > 6$, the line intensity power spectrum can be used to probe the spatial distribution of galaxies present during reionization.

Since the C II emission from the ISM of galaxies will naturally trace the underlying cosmic matter density field, we can write the C II line intensity fluctuations due to galaxy clustering as

$$\delta I_\nu^{\rm C\,II} = \bar{b}_{\rm C\,II} \bar{I}_\nu^{\rm C\,II} \delta(\mathbf{x}), \tag{15}$$

where $\bar{I}_\nu^{\rm C\,II}$ is the mean intensity of the C II emission line from the last section, $\delta(\mathbf{x})$ is the matter over-density at the location $\mathbf{x}$, and $\bar{b}_{\rm C\,II}$ is the average galaxy bias weighted by C II luminosity (see e.g., Gong et al. 2011).

Following Equation (14) and taking into account that the fluctuations in the halo number density will be a biased tracer of the dark matter, the average bias can be written as (Visbal & Loeb 2010)

$$\bar{b}_{\rm C\,II}(z) = \frac{\int_{M_{\rm min}}^{M_{\rm max}} dM \frac{dn}{dM} M_{\rm C\,II}(M) b(z, M)}{\int_{M_{\rm min}}^{M_{\rm max}} dM \frac{dn}{dM} M_{\rm C\,II}(M)}, \tag{16}$$

where $b(z,M)$ is the halo bias and dn/dM is the halo mass function (Sheth & Tormen 1999). We take $M_{\rm min} = 10^8\ M_\odot\ h^{-1}$ and $M_{\rm max} = 10^{13}\ M_\odot\ h^{-1}$. Then we can obtain the clustering power spectrum of the C II emission line

$$P_{\rm C\,II}^{\rm clus}(z, k) = \bar{b}_{\rm C\,II}^2 \bar{I}_{\rm C\,II}^2 P_{\delta\delta}(z, k), \tag{17}$$

where $P_{\delta\delta}(z, k)$ is the matter power spectrum.

The shot-noise power spectrum, due to discretization of the galaxies, is also considered here. It can be written as (Gong et al. 2011)

$$P_{\rm C\,II}^{\rm shot}(z) = \int_{M_{\rm min}}^{M_{\rm max}} dM \frac{dn}{dM} \left(\frac{L_{\rm C\,II}}{4\pi D_{\rm L}^2} y(z) D_{\rm A}^2 \right)^2, \tag{18}$$

where $D_{\rm L}$ is the luminosity distance, $D_{\rm A}$ is the comoving angular diameter distance and $y(z) = d\chi/d\nu = \lambda_{\rm C\,II}(1+z)^2/H(z)$, where χ is the comoving distance, ν is the observed frequency, $\lambda_{\rm C\,II}$ is the rest frame wavelength of the C II line. The $L_{\rm C\,II}$ is the C II luminosity which can be derived from the $I_\nu^{\rm C\,II}$, and we assume $L_{\rm C\,II}(M, z) = B \times M_Z(M, z)\ [L_\odot]$ and finally find $B = 100.63$, 100.36, and 100.17 at $z = 6$, 7, and 8, respectively. The total C II power spectrum is $P_{\rm C\,II}^{\rm tot}(z, k) = P_{\rm C\,II}^{\rm clus}(z, k) + P_{\rm C\,II}^{\rm shot}(z)$.

In Figure 8, as an example we plot the clustering, shot-noise and total power spectrum of the C II emission at $z = 6$, $z = 7$, and $z = 8$. Using the `Halofit` code (Smith et al. 2003), we calculate the nonlinear matter power spectrum. In order to calculate the intensity of the C II line we use $T_{\rm k}^{\rm e} = 10^3$ K and $n_{\rm e} = 10^2$ cm^{-3}, which are a possible representation of the conditions at which C II emits in the galaxies (Malhotra et al. 2001).

For comparison, the C II power spectrum estimated by other works are also shown here. The blue dash-dotted line denotes the $P_{\rm C\,II}^{\rm tot}$ derived from the relation $L_{\rm C\,II}/L_{\rm CO(1-0)} \simeq 10^4$ (De Breuck et al. 2011), and the $L_{\rm CO(1-0)}$ is from the calculation of

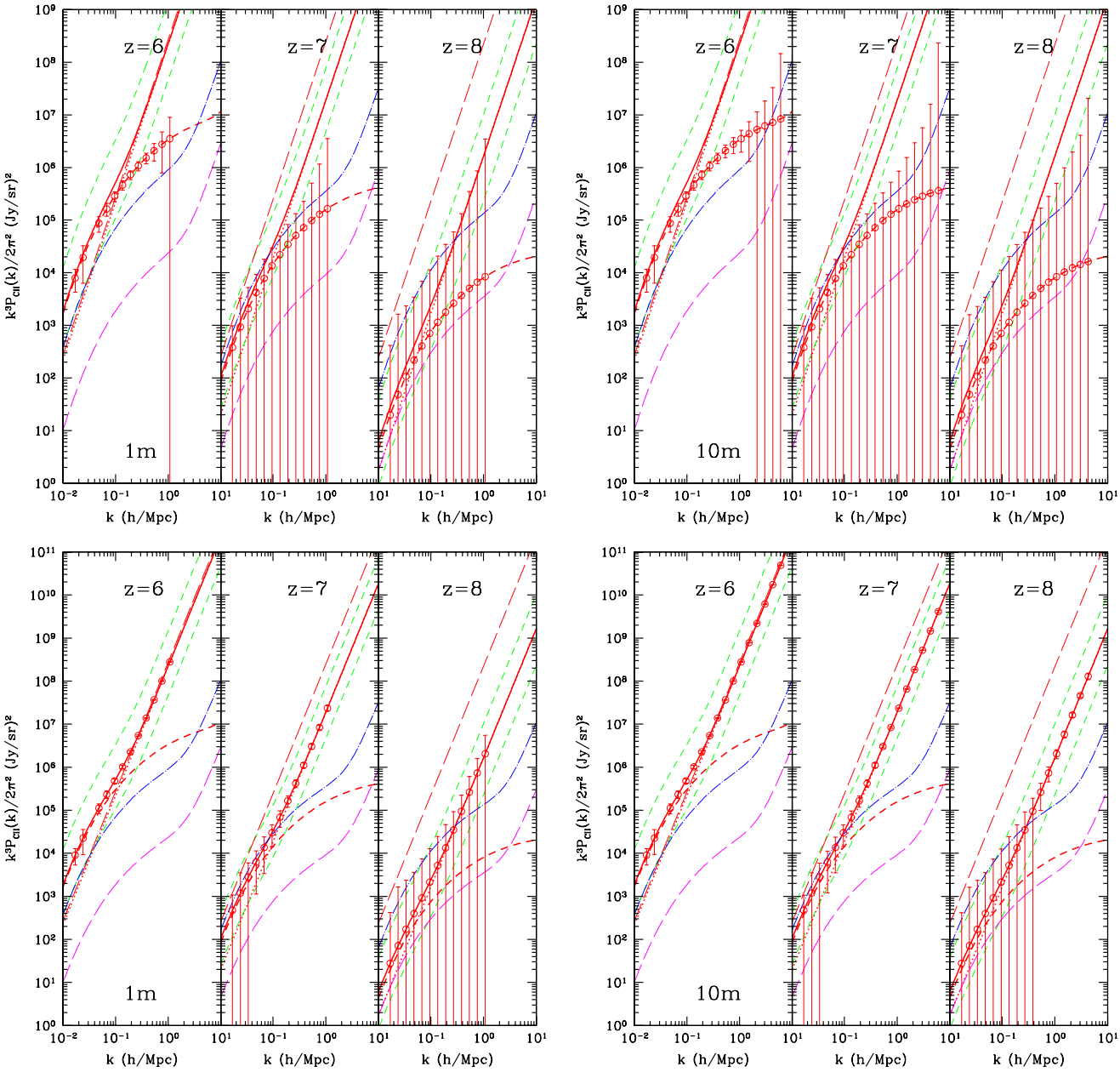

Figure 8. Clustering, shot-noise, and total power spectrum of C II emission line at $z = 6$, $z = 7$, and $z = 8$. The red solid, dashed, and dotted lines denote the C II total, clustering, and shot-noise power spectrum, respectively. The $P_{\rm CII}^{\rm clus}$ is estimated from the simulation with only the hot gas contributing to $L_{\rm CII}$, and we assuming that $T_{\rm k}^{\rm e} = 10^3$ K and $n_{\rm e} = 10^2$ cm^{-3} here. The green dashed lines are the 1σ error of the C II power spectrum which are derived from the 1σ error of M_z–M relation in Figure 5. The error bars and noise power spectrum (red long-dashed line) in the top left and top right panels are estimated with 1 m and 10 m aperture for C II line, respectively. The magenta long dashed line is derived from the C II luminosity estimated by Visbal & Loeb (2010). The blue dash-dotted line is estimated via the relation $L_{\rm CII}/L_{\rm CO(1-0)} \simeq 10^4$. The bottom left and bottom right panels are the same plots but with the error bars on the total power spectrum.

(A color version of this figure is available in the online journal.)

Visbal & Loeb (2010). The magenta long dashed line is the $P_{\rm CII}^{\rm tot}$ evaluated via the C II luminosity derived from Visbal & Loeb (2010).

As expected the C II power spectrum is larger than the CO(1-0) power spectrum calculated in Gong et al. (2011). Note that the CO intensities predicted by Gong et al. (2011) should be corrected by a factor of $1/(1+z)$ which comes from a missing conversion factor between the CO flux obtained from Obreschkow et al. (2009b) and the actual CO(1-0) luminosity. Although this correction further reduces the CO signal, we point out that the model we assumed for the CO luminosity as a function of the halo mass generates a steep dependence at the low mass end. If we use a less steep model at the low end of halo masses ($M < 10^{10}\ M_\odot\ h^{-1}$), where the simulation has a large scatter, such as $L_{\rm CO(1-0)} \propto M_{\rm halo}$, then the CO signal can increase by a factor of a few, partially compensating the $1/(1+z)$ correction.

Comparing the CO(1-0) power spectrum (using the $1/(1+z)$ correction but keeping the luminosity model used in Gong et al. 2011) with the C II one with its density estimated using only the hot gas component from the simulation implies a luminosity relation of $L_{\rm CII}/L_{\rm CO(1-0)} \approx 4 \times 10^4$ when $z \sim 6$ reducing

to below 10^4 when $z \sim 8$. The observational value for this relation as valid for $0 < z < 2$ is $L_{\rm C\,II}/L_{\rm CO(1-0)} = 4100$ as obtained by (Stacey et al. 1991; see also Stacey et al. 2010). However detections of C II emission from star-forming galaxies at $z > 6$ are almost non-existent and there is a strong possibility for an evolution with redshift for this relation. For the handful of galaxies studied, the possibility for evolution is supported by the $L_{\rm C\,II}/L_{\rm CO(1-0)} \simeq 10^4$ value derived for LESS J033229.4-275619 at $z = 4.76$ (De Breuck et al. 2011), which is one of the highest redshift C II detections in a sub-mm-selected, star-formation-dominated galaxy by far, though higher redshift detections are soon expected as part of *Herschel* follow-up campaigns. In Figure 8 we show that this observational ratio (blue dash-dotted line) is consistent with our direct C II prediction from the simulation with the hot gas case (red solid line) around 1σ level (green dashed lines, calculated using the 1σ error of the M_Z–M relation). The noise power spectrum and the error bars are estimated for an assumed (sub-)millimeter survey, which we will discuss in some detail in Section 7.

The luminosity formula in Visbal & Loeb (2010) based on the observed sub-mm and mm emission line ratios (see below for CO version) can also be used to calculate the C II power spectrum as a function of the redshift, but it leads to a result (long dashed magenta line) that is smaller than that estimated by the $L_{\rm C\,II}$–$L_{\rm CO(1-0)}$ relation (blue dash-dotted line) and our C II power spectrum. This is effectively due to a difference in the calibration with CO(1-0) luminosity from M82 and C II luminosity from a sample of low-redshift galaxies (Malhotra et al. 2001). The ratio $L_{\rm C\,II}/L_{\rm CO(1-0)}$ can be as low as 1.6×10^3 for luminous low-redshift galaxies such ultraluminous infrared galaxies (ULIRGs) (Stacey et al. 2010). This sets a lower bound on the $L_{\rm C\,II}$ estimation if we assume that $z > 6$ galaxies are analogous to local ULIRGs.

In Figure 9, we plot the intensity maps of the C II emission at $z = 6$, 7, and 8 using De Lucia & Blaizot (2007) simulations to calculate the C II line intensities to show what the sky looks like at each of these redshifts when mapped with C II. The emission can be traced to individual galaxies. Each of these maps spans 3 deg in each direction and the color bar to the right shows the intensity scaling in units of Jy sr^{-1}. Note the large reduction in the maximum intensity from $z = 6$ to $z = 8$ due to the decrease in the overall abundance of metal content in the ISM of galaxies at high redshifts.

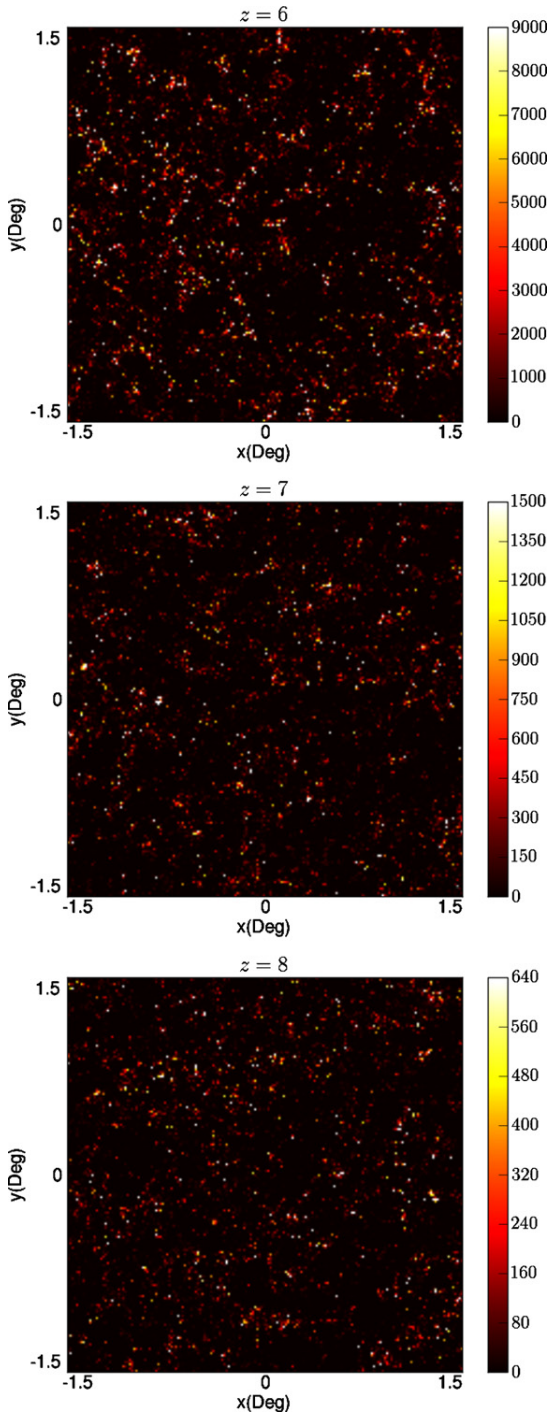

Figure 9. Sky maps of the C II emission at $z = 6$, 7, and 8 from top to bottom, respectively, using De Lucia & Blaizot (2007) simulations to calculate the C II line intensities. Each of these maps spans 3 deg in each direction and the color bar to the right shows the intensity scaling in units of Jy sr^{-1}.

(A color version of this figure is available in the online journal.)

5. CO CONTAMINATION TO C II LINE INTENSITY VARIATIONS

When attempting to observe the $z > 6$ C II line intensity variations, the same observations will become sensitive to variations in the intensity of other emission lines along the line of sight. In particular low-redshift variations will be imprinted by a variety of CO transitions. This foreground line contamination distorts the C II signal and introduces additional corrections to the measured power spectrum, which will not be due to C II alone.

As an example here we will focus on the contamination from the CO lines as we expect those intensities to be of the same order of magnitude as the C II line intensity. Given the difference in the C II rest frequency and those of the CO spectrum for each of the transitions, for a given redshift targeting C II line emission, the frequency of observations and the bandwidth of the observations will correspond to a certain low redshift range in which contaminating CO contribution will be present. Here we calculate the CO power spectrum following Visbal & Loeb (2010) with a CO luminosity formula as the function of the redshift and halo mass (Visbal & Loeb 2010)

$$L_{\rm CO(m-n)} = 6.6 \times 10^6 \left(\frac{R_{\rm line}}{3.8 \times 10^6}\right)\left(\frac{M}{10^{10}\,M_\odot}\right) \times \left(\frac{1+z}{7}\right)^{3/2} \frac{f_*}{\epsilon_{\rm duty}}\, L_\odot, \quad (19)$$

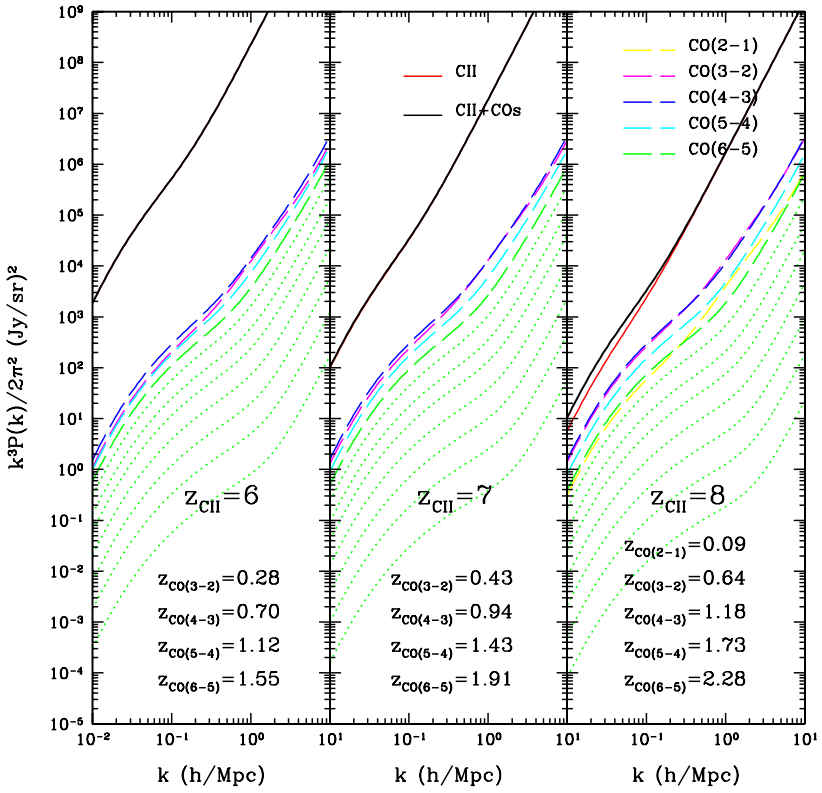

Figure 10. Contaminated C II total power spectrum $P_{\rm CII}^{\rm cont}$ (black solid lines) at $z = 6$, $z = 7$, and $z = 8$. The C II total power spectrum $P_{\rm CII}^{\rm tot}$ is calculated from the hot gas in the simulation (red solid line; note that the $P_{\rm CII}^{\rm cont}$ and $P_{\rm CII}^{\rm tot}$ are almost overlapped at $z = 6$ and $z = 7$ because of the relatively smaller CO line contamination). The other long dashed and green dotted lines are calculated with the $L_{\rm CO(m-n)}$ given in Visbal & Loeb (2010). The green dotted lines from upper to lower are CO(7-6), CO(8-7)... CO(13-12), respectively.

(A color version of this figure is available in the online journal.)

where $R_{\rm line}$ is the ratio of SFR and the luminosity for a emission line, $f_* = 0.1$ is the fraction of gas in a halo that can form stars, and $\epsilon_{\rm duty} = 0.1$ is the duty cycle which is canceled when computing the CO intensity in Visbal & Loeb (2010).

We find this formula has some deviations from the results of our previous simulations (Gong et al. 2011), but it is still a good approximation when considering the halo mass range $10^8 < M < 10^{13}\ M_\odot\ h^{-1}$ in which we perform the calculation. The advantage of this formula is that we can calculate the luminosity of the CO lines at an arbitrary halo mass and redshift. Also, note that we take $L_{\rm CO} \sim M$ instead of $L_{\rm CO} \sim M_{\rm CO}$ when calculating the large-scale structure bias factor of CO emitting galaxies.

We show how the CO contamination for C II intensity measurements from a variety of redshift ranges for $J = 2 - 1$ to $J = 13 - 12$ transitions of CO combine in Figure 10. The frequency of the C II line which is emitted at high redshift, e.g., $z = 7$, will be redshifted to $\nu_0 = \nu_{\rm CII}/(1 + z) \simeq 237$ GHz at present. As shown in Figure 10 the main contamination is from the first five CO lines, CO(2-1) to CO(6-5), and the contamination of the CO lines provide about 2% and 30% to the total intensity power spectrum at $z = 7$ and $z = 8$, respectively, for large scales ($k < 1\ {\rm h}^{-1}$ Mpc). The black solid lines shown in the plot are the contaminated C II total power spectrum for the hot gas case of our simulation, which is the sum of the C II total power spectrum $P_{\rm CII}^{\rm tot}(k)$ (red solid line) and the CO total power spectrum $P_{\rm CO}^{\rm tot}(k)$ (dashed and dotted lines). At small scales ($k > 1\ {\rm h}^{-1}$ Mpc), the shot noise becomes the dominant component in the power spectrum, and we find the shot noise of the C II emission is generally greater than that of the CO emission. We note that this result is likely subject to assumptions on the CO luminosity caused by the CO luminosity we use, since the CO luminosity and especially the CO-luminosity–halo-mass relation. We find a weaker dependence on the halo mass than Visbal & Loeb (2010) in our C II emission model.

The other atomic fine-structure emission lines at longer wavelengths than C II, for example N II at 205 μm and C I with 370 and 609 μm can also contaminate C II emission. The ratios of $L_{\rm CII}/L_{\rm NII}$ and $L_{\rm CII}/L_{\rm CI}$ are about $8 \sim 10$ according to the observations (Malhotra et al. 2001; Oberst et al. 2006), while their luminosities are either comparable or slightly lower than the CO luminosity. A C II study of reionization will also involve cross-correlation studies at low redshifts to untangle various line contaminations. In a future paper we will return to such a study using a numerical setup of a C II experiment of the type we propose here.

6. CROSS-CORRELATION STUDIES BETWEEN C II AND 21 cm OBSERVATIONS

Since the above described CO contamination lines come from different redshifts it is necessary that any C II mapping experiment be considered with another tracer of the same high-redshift universe. In particular, low-frequency radio interferometers now target the $z > 6$ universe by probing the neutral hydrogen distribution via the 21 cm spin-flip transition. Thus, we consider the cross-correlation of the C II line and the 21 cm emission at the same redshift to eliminate the low-redshift contamination,

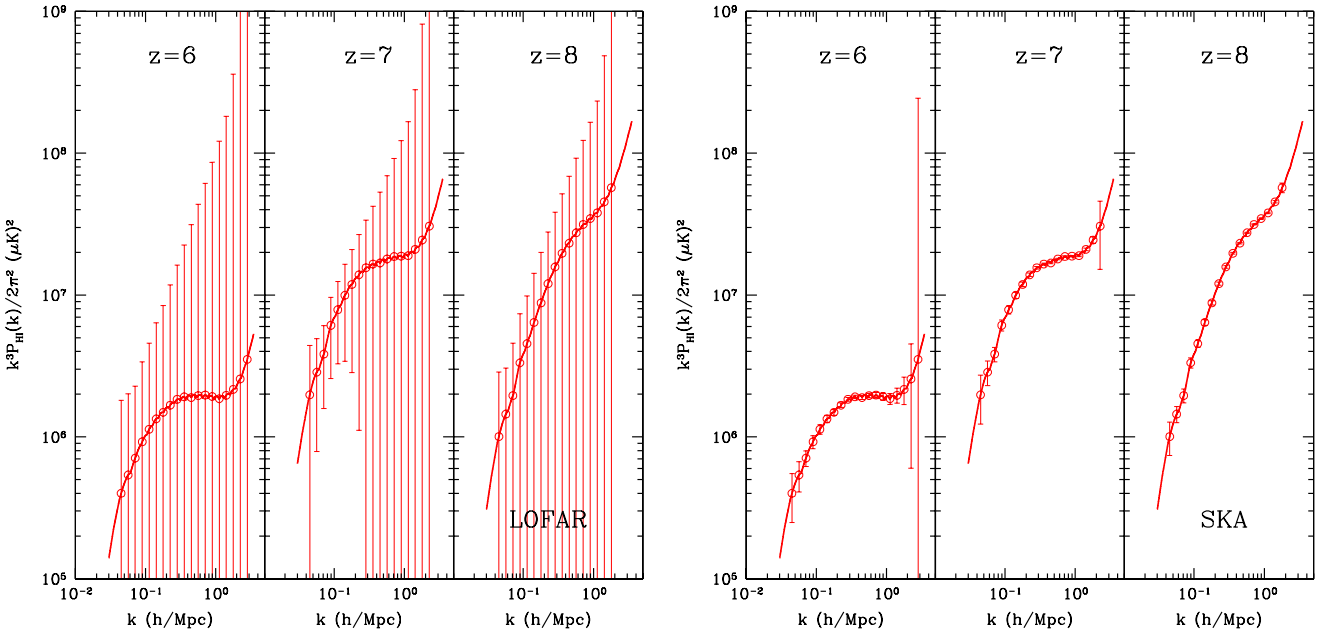

Figure 11. Power spectrum of 21 cm emission at $z = 6$, 7, and 8. The error bars in the left panel are estimated with a setup similar to LOFAR while the ones in the right panel are from a setup similar to SKA.
(A color version of this figure is available in the online journal.)

foregrounds, and to obtain a combined probe of the high-redshift universe with two techniques that complement each other. We expect a strong correlation between the C II and 21 cm lines because they both trace the same underlying density field and such a cross-correlation will be insensitive to CO lines since they are from different redshift which depart far away from each other. There could still be lower order effects, such as due to radio foregrounds. For example, the same galaxies that are bright in CO could also harbor active galactic nuclei (AGNs) that are bright in radio and be present as residual point sources in the 21 cm data. Then the cross-correlation will contain the joint signal related to low-redshift CO emission and the residual point source radio flux from 21 cm observations. The issue of foregrounds and foreground removal for both C II alone and joint C II and 21 cm studies are beyond the scope of this paper. We plan to return to such a topic in an upcoming paper (M. Silva et al. in preparation).

Here we calculate the power spectra for the C II-21 cm correlation using the correlation between the matter density field and the 21 cm brightness temperature obtained from a simulation made using the Simfast21 code (Santos et al. 2010), with the further modifications described in Santos et al. (2011) to take into account the unresolved halos. This code uses a semi-numerical scheme in order to simulate the 21 cm signal from the Reionization Epoch. The simulation generated has boxes with a resolution of 1800^3 cells and a size of $L = 1$ Gpc. With an ionizing efficiency of 6.5 we have obtained the mean neutral fraction of 0.05, 0.35, and 0.62 and an average brightness temperature of 0.63 mK, 6.44 mK, and 14.41 mK for $z = 6$, $z = 7$, and $z = 8$, respectively. The power spectrum of 21 cm emission is also shown in Figure 11, the blue dashed error bars are estimated from the LOFAR and the red solid ones are from the SKA (see Table 2 for experimental parameters).

In Figure 12, we show the cross power spectrum of the C II and 21 cm emission line (red thick lines) and 1σ uncertainty (red thin lines) at $z = 6$, $z = 7$, and $z = 8$. The error bars of the cross power spectrum are obtained by the assumed millimeter spectrometric survey with 1 m and 10m aperture for C II line and LOFAR (left panel) and SKA (right panel) for 21 cm emission. Note that the correlation is negative on large scales (small k) when the correlation between the ionization fraction and the matter density dominates and positive on small scales when the matter density auto-correlation is dominating. This can be seen by looking at the expression for the cross-power spectrum, which to linear order is given by

$$P_{\rm C\,II,HI}(z,k) \propto 4/3(1-\bar{x}_{\rm i})P_{\delta\delta} - \bar{x}_{\rm i}P_{\delta_x\delta}, \qquad (20)$$

where $\bar{x}_{\rm i}$ is the average ionization fraction and $P_{\delta_x\delta}$ is the cross power spectrum of the ionized fraction and the dark matter. To show the cross-correlation illustratively, we also plot the cross-correlation coefficient at $z = 6$, $z = 7$, and $z = 8$ in Figure 13, which is estimated by $r_{\rm C\,II,HI}(k) = P_{\rm C\,II,HI}(k)/\sqrt{P_{\rm C\,II}(k)P_{\rm HI}(k)}$. The typical ionized bubble size can be reflected by the scale that $r_{\rm C\,II,HI}(k)$ rises up from -1 toward zero. As indicated by the $r_{\rm C\,II,HI}(k)$ at $z = 6$, 7, and 8 in the top panels of Figure 13, the ionized bubble size at $z = 6$ is greater than that at $z = 7$ and 8 which is consistent with the current reionization scenario.

7. OUTLINE OF A C II INTENSITY MAPPING EXPERIMENT

We now discuss the requirements on an instrument designed to measure the C II line intensity variations and the power spectrum at $z > 6$. Here we provide a sketch of a possible instrument design including calculated noise requirements based on current technology; a detailed design study will be left to future work as our concept is further developed.

An experiment designed to statistically measure the C II transition at high redshift requires a combination of a large survey area and low spectral resolution; because of this, the use of an interferometer array such as the one suggested in

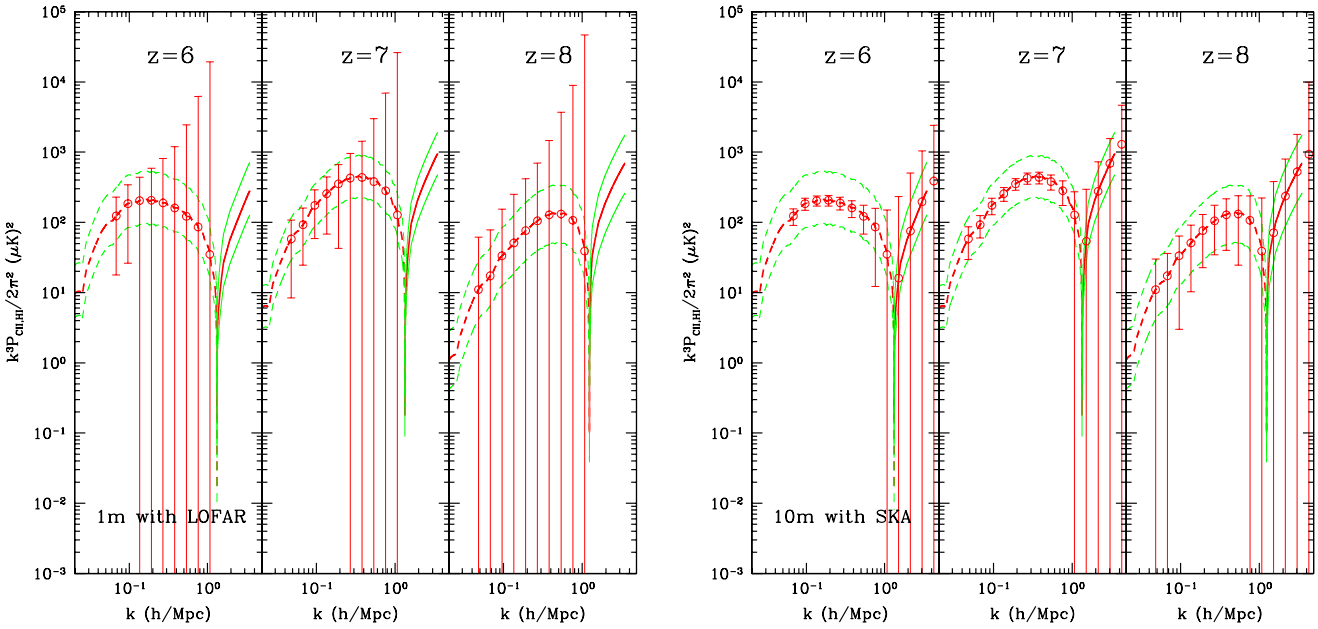

Figure 12. Cross power spectrum of the C II and the 21 cm emission line at $z = 6$, $z = 7$, and $z = 8$. The red dashed lines denote the negative correlations while the red solid lines denote positive correlations. The 1σ errors are also shown in thin red lines. Here we just consider the 21 cm signal from the IGM, since the 21 cm signal from neutral gas in galaxies is about 10^{-4} of the IGM signal (Gong et al. 2011). The error bars in the left panel are estimated using the (sub-) millimeter survey with a 1 m aperture for C II line with a setup similar to LOFAR for 21 cm measurements, while 10 m aperture for C II line with a setup similar to SKA for 21 cm measurements in the right panel.

(A color version of this figure is available in the online journal.)

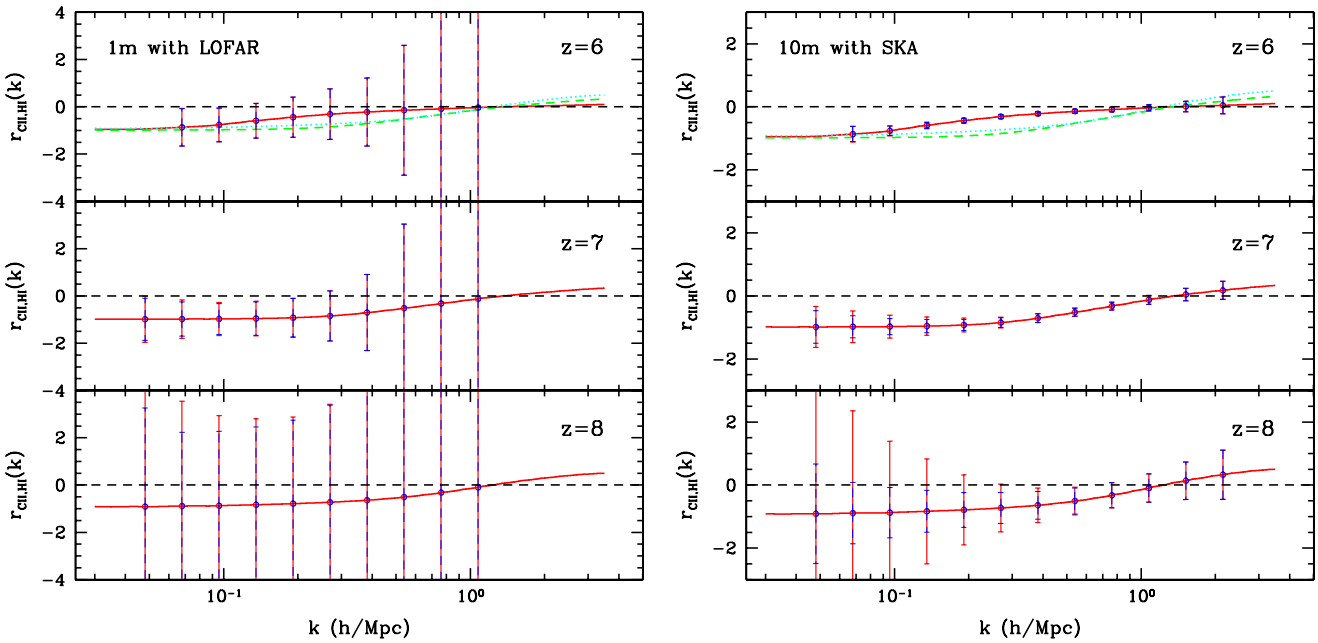

Figure 13. Cross-correlation coefficient of the C II and 21 cm emission for 1 m and 10 m aperture at $z = 6$, $z = 7$, and $z = 8$. The error bars of r are also shown (red solid), and the blue dashed ones are the contribution from the 21 cm emission with the LOFAR (left panel) and with the SKA (right panel). We find the 21 cm noise dominates the errors at $z = 6$ and 7. In the two top panels, the $r_{\rm CII,HI}(k)$ at $z = 7$ (green dashed) and $z = 8$ (cyan dotted) are also shown to denote to show the evolution of the ionized bubble size at these redshifts relative to $z = 6$. As expected, the bubble size is greater at $z = 6$ than that at $z = 7$ and 8.

(A color version of this figure is available in the online journal.)

Gong et al. (2011) for CO seems impractical. Instead we opt for a single aperture scanning experiment employing a diffraction grating and bolometer array in order to provide large throughput. A set of useful equations are outlined in the Appendix to convert from bolometer noise to the noise of the actual intensity power spectrum measurement.

For proper sampling of the C II signal on cosmological scales and cross-correlation with 21 cm experiments, we would require at minimum a survey area of 16 deg^2 and a free spectral range (FSR) of 20 GHz. At a redshift of $z = 7$, a box 4 deg on a side and 20 GHz deep corresponds to a rectangular box with a comoving angular width of 443 Mpc h^{-1} and a depth along the

Table 1
Experimental Parameters for a Possible C II Mapping Instrument

Aperture Diameter (m)	1	3	10
Survey Area (A_S; deg^2)	16	16	16
Total integration time (hours)	4000	4000	4000
Free spectral range (B_ν; GHz)	185−310	185−310	185−310
Freq. resolution (δ_ν; GHz)	0.4	0.4	0.4
Number of bolometers	20,000	20,000	20,000
Number of spectral channels	312	312	312
Number of spatial pixels	64	64	64
Beam size[a] ($\theta_{\rm beam}$; FWHM, arcmin)	4.4	1.5	0.4
Beams per survey area[a]	2.6×10^3	2.3×10^4	2.6×10^5
$\sigma_{\rm pix}$: Noise per detector sensitivity[a] (Jy$\sqrt{\rm s}$/sr)	2.5×10^6	2.5×10^6	2.5×10^6
$t_{\rm pix}^{\rm obs}$: Integration time per beam[a] (hours)	100	11	1.0
$z = 6$ $V_{\rm pix}$ (Mpc h^{-1})^3	217.1	24.1	2.2
$z = 7$ $V_{\rm pix}$ (Mpc h^{-1})^3	332.9	37.0	3.3
$z = 8$ $V_{\rm pix}$ (Mpc h^{-1})^3	481.3	53.5	4.8
$z = 6$ $P_N^{\rm C\,II}$ (Jy sr^{-1})^2 (Mpc h^{-1})^3	5.4×10^9	5.4×10^9	5.3×10^9
$z = 7$ $P_N^{\rm C\,II}$ (Jy sr^{-1})^2 (Mpc h^{-1})^3	4.8×10^9	4.9×10^9	4.8×10^9
$z = 8$ $P_N^{\rm C\,II}$ (Jy sr^{-1})^2 (Mpc h^{-1})^3	4.4×10^9	4.4×10^9	4.3×10^9

Note. [a] Values computed at 238 GHz, corresponding to C II at $z = 7$.

line of sight of 175 Mpc h^{-1}. However, since larger FSRs are easily achieved with diffraction grating architectures and would allow for better measurement of the reionization signal and separation of its foregrounds, the instrumental concept presented here covers the 220 GHz atmospheric window with an FSR of 125 GHz. Concretely, covering from 185 to 310 GHz with a spectral resolution of 0.4 GHz allows measurement of C II in the range $5.1 \leqslant z \leqslant 9.3$ with a smallest redshift interval Δz of 0.01.

The integration time per beam on the sky required to survey a fixed area depends on a number of parameters including the size of the aperture, the number of independent spatial pixels in the spectrometer, and the bandwidth of each spectral element. Changing the survey area or bandwidth will affect the minimum k values probed in the three-dimensional power spectrum as well as the number of modes used in the error calculation. To generate concrete examples in this discussion, we concentrate on calculating the C II power spectrum at $z = 6$, 7, and 8 and assume that we will make use of 20 GHz effective bandwidths at frequencies centered at these redshifts; such effective bands are readily achieved by summing neighboring high resolution spectral bins. At $z = 7$, for example, a 20 GHz bandwidth corresponds to a $\Delta z = 0.62$. Averaging over a larger spectral window to reduce noise will make the cosmological evolution along the observational window non-negligible.

To understand the effect of spatial resolution on this measurement we consider three possible primary aperture sizes of 1, 3, and 10 m; the resulting instrumental parameters are listed in Table 1. These apertures correspond to yield beams of 4.4, 1.5, and 0.4 arcmin and comoving spatial resolutions of 8.3, 2.8, and 0.8 Mpc h^{-1} at an observing frequency of 238 GHz ($z = 7$), respectively. These apertures probe the linear scales ($k < 1.0\,{\rm h}^{-1}$ Mpc) and are well matched to 21 cm experiments. In this experimental setup light from the aperture is coupled to an imaging grating dispersive element illuminating a focal plane of bolometers, similar to the Z-Spec spectrometer but with an imaging axis (Naylor et al. 2003; Bradford et al. 2009).

We assume a fixed spectral resolution of ∼500 km s^{-1} (=0.4 GHz as discussed above) in each of the three cases giving a spatial resolution of 3.5 Mpc h^{-1} and a maximum k mode of $k \approx 0.91$ h^{-1} Mpc. Current technology can allow fabrication of ∼20,000 bolometers in a single focal plane; for the instrument concept we freeze the number of detectors at this value. The spectrometric sensitivity of the grating spectrometer design is estimated using a model of the instrument which includes loading from the CMB, atmosphere and instrument contributions assuming realistic temperatures and emissivities for each.

As an example, using equations in the Appendix, for a 3 m aperture at 238 GHz and an NEP$_{\rm Det} = 1 \times 10^{-18}$ W HZ$^{-1/2}$, a value readily achieved using current detector technology, we find a noise equivalent flux density (NEFD) of 0.42 Jy s$^{1/2}$ per pixel per spectral resolution element. This NEFD can then be converted to the units of Jy s$^{1/2}$/sr used in Table 1 by multiplication by the solid angle of the telescope response. For observations corresponding to $z = 7$, this results in a noise per pixel of 2.5×10^6 Jy s$^{1/2}$/sr.

These noise power spectra based on Table 1 are shown for the 1 and 10 m aperture in Figure 8. The proposed C II experiments involve three different apertures at 1, 3, and 10 m, but all three options make use of the same spectrometer with a total ∼20,000 bolometers that make up 64 individual pixels on the sky. The statistical detection shown in Figure 8 using the instrumental parameters listed in Table 1 can be obtained by noting that the error on each of the binned power spectrum measurements is $\Delta P = (P_N^{\rm C\,II} + P_{\rm C\,II})/\sqrt{N_m}$, where $P_{\rm C\,II}$ is the C II power spectrum, including shot-noise and N_m is the number of k-modes available for each power spectrum measurement.

The noise parameters are such that with an integration time of 4000 hr the C II power spectrum at $z = 6$ is detected with a signal-to-noise ratio, $\mathrm{S/N} = \sqrt{\sum_{\rm bins} \frac{(P(k)}{\Delta P(k))^2}}$, of 12.6, 13.2, and 13.5 for 1, 3, and 10 m aperture cases, respectively. The corresponding values for $z = 7$ are 2.2, 2.2, and 2.3, respectively, while at $z = 8$ the signal-to-noise ratios are less than 1 for all three options.

For the cross-correlation with 21 cm data, we assume that observations will be conducted in overlapping areas on the sky by both the C II and the 21 cm experiment. This is a

Table 2
Sensitivities of LOFAR and SKA 21 cm Experiments at 150 MHz

Instrument	LOFAR	SKA
FoV (deg^2)	25	25
Bandwidth (MHz)	12	12
Freq. resolution (MHz)	0.25	0.25
System temperature (K)	449	369
Maximum baseline (m)	2000	5000
Total integration time (hours)	1000	4000
Total collecting area at 150 MHz (m^2)	2.46×10^4	1.4×10^6
$z=6$ $P_N^{21\,\mathrm{cm}}$ (K^2 $(\mathrm{Mpc\,h^{-1}})^3$)	7.8×10^{-1}	1.0×10^{-3}
$z=7$ $P_N^{21\,\mathrm{cm}}$ (K^2 $(\mathrm{Mpc\,h^{-1}})^3$)	1.0	1.5×10^{-3}
$z=8$ $P_N^{21\,\mathrm{cm}}$ (K^2 $(\mathrm{Mpc\,h^{-1}})^3$)	1.4	2.3×10^{-3}

necessary feature of cross-correlation study leading to some coordination between two experiments. We reduce both data sets to a common, and a lower resolution cube in frequency and count the total number of common modes contributing to a given bin in k space using the same method for noise calculation as in Gong et al. (2011). The error in a given k bin can be written as $\sqrt{(P^2_{\mathrm{CII,H}} + P_{\mathrm{C\,II}}P_{\mathrm{H}})/(2N_m(k))}$, where $N_m(k)$ is the number of modes falling in that bin.

When describing the 21 cm observations we assume sensitivities similar to LOFAR with parameters $A_{\mathrm{tot}} = 2.46 \times 10^4$ m^2 and $T_{\mathrm{sys}} = 449$ K at 150 MHz, bandwidth of 12 MHz, and resolution of 0.25 MHz (see Table 2 for SKA parameters). Here, we further assume that the baseline density distribution for LOFAR and SKA is constant on the u–v plane up to a maximum baseline D_{max}. This is a reasonable approximation for the dense central core of these experiments which is the only configuration we are using for the measurements. The cross-correlation is detected with a signal-to-noise ratio of 3–4 at $z = 6$ and 4–5 at $z = 7$ when any of the three C II options is combined with LOFAR. There is a factor of a 3 to 4 improvement when combined with SKA leading to signal-to-noise ratios of 10, 11, and 12 for the $z = 6$ cross-correlation with 1, 3, and 10 m options, respectively. At $z = 7$, the signal-to-noise ratios are 10, 12, and 13, while at $z = 8$ they are 3, 4, and 5, respectively. While the C II power spectrum cannot be detected at $z = 8$ using any of the three options in Table 1, the cross-correlations can be detected when one of the proposed C II experiments is combined with SKA.

The cross-correlation coefficient between C II and 21 cm (Figure 13) shows a scale that $r_{\mathrm{CII,HI}}(k)$ begins to rise from -1 to 0 due to the size of the ionized bubbles surrounding galaxies during reionization (Equation (20)). This scale captures both the size of the typical ionized bubbles and the mean value of the ionization fraction $\bar{x}_i$. The observational measurement of this rise-up scale is challenging for a first-generation C II experiment involving 1 or 3 m aperture combined with a first-generation 21 cm experiment like LOFAR, but is likely to be feasible with an improved C II experiment combined with SKA.

8. CONCLUSION AND DISCUSSION

In this paper, we have estimated the mean intensity and the spatial intensity power spectrum of the C II emission from galaxies at $z > 6$. We first calculated the C II intensity analytically for both the ISM of galaxies and the diffuse IGM and showed that the C II emission from dense gas in the ISM of galaxies is much stronger than that from the IGM. Then, to check the analytical calculation, we used the hot gas or the hot+warm gas from a simulation to find the C II mass in a halo and further calculated the C II number density and intensity. We found that the two methods are in good agreement especially at high redshifts we are interested in. Next, we computed the C II clustering power spectrum assuming the C II luminosity is proportional to the C II mass, $L_{\mathrm{C\,II}} \sim M_{\mathrm{C\,II}}$. We compared our C II power spectrum with that derived from the $L_{\mathrm{C\,II}}$–$L_{\mathrm{CO(1-0)}}$ relation, and found that they are consistent in the 1σ level. We also explored the contamination of the C II emission by the CO lines at lower redshift, and found the contamination can lead to 2% and 30% enhancement of the C II power spectrum at $z = 7$ and $z = 8$.

To reduce the foreground contamination and to improve our scientific understanding of reionization we propose here a cross-correlation study between the C II and 21 cm emission in the overlapping redshift ranges and the same part of the sky. The cross-correlation exists since they both trace the same matter distribution. At large scales the correlation is due to ionized bubbles surrounding C II bright galaxies while at smaller scales both C II galaxies and ionized bubbles trace the underlying density field. We have outlined three potential C II experiments using 1, 3, and 10 m aperture telescope outfitted with a bolometer array spectrometer with 64 independent spectral pixels. A 1 or 3 m aperture C II experiment is matched to a first-generation 21 cm experiment such as LOFAR while an improved C II experiment can be optimized to match a second-generation 21 cm experiment like SKA. We find that the overall ability to extract details on reionization requires a careful coordination and an optimization of both C II and 21 cm experiments. We have not discussed the issues related to foregrounds, including AGN-dominated radio point sources that dominate the low-frequency observations and dusty galaxies that dominate the high-frequency C II observations and Galactic foregrounds such as dust and synchrotron. In future papers we will return to these topics and also expand our discussion related to the instrumental concept as we improve the existing outline to an actual design.

We thank participants of the Keck Institute for Space Studies' (KISS) Billion Years workshop for helpful discussions. This work was supported by NSF CAREER AST-0645427 and NASA NNX10AD42G at UCI. M.G.S. and M.B.S. acknowledge support from FCT-Portugal under grant PTDC/FIS/100170/2008.

APPENDIX

In this appendix, we summarize a set of key equations necessary to obtain the final noise power spectrum of the intensity fluctuation measurements. We focus here on a single aperture scanning experiment with a bolometer array, but intensity fluctuation measurements can also be pursued with interferometric measurements (especially 21 cm and CO). In the context of 21 cm cross-correlation, we also provide the interferometer noise formula below without a detailed derivation.

Unlike the case of CMB, where intensity fluctuation measurements are two-dimensional on the sky with the noise given in Knox (1995), the C II line intensity fluctuation measurements we pursue here are three-dimensional with information related to the spatial inhomogeneities both in angular and redshift space. For simplicity, we ignore redshift space distortions here and only consider a case where spatial variations are isotropic, thus the three-dimensional power spectrum is directional independent. The line of sight mode $k_\parallel$ and angular/transverse mode $k_\perp$ are

related to each of the k-mode via, $k_\parallel = \mu k$, $k_\perp = \sqrt{k^2 - k_\parallel^2}$, as a function of the angle in Fourier space μ.

The noise power spectrum of intensity fluctuations take the form

$$P_N^{\rm C\,II}(k,\mu) = V_{\rm pix}\frac{\sigma_{\rm pix}^2}{t_{\rm pix}^{\rm obs}} e^{(k_\parallel/k_1)^2+(k_\perp/k_2)^2}, \quad \text{(A1)}$$

where $\sigma_{\rm pix}$ is the noise per detector sensitivity, $t_{\rm pix}^{\rm obs}$ is the integration time per beam/pixel, and $V_{\rm pix}$ is the pixel volume in real space. The exponential factor captures both the spatial (k_2) and radial (k_1) resolution. The spatial resolution is set by the instrumental beam while the resolution along the radial direction are set by the spectral bin δ_ν. These are, respectively, $k_2(z) = 2\pi/(r(z)\theta_{\rm beam})$ and $k_1(z) = H(z)\nu/[c(1+z)\,\delta_\nu]$, where $r(z)$ is the comoving radial distance and $H(z)$ is the Hubble parameter. The former can be obtained from the integral $r(z) = \int_0^z c/H(z)\,dz$. For reference, $k_1 \simeq 0.29(5\,{\rm arcmin}/\theta_{\rm beam})\,({\rm h^{-1}\ Mpc})$ and $k_2 \simeq 0.69(400\,{\rm MHz}/\delta_\nu)\,({\rm h^{-1}\ Mpc})$ at $z = 7$.

The total variance of the power spectrum is then

$$\mathrm{var}[P_{\rm C\,II}(k,\mu)] = \left[P_{\rm C\,II}(k) + P_N^{\rm C\,II}(k,\mu)\right]^2, \quad \text{(A2)}$$

where the first team denotes the usual cosmic variance. In the case where a spherically averaged power spectrum measurement is pursued, one can simply take the minimum variance estimate given the above μ-dependent noise associated with the exponential factor. Assuming $\sigma_{\rm pix}$ is μ-independent, the μ-averaged variance of the power spectrum measurement is then simply (Lidz et al. 2011)

$$\mathrm{var}[\bar{P}_{\rm C\,II}(k)] = \frac{\left[P_{\rm C\,II}(k) + \bar{P}_N^{\rm C\,II}(k)\right]^2}{N_m(k)}, \quad \text{(A3)}$$

where $N_m(k)$ is the number of total modes that leads to the power spectrum measurement at each k and

$$\bar{P}_N^{\rm C\,II}(k) = V_{\rm pix}\frac{\sigma_{\rm pix}^2}{t_{\rm pix}^{\rm obs}}. \quad \text{(A4)}$$

The number of modes at each k for the $P(k)$ measurement is

$$N_m(k) = 2\pi k^2 \Delta k \frac{V_{\rm S}}{(2\pi)^3}, \quad \text{(A5)}$$

where Δk is the Fourier bin size and $(2\pi)^3/V_{\rm S}$ is the resolution in Fourier space. Note that the result is obtained by integrating the positive angular parameter only (i.e., $0 < \mu = \cos(\theta) < 1$, no $k < 0$ case is considered).

The total survey volume is $V_{\rm S} = r(z)^2 y A_{\rm S} B_\nu$, where $A_{\rm S}$ is the survey area (in radians), B_ν is the total bandwidth of the measurement, $y = \lambda(1+z)^2/H(z)$ is the factor to convert the frequency intervals to the comoving distance at the wavelength λ. A useful scaling relation for $V_{\rm S}$ for C II measurements is

$$V_{\rm S}(z) = 3.3\times 10^7 ({\rm Mpc\ h^{-1}})^3 \left(\frac{\lambda}{158\,\mu{\rm m}}\right)\sqrt{\frac{1+z}{8}} \times \left(\frac{A_{\rm S}}{16\,{\rm deg}^2}\right)\left(\frac{B_\nu}{20\,{\rm GHz}}\right), \quad \text{(A6)}$$

where λ is the emission line wavelength in the rest frame.

In $\bar{P}_N^{\rm C\,II}(k)$, the volume surveyed by each pixel is $V_{\rm pix} = r^2 y A_{\rm pix}\delta_\nu$. Here $A_{\rm pix}$ is the spatial area provided by the beam, or an individual pixel depending on the instrument design (in radians). A simple scaling relation for $V_{\rm pix}$ as a function of the redshift z is

$$V_{\rm pix}(z) = 1.1\times 10^3 ({\rm Mpc\ h^{-1}})^3 \left(\frac{\lambda}{158\,\mu{\rm m}}\right)\sqrt{\frac{1+z}{8}} \times \left(\frac{\theta_{\rm beam}}{10\,{\rm arcmin}}\right)^2\left(\frac{\delta_\nu}{400\,{\rm MHz}}\right). \quad \text{(A7)}$$

Bolometer noise formula. To obtain $\sigma_{\rm pix}$, for the C II case with a bolometer array, we make use of a calculation that estimates the noise equivalent power of the background ($\mathrm{NEP_{BG}}$) via the quadrature sum of contributions from Phonon, Johnson, Shot, and Bose noise terms using these loadings and estimates of realistic instrument parameters from existing experiments (e.g., Brevik et al. 2010). Similarly, the total $\mathrm{NEP_{tot}}$ of the instrument is the square root of the quadrature sum of $\mathrm{NEP_{BG}}$ and a detector with $\mathrm{NEP_{Det}} = 1\times 10^{-18}$ W $\mathrm{HZ^{-1/2}}$, a value readily achieved using current detector technology. $\mathrm{NEP_{tot}}$ does not depend on the size of the telescope aperture; to convert this to the corresponding noise equivalent flux density (NEFD) in Jy $\mathrm{s^{1/2}}$ we use

$$\mathrm{NEFD} = \frac{\mathrm{NEP_{tot}}}{\eta_{\rm sys} A\sqrt{2\Delta\nu}\exp(-\eta_{\rm sky})}, \quad \text{(A8)}$$

where A is the area of the telescope aperture. The numerical values obtained are in Table 1.

21 cm interferometer noise formula. When estimating the cross-correlation, for simplicity, we assume that the noise power spectrum amplitude $P_N^{21\,\rm cm}$ is a constant and it takes the form (e.g., Santos et al. 2010)

$$P_N^{21\,\rm cm}(k,\theta) = D_A^2 y(z)\frac{\lambda^4 T_{\rm sys}^2}{A_{\rm tot}^2 t_0 n\,(D_A k\sin(\theta)/2\pi)}, \quad \text{(A9)}$$

where D_A is the comoving angular diameter distance, $A_{\rm tot}$ is the collecting area for one element of the interferometer, t_0 is the total integration time and the function $n()$ captures the baseline density distribution on the plane perpendicular to the line of sight, assuming that it is already rotationally invariant (k is the moduli of the wave mode $\mathbf{k}$ and θ is the angle between $\mathbf{k}$ and the line of sight; Santos et al. 2011; Gong et al. 2011). The values are LOFAR and SKA are tabulated in Table 2.

REFERENCES

Aguirre, A., & Schaye, J. 2005, in IAU Colloq. Proc., Probing Galaxies through Quasar Absorption Lines, ed. P. R. Williams, C.-G. Shu, & B. Menard (Cambridge: Cambridge Univ. Press), 289

Arnett, D. 1996, Supernovae and Nucleosynthesis (Princeton, NJ: Princeton Univ. Press)

Basu, K., Hernandez-Monteagudo, C., & Sunyaev, R. A. 2004, A&A, 416, 447

Bock, J. J., Hristov, V. V., Kawada, M., et al. 1993, ApJ, 410, L115

Boselli, A., Gavazzi, G., Lequeux, J., & Pierini, D. 2002, A&A, 358, 454

Bouwens, R. J., Illingworth, G. D., Franx, M., & Ford, H. 2008, ApJ, 686, 230

Bradford, C. M., Aguirre, J. E., Aikin, R., et al. 2009, ApJ, 705, 112

Brevik, J. A., Aikin, R. W., Amiri, M., et al. 2010, Proc. SPIE, 7741, 41

Carilli, C. L. 2011, ApJ, 730, L30

Crawford, M. K., Genzel, R., Townes, C. H., & Watson, D. M. 1985, ApJ, 291, 755

Dalgarno, A., & McCray, R. 1972, ARA&A, 10, 375

De Breuck, C., Maiolino, R., Caselli, P., et al. 2011, A&A, 530, L8
De Looze, I., Baes, M., Bendo, G. J., Cortese, L., & Fritz, J. 2011, MNRAS, 416, 2712
De Lucia, G., & Blaizot, J. 2007, MNRAS, 375, 2
Field, G. B. 1958, Proc. I. R. E., 46, 240
Fukugita, M., & Kawasaki, M. 1994, MNRAS, 269, 563
Giallongo, E., Cristiani, S., D'Odorico, S., Fontana, A., & Savaglio, S. 1997, Structure and Evolution of the Intergalactic Medium from QSO Absorption Line System, Proc. 13th IAP Astrophys. Colloq. (1–5 July 1997) (Paris: Editions Frontieres), 127
Gong, Y., Cooray, A., Silva, M. B., Santos, M. G., & Lubin, P. 2011, ApJ, 728, L46
Haiman, Z., Abel, T., & Rees, M. 2000, ApJ, 534, 11
Hernandez-Monteagudo, C., Haiman, Z., Jimenez, R., & Verde, L. 2006, arXiv:astro-ph0/612363
Keenan, F. P., Lennon, D. J., Johnson, C. T., & Kingston, A. E. 1986, MNRAS, 220, 571
Kistler, M. D., Yüksel, H., Beacom, J. F., Hopkins, A. M., & Wyithe, J. S. B. 2009, ApJ, 705, L104
Knox, L. 1995, Phys. Rev. D, 52, 4307
Komatsu, E., Smith, K. M., Dunkley, J., et al. 2011, ApJS, 192, 18
Kramer, R. H., Haiman, Z., & Madau, P. 2010, arXiv:1007.3581
Kulkarni, V. P., Fall, S. M., Lauroesch, J. T., et al. 2005, ApJ, 618, 68
Lehner, N., Wakker, B. P., & Savage, B. D. 2004, ApJ, 615, 767
Lidz, A., Furlanetto, S. R., Oh, S. P., et al. 2011, ApJ, 741, 70
Malaney, R. A., & Chaboyer, B. 1996, ApJ, 462, 57
Malhotra, S., Kaufman, M. J., Hollenbach, D., et al. 2001, ApJ, 561, 766
Nagamine, K., Wolfe, A. M., & Hernquist, L. 2006, ApJ, 647, 60
Naylor, B. J., Ade, P. A. R., Bock, J. J., et al. 2003, Proc. SPIE, 4855, 239
Oberst, T. E., Parshley, S. C., Stacey, G. J., et al. 2006, ApJ, 652, L125
Obreschkow, D., Croton, D., De Lucia, G., Khochfar, S., & Rawlings, S. 2009a, ApJ, 698, 1467
Obreschkow, D., Klockner, H.-R., Heywood, I., Levrier, F., & Rawlings, S. 2009b, ApJ, 703, 1890
Osterbrock, D. E. 1989, Astrophysics of Gaseous Nebulae and Active Galactic Nuclei (Mill Valley, CA: Univ. Science Books)
Pei, Y. C., & Fall, S. M. 1995, ApJ, 454, 69
Pei, Y. C., Fall, S. M., & Hauser, M. G. 1999, ApJ, 522, 604
Santos, M. G., Ferramacho, L., Silva, M. B., Amblard, A., & Cooray, A. 2010, MNRAS, 406, 2421
Santos, M. G., Silva, M. B., Pritchard, J. R., Cen, R., & Cooray, A. 2011, A&A, 527, A93
Savaglio, S. 1997, Structure and Evolution of the Intergalactic Medium from QSO Absorption Line System, Proc. 13th IAP Astrophys. Colloq. (1–5 July 1997) (Paris: Editions Frontieres), 73
Sheth, R. K., & Tormen, G. 1999, MNRAS, 308, 119
Smith, R. E., Peacock, J. A., Jenkins, A., et al. 2003, MNRAS, 341, 1311
Spitzer, L. J. 1978, Physical Processes in the Interstellar Medium (New York: Wiley)
Springel, V., White, S. D. M., Jenkins, A., et al. 2005, Nature, 435, 629
Stacey, G. J., Geis, N., Genzel, R., et al. 1991, ApJ, 373, 423
Stacey, G. J., Hailey-Dunsheath, S., Ferkinhoff, C., et al. 2010, ApJ, 724, 957
Suginohara, M., Suginohara, T., & Spergel, N. 1999, ApJ, 512, 547
Tayal, S. S. 2008, A&A, 486, 629
Tielens, A. G. G. M., & Hollenbach, D. 1985, ApJ, 291, 722
Visbal, E., & Loeb, A. 2010, J. Cosmol. Astropart. Phys., JCAP11(2010)016
Walter, F., Riechers, D., Cox, P., et al. 2009, Nature, 457, 699
Wolfire, M. G., Hollenbach, D., McKee, C. F., Tielens, A. G. G. M., & Bakes, E. L. O. 1995, ApJ, 443, 152
Wouthuysen, S. A. 1952, AJ, 57, 31
Wright, E. L., Mather, J. C., Bennett, C. L., et al. 1991, ApJ, 381, 200

A.3 Paper III

THE OH LINE CONTAMINATION OF 21 CM INTENSITY FLUCTUATION MEASUREMENTS FOR Z = 1 âĹij 4

Gong Y., **Silva M. B.**, Chen X., Cooray A., Santos M. G., Bock J., Bradford C. and Zemcov M.

ApJL, 740, 1 (2011)
arXiv:1108.0947

The Astrophysical Journal Letters, 740:L20 (5pp), 2011 October 10 doi:10.1088/2041-8205/740/1/L20

THE OH LINE CONTAMINATION OF 21 cm INTENSITY FLUCTUATION MEASUREMENTS FOR $z = 1$–4

Yan Gong[1], Xuelei Chen[2,3], Marta Silva[4], Asantha Cooray[1], and Mario G. Santos[4]
[1] Department of Physics and Astronomy, University of California, Irvine, CA 92097, USA
[2] National Astronomical Observatories, Chinese Academy of Sciences, Beijing 100012, China
[3] Center of High Energy Physics, Peking University, Beijing 100871, China
[4] CENTRA, Instituto Superior Tecnico, Technical University of Lisbon, Lisboa 1049-001, Portugal
Received 2011 August 4; accepted 2011 September 1; published 2011 September 21

ABSTRACT

The large-scale structure of the universe can be mapped with unresolved intensity fluctuations of the 21 cm line. The power spectrum of the intensity fluctuations has been proposed as a probe of the baryon acoustic oscillations at low to moderate redshifts with interferometric experiments now under consideration. We discuss the contamination to the low-redshift 21 cm intensity power spectrum generated by the 18 cm OH line since the intensity fluctuations of the OH line generated at a slightly higher redshift contribute to the intensity fluctuations observed in an experiment. We assume the OH megamaser luminosity is correlated with the star formation rate and use the simulation to estimate the OH signal and the spatial anisotropies. We also use a semi-analytic simulation to predict the 21 cm power spectrum. At $z = 1$–3, we find that the OH contamination could reach 0.1%–1% of the 21 cm rms fluctuations at the scale of the first peak of the baryon acoustic oscillation. When $z > 3$ the OH signal declines quickly, so that the contamination on the 21 cm becomes negligible at high redshifts.

Key words: cosmology: theory – diffuse radiation

Online-only material: color figures

1. INTRODUCTION

The large-scale structure of the universe can be observed efficiently with the *intensity mapping* technique, where the distribution of the radiation intensity of a particular line emission from large volume cells is observed without attempting to resolve the individual emitters, galaxies, within the volume. This technique is particularly suitable for radio observations, where the angular resolution is relatively low. By observing the radiation at different wavelengths, the emissivity from different redshifts is obtained, thus revealing the three-dimensional matter distribution on large scales. It was first recognized that this method can be applied to the 21 cm line of the neutral hydrogen (Chang et al. 2008; Peterson et al. 2009; Chang et al. 2010) and provides a very powerful tool for precise determination of the equation of state of dark energy by using the baryon acoustic oscillation (BAO) peak of large-scale structure as a standard ruler (Chang et al. 2008; Ansari et al. 2008; Seo et al. 2010). More recently, it has also been proposed that the intensity mapping method be used for molecular and fine-structure lines, such as CO (Gong et al. 2011a; Carilli 2011; Lidz et al. 2011; Visbal & Loeb 2010) and C II (Gong et al. 2011b).

A possible problem with the intensity mapping technique is the contamination by other lines. Unlike the observation of individual sources, where different lines from two different sources overlapping along the line of sight can be separated through high-resolution imaging, in intensity mapping the contamination from a different line at a different redshift cannot be easily separated. For optical (e.g., the Lyα line) and for many of the important radio lines, there are many spectral lines with wavelengths longer than the line being observed, thus emitters at lower redshifts could become contaminants and these could be obstacles in the application of this method. An advantage of the 21 cm line for intensity mapping is that due to its low frequency (1420 MHz), there are few strong lines at a lower redshift that could contaminate the observations.[5]

Nevertheless, the hydroxyl radical (OH) lines of 18 cm wavelength at slightly higher redshifts can potentially contaminate H I 21 cm observations at lower redshifts.[6] The $\lambda = 18$ cm lines of OH correspond to four possible transitions, with frequencies at 1612, 1665, 1667, and 1720 MHz. Strong OH emission is produced by masers, originating typically in high density ($n(H_2) > 10^7$ cm^{-3}) gas near an excitation source, though the exact environment for the masers to happen is still not clear (Lo 2005). The 1665 MHz and 1667 MHz are usually much stronger than the other two lines, and hence are named "main lines." In masers, the 1667 MHz line is the strongest, whose flux is typically about 2–20 times greater than the 1665 MHz line (Randell et al. 1995).

In an intensity mapping observation, the 21 cm autocorrelation power spectrum at a redshift z is observed. However, the OH emission at $1+z' = (1+z)\lambda_{\rm H\,I}/\lambda_{\rm OH}$ would also give rise to brightness temperature fluctuations which cannot be distinguished from the redshifted 21 cm fluctuations in such observations. Thus, for example, the H I 21 cm signal at $z_{\rm H\,I} = 1$, 2, and 3 would be contaminated by the OH 18 cm emission at $z_{\rm OH} = 1.35$, 2.52, and 3.70, respectively. Since the OH fluctuations at redshift z' are uncorrelated with the 21 cm fluctuations at redshift z, the two power spectra would simply add. Although the OH line emission is produced with a different mechanism and depends on the star formation activity, on large scales, we

[5] See, e.g., Thompson et al. (2001, Table 1.1) for a list of important radio spectral lines; the only one below H I frequency is the 327 MHz deuterium line, which is relatively weak due to the low deuterium abundance.
[6] Other lines at $\nu < 10$ GHz listed in the above reference are the CH line at 3.335 GHz, the OH line at 4.766 GHz, the formaldehyde (H_2CO) line at 4.83 GHz, the OH line at 6.035 GHz, the methanol (CH_3OH) line at 6.668 GHz, and the ^{3}He line at 8.665 GHz. These lines should be less significant than the OH 18 cm line and we will not consider them in this work.

still expect the OH intensity fluctuations to trace the total matter densities. Its power spectrum should be proportional to the matter power spectrum at z', with a different bias factor. If not properly accounted for, this may introduce a distortion to the total intensity power spectrum extracted from the 21 cm observations resulting in a shift to the BAO peaks. Given the low-redshift 21 cm BAO experiments are now being developed (e.g., the proposal to conduct wider area surveys with the Green Bank Telescope by building a multi-beam receiver,[7] the Tianlai project in China, and the CHIME project in Canada[8]), it is important to estimate the magnitude of the potential contamination.

For this purpose, we make use of simulations to predict both the 21 cm and the OH intensity power spectra from $z = 1$ to 4. We find that the contamination is generally small and below 1% of the rms fluctuations at $z = 1$–3 with a large uncertainty related to the overall predictions on the OH signal. This Letter is organized as follows. In the next section we present the method of the intensity calculation, and in Section 3 we present our results and discuss the contamination. We will assume a *Wilkinson Microwave Anisotropy Probe* seven-year flat ΛCDM cosmological model (Komatsu et al. 2011).

2. CALCULATION

In order to estimate the 21 cm emission at low redshifts, we make use of the semi-analytic simulations by Obreschkow et al. (2009), which are available as part of the SKA Simulated Skies,[9] and are based on the galaxy catalog derived from the Millennium simulation (De Lucia & Blaizot 2007; Springel et al. 2005). These are the same simulations we have used in Gong et al. (2011a). As the H I mass of each galaxy is assigned using the galaxy properties provided by the semi-analytical modeling of galaxy formation, we will use those neutral hydrogen masses to calculate the 21 cm line intensities.

The calculation of the 21 cm power spectrum is similar to what we have done in Gong et al. (2011a). The 21 cm temperature from galaxies assuming the signal seen in emission is (Santos et al. 2008)

$$\bar{T}_{\rm b}^{\rm G} = c(z)\frac{\rho_{\rm H\,I}}{X_{\rm H}\rho_{\rm b}}\,({\rm mK}), \tag{1}$$

where $X_{\rm H} = 0.74$ is the mean hydrogen mass fraction in the universe, $\rho_{\rm b} = \Omega_{\rm b}\rho_{\rm c}$ is the baryon density, and $\rho_{\rm c}$ is the critical density. The $c(z)$ takes the form as

$$c(z) \approx 23\left(\frac{0.7}{h}\right)\left(\frac{\Omega_{\rm b}h^2}{0.02}\right)\left(\frac{0.15}{\Omega_{\rm m}h^2}\frac{1+z}{10}\right)^{1/2}({\rm mK}). \tag{2}$$

The parameter $c(z)\bar{x}_{\rm H}$ gives the mean brightness temperature of the 21 cm emission, where $\bar{x}_{\rm H}$ is the mean neutral fraction. We assume that the neutral hydrogen is mostly contained within the galaxies after reionization; the mass density $\rho_{\rm H\,I}$ is then given by

$$\rho_{\rm H\,I} = \int_{M_{\rm min}}^{M_{\rm max}} dM\frac{dn}{dM}M_{\rm H\,I}(M), \tag{3}$$

where dn/dM is the mass function, we take $M_{\rm min} = 10^8\,M_\odot\,h^{-1}$ to be the minimum mass for a halo to retain neutral hydrogen (Loeb & Barkana 2001), and $M_{\rm max} = 10^{13}\,M_\odot\,h^{-1}$ is the maximum mass for which the gas has sufficient time to cool and form galaxies (the result is insensitive to this number).

In the above the $M_{\rm H\,I}$ is the neutral hydrogen mass in a halo with mass M. The H I mass is correlated with the halo mass, though with some scatter. Inspired by the shape of the distribution seen in the semi-analytic simulation generated from Obreschkow et al. (2009), we fit a relation of the form

$$M_{\rm H\,I}(M) = A\times\left(1+\frac{M}{c_1}\right)^b\left(1+\frac{M}{c_2}\right)^d. \tag{4}$$

The best-fit values of the parameters A, c_1, c_2, b, and d are given in Table 1.

Table 1
The Best-fit Values of the Parameters in the $M_{\rm H\,I}$–M Relation

	$z = 1$	$z = 2$	$z = 3$
A	2.1×10^8	2.1×10^8	1.7×10^8
c_1	1.0×10^{11}	1.0×10^{11}	1.0×10^{11}
c_2	4.55×10^{11}	5.60×10^{11}	5.0×10^{11}
b	2.65	2.4	2.4
d	−2.64	−2.40	−2.25

Due to the mass resolution limit of the Millennium simulation, for $M < 10^{10}\,M_\odot$, we cannot use the same fitting formula. Instead, we assume $M_{\rm H\,I} = X_{\rm H\,I}^{\rm gal}(\Omega_b/\Omega_m)M$ to estimate the neutral hydrogen mass in halos, where $X_{\rm H\,I}^{\rm gal}$ is the neutral hydrogen mass fraction in the galaxy. We set $X_{\rm H\,I}^{\rm gal} = 0.15$ which is estimated at $M = 10^{10}\,M_\odot$ in the simulation and assume that it does not change when $M < 10^{10}\,M_\odot$. The simulation result and the best-fitting curves at $z = 1$, $z = 2$, and $z = 3$ are shown in the upper panel of Figure 1, which are consistent with the other results (e.g., Marin et al. 2010; Duffy et al. 2011).

We find that the H I energy density parameter $\Omega_{\rm H\,I} = \rho_{\rm H\,I}/\rho_c$ is about 10^{-3} and is insensitive to the redshift (for $z \lesssim 3$) in our calculation, which is consistent with the observational results (e.g., Rao et al. 2006; Lah et al. 2007; Noterdaeme et al. 2009). Finally, we find that the 21 cm mean brightness temperatures are 481, 573, and 544 μK at $z = 1$, 2, and 3, respectively. These values are also consistent with an observation at $z = 0.94$ (Chang et al. 2010) and previous predictions in the literature (Chang et al. 2008).

Assuming that the 21 cm flux from galaxies is proportional to the neutral hydrogen mass $M_{\rm H\,I}$, the 21 cm signal will then follow the underlying dark matter distribution with a bias

$$b_{\rm H\,I}(z) = \frac{\int_{M_{\rm min}}^{M_{\rm max}} dM\frac{dn}{dM}M_{\rm H\,I}b(z,M)}{\rho_{\rm H\,I}}, \tag{5}$$

where $b(z, M)$ is the halo bias (Sheth & Tormen 1999). The 21 cm temperature from galaxies is then $T_{\rm b}^{\rm G}(\mathbf{x}) = \bar{T}_{\rm b}^{\rm G}[1 + b_{\rm H\,I}\delta(\mathbf{x})]$, and the clustering power spectrum is given by $P_{\rm H\,I}^{\rm G}(z,k) = (\bar{T}_{\rm b}^{\rm G})^2 b_{\rm H\,I}^2 P(k,z)$. We use the `Halofit` code (Smith et al. 2003) to calculate the nonlinear matter power spectrum $P(k, z)$. Additionally, there is a shot-noise contribution to the power spectrum due to the discreteness of galaxies,

$$P_{\rm H\,I}^{\rm shot}(z) = \int_{M_{\rm min}}^{M_{\rm max}} dM\frac{dn}{dM}\left[c(z)\frac{M_{\rm H\,I}}{X_{\rm H}\rho_{\rm b}}\right]^2. \tag{6}$$

While the OH molecule is not as abundant as neutral hydrogen, the OH maser is brighter than the 21 cm line intensity

[7] https://science.nrao.edu/facilities/gbt/index
[8] http://www.phas.ubc.ca/chime/
[9] http://s-cubed.physics.ox.ac.uk

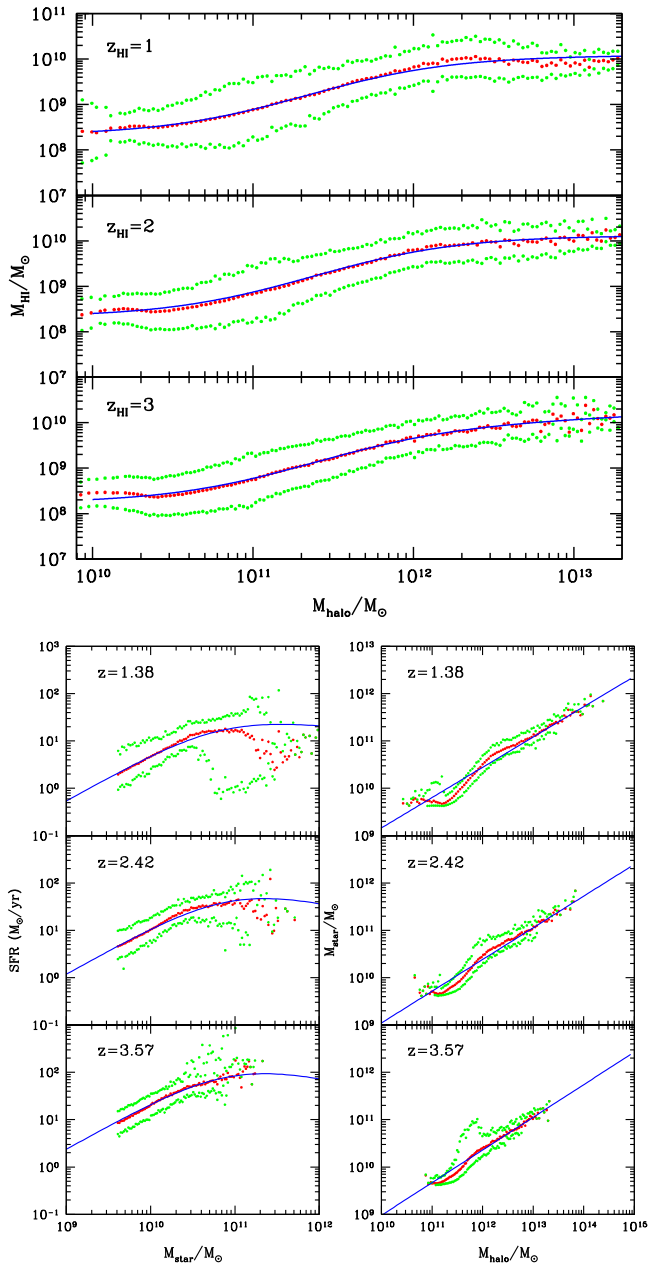

Figure 1. Upper panel: the $M_{\rm H\,I}$–M relation from the simulation at $z = 1$, $z = 2$, and $z = 3$. Lower panel: the SFR vs. the stellar mass $M_\star$ and the stellar mass vs. the halo mass at different redshifts as derived from the galaxy catalog in De Lucia & Blaizot (2007). The red dots are the mean value and the green dots show the 1σ error from the simulation. The best fits are shown in blue solid line.

(A color version of this figure is available in the online journal.)

for the same number density of baryons. It is believed that OH masers are associated with star formation activity. OH megamasers (OHMs) are 10^6 times brighter than typical OH maser sources within the Milky Way and are found in the luminous infrared galaxies (LIRGs with $L_{\rm IR} > 10^{11}\ L_\odot$) and ultra-luminous infrared galaxies (ULIRGs with $L_{\rm IR} > 10^{12}\ L_\odot$) (Darling & Giovanelli 2002). The luminosity of the isotropic OHM luminosity $L_{\rm OH}$ is correlated with the IR luminosity $L_{\rm IR}$.

Previous studies found several relations that take the form as $L_{\rm OH} \propto L_{\rm IR}^{\beta}$, where the power index β is between 1 and 2. For example, Baan (1989) found a relation $L_{\rm OH} \propto L_{\rm IR}^2$ using a sample of 18 OHM galaxies. However, a flatter relation of

Table 2
The Best-fit Values of the Parameters in the SFR–$M_\star$ and $M_\star$–M Relation

	$z = 1.38$	$z = 2.42$	$z = 3.57$
A	5.5×10^{-10}	1.2×10^{-9}	2.4×10^{-9}
c	7×10^{10}	9×10^{10}	9×10^{10}
d	-1.2	-1.4	-1.4
B	5.8×10^2	2.2×10^2	1.2×10^2
e	0.64	0.67	0.69

$L_{\rm OH} \propto L_{\rm IR}^{1.38}$ was obtained by Kandalian (1996) using a sample of 49 OHM galaxies, after correcting for the Malmquist bias. A nearly linear relation between $L_{\rm OH}$ and $L_{\rm IR}$ was derived from the Arecibo Observatory OHM survey (Darling & Giovanelli 2002):

$$\log L_{\rm OH} = (1.2 \pm 0.1)\log L_{\rm IR} - (11.7 \pm 1.2). \quad (7)$$

This relation has also been corrected for the Malmquist bias, and about one hundred OHM galaxies are used in this calibration. We will use this relation in our model.

The $L_{\rm IR}$ is tightly correlated with the star formation rate (SFR) and we adopt a relation of the form (Magnelli et al. 2011; Tekola et al. 2011)

$$L_{\rm IR}\ [L_\odot] = 5.8 \times 10^9\ {\rm SFR}\ [M_\odot\ {\rm yr}^{-1}]. \quad (8)$$

This relation is consistent with other works (e.g., Evans et al. 2006) and has about 30% $\sim$ 40% uncertainty (Kennicutt 1998; Aretxaga et al. 2007).

The SFR is on a statistical sense linearly correlated with the halo mass (Loeb et al. 2005; Shimasaku et al. 2008), with a nearly Gaussian distribution whose central value and variance changes as a function of redshift (Conroy & Wechsler 2009). For the purpose of statistical calculation of OH emissivity, it is sufficient to relate the SFR to the halo mass. We use the galaxy catalog in De Lucia & Blaizot (2007) to derive the SFR and stellar mass relation SFR–$M_\star$ and the star mass and halo mass relation $M_\star$–M as shown in the lower panel of Figure 1. The simulation has outputs at $z = 1.38$, 2.42, and 3.57, which are fairly close to the redshifts $z_{\rm OH} = 1.35$, $z_{\rm OH} = 2.52$, and $z_{\rm OH} = 3.70$, which could contaminate the 21 cm at $z_{\rm H\,I} = 1$, $z_{\rm H\,I} = 2$, and $z_{\rm H\,I} = 3$, respectively.

We fit the SFR–$M_\star$ and $M_\star$–M relations using the form as ${\rm SFR} = A \times M_\star(1 + M_\star/c)^d$ and $M_\star = B \times M^e$, respectively, and the best-fit values for the parameters are listed in Table 2. For $M < 10^{12}\ M_\odot$, analysis from the simulation indicates ${\rm SFR}/M \sim 10^{-11}$–$10^{-10}$ yr^{-1} at $1 < z < 4$, which matches well with previous results (Loeb et al. 2005; Shimasaku et al. 2008; Conroy & Wechsler 2009) in their applicable redshift ranges.

We can now calculate the mean intensity of the OH emission

$$\bar{I}_{\rm OH}(z) = f_{\rm OH} \int_{M_{\rm min}}^{M_{\rm max}} dM \frac{dn}{dM} f_{\rm IR}(M) \frac{L_{\rm OH}(M, z)}{4\pi D_L^2} y(z) D_A^2, \quad (9)$$

where the dn/dM is the halo mass function (Sheth & Tormen 1999), D_L and D_A are the luminosity distance and comoving angular diameter distance, respectively, and $y(z) = d\chi/d\nu = \lambda_{\rm OH}(1+z)^2/H(z)$, where χ is the comoving distance, ν is the observed frequency, and $\lambda_{\rm OH} = 18$ cm is the rest-frame OH wavelength. The $f_{\rm OH}$ is the fraction of the LIRGs together with ULIRGs that host the OHMs. We set $f_{\rm OH}$[10] $= 0.2$ which is

[10] This value also can be as low as 0.05, see Klöckner (2004).

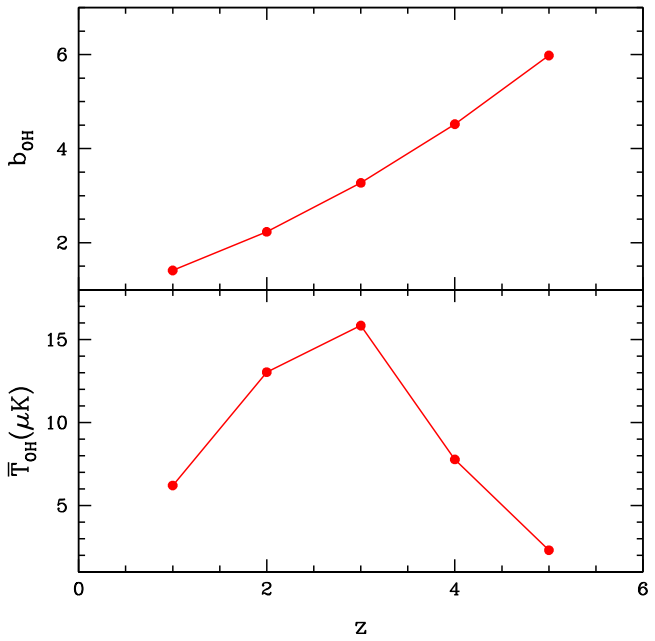

Figure 2. OHM clustering bias and the mean Rayleigh–Jeans temperature at $z = 1, 2, 3, 4$, and 5. We find the OHM signal declines quickly when $z > 3$.
(A color version of this figure is available in the online journal.)

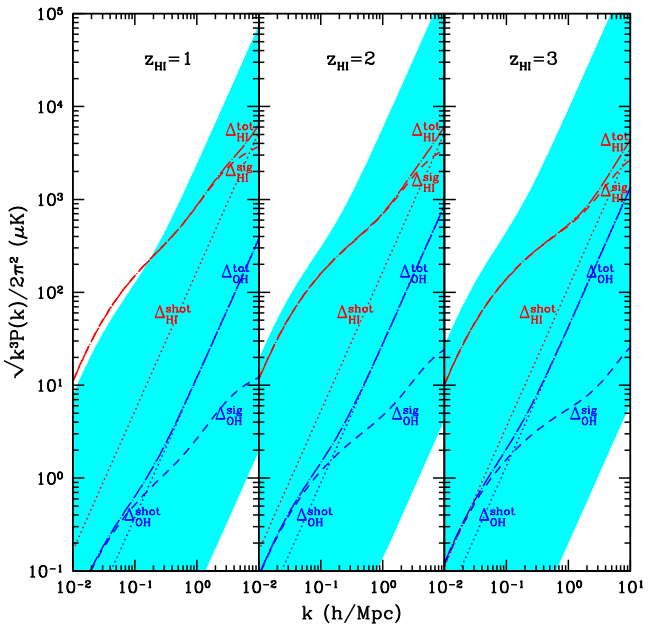

Figure 3. rms intensity fluctuations using the power spectrum of the OHM and 21 cm emission. The blue dashed, dotted, and dash-dotted lines are the OHM signal, shot-noise, and total power spectrum. The uncertainty of the OHM emission is also shown in cyan region, which is estimated using the errors in Equation (7) only. The red lines are 21 cm power spectrum. Because the shot-noise power spectrum is too small compared to the signal power spectrum for 21 cm, the total and the signal power spectra are almost overlapped together.
(A color version of this figure is available in the online journal.)

estimated using the sample in Darling & Giovanelli (2002). This takes account of the fact that the OHMs are caused by the far-IR pumping (53 μm) in the warm dust ($T > 45$ K) which is produced and supported by the star formation in LIRGs or ULIRGs (Lockett & Elitzur 2008). Note that the duty cycle does not appear in our formula, since it is already included in our SFR–M relation.

Here we assume that the megamasers would dominate the contribution, so we can take $M_{\rm min} = 10^{11}\ M_\odot\, h^{-1}$, as the OHMs are hosted in galaxies with molecular gas $M_{\rm H_2} \gtrsim 4 \times 10^9\ M_\odot$ (Burdyuzha & Vikulov 1990; Lagos et al. 2011; Duffy et al. 2011). The $f_{\rm IR}(M)$ is the fraction of the LIRGs and ULIRGs for galaxies hosted by the halos with $M > 10^{11}\ M_\odot\, h^{-1}$, which is estimated from the catalog in De Lucia & Blaizot (2007). We find $f_{\rm IR} \sim 1$ when $M > 1.2 \times 10^{12}\ M_\odot$ and quickly decreases for lower halo masses. After getting the OHM intensity, we can convert it into a mean Rayleigh–Jeans temperature $\bar{T}_{\rm OH}$.

The OHM clustering bias can be calculated in the same way as the H I bias (cf. Equation (5)), except for the weight by $L_{\rm OH}$ instead of $M_{\rm H\,I}$. The OHM bias $b_{\rm OH}$ and $\bar{T}_{\rm OH}$ at $z = 1$, 2, 3, 4, and 5 are shown in Figure 2. We find that the OHM signal declines quickly when $z > 3$.

The OHM power spectrum is given by $P_{\rm OH}(k, z) = \bar{I}_{\rm OH}^2 b_{\rm OH}^2 P(k, z)$, and similar to the H I case, the shot-noise power spectrum is given by

$$P_{\rm OH}^{\rm shot}(z) = f_{\rm OH} \int_{M_{\rm min}}^{M_{\rm max}} dM \frac{dn}{dM} \times f_{\rm IR}(M) \left[\frac{L_{\rm OH}(M, z)}{4\pi D_L^2} y(z) D_A^2\right]^2. \quad (10)$$

3. RESULTS AND DISCUSSION

In Figure 3, we plot the rms fluctuations associated with the power spectrum of the OH and 21 cm emission at different redshifts for comparison. The 21 cm signal is plotted in red, while the OH is in blue. In the case of the 21 cm power spectrum, the shot-noise power is relativity insignificant, as the number of H I galaxies is large.

In the case of the OH power spectrum, the signal power spectrum evolves slowly in this redshift range, because the SFR is higher at high redshifts, so it counteracts the decrease in the matter power spectrum at high redshifts. The contribution of the shot noise is however very significant, especially at small scales (larger k), as the emission is mostly from the rare LIRG and ULIRG populations.

Comparing the 21 cm power to the OH power, we find that on the scale of the first peak of the BAO (about $k = 0.075h\,{\rm Mpc}^{-1}$), the OH rms fluctuations are about 0.03%, 0.07%, and 0.11% of the 21 cm rms fluctuations at $z_{\rm H\,I} = 1$, 2, and 3, respectively. At higher redshifts, while we do not show it here, we found that the 21 cm signal becomes stronger as we approach the epoch of reionization, while the OH power becomes smaller and insignificant compared with the H I signal.

We note that this result depends on the modeling of the H I and OH emission, which still has a lot of uncertainty. The exact conditions for the occurrence of OHMs are not completely understood (Lo 2005), and the actual OH emission from a source of a certain SFR may be quite different from our model prediction. Moreover, the OH emissivity may not even be strongly correlated with the halo mass, though on very large scales we still expect the OH intensity power spectrum to be proportional to the underlying matter power spectrum. The 21 cm power depends on the H I content of the low mass halos, which is also largely uncertain.

Considering variations to our model predictions, we do find that in an extreme case, as shown the upper limit of the cyan

region in Figure 3, the OH could even supersede the 21 cm power spectrum and become the major contribution to the observed temperature fluctuations. Note that we just consider the errors in the $L_{\rm OH}$–$L_{\rm IR}$ relation (Equation (7)) to get the uncertainty (cyan region), which can be greater if the error in the $L_{\rm IR}$–SFR relation (Equation (8)) is included. Also, we note that the two relations above are calibrated at low redshift and are tightly related to the redshift-dependent properties of galaxies, such as the galaxy metallicity. So, the OH intensity may also increase if considering the redshift evolution effect. Of course, in that case, it would be more advantageous to use the OH emission as the tracer instead, though at present this does not seem to be very likely.

As a lot of the OH power comes from shot noise, it may be possible to find a way to remove some of its contribution. For example, we may consider conducting a targeted maser survey on the ULIRGs and LIRGs with sensitive telescopes which have small fields of view, and subtract their contributions to the temperature fluctuation. This could significantly reduce the noise power due to these sources.

One way to identify and estimate the amount of possible contamination is to cross-correlate the temperature fluctuation at the redshift pair (z_1, z_2). We expect that the temperature fluctuations should be uncorrelated, while contamination by OH would give rise to a correlation given by $\langle \delta T(k, z_1) \delta T(k, z_2) \rangle = b_{\rm H_I}(z_2) b_{\rm OH}(z_2) P(k, z_2)$.

Finally, it may also be possible to make use of the multiple lines of OH (including the four lines at 18 cm and the lines with shorter wavelengths) to check for the contamination. If observations for individual OHM sources show that most of them have similar line ratios, then one may construct a template of OHM spectrum and apply it as a matched filter on the observed spectrum to check for possible OH contamination. However, this would not be possible if observations show that the line ratios vary a lot.

We thank Professor Xingwu Zheng for helpful discussion. This work was supported by NSF CAREER AST-0645427 at UCI, by the 973 program No. 2007CB815401, the NSFC grant No. 11073024, and the John Templeton Foundation at NAOC; and M.G.S. and M.B.S. acknowledge support from FCT Portugal under grant PTDC/FIS/100170/2008.

REFERENCES

Ansari, R., Le Goff, J.-M., Magneville, Ch., et al. 2008, arXiv:0807.3614
Aretxaga, I., Hughes, D. H., Coppin, K., et al. 2007, MNRAS, 379, 1571
Baan, W. A. 1989, ApJ, 338, 804
Burdyuzha, V. V., & Vikulov, K. A. 1990, MNRAS, 244, 86
Carilli, C. 2011, ApJ, 730, 30
Chang, T., Pen, U., Bandura, K., & Peterson, J. B. 2010, Nature, 466, 463
Chang, T., Pen, U., Peterson, J. B., & McDonald, P. 2008, Phys. Rev. Lett., 100, 091303
Conroy, C., & Wechsler, R. H. 2009, ApJ, 696, 620
Darling, J., & Giovanelli, R. 2002, AJ, 124, 100
De Lucia, G., & Blaizot, J. 2007, MNRAS, 375, 2
Duffy, A. R., Kay, S. T., Battye, R. A., et al. 2011, arXiv:1107.3720
Evans, A. S., Solomon, P. M., Tacconi, L. J., & Downes, D. 2006, ApJ, 132, 2398
Gong, Y., Cooray, A., Silva, M. B., Santos, M. G., & Lubin, P. 2011a, ApJ, 728, L46
Gong, Y., Cooray, A., Silva, M., et al. 2011b, arXiv:1107.3553
Kandalian, R. A. 1996, Astrophysics, 39, 237
Kennicutt, R. C. 1998, ARA&A, 36, 189
Klöckner, H.-R. 2004, PhD thesis, Univ. Groningen
Komatsu, E., Smith, K. M., Dunkley, J., et al. 2011, ApJS, 192, 18
Lagos, C. P., Baugh, C. M., Lacey, C. G., et al. 2011, arXiv:1105.2294
Lah, P., Chengalur, J. N., Briggs, F. H., et al. 2007, MNRAS, 376, 1357
Lidz, A., Furlanetto, S. R., Oh Peng, S., et al. 2011, arXiv:1104.4800
Lo, K. Y. 2005, ARA&A, 43, 625
Lockett, P., & Elitzur, M. 2008, ApJ, 677, 985
Loeb, A., & Barkana, R. 2001, ARA&A, 39, 19
Loeb, A., Barkana, R., & Hernquist, L. 2005, ApJ, 620, 553
Magnelli, B., Elbaz, D., Chary, R. R., et al. 2011, A&A, 528, A35
Marin, F. A., Gnedin, N. Y., Seo, H., & Vallinotto, A. 2010, ApJ, 718, 972
Noterdaeme, P., Petitjean, P., Ledoux, C., & Srianand, R. 2009, A&A, 505, 1087
Obreschkow, D., Klöckner, H.-R., Heywood, I., Levrier, F., & Rawlings, S. 2009, ApJ, 703, 1890
Peterson, J. B., Aleksan, R., Ansari, R., et al. 2009, arXiv:0902.3091
Randell, J., Field, D., Jones, K. N., Yates, J. A., & Gray, M. D. 1995, A&A, 300, 659
Rao, S. M., Turnshek, D. A., & Nestor, D. B. 2006, ApJ, 636, 610
Santos, M. G., Amblard, A., Pritchard, J., et al. 2008, ApJ, 689, 1
Seo, H. J., Dodelson, S., Marriner, J., et al. 2010, ApJ, 721, 164
Sheth, R. K., & Tormen, G. 1999, MNRAS, 308, 119
Shimasaku, K., Hayashi, M., Motohara, K., et al. 2008, in ASP Conf. Ser. 399, Panoramic Views of Galaxy Formation and Evolution, ed. T. Kodama, T. Yamada, & K. Aoki (San Francisco, CA: ASP), 75
Smith, R. E., Peacock, J. A., Jenkins, A., et al. 2003, MNRAS, 341, 1311
Springel, V., White, S. D. M.m, Jenkins, A., et al. 2005, Nature, 435, 629
Tekola, A. G., Vaisanen, P., & Berlind, A. 2011, arXiv:1101.3495
Thompson, A. R., Moran, J. M., & Swenson, G. W. Jr 2001, Interferometry and Synthesis in Radio Astronomy (New York: Wiley)
Visbal, E., & Loeb, A. 2010, J. Cosmol. Astropart. Phys., JCAP011(2010)016

A.4 Paper IV

Intensity Mapping of Lyman-alpha emission during the Epoch of Reionization

Silva M. B., Santos M. G., Gong Y., Cooray A. and Bock, J.
The Astrophysical Journal, 763:132, 16pp (2013)
arXiv:1205.1493

The Astrophysical Journal, 763:132 (16pp), 2013 February 1 doi:10.1088/0004-637X/763/2/132

INTENSITY MAPPING OF Lyα EMISSION DURING THE EPOCH OF REIONIZATION

Marta B. Silva[1,2], Mario G. Santos[1], Yan Gong[2], Asantha Cooray[2], and James Bock[3,4]
[1] CENTRA, Instituto Superior Técnico, Technical University of Lisbon, Lisboa 1049-001, Portugal
[2] Department of Physics & Astronomy, University of California, Irvine, CA 92697, USA
[3] Department of Physics, Mathematics and Astronomy, California Institute of Technology, Pasadena, CA 91125, USA
[4] Jet Propulsion Laboratory (JPL), National Aeronautics and Space Administration (NASA), Pasadena, CA 91109, USA
Received 2012 May 10; accepted 2012 November 30; published 2013 January 17

ABSTRACT

We calculate the absolute intensity and anisotropies of the Lyα radiation field present during the epoch of reionization. We consider emission from both galaxies and the intergalactic medium (IGM) and take into account the main contributions to the production of Lyα photons: recombinations, collisions, continuum emission from galaxies, and scattering of Ly*n* photons in the IGM. We find that the emission from individual galaxies dominates over the IGM with a total Lyα intensity (times frequency) of about (1.43–3.57) $\times 10^{-8}$ erg s^{-1} cm^{-2} sr^{-1} at a redshift of 7. This intensity level is low, so it is unlikely that the Lyα background during reionization can be established by an experiment aiming at an absolute background light measurement. Instead, we consider Lyα intensity mapping with the aim of measuring the anisotropy power spectrum that has rms fluctuations at the level of 1×10^{-16} [erg s^{-1} cm^{-2} sr^{-1}]^2 at a few Mpc scales. These anisotropies could be measured with a spectrometer at near-IR wavelengths from 0.9 to 1.4 μm with fields in the order of 0.5 to 1 deg^2. We recommend that existing ground-based programs using narrowband filters also pursue intensity fluctuations to study statistics on the spatial distribution of faint Lyα emitters. We also discuss the cross-correlation signal with 21 cm experiments that probe H I in the IGM during reionization. A dedicated sub-orbital or space-based Lyα intensity mapping experiment could provide a viable complimentary approach to probe reionization, when compared to 21 cm experiments, and is likely within experimental reach.

Key words: cosmology: theory – diffuse radiation – large-scale structure of universe

Online-only material: color figures

1. INTRODUCTION

The epoch of reionization (EoR) is a crucial stage in the history of galaxy formation, signaling the birth of the first luminous objects, during which the universe went from completely neutral to almost completely ionized (Barkana & Loeb 2001). This phase has been largely unexplored so far, although current observations suggest that it was reasonably extended (Komatsu et al. 2011; Fan et al. 2006) and a wide variety of observational avenues are being explored to probe it. In particular, the 21 cm line of neutral hydrogen is now understood to be a promising tool to study reionization and to understand the formation and evolution of galaxies during that epoch (see, e.g., Furlanetto et al. 2006). It is also now becoming clear that we need complimentary data in order to obtain extra insight into the sources of reionization. Such complimentary data could also aid in the interpretation of the H I signal by allowing ways to pursue cross-correlations and providing ways to reduce systematics and foregrounds encountered in 21 cm observations.

Recently, intensity mapping of other atomic and molecular lines at high redshifts, in particular CO and C II (Gong et al. 2011, 2012; Lidz et al. 2011; Visbal & Loeb 2010), has been proposed as a probe of reionization. In this work, we study the viability of also using intensity mapping of the Lyα line as an additional probe. For this study, we include several Lyα emission mechanisms involving both individual sources of emission such as galaxies and the emission and scattering associated with the intergalactic medium (IGM).

We consider both the integrated intensity and anisotropies of the Lyα line and suggest the latter as a new probe of reionization. In particular, we suggest that it will be possible to measure the amplitude of the Lyα intensity fluctuations with a narrowband spectrometer either from the ground with a suppression of atmospheric lines or from the orbital/sub-orbital platform.

The Lyα line, corresponding to transitions between the second and first energy level of the hydrogen atom, has a rest wavelength of approximately $\lambda_{\mathrm{Ly}\alpha} = 1216$ Å. The signal present during reionization is observable in near-IR wavelengths today. Existing imaging observations made with narrowband filters on 10 m class telescopes focus on individual galaxy detections and are limited to a handful of narrow atmospheric windows at near-IR wavelengths. Given the strength of the line, it has now been seen in galaxies at $z \approx 6.98$ (Iye et al. 2006), $z \approx 8.2$ (Salvaterra et al. 2009), and $z \approx 8.6$ (Lehnert et al. 2010), reaching well into the EoR.

Deep narrowband surveys of high-redshift Lyα emitters have led to detections of a sufficient number of galaxies at redshifts 5.7, 6.6, 7.0, and 7.7 to allow constraints on the bright end of the Lyα luminosity function (LF) and its redshift evolution (e.g., Ouchi et al. 2008; Ota et al. 2010; Taniguchi et al. 2005; Iye et al. 2006; Shibuya et al. 2012). Observations of the Lyα LF indicate a decrease in the Lyα intensity from redshift 5.7 to 7.0. This would require a strong evolution of the Lyα emitter population, which is not predicted by most recent galaxy evolution models (Ota et al. 2010; Shibuya et al. 2012), or could be explained as the result of an increase in the fraction of IGM neutral hydrogen that would absorb or scatter Lyα photons from the observed galaxies (Haiman et al. 2000; Ota et al. 2008).

The scattering of Lyα photons by neutral hydrogen in the interstellar medium (ISM) and the IGM is expected to disperse the photons in both frequency and direction (Santos 2004). Such scattering could considerably decrease the Lyα intensity

per frequency bin from an individual galaxy, making the detection of most of the high-redshift galaxies impossible with current instruments. Exact calculations related to scattering are a difficult problem to solve analytically, and in simulations the scattering problem requires ray tracing of photons through the neutral medium in a simulation box (Zheng et al. 2010). While scattering makes individual galaxies dimmer, intensity mapping of the Lyα line at high redshifts can be an improvement over the usual experiments that make detections of Lyα emission from point sources and are only sensible to the strongest Lyα emitters. These are likely to be some of the brightest star-forming galaxies; however, any dust that is present in such galaxies, especially during the late stages of reionization, is likely to suppress the Lyα line. An experiment targeting the integrated emission will be able to measure all the sources of Lyα photons in a large region and will be sensitive to the extended, low surface brightness Lyα emission that is now known to generally form around star-forming regions (e.g., Steidel et al. 2011; Zheng et al. 2011). The anisotropy power spectrum of Lyα intensity then would be a probe of the Lyα halos around star-forming galaxies present during reionization. The cross-correlation with the 21 cm data could provide a direct test on the presence of neutral hydrogen in the extended Lyα halo.

The paper is organized as follows: In the next section we estimate the contribution to the Lyα emission from galaxies. In Section 3 we analyze the contributions to the Lyα emission from the IGM. In Section 4 we calculate the intensity of the Lyα signal, as well as its power spectrum, using a modified version of the code SimFast21 (Santos et al. 2010, 2011). In Section 5 we discuss the correlation of Lyα intensity maps with the 21 cm signal. Finally, in Section 6 we comment on the experimental feasibility of measuring the Lyα intensity power spectrum.

2. Lyα EMISSION FROM GALAXIES

The observed Lyα flux is mainly the result of line emission from hydrogen recombinations and collisional excitations in the interstellar clouds or in the IGM powered, respectively, by UV emission or UV and X-ray emission from galaxies. High-energy photons emitted by stars ionize hydrogen that then recombines to emit a rich spectrum of lines including an Lyα photon (Gould & Weinberg 1996; Fernandez & Komatsu 2006). Moreover, the electron ejected during this ionization heats the ISM or the IGM, increasing the probability of Lyα photon emission caused by collisional excitation (Gould & Weinberg 1996; Cantalupo et al. 2008). There is also a small contribution to the Lyα flux originated in the continuum emission from stars between the Lyα line and the Lyman limit (Chuzhoy & Zheng 2007; Barkana & Loeb 2005) plus Lyα from continuum free–free or free–bound emission, as well as two-photon emission during recombinations. This continuum will also make contributions to a given observation from lower redshifts besides the "Lyα" redshift (Cooray et al. 2012), which will confuse the Lyα signal. However, due to the smoothness of that continuum across frequency, we expect it should be possible to remove this contribution, for instance, by fitting a smooth polynomial in frequency for each pixel.

Another source of Lyα emission in the universe is cooling of gas that has suffered infall into a dark matter halo potential well. Several studies show that much of this cooling is made in the form of Lyα emission (Haiman et al. 2000; Fardal et al. 2001; Dijkstra et al. 2006a, 2006b; Dayal et al. 2010; Latif et al. 2011). Cold gas is used by galaxies as fuel to form stars, so there is a relation between the star formation rate (SFR) of a galaxy and the Lyα flux emitted as gas cools in that galaxy.

Since emission of Lyα radiation is closely connected with the star formation, the contribution from the several mechanisms by which Lyα radiation is emitted in galaxies and in the IGM can be related to the SFR of individual galaxies or galaxy samples. In order to calculate the emission of Lyα radiation from the IGM during the EoR, we also need to know the ionized fraction of hydrogen and the temperature of the gas in the IGM. Unfortunately, both these quantities are poorly constrained at $z \geqslant 6$ (Larson et al. 2011; Ouchi et al. 2010; Zahn et al. 2012). Since hydrogen ionization should be a consequence of stellar ionization/X-ray emission, we can in principle estimate it by following the SFR history and making sure that the resulting evolution of hydrogen ionized fraction is consistent with current constraints on the cosmic microwave background optical depth.

In order to obtain the SFR of galaxies at the high redshifts during the EoR, we make use of parameterizations that reproduce a correct reionization history. Our parameterizations are nonlinear in a similar way to the relations found in the Guo et al. (2011) and the De Lucia & Blaizot (2007) galaxy catalogs derived, respectively, from the high-resolution Millennium II (Boylan-Kolchin et al. 2009) and Millennium I (Springel et al. 2005) simulations. Such relations, when available from observations, make an improvement on the models instead of relying purely on theoretical calculations and semi-numerical simulations to predict all of the observations (Mesinger & Furlanetto 2007; Santos et al. 2010).

There are additional sources of radiation contributing to the Lyα emission, such as strong non-local sources of ionizing photons as expected from quasars, which would emit a large amount of energy in X-ray photons that would be able to ionize several neutral atoms, giving origin to a locally strong Lyα emission from recombinations. However, since the number of quasars is very small compared to the number of normal galaxies at the redshifts we are considering, we will neglect their contribution in the following calculations. We encourage future works on Lyα intensity to see if the shape of the power spectrum and other statistics can be used to choose between reionization histories that involve both galaxies and quasars.

In the following sub-sections we discuss in more detail the four processes for Lyα emission from galaxies: recombinations, excitations/relaxations, gas cooling, and photon emission from continuum processes.

2.1. Lyα Emission from Hydrogen Recombinations

Assuming ionizing equilibrium, the number of recombinations in galaxies is expected to match the number of ionizing photons that are absorbed in the galaxy and does not escape into the IGM. Depending on the temperature and density of the gas, a fraction of the radiation due to these recombinations is emitted in the Lyα line.

In the interstellar gas, most of the neutral hydrogen is in dense clouds with column densities greater than 3×10^{18} cm^{-2}. These clouds are optically thick to Lyα radiation, and Lyman photons are scattered in the galaxy several times before escaping into the IGM. Such multiple scatterings increase the probability of absorption. Assuming that these clouds are spherical and that the gas temperature is of the order of 10^4 K, Gould & Weinberg (1996) used atomic physics to study the probability of the Lyα emission per hydrogen recombination. They estimated that a fraction $f_{\rm rec} \approx 66\%$ of the hydrogen recombinations would result in the emission of an Lyα photon and that most of the other

recombinations would result in two-photon emission. These fractions should change with the temperature and the shape of the cloud, but such variations are expected to be small. Other calculations yield fractions between 62% and 68% according to the conditions in the cloud. In this paper we have chosen to use a value of $f_{\rm rec} = 66\%$ since the overall uncertainty on this number is lower than the uncertainty on the number of hydrogen recombinations.

The absorption of Lyα photons by dust is difficult to estimate and changes from galaxy to galaxy. Gould & Weinberg (1996) estimated that for a cloud with a column density $N \sim 10^{19}$ cm^{-2} the dust in the galaxy absorbs a fraction $f_{\rm dust} \approx 4\%$ of the emitted Lyα photons before they reach the galaxy virial radius; however, recent observations of high-redshift galaxies indicate a much higher $f_{\rm dust}$. In this study, we will use a redshift parameterization for the fraction of Lyα photons that are not absorbed by dust $f_{\rm Ly\alpha} = 1 - f_{\rm dust}$ that is double the value predicted by the study made by Hayes et al. (2011):

$$f_{\rm Ly\alpha}(z) = C_{\rm dust} \times 10^{-3}(1+z)^{\xi}, \quad (1)$$

where $C_{\rm dust} = 3.34$ and $\xi = 2.57$. The Hayes et al. (2011) parameterization was made so that $f_{\rm Ly\alpha}$ gives the difference between observed Lyα luminosities and Lyα luminosities scaled from SFRs assuming that the Lyα photons emitted in galaxies are only originated in recombinations. The high-redshift observations used to estimate $f_{\rm Ly\alpha}$ are only of massive stars, while the bulk of Lyα emission is originated in the low-mass stars that cannot be detected by current surveys. According to several studies (Forero-Romero et al. 2011), $f_{\rm Ly\alpha}$ decreases with halo mass, so it is possible that it is being underestimated in Hayes et al. (2011), which is why we decided to use a higher $f_{\rm Ly\alpha}$. Our results can, however, be easily scaled to other $f_{\rm dust}$ evolutions.

The number of Lyα photons emitted in a galaxy per second, $\dot{N}_{\rm Ly\alpha}$, that reach its virial radius is therefore given by

$$\dot{N}_{\rm Ly\alpha} = A_{\rm He} f_{\rm rec} \times f_{\rm Ly\alpha} \times (1 - f_{\rm esc}) \times \dot{N}_{\rm ion}, \quad (2)$$

where $A_{\rm He} = (4 - 4Y_p)/(4 - 3Y_p)$ accounts for the fraction of photons that go into the ionization of helium (Y_p is the mass fraction of helium), $\dot{N}_{\rm ion}$ is the rate of ionizing photons emitted by the stars in the galaxy, and $f_{\rm esc}$ is the fraction of ionizing photons that escape the galaxy into the IGM.

The ionizing photon escape fraction depends on conditions inside each galaxy and is difficult to estimate, especially at high redshifts. The precise determination of its value is one of the major goals of future observations of high-redshift galaxies at $z \gtrsim 7$. This parameter can be measured from deep imaging observations or can be estimated from the equivalent widths of the hydrogen and helium Balmer lines. The ionizing photon escape fraction dependence with the galaxy mass and the SFR, as a function of redshift, has been estimated using simulations that make several assumptions about the intensity of this radiation and its absorption in the ISM. However, for the halo virial mass range, 10^8–10^{13} $M_\odot$, and during the broad redshift range related to the EoR, there are no simulations that cover the full parameter space. Moreover, the limited simulations that exist do not always agree with each other (Gnedin et al. 2008; Wise & Cen 2009; Fernández-Soto et al. 2003; Siana et al. 2007; Haardt & Madau 2012). Razoumov & Sommer-Larsen (2010) computed the escape fraction of UV radiation for the redshift interval $z = 4$ to $z = 10$ and for halos of masses from $10^{7.8}$ to $10^{11.5}$ $M_\odot$ using a high-resolution set of galaxies. Their simulations cover most of the parameter space needed for reionization-related calculations, and their escape fraction parameterization is compatible with most of the current observational results. Thus, we use it for our calculations here.

Table 1
Fits to the Escape Fraction of UV Radiation from Galaxies as a Function of Redshift (based on Razoumov & Sommer-Larsen 2010)

z	α	β	$f_{\rm esc}(M = 10^{10}\,M_\odot)$
10.4	2.78×10^{-2}	0.105	0.732
8.2	1.30×10^{-2}	0.179	0.449
6.7	5.18×10^{-3}	0.244	0.240
5.7	3.42×10^{-3}	0.262	0.240

According to Razoumov & Sommer-Larsen (2010) simulations, the escape fraction of ionizing radiation can be parameterized as

$$f_{\rm esc}(M, z) = \exp[-\alpha(z) M^{\beta(z)}], \quad (3)$$

where M is the halo mass and α and β are functions of redshift (Table 1).

The number of ionizing photons emitted by the stars in a galaxy depends on its SFR, metallicity, and the stellar initial mass function (IMF). Making reasonable assumptions for these quantities, we will now estimate $\dot{N}_{\rm ion}$. Since this UV emission is dominated by massive, short-lived stars, we can assume that the intensity of ionizing photons emitted by a galaxy is proportional to its SFR. In terms of the SFR in one galaxy,

$$\dot{N}_{\rm ion} = Q_{\rm ion} \times {\rm SFR}, \quad (4)$$

where $Q_{\rm ion}$ is the average number of ionizing photons emitted per solar mass of star formation. This can be calculated through

$$Q_{\rm ion} = \frac{\int_{M_{\rm min}}^{M_{\rm max}} \Psi(M) Q_\star(M) t_\star(M) dM}{\int_{M_{\rm min}}^{M_{\rm max}} \Psi(M) M dM}, \quad (5)$$

where $\Psi(M) = K M^{-\alpha}$ is the stellar IMF, K is a constant normalization factor, and α is the slope of the IMF. In our calculation, we used a Salpeter IMF, with $\alpha = 2.35$. $t_\star(M)$ is the star lifetime and $Q_\star(M)$ its number of ionizing photons emitted per unit time. The values of $Q_\star$ and $t_\star$ were calculated with the ionizing fluxes obtained by Schaerer (2002) using realistic models of stellar populations and non-LTE atmospheric models, appropriated for Pop II stars with a $Z_\star = 0.02\,Z_\odot$ metallicity.

Assuming that ionizing photons are only emitted by massive OB stars sets a low mass effective limit for the mass of stars contributing to the UV radiation field of a galaxy. This limit is a necessary condition for the star to be able to produce a significant number of ionizing photons. For the stellar population used for this work we take $M_{\rm min} \approx 7\,M_\odot$ (Schaerer 2002; Shull et al. 2012). The integration upper limit is taken to be $M_{\rm max} = 150\,M_\odot$. In this paper, we calculated $Q_{\rm ion}$ using the parameterization values published in Schaerer (2002). The number of ionizing photons per second emitted by a star as a function of its mass is given by

$$\log_{10}[Q_\star/{\rm s}^{-1}] = 27.80 + 30.68x - 14.80x^2 + 2.5x^3 \text{ for } 7\,M_\odot < M_\star < 150\,M_\odot, \quad (6)$$

where $x = \log_{10}(M_\star/M_\odot)$ and the star's lifetime in years is given by

$$\log_{10}[t_\star/{\rm yr}] = 9.59\text{–}2.79x + 0.63x^2. \quad (7)$$

The use of these parameters results in $Q_{\rm ion} \approx 5.38 \times 10^{60}\, M_{\odot}^{-1}$. Shull et al. (2012) suggest the use of a different model for stellar atmosphere and evolution (R. S. Sutherland & J. M. Shull, unpublished) that yields $Q_{\rm ion} \approx 3.97 \times 10^{60}\, M_{\odot}^{-1}$. This may imply that the stellar emissivity we calculated is an overestimation and that consequently our Lyα flux powered by stellar emission may be overestimated by about 35%. This is comparable to other large uncertainties, such as the ones in the parameters $f_{\rm esc}$ and $f_{\rm dust}$. The Lyα luminosity is calculated assuming that the Lyα photons are emitted at the Lyα rest frequency, $\nu_0 = 2.47 \times 10^{15}$ Hz with an energy of $E_{\rm Ly\alpha} = 1.637 \times 10^{-11}$ erg. To proceed, we will assume that the SFR for a given galaxy is only a function of redshift and the mass of the dark halo associated with that galaxy. The Lyα luminosity due to recombinations in the ISM, $L_{\rm rec}^{\rm GAL}$, can then be parameterized as a function of halo mass and redshift as

$$\begin{aligned} L_{\rm rec}^{\rm GAL}(M,z) &= E_{\rm Ly\alpha}\dot{N}_{\rm Ly\alpha} \\ &\approx 1.55 \times 10^{42}\,[1 - f_{\rm esc}(M,z)]\, f_{\rm Ly\alpha}(z) \\ &\quad \times \frac{\rm SFR(\mathit{M},\mathit{z})}{M_{\odot}\ {\rm yr}^{-1}}\ {\rm erg\ s}^{-1}. \end{aligned} \tag{8}$$

2.2. Lyα Emission from Excitations/Relaxations

The kinetic energy of the electron ejected during the hydrogen ionization heats the gas, and assuming thermal equilibrium, this heat is emitted as radiation. Using atomic physics, Gould & Weinberg (1996) estimated that for a cloud with a hydrogen column density of $\approx 10^{19}$ cm^{-2}, the energy emitted in the form of Lyα photons is about 60% for ionizing photons with energy $E_{\nu_{\rm lim}} < E_{\nu} < 4E_{\nu_{\rm lim}}$ and $\approx$50% for photons with energy $E_{\nu} > 4E_{\nu_{\rm lim}}$, where $E_{\nu_{\rm lim}} = 13.6$ eV is the Rydberg energy. The remaining energy is emitted in other lines.

Using the spectral energy distribution (SED) of galaxies with a metallicity $Z = 0.02\, Z_{\odot}$ from the code of Maraston (2005), we estimated that the average ionizing photon energy is $E_{\nu} = 21.4$ eV and that more than 99% of the photons have an energy lower than $4E_{\nu_{\rm lim}}$. According to the Gould & Weinberg (1996) calculation, the fraction of energy of the UV photon that is emitted as Lyα radiation due to the collisional excitations/relaxations is given by

$$E_{\rm exc}/E_{\nu} \sim 0.08 + 0.1\left(1 - \frac{2\nu_{\rm lim}}{\nu}\right) \sim 0.1. \tag{9}$$

For a cloud with the properties considered here this yields an energy in Lyα per ionizing photon of $E_{\rm exc} \approx 2.14$ eV or 3.43×10^{-12} erg. This results in an average of 0.16 Lyα photons per ionizing photon.

Finally, the Lyα luminosity due to excitations in the ISM, $L_{\rm exc}^{\rm GAL}$, is then

$$\begin{aligned} L_{\rm exc}^{\rm GAL}(M,z) &= [1 - f_{\rm esc}(M,z)] f_{\rm Ly\alpha}(z) A_{\rm He} \dot{N}_{\rm ion} E_{\rm exc} \\ &\approx 4.03 \times 10^{41}\,[1 - f_{\rm esc}(M,z)]\, f_{\rm Ly\alpha}(z) \\ &\quad \times \frac{\rm SFR(\mathit{M},\mathit{z})}{M_{\odot}\ {\rm yr}^{-1}}\ {\rm erg\ s}^{-1}, \end{aligned} \tag{10}$$

where again it is assumed to be a function of the SFR.

2.3. Lyα Emission from Gas Cooling

During the formation of galaxies, gas from the IGM falls into potential wells composed mainly by dark matter that collapsed under its own gravity. The increase in the gas density leads to a high rate of atomic collisions that heat the gas to a high temperature. According to the study of Fardal et al. (2001), most of the gas in potential wells that collapses under its own gravity never reaches its virial temperature, and so a large fraction of the potential energy is released by line emission induced by collisions and excitations from gas with temperatures $T_K < 2 \times 10^4$ K. At this temperature approximately 50% of the energy is emitted in Lyα alone.

From Fardal et al. (2001), we can relate the luminosity at the Lyα frequency due to the cooling in galaxies to their baryonic cold mass, $M_{\rm cool}^{\rm bar}$, using

$$\log_{10}\left(L_{\rm cool}^{\rm GAL}\right) = 1.52 \log_{10}\left(M_{\rm cool}^{\rm bar}\right) + 26.32, \tag{11}$$

where both the luminosity and the mass are in solar units. To relate this baryonic cold mass to a quantity we can use in our models, we used the relation between cold baryonic mass and the halo mass from the galaxies in the Guo et al. (2011) catalog. From the equation above, we can then obtain an expression for the luminosity, which can be fitted by

$$\begin{aligned} L_{\rm cool}^{\rm GAL}(M) &\approx 1.69 \times 10^{35} f_{\rm Ly\alpha}(z) \left(1 + \frac{M}{10^8}\right) \\ &\quad \times \left(1 + \frac{M}{2 \times 10^{10}}\right)^{2.1} \left(1 + \frac{M}{3 \times 10^{11}}\right)^{-3}\ {\rm erg\ s}^{-1}, \end{aligned} \tag{12}$$

with M in units of $M_{\odot}$. The relation between the cold gas mass and the mass of the halo shows very little evolution with redshift during reionization. Thus, we expect the relation in Equation (13) to only depend on redshift due to the redshift evolution of $f_{\rm Ly\alpha}$.

2.4. Contributions from Continuum Emission

Continuum emission can also contribute to the Lyα observations. These include stellar emission, free–free emission, free–bound emission, and two-photon emission. Photons emitted with frequencies close to the Lyn lines should scatter within the ISM and eventually get re-emitted out of the galaxy as Lyα photons. Otherwise, they will escape the ISM before redshifting into one of the Lyn lines and being reabsorbed by a hydrogen atom.

The fraction of photons that scatter in the galaxy can be estimated from the intrinsic width of the Lyα line, which has $\approx$4 Å (Jensen et al. 2013). We calculated the stellar contribution assuming an emission spectrum for stars with a metallicity of $Z_{\star} = 0.02\, Z_{\odot}$ estimated with the code from Maraston (2005) that can be approximated by the emission of a blackbody with a temperature of 6.0×10^4 K for $h\nu < 13.6$ eV. The number of stellar origin Lyα photons per solar mass in star formation obtained with this method is

$$\begin{aligned} Q_{\rm Ly\alpha}^{\rm stellar} &= 4.307 \int_{\nu_{\rm Ly\alpha+2\,\AA}}^{\nu_{\rm Ly\alpha-2\,\AA}} d\nu \frac{\nu^3}{e^{h\nu/K_b T_K} - 1}\, M_{\odot}^{-1} \\ &= 9.92 \times 10^{58}\, M_{\odot}^{-1}. \end{aligned} \tag{13}$$

We note that we are not accounting for the higher opacity at the center of the Lyα line, which should push the photons out of the line center before exiting the star, and so we may be overestimating the stellar Lyα photon emission.

Free–bound emission and free–free emission are, respectively, originated when free electrons scatter off ions with or without being captured. Following the approach of Fernandez & Komatsu (2006), the free–free and free–bound continuum luminosity can be obtained using

$$L_\nu(M, z) = V_{\rm sphere}(M, z)\varepsilon_\nu, \quad (14)$$

where $V_{\rm sphere}$ is the volume of the Strömgren sphere, which can be roughly estimated using the ratio between the number of ionizing photons emitted and the number density of recombinations in the ionized volume,

$$V_{\rm sphere}(M, z) = \frac{Q_{\rm ion}{\rm SFR}(M, z)(1 - f_{\rm esc})}{n_e n_p \alpha_\beta}. \quad (15)$$

Here ε_ν is the total volume emissivity of free–free and free–bound emission, n_p is the number density of protons (ionized atoms), and α_i is the case A or case B recombination coefficient (see Furlanetto et al. 2006).

The volume emissivity estimated by Dopita & Sutherland (2003) is given by

$$\varepsilon_\nu = 4\pi n_e n_p \gamma_c \frac{e^{-h\nu/kT_K}}{T_K^{1/2}}\ {\rm J\ cm^{-3}\ s^{-1}\ Hz^{-1}}, \quad (16)$$

where γ_c is the continuum emission coefficient including free–free and free–bound emission given in SI units by

$$\gamma_c = 5.44 \times 10^{-46}\left[\bar{g}_{\rm ff} + \Sigma_{n=n'}^{\infty}\frac{x_n e^{x_n}}{n} g_{\rm fb}(n)\right]. \quad (17)$$

Here $x_n = Ry/(k_B T_K n^2)$ (k_B is the Boltzmann constant, n is the level to which the electron recombines, and $Ry = 13.6$ eV is the Rydberg unit of energy) and $\bar{g}_{\rm ff} \approx 1.1$–$1.2$ and $g_{\rm fb}(n) \approx 1.05$–$1.09$ are the thermally averaged Gaunt factors for free–free and free–bound emission (Karzas & Latter 1961, values from). The initial level n' is determined by the emitted photon frequency and satisfies the condition $cR_\infty/n'^2 < \nu < cR_\infty/(n'-1)^2$, where $R_\infty = 1.1 \times 10^7\ {\rm m^{-1}}$ is the Rydberg constant.

The continuum luminosity per frequency interval (L_ν) is related to the Lyα luminosity emitted from the galaxies by $L_{\rm cont} = L_\nu \times d\nu(4\,\text{Å}) = f_{{\rm Ly}\alpha} Q_{{\rm Ly}\alpha} E_{{\rm Ly}\alpha}{\rm SFR}(M, z)$, where $Q_{{\rm Ly}\alpha}$ is the number of emitted Lyα photons per solar mass in star formation. We then obtain $Q_{{\rm Ly}\alpha}^{\rm free-free} = 2.13 \times 10^{53}\ M_\odot^{-1}$ for free–free emission and $Q_{{\rm Ly}\alpha}^{\rm free-bound} = 2.22 \times 10^{55}\ M_\odot^{-1}$ for free–bound emission.

During recombination there is also the probability of two-photon emission and although these photons have frequencies below the Lyα frequency there is a small fraction of them of $Q_{{\rm Ly}\alpha}^{\rm 2-photon}$ that are emitted so close to the Lyα line, which are included in the Lyα intrinsic width.

The number of Lyα photons that can be originated due to two-photon emission during recombination is given by

$$Q_{{\rm Ly}\alpha}^{\rm 2-photon} = \int_{\nu_{{\rm Ly}\alpha+2\,\text{Å}}}^{\nu_{{\rm Ly}\alpha}} \frac{2}{\nu_{{\rm Ly}\alpha}} P(\nu/\nu_{{\rm Ly}\alpha}) d\nu, \quad (18)$$

where $P(y)dy$ is the normalized probability that in a two-photon decay one of them is the range $dy = d\nu/\nu_{{\rm Ly}\alpha}$ and $1 - f_{{\rm Ly}\alpha} \approx 1/3$ is the probability of two-photon emission during a hydrogen $n = 2 \rightarrow 1$ transition. The probability of two-photon decay was fitted by Fernandez & Komatsu (2006) using Table 4 of Brown & Mathews (1970) as

$$P(y) = 1.307\text{–}2.627(y - 0.5)^2 + 2.563(y - 0.5)^4 - 51.69(y - 0.5)^6. \quad (19)$$

Finally, the different contributions to the total Lyα luminosity from galaxies due to continuum emission, $L_{\rm cont}^{\rm GAL} = L_{\rm cont}^{\rm stellar} + L_{\rm cont}^{\rm free-free} + L_{\rm cont}^{\rm free-bound} + L_{\rm cont}^{\rm 2-photon}$, are given by

$$L_{\rm cont}^{\rm stellar}(M, z) = f_{{\rm Ly}\alpha} Q_{{\rm Ly}\alpha}^{\rm stellar} E_{{\rm Ly}\alpha}{\rm SFR}(M, z) \approx 5.12 \times 10^{40} f_{{\rm Ly}\alpha} \frac{{\rm SFR}(M, z)}{M_\odot\ {\rm yr^{-1}}}\ {\rm erg\ s^{-1}} \quad (20)$$

for stellar emission,

$$L_{\rm cont}^{\rm free-free}(M, z) = f_{{\rm Ly}\alpha} Q_{{\rm Ly}\alpha}^{\rm stellar} E_{{\rm Ly}\alpha}{\rm SFR}(M, z) \approx 1.10 \times 10^{35} f_{{\rm Ly}\alpha} \frac{{\rm SFR}(M, z)}{M_\odot\ {\rm yr^{-1}}}\ {\rm erg\ s^{-1}} \quad (21)$$

for free–free emission,

$$L_{\rm cont}^{\rm free-bound}(M, z) = f_{{\rm Ly}\alpha} Q_{{\rm Ly}\alpha}^{\rm stellar} E_{{\rm Ly}\alpha}{\rm SFR}(M, z) \approx 1.47 \times 10^{37} f_{{\rm Ly}\alpha} \frac{{\rm SFR}(M, z)}{M_\odot\ {\rm yr^{-1}}}\ {\rm erg\ s^{-1}} \quad (22)$$

for free–bound emission, and

$$L_{\rm cont}^{\rm 2-photon}(M, z) = f_{{\rm Ly}\alpha} Q_{{\rm Ly}\alpha}^{\rm stellar} E_{{\rm Ly}\alpha}{\rm SFR}(M, z) \approx 2.41 \times 10^{38} f_{{\rm Ly}\alpha} \frac{{\rm SFR}(M, z)}{M_\odot\ {\rm yr^{-1}}}\ {\rm erg\ s^{-1}} \quad (23)$$

for two-photon emission.

Note that here we are only considering the part of the continuum emission from galaxies that could contribute to the same "Lyα redshift." There will be a continuum emission spectrum with frequencies below the Lyα line from the mechanisms above that will contribute to the same observation from lower redshifts and will generate a "foreground" to the Lyα signal that needs to be removed. This should be possible due to the smoothness of this background across frequency, in the same manner as foregrounds of the 21 cm signal are removed (e.g., Wang et al. 2006).

2.5. Modeling the Relation between Star Formation Rate and Halo Mass

Simulations of galaxy formation and observations indicate that the star formation of a halo increases strongly for small halo masses, but at high halo masses ($M \gtrsim 10^{11}\ M_\odot$) it becomes almost constant (Conroy & Wechsler 2009; Popesso et al. 2012).

In order to better estimate and constrain the SFR of a halo, we used three nonlinear SFR versus halo mass parameterizations that are in good agreement with different observational constraints. In *Sim1* we adjusted the SFR to reproduce a reasonable reionization history and an Lyα LF evolution compatible with different observational constraints, and in *Sim2* we adjusted the SFR versus halo mass relation to the parameterizations from the Guo et al. (2011) galaxy catalog (low halo masses) and the De Lucia & Blaizot (2007) galaxy catalog (high halo masses). *Sim2* results in an early reionization history with an optical depth to

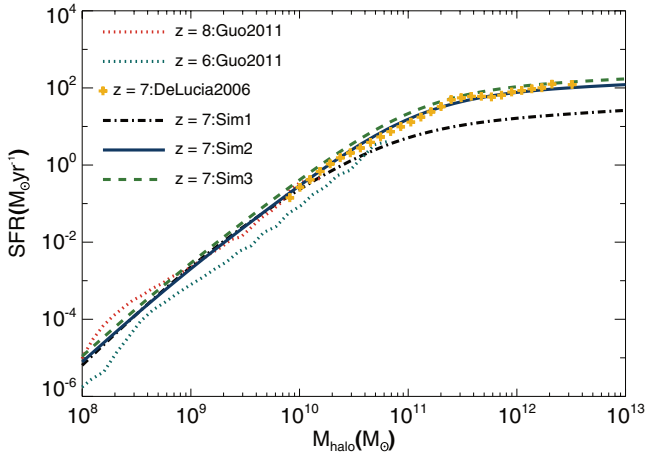

Figure 1. Star formation rate vs. halo mass. The dotted lines show the relations taken from the Guo et al. (2011) catalog for low halo masses at $z = 6$ (bottom dotted line) and $z = 8$ (upper dotted line); the yellow crosses show the relation taken from the DeLucia catalog for high halo masses at $z = 7$. The dash-dotted, solid, and dashed lines show the parameterizations used in simulations *Sim1*, *Sim2*, and *Sim3*, respectively, for $z = 7$.

(A color version of this figure is available in the online journal.)

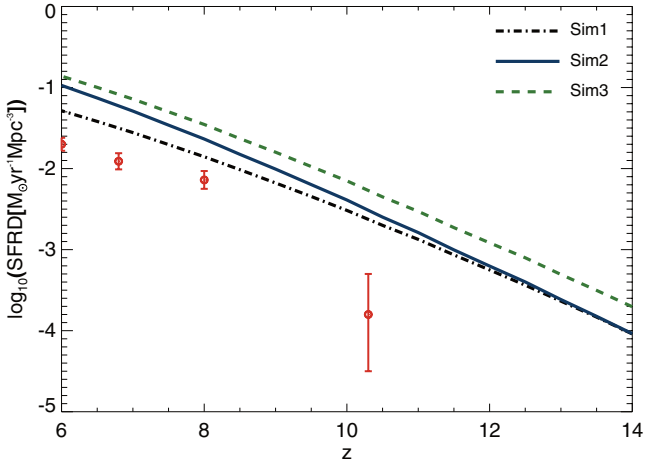

Figure 2. Star formation rate density evolution as a function of redshift. The blue solid line, the green dashed line, and the black dash-dotted line were obtained from simulations made using the SimFast21 code (for information about the code see Section 4 and Santos et al. 2010) and the SFR vs. halo mass relations from Equations (24)–(26). The red dots are observational constraints derived from the UV luminosities corrected for dust extinction from Bouwens et al. (2012b). Please note that these observational values correspond to high-mass galaxies, while our results integrate over the halo-mass function starting at $\sim 10^8$ solar masses (which at redshift 7 corresponds to star formation rates of $6.41 \times 10^{-5}\ M_\odot\ \mathrm{s}^{-1}$ for *Sim1*, $7.83 \times 10^{-6}\ M_\odot\ \mathrm{s}^{-1}$ for *Sim2*, and $1.1 \times 10^{-5}\ M_\odot\ \mathrm{s}^{-1}$ for *Sim3*), so our star formation rate densities are expected to be higher.

(A color version of this figure is available in the online journal.)

reionization compatible with the low bound of the current observational constraints. Finally, *Sim3* has the same halo mass dependence as *Sim2* but evolves with redshift in a similar way to the De Lucia & Blaizot (2007) and Guo et al. (2011) galaxy catalogs.

We parameterized the relations between the SFR and halo mass as

$$\frac{\mathrm{SFR}(M,z)}{M_\odot/\mathrm{yr}} = (2.8\times10^{-28})M^a\left(1+\frac{M}{c_1}\right)^b\left(1+\frac{M}{c_2}\right)^d, \quad (24)$$

where $a = 2.8$, $b = -0.94$, $d = -1.7$, $c_1 = 1 \times 10^9\ M_\odot$, and $c_2 = 7 \times 10^{10}\ M_\odot$ for *Sim1*;

$$\frac{\mathrm{SFR}(M,z)}{M_\odot/\mathrm{yr}} = 1.6\times10^{-26}M^a\left(1+\frac{M}{c_1}\right)^b \times\left(1+\frac{M}{c_2}\right)^d\left(1+\frac{M}{c_3}\right)^e, \quad (25)$$

where $a = 2.59$, $b = -0.62$, $d = 0.4$, $e = -2.25$, $c_1 = 8 \times 10^8\ M_\odot$, $c_2 = 7 \times 10^9\ M_\odot$, and $c_3 = 1 \times 10^{11}\ M_\odot$ for *Sim2*; and

$$\frac{\mathrm{SFR}(M,z)}{M_\odot/\mathrm{yr}} = 2.25\times10^{-26}\,(1+0.075\times(z-7))\,M^a \times\left(1+\frac{M}{c_1}\right)^b\left(1+\frac{M}{c_2}\right)^d\left(1+\frac{M}{c_3}\right)^e, \quad (26)$$

where $a = 2.59$, $b = -0.62$, $d = 0.4$, $e = -2.25$, $c_1 = 8 \times 10^8\ M_\odot$, $c_2 = 7 \times 10^9\ M_\odot$, and $c_3 = 1 \times 10^{11}\ M_\odot$ for *Sim3*. Figure 1 shows these relations.

In Figure 2, the strong decline in the observational SFR density (SFRD) from $z \approx 8$ to $z \approx 10$, imposed by the observational point at $z = 10.3$, was obtained with the observation of a single galaxy using the Hubble Deep Field 2009 two years' data (Bouwens et al. 2011; Oesch et al. 2012). It was argued in Bouwens et al. (2012a), based on an analytical calculation, that even with such low SFRD at high redshifts it was possible to obtain an optical depth to reionization compatible with the value obtained by *Wilkinson Microwave Anisotropy Probe* (*WMAP*; $\tau = 0.088 \pm 0.015$) (Komatsu et al. 2011). However, this derivation would imply a high escape fraction of ionizing radiation, and that reionization would end at $z \approx 8$, which is hard to reconcile with the constraints from observations of quasar spectra (Mesinger & Haiman 2007; Zaldarriaga et al. 2008). Our SFRDs are considerably higher than the current observational constraints, although the difference can be explained by a systematic underestimation of the SFR in observed galaxies. Moreover, current observations only probe the high-mass end of the high-redshift galaxies' mass function, which will underestimate the SFRD (also the obtained SFRs have very high error bars due to uncertainties in the correction due to dust extinction, the redshift, and the galaxy type). In the following sections the results shown were obtained using *Sim1* unless stated otherwise.

2.6. Total Lyα Luminosity: Comparison with Observations

In the previous sections we calculated the Lyα luminosity as a function of the SFR for several effects. The commonly used "empirical" relation between these two quantities is (Jiang et al. 2011)

$$L_{\mathrm{Gal}} = 1.1\times10^{42}\frac{\mathrm{SFR}(M,z)}{M_\odot\ \mathrm{yr}^{-1}}\ \mathrm{erg\ s}^{-1}, \quad (27)$$

and it is based on the relation between SFR and the Hα luminosity from Kennicutt (1998a) and on the line emission ratio of Lyα to Hα in case B recombinations calculated assuming a gas temperature of 10^4 K. This empirical relation gives the Lyα luminosity without dust absorption (we have labeled it *K98* for the remainder of the paper).

Our relation between luminosity and star formation is mass dependent (both from the escape fraction and due to the

Table 2
Average Luminosity per Star Formation Rate (in Units of erg $s^{-1}/M_\odot\ yr^{-1}$) Averaged over the Halo Mass Function for Redshifts 10, 9, 8, and 7, from Top to Bottom

$A_{rec}(z)$	$A_{exc}(z)$	$A_{cool}(z)$	$A_{cont}(z)$	$A_{total}(z)$
4.4×10^{41}	1.1×10^{41}	1.3×10^{39}	8.1×10^{40}	6.4×10^{41}
1.2×10^{42}	3.2×10^{41}	7.8×10^{38}	6.4×10^{40}	1.6×10^{42}
9.3×10^{41}	2.4×10^{41}	4.9×10^{38}	4.9×10^{40}	1.2×10^{42}
8.5×10^{41}	2.2×10^{41}	3.3×10^{38}	3.6×10^{40}	1.1×10^{42}

expression from the cooling mechanism), so in order to compare it with the result above, we calculate

$$A(z) = \frac{\langle L_{\rm Gal}(M, z)\rangle}{\langle {\rm SFR}(M, z)\rangle}, \quad (28)$$

where the average $\langle x\rangle$ of quantity x is done over the halo mass function for the mass range considered. The results are presented in Table 2 for a few redshifts.

Although our Lyα luminosities per SFR are slightly higher, at least for low redshifts, we point out that the "empirical" relation is based on a theoretical calculation that only accounts for Lyα emission due to recombinations. Moreover, the observational measurements of Hα and Lyα are primarily made at low redshifts, where the absorption of Lyα photons by dust in galaxies is expected to be high. Our relation has the advantage of evolving with redshift since it accounts for the evolution of the escape fraction of ionizing photons and for the evolution of the escape fraction of Lyα photons. This z-dependence is not present in the standard empirical relation. This redshift evolution of the UV photons' escape fraction is a consequence of the increase in the number of massive galaxies with more clumpy structure as the redshift decreases. The star-forming regions of massive galaxies are embedded in clumps, and therefore it becomes more difficult for the ionizing photons to escape from such dense regions (Razoumov & Sommer-Larsen 2010; Yajima et al. 2011). The redshift evolution of the relation presented in Equation (28) justifies why a theoretical calibration between Lyα luminosity and the SFR of a galaxy is useful for our work.

To check the consistency between our theoretical estimation of the Lyα luminosity and the existing observations during reionization, we show in Figure 3 the LF using two of the SFR versus halo mass parameterizations presented in Section 2.5. This prediction is then compared to Lyα LFs of photometric identified objects in Shimasaku et al. (2006) and in Kashikawa et al. (2006) near the end of the reionization epoch.

Our LFs were calculated assuming a minimum halo mass of $8 \times 10^8\ M_\odot$, which corresponds to a minimum luminosity of 3.72×10^{36} erg s^{-1} for *Sim1*, 4.49×10^{36} erg s^{-1} for *Sim2*, and 6.22×10^{36} erg s^{-1} for *Sim3*. The agreement between our LFs and observations is reasonable for *Sim1*; however, our *Sim2* overpredicts the abundance of high-luminosity Lyα emitters. This difference can be due to sample variance or a result of the high sensitivity of theoretical predictions to several parameters in our model. We point out that the luminosity range relevant for this comparison falls in a halo mass range outside the one for which the escape fraction of UV radiation we are using was estimated, so we could easily get a better fit between observations and *Sim2* by reducing this escape fraction for high halo masses. This difference could also be related with the choice of halo mass function. Here we choose the Sheth–Tormen halo mass function (Sheth & Tormen 1999), which has been shown to fit low-redshift simulations more accurately, but it

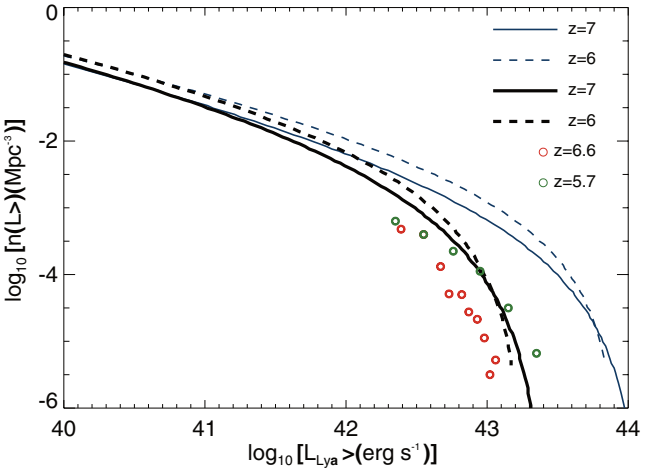

Figure 3. Lyα luminosity functions obtained with our calculations are shown for redshifts $z = 6$ (dashed lines) and $z = 7$ (solid lines) for *Sim1* (black thick lines) and *Sim2* (blue thin lines). The green and red circles show the intrinsic (i.e., not affected by the IGM) Lyα LF from photometric identified objects in Shimasaku et al. (2006) and in Kashikawa et al. (2006) for $z = 5.7$ and 6.6, respectively.

(A color version of this figure is available in the online journal.)

is yet to be established the extent to which such a halo mass function can reproduce the halo distribution during reionization. Another possible explanation for this difference is the existence of a small amount of neutral gas in the IGM, which would severely decrease the observed Lyα luminosity from galaxies. Also, we could have decreased the high-luminosity end of our LFs if we had use an Lyα escape fraction that decreased with halo mass such as the one used in Forero-Romero et al. (2011). We do not consider a model fit to the data to optimize various parameters in our model given that the current constraints on the observed Lyα LFs have large overall uncertainties, especially considering variations from one survey to another.

2.7. Lyα Average Intensity

In this section and the next one we will attempt to estimate the intensity and power spectrum of the Lyα signal using an analytical model. In Section 4, we will improve the estimation by doing the same calculation using a semi-numerical simulation.

The total intensity of Lyα emission can be obtained from the combined luminosity of Lyα photons associated with different mechanisms described in the previous sub-sections, such that

$$\bar{I}_{\rm Gal}(z) = \int_{M_{\rm min}}^{M_{\rm max}} dM \frac{dn}{dM} \frac{L_{\rm Gal}(M, z)}{4\pi D_{\rm L}^2} y(z) D_{\rm A}^2, \quad (29)$$

where dn/dM is the halo mass function (Sheth & Tormen 1999), M is the halo mass, $M_{\rm max} = 10^{13}\ M_\odot$, $M_{\rm min} = M_{\rm OB}$, $D_{\rm L}$ is the proper luminosity distance, and $D_{\rm A}$ is the comoving angular diameter distance. Finally, $y(z) = d\chi/d\nu = \lambda_{{\rm Ly}\alpha}(1+z)^2/H(z)$, where χ is the comoving distance, ν is the observed frequency, and $\lambda_{{\rm Ly}\alpha} = 2.46 \times 10^{-15}$ m is the rest-frame wavelength of the Lyα line.

The evolution of the Lyα intensity predicted by this calculation is shown in Figure 4 together with the scaling expected under the "empirical" relation from Kennicutt (1998a) combined with an assumption related to the gas temperature. The intensities of Lyα emission from different sources are presented in Table 3 for several redshifts.

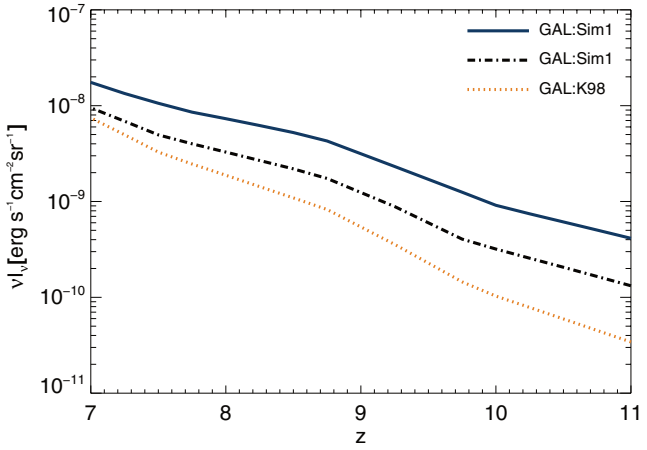

Figure 4. Lyα intensity from galaxies in erg s^{-1} cm^{-2} sr^{-1} as a function of redshift. The black dash-dotted line and the blue solid line were obtained using our theoretical calculation of the Lyα luminosity and the SFR halo mass relation from *Sim1* and *Sim2*, respectively. The orange dotted line uses the Lyα luminosity SFR relation based on the relation between SFR and the Hα luminosity from Kennicutt (1998a) and the line emission ratio of Lyα to Hα in case B recombinations calculated assuming a gas temperature of 10,000 K (labeled as the K98 relation). The K98 line is not corrected for dust absorption.

(A color version of this figure is available in the online journal.)

Table 3
Surface Brightness (in Observed Frequency times Intensity) of Lyα Emission from the Different Sources in Galaxies at $z \approx 7$, $z \approx 8$, and $z \approx 10$ for *Sim1*

Source of emission in (erg s^{-1} cm^{-2} sr^{-1})	$\nu I_\nu(z=7)$	$\nu I_\nu(z=8)$	$\nu I_\nu(z=10)$
Recombinations	7.3×10^{-9}	2.5×10^{-9}	2.3×10^{-10}
Excitations	1.9×10^{-9}	6.5×10^{-10}	6.0×10^{-11}
Cooling	2.8×10^{-12}	1.5×10^{-12}	4.7×10^{-13}
Continuum	3.1×10^{-10}	3.5×10^{-10}	3.0×10^{-11}
Total	9.5×10^{-9}	3.5×10^{-9}	3.2×10^{-10}

These intensities can be extrapolated to other SFRDs, assuming that the only change is in the amplitude of the SFR halo mass relations presented in Figure 1 by using the coefficients in Table 4.

The intensities from emission at $z \approx 7$, 8, and 10 are 9.5×10^{-9}, 3.5×10^{-9}, and 3.2×10^{-10} erg s^{-1} cm^{-2} sr^{-1}, respectively. Such an intensity is substantially smaller than the background intensity of integrated emission from all galaxies (around 1×10^{-5} erg s^{-1} cm^{-2} sr^{-1}; Madau & Pozzetti 2000), or from the total emission of galaxies during reionization, estimated to be at most 1×10^{-6} erg s^{-1} cm^{-2} sr^{-1} (Cooray et al. 2012).

2.8. Lyα Intensity Power Spectrum

The Lyα emission from galaxies will naturally trace the underlying cosmic matter density field, so we can write the Lyα line intensity fluctuations due to galaxy clustering as

$$\delta I_{\rm GAL} = b_{\rm Ly\alpha}\, \bar{I}_{\rm GAL}\, \delta(\mathbf{x}), \tag{30}$$

where $\bar{I}_{\rm GAL}$ is the mean intensity of the Lyα emission line, $\delta(\mathbf{x})$ is the matter overdensity at the location $\mathbf{x}$, and $b_{\rm Ly\alpha}$ is the average galaxy bias weighted by the Lyα luminosity (see, e.g., Gong et al. 2011).

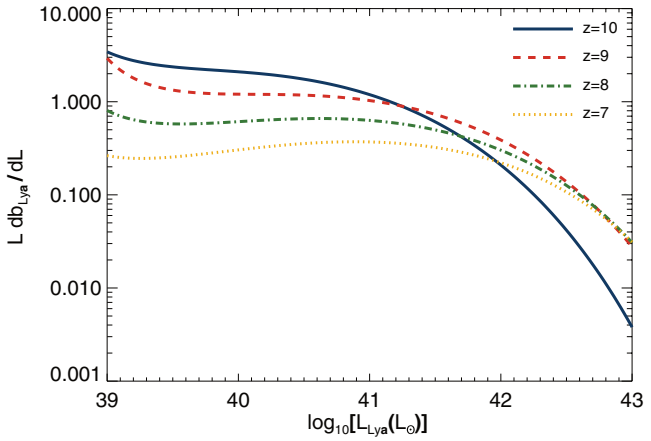

Figure 5. Bias between dark matter fluctuations and Lyα surface brightness (νI) from galaxies as a function of the galaxy Lyα luminosity at redshifts 7, 8, 9, and 10.

(A color version of this figure is available in the online journal.)

Table 4
Average Lyα Intensity from Galaxies per SFRD ($A_{\rm SFRD}$) in Units of erg s^{-1} cm^{-2} sr^{-1}/$M_\odot$ yr^{-1}, Calculated Using the Star Formation Rate Halo Mass Relation from Simulations *Sim1* and *Sim2*

Redshift	$A_{\rm SFRD}$(*Sim1*)	$A_{\rm SFRD}$(*Sim2*)
10	1.05×10^{-03}	2.20×10^{-03}
9	2.17×10^{-03}	3.75×10^{-03}
8	2.34×10^{-03}	3.15×10^{-03}
7	3.42×10^{-03}	3.42×10^{-03}

Using one of the relations between the SFR and halo mass from Section 2.5, we can calculate the luminosity and obtain the Lyα bias following Visbal & Loeb (2010):

$$b_{\rm Ly\alpha}(z) = \frac{\int_{M_{\rm min}}^{M_{\rm max}} dM \frac{dn}{dM} L_{\rm GAL}\, b(z, M)}{\int_{M_{\rm min}}^{M_{\rm max}} dM \frac{dn}{dM} L_{\rm GAL}}, \tag{31}$$

where $b(z, M)$ is the halo bias and dn/dM is the halo mass function (Sheth & Tormen 1999). We take $M_{\rm min} = 10^8\, M_\odot/h$ and $M_{\rm max} = 10^{13}\, M_\odot/h$. The bias between dark matter fluctuation and the Lyα luminosity, as can be seen in Figure 5, is dominated by the galaxies with low Lyα luminosity independently of the redshift.

We can then obtain the clustering power spectrum of Lyα emission as

$$P_{\rm GAL}^{\rm clus}(z, k) = b_{\rm Ly\alpha}^2 \bar{I}_{\rm GAL}^2 P_{\delta\delta}(z, k), \tag{32}$$

where $P_{\delta\delta}(z, k)$ is the matter power spectrum. The shot-noise power spectrum, due to discretization of the galaxies, is also considered here. It can be written as (Gong et al. 2011)

$$P_{\rm Ly\alpha}^{\rm shot}(z) = \int_{\rm M_{max}}^{\rm M_{min}} dM \frac{dn}{dM} \left(\frac{L_{\rm GAL}}{4\pi D_{\rm L}^2}\, y(z) D_{\rm A}^2 \right)^2. \tag{33}$$

The resulting power spectrum of Lyα emission from galaxies is presented in Figure 6. At all scales presented the Lyα intensity and fluctuations are dominated by the recombination emission from galaxies.

3. Lyα EMISSION FROM THE IGM

The Lyα emission from the IGM is mostly originated in recombinations and collisions powered by the ionizing

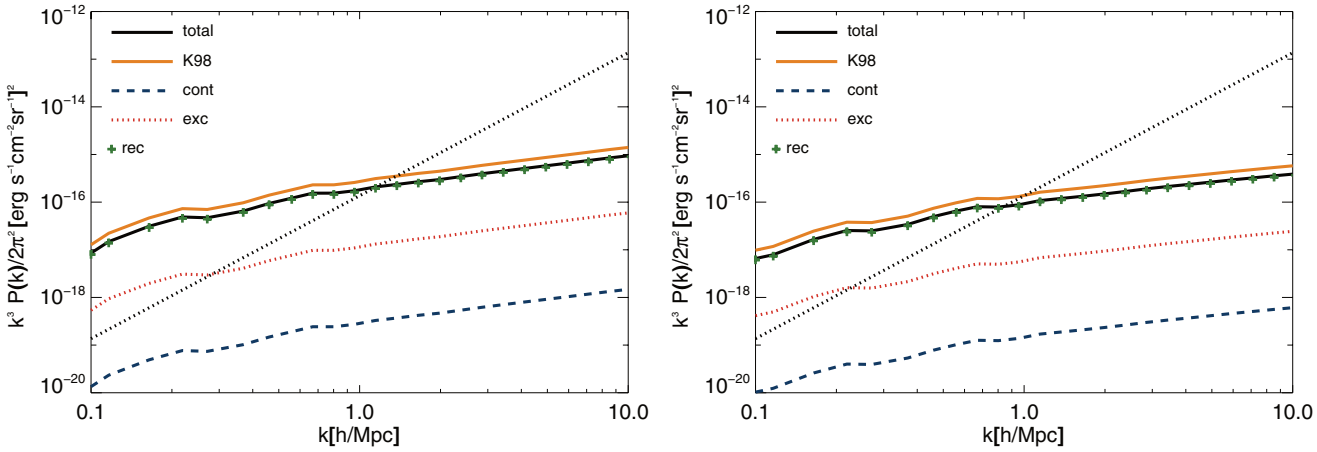

Figure 6. Clustering power spectrum of the Lyα surface brightness (νI) from galaxies at redshifts 7–10 (from top to bottom), from several sources: collisions and excitations, recombinations, and continuum emission with frequencies inside the Lyα width. The power spectra from cooling emission are not shown since they are several orders of magnitude smaller than the contributions from the other sources. Also shown are the total power spectra (clustering (solid black line) and shot-noise power spectra (dotted black line)) of the total contribution for Lyα emission in galaxies predicted by our theoretical calculation and total Lyα clustering power spectra predicted using the $K98$ relation (orange solid line).

(A color version of this figure is available in the online journal.)

background. These processes are similar to the ones described inside the galaxies, although, since the physical conditions of the gas in the IGM are different from those in the ISM, the intensity of Lyα emission can no longer be connected to the ionizing photon intensity using the previous relations. The biggest challenge in doing these calculations is to connect the IGM ionizations and heating of the gas to the emission of ionizing radiation and the SFR assumed in the previous sections. Moreover, in the IGM, we also have to take into account the contribution of continuum radiation from stars between the Lyα and the Lyman limit, which redshifts into the Lyα line.

In a schematic view, we have to take into account the following processes:

1. The amount of energy in UV photons that escapes the galaxy.
2. This energy will then be distributed in the IGM into
   (a) ionizations,
   (b) direct excitations (followed by emission, partially into the Lyα line), and
   (c) heating of the gas.
3. Taking into account the state of the IGM in terms of temperature and ionization, we can then further determine how much it will radiate through the Lyα line from
   (a) recombinations and
   (b) radiative cooling (usually through excitations followed by decay in several lines including Lyα).
4. The amount of Lyn photons that escape the galaxy, rescattering in the IGM into Lyα photons.

The proper calculation of all these processes will require simulations, which we will address in Section 4. In the following sub-sections we review the contributions through analytical calculations in order to get a better understanding of the dominating effects.

3.1. Lyα Emission from Hydrogen Recombinations

The UV radiation that escapes the ISM into the IGM ionizes low-density clouds of neutral gas. Part of the gas in these clouds then recombines, giving rise to Lyα emission. The radiation emitted in the IGM is often referred to as fluorescence (Santos 2004). The comoving number density of recombinations per second in a given region, $\dot{n}_{\rm rec}$, is given by

$$\dot{n}_{\rm rec}(z) = \alpha n_e(z) n_{\rm H\,II}(z), \quad (34)$$

where α changes between the case A and the case B recombination coefficient and $n_{\rm H\,II} = x_i(n_b(1 - Y_p)/((1–3)/4Y_p))$ is the ionized hydrogen comoving number density (x_i is the ionization fraction, n_b the baryonic comoving number density). The free electron density can be approximated by $n_e = x_i n_b$.

The recombination coefficients are a function of the IGM temperature, T_K. The case A comoving recombination coefficient is appropriate for the highly ionized low-redshift universe (Furlanetto et al. 2006),

$$\alpha_A \approx 4.2 \times 10^{-13} (T_K/10^4\ {\rm K})^{-0.7} (1+z)^3\ {\rm cm^3\ s^{-1}}, \quad (35)$$

while the case B comoving recombination coefficient is appropriate for the high-redshift universe,

$$\alpha_B \approx 2.6 \times 10^{-13} (T_K/10^4\ {\rm K})^{-0.7} (1+z)^3\ {\rm cm^3\ s^{-1}}. \quad (36)$$

The use of a larger recombination coefficient when the process of hydrogen recombination is close to its end accounts for the fact that, at this time, ionizations (and hence recombinations) take place in dense, partially neutral gas (Lyman-limit systems) and the photons produced after recombinations are consumed inside these systems, so they do not help ionize the IGM (see, e.g., Furlanetto et al. 2006).

The fraction of Lyα photons emitted per hydrogen recombination, $f_{\rm rec}$, is temperature dependent, so we used the parameterization for $f_{\rm rec}$ made by Cantalupo et al. (2008) using a combination of fits tabulated by Pengelly (1964) and Martin (1988) for $T_K > 10^3$ and $T_K < 10^3$, respectively:

$$f_{\rm rec} = 0.686\text{–}0.106 \log_{10}(T_K/10^4\ {\rm K}) - 0.009 (T_K/10^4\ {\rm K})^{-0.4}. \quad (37)$$

The luminosity density (per comoving volume) in Lyα from hydrogen recombinations in the IGM, $\ell_{\rm rec}^{\rm IGM}$, is then given by

$$\ell_{\rm rec}^{\rm IGM}(z) = f_{\rm rec} \dot{n}_{\rm rec} E_{{\rm Ly}\alpha}. \quad (38)$$

3.2. Lyα Emission from Excitations in the IGM

The UV radiation that escapes the galaxies without producing ionization ends up ionizing and exciting the neutral hydrogen in the IGM and heating the gas around the galaxies. The high energetic electron released after the first ionization spends its energy in collisions/excitations, ionizations, and heating the IGM gas until it thermalizes (Shull & van Steenberg 1985). We estimated the contribution of the direct collisions/excitations to the Lyα photon budget and concluded that it is negligible.

The Lyα luminosity density due to the collisional emission (radiative cooling in the IGM), $\ell_{\rm exc}^{\rm IGM}$, is given by

$$\ell_{\rm exc}^{\rm IGM}(z) = n_e n_{\rm H\,I} q_{\rm Ly\alpha} E_{\rm Ly\alpha}, \quad (39)$$

where $n_{\rm H\,I} = n_b(1 - x_i)((1 - Y_p)/((1–3)/4Y_p))$ is the neutral hydrogen density, x_i is the IGM ionized fraction, and $q_{\rm Ly\alpha}$ is the effective collisional excitation coefficient for Lyα emission, which we calculated in the same way as Cantalupo et al. (2008), but using different values for the gas temperature and IGM ionization fraction.

Considering excitation processes up to the level $n = 3$ that could eventually produce Lyα emission, the effective collisional excitation coefficient is given by

$$q_{\rm Ly\alpha} = q_{1,2p} + q_{1,2s} + q_{1,3p}. \quad (40)$$

The collisional excitation coefficient for the transition from the ground level (1) to the level (nl) is given by

$$q_{1,nl} = \frac{8.629 \times 10^{-6}}{T_K^{1/2}} \frac{\Omega(1, nl)}{\omega_1} e^{E_{1,n}/k_B T_K} \ {\rm cm^3\ s^{-1}}, \quad (41)$$

where $\Omega(1, nl)$ is the temperature-dependent effective collision strength, ω_1 is the statistical weight of the ground state, $E_{1,n}$ is the energy difference between the ground and the nl level, and k_B is the Boltzmann constant.

3.3. Scattering of Lyn Photons Emitted from Galaxies

Continuum emission of photons, by stars, from Lyα to the Lyman limit travels until it reaches one of the Lyn lines, where it gets scattered by neutral hydrogen. Most of this scattering will have as an end result the production of Lyα photons, which eventually redshift out of the line. Since a considerable fraction of these photons only reach a given Lyn frequency in the IGM, this Lyα emission is formed as a flux that decays with r^2 around the star that emitted the continuum photons, so it appears diluted in frequency in line observations of point sources (Chen & Miralda-Escudé 2008). These continuum photons are much less likely to be absorbed by the dust in the ISM than photons originated in recombinations.

In intensity mapping, the frequency band observed is much larger than in line observations, so in principle all the continuum Lyα photons can be detected. Using the spectral energy distribution (SED) made with the code from Maraston (2005), we estimated that the number of photons emitted by stars between the Lyα plus the Lyα equivalent width and the Lyman limit is equivalent to $Q_{\rm Lyn}^{\rm IGM} = 9.31 \times 10^{60}\, M_\odot^{-1}\ {\rm s^{-1}}$. The higher frequency photons are absorbed by hydrogen atoms as they reach the Lyβ frequency, re-emitted, and suffer multiple scattering until they reach the Lyα line. The fraction of the continuum photons emitted close to the Lyα line have already redshifted to lower frequencies before reaching the IGM, so they will not be scattered by the neutral hydrogen in the IGM and will not contribute to the radiative coupling of the 21 cm signal (they are already included in the calculation of the Lyα emission from galaxies).

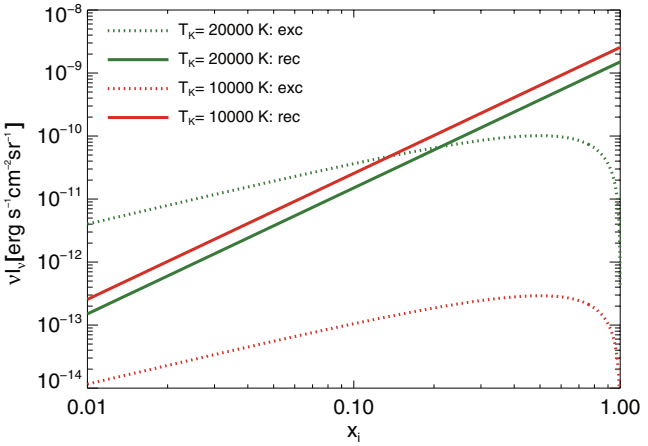

Figure 7. Intensity of Lyα emission at redshift 7 due to recombinations and excitations in the IGM as a function of the hydrogen ionized fraction. The green and red lines assume a constant gas temperature of 20,000 K and 10,000 K, respectively.

(A color version of this figure is available in the online journal.)

The intensity of this emission was calculated with a stellar emissivity that evolves with frequency as $\nu^{-\alpha}$ with $\alpha = 0.86$ and normalized to $Q_{\rm Lyn}^{\rm IGM}$. The Lyα luminosity density originated from continuum stellar radiation and emitted in the IGM, $\ell_{\rm cont}^{\rm IGM}$, is then approximately given by

$$\ell_{\rm cont}^{\rm IGM}(z) \approx Q_{\rm ly\alpha}^{\rm IGM} E_{\rm Ly\alpha} {\rm SFRD}(z), \quad (42)$$

where the SFRD is in units of $M_\odot\ {\rm s^{-1}}$. Note that in Section 4, this calculation is done through a full simulation.

3.4. Lyα Intensity

We calculated the intensities for the several Lyα sources in the IGM from their luminosity densities using

$$\bar{I}_{\rm IGM}(z) = \frac{\ell^{\rm IGM}(z)}{4\pi D_L^2} y(z) D_A^2. \quad (43)$$

The luminosity and hence the intensity of Lyα emission in the IGM depend on local values of the hydrogen ionized fraction, the gas temperature, and the gas density. These parameters are correlated with each other, and so theoretical calculations of the average intensity made with the average of these parameters may be misleading. Since this emission is dominated by overdense regions, a clumping factor of a few units is usually assumed in theoretical calculations. However, we decided to estimate this intensity without using a clumping factor since its effect can be extrapolated from the intensity without clumping. The intensity of Lyα emission due to recombinations or collisions in the IGM is shown in Figure 7 as a function of the hydrogen ionized fraction for different values of the gas temperature.

Even for a fixed average IGM ionized fraction, the intensity of Lyα emission is the result of emission from several regions, and so all the values shown in Figure 7 are relevant. As can be seen in Figure 7, the intensity of Lyα due to recombinations and collisions in the IGM is very sensitive to the gas temperature and to the fluctuations in the IGM ionized fraction.

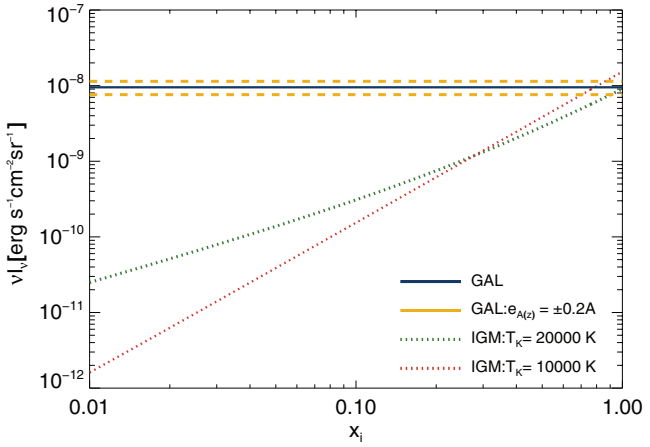

Figure 8. Intensity of Lyα emission at redshift 7 from the IGM and from galaxies as a function of the hydrogen ionized fraction and including all contributions. The green and red lines are the intensity of Lyα emission in the IGM assuming a constant gas temperature of 20,000 K and 10,000 K, respectively. The blue solid line is the intensity of Lyα emission from galaxies as calculated in the previous section. The yellow dashed lines show the intensity in galaxies assuming an error in $A(z)$ of 20% due to the uncertainty in the ionizing photons' escape fraction and due to the uncertainty in the emissivity of ionizing photons. The intensities in the IGM were calculated assuming a clumping factor of 6 compatible with current conservative estimates (Pawlik et al. 2010).

(A color version of this figure is available in the online journal.)

Numerical simulations predict that the temperatures in the hydrogen gas in the IGM can vary from 5000 to 20,000 K (Davé et al. 2001; Smith et al. 2011). The theoretical intensities of Lyα emission in galaxies and in the IGM shown in Figure 8 indicate that unless the IGM clumping factor is very high, or the Lyα photon escape fraction is very low, the Lyα intensity from the IGM at $z = 7$ is lower than the emission from galaxies. At higher redshifts the SFRD will decrease, causing the Lyα intensities from galaxies and from the IGM to decrease. The escape fraction of UV photons from galaxies increases as the redshift increases, which will contribute negatively to the intensity of emission in galaxies and positively to the intensity of emission in the IGM. At high redshifts the IGM ionized fraction is small, which contributes to a strong decrease in the intensity of emission from the IGM compared to the intensity at $z = 7$.

4. Lyα INTENSITY AND POWER SPECTRUM USING NUMERICAL SIMULATIONS

The intensity of Lyα emission in the IGM at a given time and a given region is proportional to the ionized fraction, the gas temperature, and the matter density in that region. Since these three quantities are correlated, the use of average values in the Lyα intensity calculation highly underestimates the emission in the more overdense regions. Also the evolution of the average of the IGM ionized fraction is poorly known during the EoR.

Some of these problems can be resolved using a computational code able to produce simulations of the IGM ionized fraction, the gas temperature, and the matter density in a volume high enough to properly represent our universe. The use of simulations has an additional advantage of allowing the calculation of the three-dimensional power spectra of Lyα emission in the IGM without the need for assuming a bias relation with the underlying dark matter distribution.

In this section we will estimate the inhomogeneous Lyα intensity from galaxies and the IGM using a modified version of the SimFast21 code (Santos et al. 2010). Given a set of astrophysical and cosmological parameters, this code is able to consistently produce three-dimensional simulations of the dark matter density field, the ionization field, the SFRD, the scattering of Lyn photons in the IGM, the X-ray heating of the IGM, and even 21 cm spin and brightness temperature fluctuations for the several redshifts of the EoR.

A proper calculation of all the heating and cooling mechanisms would add a high level of complexity to this calculation and would require a small redshift step in the IGM fraction calculation, so we assumed a constant temperature in ionized regions of 10,000 K. Moreover, the results from our calculations can be easily extrapolated to account for a higher temperature. For example, for a temperature of 20,000 K the number of recombinations in the IGM would decrease by a factor of 1.7 and the number of collisions would increase more than two orders in magnitude. Assuming that the clumping of the IGM is not very high, and so Lyα recombination emission dominates over collisional emission during most of the EoR, this higher temperature would cause a small decrease in the intensity of emission in the IGM and the reionization period would be less extended than what we predict in Section 4.1. We made a few modifications to the SimFast21 code in order to provide a consistent description of the ionization history and its relations to the Lyα emission, which we now describe.

4.1. IGM Ionized Fraction Calculation

In the previous version of the SimFast21 code, the IGM ionized fraction was computed assuming that at each redshift the ionization state of a region could be estimated from the collapsed mass in that region assuming a linear relation between collapsed mass and ionizing power. So a given spherical region of radius R is considered ionized if (Furlanetto et al. 2006)

$$\zeta M_{\rm coll}(R) \geqslant M_{\rm tot}(R), \tag{44}$$

where $M_{\rm coll}$ is the collapsed mass that corresponds to the total mass in halos in that region, $M_{\rm tot}$ is the total mass in the region, and ζ is an ionizing efficiency parameter. This efficiency parameter tries to include all the ionizations and recombinations produced by a halo as a function of its mass but has no actual physical meaning, although its use is somewhat justified by the large uncertainty in the astrophysical quantities involved in the determination of the relation between halo mass and ionizing efficiency and in the adjustment of this parameter in order to reproduce a reionization history compatible with observations.

In order to calculate the Lyα field, however, we need to include the recombinations in the IGM explicitly, as well as directly relate the ionization process to the emitted stellar radiation. We therefore modified the SimFast21 code to include these improvements. This new method allows a nonlinear relation between collapsed mass and ionizing power, and all the parameters involved in the calculation have values based on current astrophysical constraints. Also, the size of ionized regions is now set by the volume at which the total ionizing emissivity of the sources it contains equals the number of recombinations so that the system is in equilibrium. For each redshift the implementation of this method was done with the following steps:

1. A halo catalog with the mass and three-dimensional spatial positions was generated using the same method used in the original version of the SimFast21 code.
2. We calculated SFRs from the halo catalogs using the nonlinear relations in Equations (24)–(26).

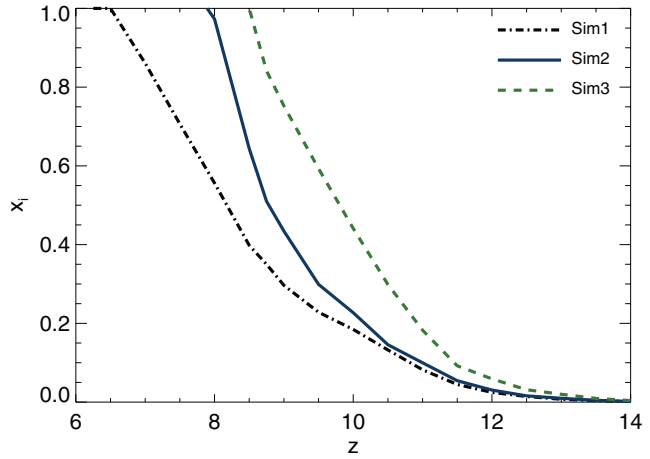

Figure 9. Evolution of the IGM ionized fraction as a function of redshift for the three star formation rate halo mass parameterizations shown in Section 2.5.
(A color version of this figure is available in the online journal.)

3. We used Equation (4) to obtain the halo ionizing rate, $\dot{N}_{\rm ion}$, and we corrected for the presence of helium using $A_{\rm He}$ and multiplied it by $f_{\rm esc}$, to account for the photons consumed inside the galaxies:

$$\dot{N}_{\rm ion}^{\rm IGM}(z, M) = A_{\rm He}\dot{N}_{\rm ion}(M) f_{\rm esc}(z, M). \quad (45)$$

   The UV ionizing rates of the halos, $\dot{N}_{\rm ion}^{\rm IGM}$, were then put in three-dimensional boxes.
4. Three-dimensional boxes with the rate of recombinations in each cell, $\dot{N}_{\rm rec}^{\rm IGM} = V_{\rm cell} \times \dot{n}_{\rm rec}^{\rm IGM}$, were obtained from a dark matter density simulation made with the SimFast21 code using Equation (34) with x_i set to 1 and $T_K = 10^4$ K.
5. Following the same procedure as in the original version of the SimFast21 code, we applied a series of top-hat filters of decreasing size (this filtering procedure was done in Fourier space) to the ionizing rate and the recombination rate boxes in order to calculate the region ionizing rate and recombination rate.
6. At each filtering step of radius R we found the ionized regions (H II bubbles) by checking if the region ionizing rate was equal to or higher than its recombination rate. With this method H II bubbles are always fully ionized:

$$\dot{N}_{\rm ion}^{\rm IGM}(z, R) \geqslant \dot{N}_{\rm rec}^{\rm IGM}. \quad (46)$$

4.2. Intensity from Recombinations and Collisions in the IGM

The SimFast21 code was built to calculate the IGM ionized state assuming two types of regions: one fully ionized (inside the H II bubbles) and the other fully neutral. The intensity of Lyα emission in the IGM due to recombinations is a smooth function of the IGM ionized fraction and is dominated by emission from fully ionized regions (see Figure 7), so the output of the SimFast21 code is good enough to estimate this intensity.

Collisions between electrons and neutral hydrogen atoms can also lead to Lyα emission; however, as was explained in Section 3.2, collisional Lyα emission only occurs in partly ionized regions, mainly in the edge of H II bubbles, so the estimation of this emission requires a more detailed description of the IGM ionized state than the one given by the limited resolution of semi-numerical simulations. Collisions are most important in regions where the IGM ionized fraction is locally close to 0.5 and the temperatures are high. Since high-temperature regions are likely to be highly ionized, we can deduce with the help of Figure 7 that Lyα emission from recombinations is dominant over Lyα emission from collisions in the IGM.

Table 5
Surface Brightness (in Observed Frequency times Intensity) of Lyα Emission from the Different Sources in the IGM at $z \approx 7$, $z \approx 8$, and $z \approx 10$

Source of emission in (erg s^{-1} cm^{-2} sr^{-1})	$\nu I_\nu(z=7)$	$\nu I_\nu(z=8)$	$\nu I_\nu(z=10)$
Recombinations	9.3×10^{-10}	4.8×10^{-10}	9.6×10^{-11}
Continuum	3.5×10^{-13}	1.2×10^{-13}	1.5×10^{-14}
Total	1.6×10^{-9}	6.7×10^{-10}	1.1×10^{-10}

4.3. Intensity from the Scattering of Lyn Photons in the IGM

The IGM Lyα intensity from scattering of Lyn photons emitted from galaxies can also be calculated using data from the code SimFast21. This code uses Equation (10) in Santos et al. (2010) to calculate the spherical average of the number of Lyα photons, J_α, hitting a gas element per unit proper area per unit time per unit frequency per steradian. The Lyα intensity originated from these continuum photons is given by

$$I_{\rm cont}^{\rm IGM} = \frac{6 J_\alpha E_{\rm Ly\alpha} D_{\rm A}^2}{(1+z)^2 D_{\rm L}^2}. \quad (47)$$

4.4. Results

Using the prescriptions described in the previous sections, we ran simulations *Sim1*, *Sim2*, and *Sim3* with a volume of $54^3\ h^{-3}$ Mpc^3 and 1800 cells from redshift 14 to redshift 6. The obtained IGM ionization fractions, at redshift 7, where $x_i = 0.86$ for simulation *Sim1* and $x_i = 1.0$ for simulations *Sim2* and *Sim3*. These values are consistent with the current most likely values for this parameter, $0.8 \leqslant x_i(z=7) \leqslant 1.0$ (Mitra et al. 2012). The IGM ionized fraction evolution for *Sim2* and for *Sim3* (see Figure 9) resulted in optical depths to reionization of 0.073 and 0.082. These optical depths are consistent with the value obtained by *WMAP* ($\tau = 0.088 \pm 0.015$; Komatsu et al. 2011). The optical depth corresponding to *Sim1* is 0.66, which is lower than the current observational constraints. Based on the optical depth constraint, *Sim2* and *Sim3* have the most likely reionization histories, and the IGM ionized fraction evolution obtained with *Sim1* can be seen as a lower bound.

The intensities of Lyα emission from galaxies at redshift 7 obtained with the SimFast21 code are similar to the more theoretical estimates summarized in Table 3.

Intensities of Lyα emission in the IGM made with the same code are presented in Table 5.

The intensity values found in Tables 3 and 5 and the theoretical estimations plotted in Figure 8 indicate that for the Lyα intensity from the IGM to reach a value close to the emission from galaxies at $z = 7$ would require a very large absorption of Lyα photons by dust in galaxies.

The resulting power spectra of Lyα emission in galaxies and in the IGM obtained with the SimFast21 code are presented in Figure 10 for $z = 7$ and $z = 10$.

We repeated the Lyα power spectra calculation for several redshifts during the EoR and plotted the Lyα power spectra as a function of redshift for several k in Figure 11.

We calculated the intensity of Lyα emission from galaxies and from the IGM (intensities are shown in Figure 12) and found

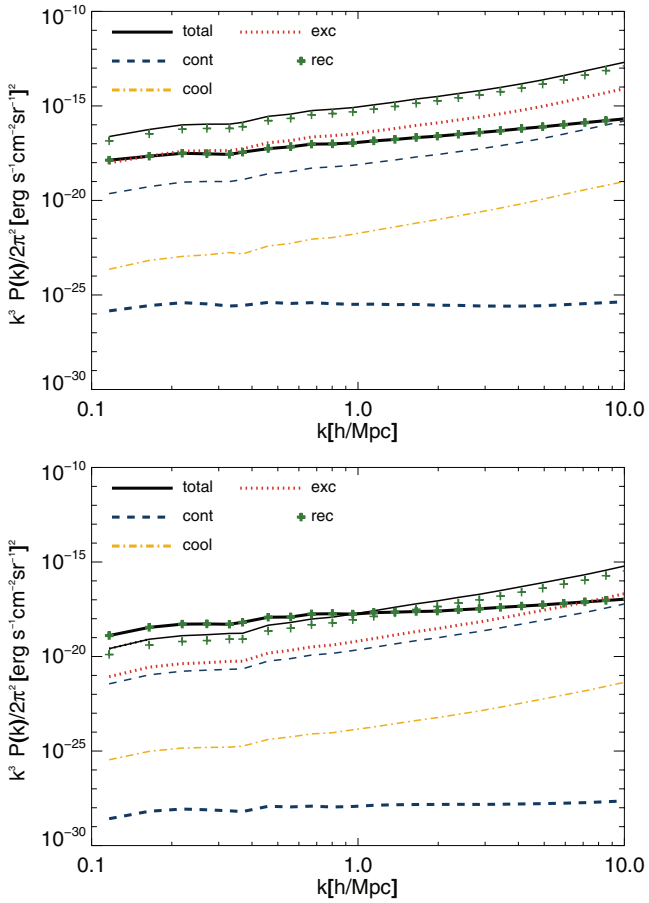

Figure 10. Power spectrum of Lyα surface brightness (νI) from galaxies (thin lines) and from the IGM (thick lines) at redshifts 7 (top) and 10 (bottom). The shown contributions to the Lyα flux are from excitations and collisions, recombinations, continuum emission inside the Lyα width (from galaxies), scattering of Lyn photons (from the IGM), cooling emission in galaxies, and the total emission.

(A color version of this figure is available in the online journal.)

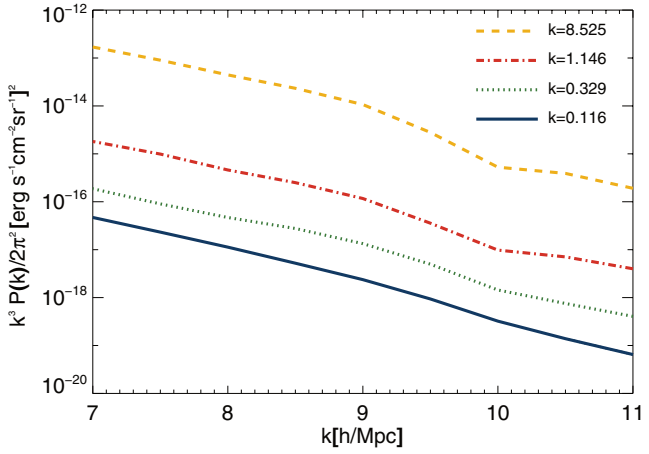

Figure 11. Total power spectrum of Lyα emission during the EoR as a function of redshift.

(A color version of this figure is available in the online journal.)

that, according to our assumptions and as already previously seen, the Lyα emission from galaxies is dominant over the Lyα emission from the IGM at least during the redshift interval from $z = 6$ to $z = 9$.

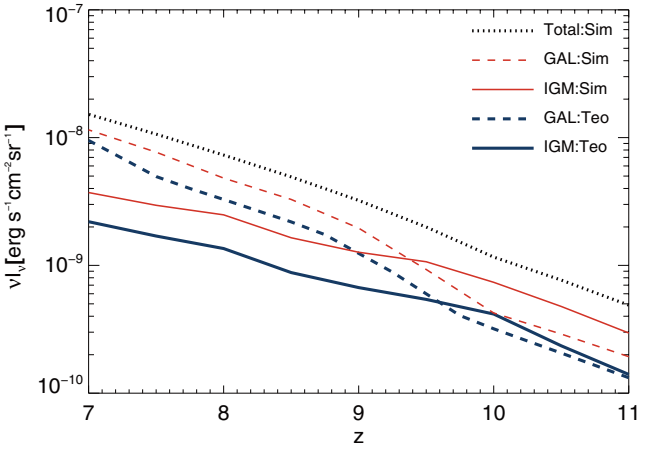

Figure 12. Lyα intensity from galaxies (dashed lines), from the IGM (solid lines) as a function of redshift from our simulation (red thin lines), and from the theoretical calculations (blue thick lines). Also shown is the total Lyα emission from the simulation (dotted line). All the intensities were calculated using the star formation halo mass relation from *Sim1*. The theoretical intensity of Lyα emission from the IGM was calculated using the average IGM ionization values obtained from *Sim1*.

(A color version of this figure is available in the online journal.)

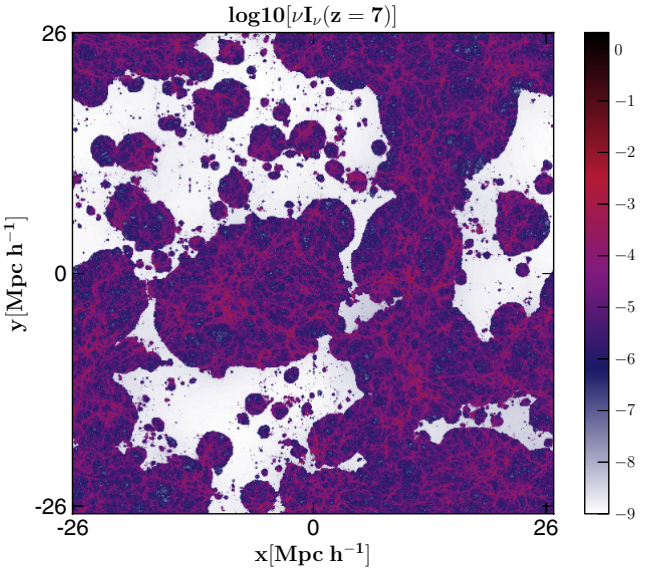

Figure 13. Total Lyα intensity from galaxies and the IGM in erg s^{-1} cm^{-2} sr^{-1} at redshift 7.

(A color version of this figure is available in the online journal.)

Also, a map of the total Lyα intensity in galaxies and in the IGM is presented in Figure 13 for $z = 7$.

Since the star formation halo mass relation is not very constrained, we can use the results obtained with *Sim1* and *Sim3* as the lower and upper bounds to the expected Lyα intensity. The evolution of the Lyα intensity from galaxies, from the IGM, and from galaxies plus IGM can be seen, respectively, in Tables 6, 7, and 8 for simulations *Sim1*, *Sim2*, and *Sim3*.

5. CROSS-CORRELATION BETWEEN Lyα AND 21 cm OBSERVATIONS

Observations of the 21 cm signal from the EoR will suffer from contamination by foregrounds and systematic effects. Since both 21 cm line emission and Lyα line emission trace

Table 6
Surface Brightness (in Observed Frequency times Intensity) in Units of erg s^{-1} cm^{-2} sr^{-1} of Lyα Emission from Galaxies at $z \approx 7$, $z \approx 8$, and $z \approx 10$ for *Sim1*, *Sim2*, and *Sim3*

Simulation	$\nu I_\nu(z=7)$	$\nu I_\nu(z=8)$	$\nu I_\nu(z=10)$
Sim1	1.43×10^{-8}	5.13×10^{-9}	4.55×10^{-11}
Sim2	2.54×10^{-8}	8.34×10^{-9}	5.68×10^{-11}
Sim3	3.57×10^{-8}	1.26×10^{-8}	9.73×10^{-11}

Table 7
Surface Brightness (in Observed Frequency times Intensity) in Units of erg s^{-1} cm^{-2} sr^{-1} of Lyα Emission from the IGM at $z \approx 7$, $z \approx 8$, and $z \approx 10$ for *Sim1*, *Sim2*, and *Sim3*

Simulation	$\nu I_\nu(z=7)$	$\nu I_\nu(z=8)$	$\nu I_\nu(z=10)$
Sim1	4.33×10^{-9}	3.76×10^{-9}	1.74×10^{-9}
Sim2	6.07×10^{-9}	5.17×10^{-9}	2.18×10^{-9}
Sim3	8.53×10^{-9}	7.81×10^{-9}	3.76×10^{-9}

Table 8
Surface Brightness (in Observed Frequency times Intensity) in Units of erg s^{-1} cm^{-2} sr^{-1} of Total Lyα Emission at $z \approx 7$, $z \approx 8$, and $z \approx 10$ for *Sim1*, *Sim2*, and *Sim3*

Simulation	$\nu I_\nu(z=7)$	$\nu I_\nu(z=8)$	$\nu I_\nu(z=10)$
Sim1	1.86×10^{-8}	8.89×10^{-9}	1.79×10^{-9}
Sim2	3.15×10^{-8}	1.35×10^{-8}	2.24×10^{-9}
Sim3	4.42×10^{-8}	2.04×10^{-8}	3.86×10^{-9}

neutral hydrogen, these two lines are expected to be strongly correlated. The cross-correlation of these two lines can be used as an extra method to probe the evolution of the IGM ionized hydrogen fraction. In particular, the power spectra of this cross-correlation will have a discontinuity at a scale that is related to the average bubble size and hence the average ionization fraction in the universe.

During the EoR, the 21 cm signal from galaxies is much smaller than the emission from the IGM, so it is safe to neglect both this galaxy emission and the shot-noise emission in the cross-correlation. Since the Lyα emission from galaxies is dominating over the IGM for most redshifts, we can just concentrate on the Lyα-galaxy/21 cm IGM cross-correlation when analyzing the cross-power spectrum. The cross-correlation between the 21 cm signal and the Lyα line in galaxies is therefore given by

$$P_{\mathrm{Ly}\alpha,21}(z,k) = I_{\mathrm{GAL}} I_{21} \left[P_{\delta\delta} - \frac{1}{1-\bar{x}_i} P_{x_i\delta} \right], \qquad (48)$$

where I_{21} is the average intensity of 21 cm emission, $P_{x_i\delta}(z,k)$ is the cross-correlation power spectra between the ionized field and the matter density fluctuations, $P_{\delta\delta}(z,k)$ is the power spectra of matter density fluctuations, and we are assuming that the Lyα emission is a biased tracer of the underlying dark matter field.

In Figure 14, we show the cross-correlation power spectrum between the total Lyα emission and the 21 cm signal at redshifts 7, 8, 9, and 10. For simulation *Sim1*, these redshifts correspond to ionizing fractions of $x_i = 0.86$, 0.56, 0.35, and 0.23 for redshifts 7, 8, 9, and 10, respectively. In Figure 14, the scale at which $P_{\mathrm{Ly}\alpha,21}(k)$ goes from negative to positive is determined by the average size of the ionized regions. For small scales, the correlation is positive since fluctuations from both lines should be proportional to the underlying density fluctuations, but for large scales (small k), the correlation is negative since the 21 cm line and the Lyα line are characteristic of neutral gas and ionized gas, respectively (and there will be an extra negative contribution from the ionized bubbles).

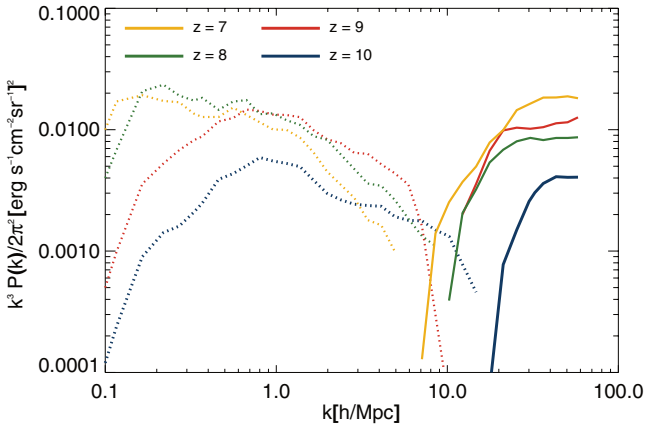

Figure 14. Cross-correlation power spectrum between Lyα emission and the 21 cm signal for redshifts 7, 8, 9, and 10. Dotted lines indicate a negative correlation, and solid lines indicate a positive correlation.
(A color version of this figure is available in the online journal.)

6. OBSERVATIONS

Current observations related to Lyα emission are restricted to narrowband imaging of Lyα emitters during reionization and the direct detection of individual emitters. This has led to order $\sim$200 secure detections at $z > 5$, but systematic uncertainties remain on the fraction that are arising at low redshifts and associated with [O III]/[O II] lines, among others. Due to narrow atmospheric windows, observations in near-IR bands necessary to cover the reionization epoch are also limited to multiple discrete bands. In any case, existing data could be used for a statistical study such as the power spectrum to extract properties of Lyα emitters that remain below the 5σ level of individual source/line identifications. Given that detections do exist at the bright end and our predictions are consistent with the Lyα LFs derived from observational measurements, it is likely that a modest improvement in existing technology and programs will lead to an experiment with sufficient sensitivity to measure the Lyα anisotropy power spectrum during reionization over a broad range of redshifts. The main limitation, unfortunately, is that existing ground-based observations are very limited to small fields of view with narrow bands in the redshift.

Note that from the ground we expect a noise (νI) of $\sim 2.5 \times 10^{-3}$ erg cm^{-2} sr^{-1} (assuming we can avoid the OH lines; otherwise, the intensity will be $\sim 1.0 \times 10^{-1}$ erg cm^{-2} sr^{-1}). From space, the main contamination will be the zodiacal light, which will have a value $\sim 5 \times 10^{-4}$ erg cm^{-2} sr^{-1}. It is possible that a dedicated experiment from the ground can be conceived to improve our understanding of reionization through detailed Lyα mapping over a broad range of redshifts using specific instruments and filters that suppress the atmospheric contamination. Because of this strong atmospheric contamination, sub-orbital and/or orbital experiments may, however, offer a better option. The predictions we have made here can be used as a guide in designing such instruments and experiments.

In Figure 15, we show the expected errors at $z = 7$ (central wavelength of 0.975 μm) for a dedicated compact space-borne template instrument to study Lyα EoR fluctuations. We consider a 20 cm aperture and a spectrometer with resolution

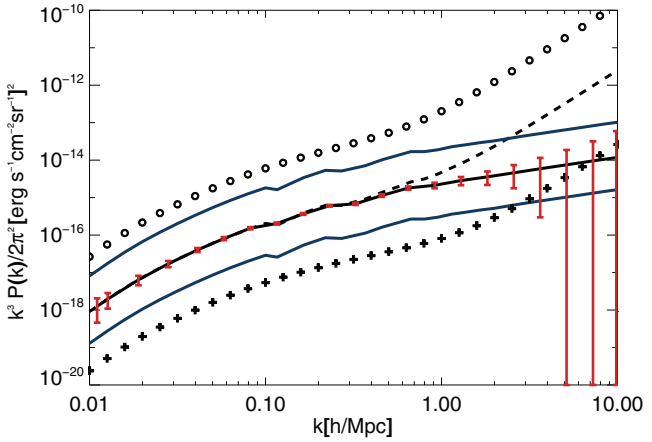

Figure 15. Expected error on the Lyα clustering power spectrum at $z = 7$ using a space-based experiment. Black solid line shows the clustering power spectrum for *Sim3*, while the dashed line includes the shot noise. Red vertical bars show the error. The lower blue solid line shows the clustering power spectrum for *Sim1*, while the top blue solid line shows the same for a model similar to *Sim3* with the same reionization history and optical depth (from *WMAP*) but with an SFR three times larger and a UV escape fraction three times lower, which will generate an Lyα luminosity function larger than what is usually expected at $z = 7$. Circles show the expected Hα power spectrum from $z = 0.5$ that will contaminate the observation, and the crosses give the expected Hα signal after galaxies with an Hα luminosity $>10^{40}\ L_{\odot}$ are removed.

(A color version of this figure is available in the online journal.)

$R = \lambda/\Delta\lambda = 200$. The imaging will be done using a 2048 × 2048 HgCdTe detector array in order to cover in one pointing a field of view of 45 × 45 arcmin with a resolution of 10 arcsec pixels on the sky and a spectral range from 0.85 to 1.10 μm. We took a survey area of 20 deg^2 and a total observation time of 2900 hr. This example shows that Lyα EoR science is well within the reach of our modest template instrument. The calculated sensitivities achieved on the deep fields are sufficient to detect Lyα in broad $\Delta k/k$ bins ranging from $k = 0.01$ to 10 h Mpc^{-1} in both clustering and Poisson fluctuations.

Ideally the spectral resolution would match the maximum k available in the angular direction; however, higher spectral resolution requires longer integration times needed to realize photon noise limited sensitivity, which tends to degrade the instrument sensitivity. The angular resolution does not affect surface brightness sensitivity directly, but it does determine the depth to which lower-redshift galaxies may be masked using a deep ancillary continuum galaxy survey. Although the continuum emission from galaxies can in principle be removed by looking at the signal across the frequency direction, as explained before, contamination from other lines at lower redshifts does pose a problem to the detection of the Lyα signal, in particular from the Hα line. The most straightforward way to remove this contamination would be by masking the pixels where these low-z galaxies are found, either from the observation itself or using another, high-sensitivity, continuum observation. For this approach, the angular resolution of the Lyα experiment has to be good enough in order to have enough pixels left after the masking. Therefore, this instrument is required to have higher angular resolution than spectral resolution. Figure 15 also shows the expected contamination from the Hα line from galaxies at $z = 0.5$ (black dots). This was calculated following the same approach as for the Lyα line and using the Hα-to-SFR relation taken from Kennicutt et al. (1994) and Kennicutt (1998b). Removing low-z galaxies down to a mass of $\sim 6.6 \times 10^{10}\ M_{\odot}$, corresponding to a cut in luminosity $L > 10^{42}$ erg s^{-1}, would bring this contamination below the Lyα signal (black crosses). Using the Hα LF from Geach et al. (2010) normalized to the SFRD at $z = 0.5$, we get an expected angular density of about 25 Hα emitters per square degree per band, which would mean that only ∼0.98% of the pixels would be masked.

Note that the rejection of interloping low-redshift galaxies requires a full treatment that is beyond the scope of this paper. Foreground rejection may also be significantly enhanced by simultaneously detecting additional EoR spectral features beyond Lyα, which are produced by interlopers with very low probability. Combining these Lyα measurements with other EoR observations (CO, C+, and particularly H I 21 cm) offers additional information on EoR star formation, metallicity, and ionization history. The possibility of constructing an experiment in a near-IR band to measure the Lyα flux in order to correlate it with the 21 cm signal was also explored by Wyithe et al. (2007). Although they used simple models to estimate the fluctuations in each of these two lines, they also considered several foregrounds that will contaminate the observations and concluded that it is possible to remove enough foregrounds that the intensity of radiation emitted from galaxies can be constrained from the cross-correlation.

7. SUMMARY

In this paper, we took into account the main contributions to Lyα emission from recombinations, collisions, continuum emission in galaxies, and scattering of Lyn photons to calculate the intensity of Lyα emission from galaxies and from the IGM during the EoR.

We started by theoretically calculating the intensities using astrophysical data from several observational results and then implemented the calculation in a simulation using a modified version of the code SimFast21 to obtain the spatial fluctuations of Lyα emission. The simulation allowed us to calculate the Lyα emission taking into account the spatial fluctuations of the different astrophysical parameters, which represents an improvement over theoretical calculations that only use the average values.

Our simulations showed that to achieve optical depths compatible with the *WMAP* constraints, the high SFRD required implies that for reasonable values of UV and Lyα escape fraction the intensity of Lyα emission from galaxies is dominant over the emission from the IGM.

By testing different SFR halo mass parameterizations, we constrained the intensity of Lyα emission from galaxies to be about (1.43–3.57) × 10^{-8} and (4.55–9.73) × 10^{-11} erg^{-1} cm^{-2} sr^{-1} at redshifts 7 and 10, respectively, which is dominant over the intensity of Lyα emission from the IGM at $z = 7$ (about 1.6×10^{-5}) but less at $z = 10$ (1.1×10^{-10} erg s^{-1} cm^{-2} sr^{-1}). Since the intensity levels we found are lower than the extragalactic background intensity from galaxies and so are too low to be detected with an experiment aiming the absolute background intensity, we propose an intensity mapping experiment that will allow us to measure the Lyα power spectrum.

For reasonable astrophysical conditions the process of hydrogen reionization was done by UV radiation originated in galaxies with luminosities below the high-redshift observational threshold. In this work, we showed the different ways by which UV emission is connected to Lyα emission, and so we stress how

it would be useful to use intensity mapping of Lyα emission to probe the overall intensity of UV radiation.

Lyα emission can also be connected to the 21 cm signal from the EoR, since the continuum photons above the Lyα line that redshift to this line in the IGM contribute to the radiative coupling of the 21 cm signal to the gas temperature. The cross-correlation of the Lyα and the 21 cm lines can be used to reduce systematics and foregrounds encountered with 21 cm observations. In particular, the discontinuity of the cross-correlation power spectra will provide constraints in the evolution of the IGM ionized fraction.

In previous studies, we have discussed the use of CO molecular and C II fine-structure atomic lines to complement 21 cm data in the attempt to probe the IGM during reionization. Our study shows that Lyα intensity mapping is also a viable approach to probe reionization and is within experimental reach over the coming decade.

This work was supported by FCT-Portugal with the grant SFRH/BD/51373/2011 for M.B.S. and under grant PTDC/FIS/100170/2008 for M.B.S. and M.G.S.

A.C. and Y.G. acknowledge support from NSF CAREER AST-0645427 and NASA NNX10AD42G at UCI.

M.B.S. was a long-term Visiting Student at UCI, supported by NSF CAREER AST-0645427, when this work was initiated, and she thanks the Department of Physics and Astronomy at UCI for hospitality during her stay.

REFERENCES

Barkana, R., & Loeb, A. 2001, PhR, 349, 125
Barkana, R., & Loeb, A. 2005, ApJ, 626, 1
Bouwens, R. J., Illingworth, G. D., Labbe, I., et al. 2011, Natur, 469, 504
Bouwens, R. J., Illingworth, G. D., Oesch, P. A., et al. 2012a, ApJL, 752, 5
Bouwens, R. J., Illingworth, G. D., Oesch, P. A., et al. 2012b, ApJ, 754, 83
Boylan-Kolchin, M., Springel, V., White, S. D. M., Jenkins, A., & Lemson, G. 2009, MNRAS, 398, 1150
Brown, R. L., & Mathews, W. G. 1970, ApJ, 160, 939
Cantalupo, S., Porciani, C., & Lilly, S. J. 2008, ApJ, 672, 48
Chen, X., & Miralda-Escudé, J. 2008, ApJ, 684, 18
Chuzhoy, L., & Zheng, Z. 2007, ApJ, 670, 912
Conroy, C., & Wechsler, R. H. 2009, ApJ, 696, 620
Cooray, A., Gong, Y., Smidt, J., & Santos, M. G. 2012, ApJ, 756, 92
Davé, R., Cen, R., Ostriker, J. P., et al. 2001, ApJ, 552, 473
Dayal, P., Ferrara, A., & Saro, A. 2010, MNRAS, 402, 1449
De Lucia, G., & Blaizot, J. 2007, MNRAS, 375, 2
Dijkstra, M., Haiman, Z., & Spaans, M. 2006a, ApJ, 649, 14
Dijkstra, M., Haiman, Z., & Spaans, M. 2006b, ApJ, 649, 37
Dopita, M. A., & Sutherland, R. S. 2003, Astrophysics of the Diffuse Universe (Berlin: Springer)
Fan, X., Strauss, M. A., Becker, R. H., et al. 2006, AJ, 132, 117
Fardal, M. A., Katz, N., Gardner, J. P., et al. 2001, ApJ, 562, 605
Fernandez, E. R., & Komatsu, E. 2006, ApJ, 646, 703
Fernández-Soto, A., Lanzetta, K. M., & Chen, H.-W. 2003, MNRAS, 342, 1215
Forero-Romero, J. E., Yepes, G., Gottlöber, S., et al. 2011, MNRAS, 415, 3666
Furlanetto, S. R., Oh, S. P., & Briggs, F. H. 2006, PhR, 433, 181
Geach, J. E., Cimatti, A., Percival, W., et al. 2010, MNRAS, 402, 1330
Gnedin, N. Y., Kravtsov, A. V., & Chen, H.-W. 2008, ApJ, 672, 765
Gong, Y., Cooray, A., Silva, M., et al. 2012, ApJ, 745, 49
Gong, Y., Cooray, A., Silva, M. B., Santos, M. G., & Lubin, P. 2011, ApJL, 728, 46
Gould, A., & Weinberg, D. H. 1996, ApJ, 468, 462
Guo, Q., White, S., Boylan-Kolchin, M., et al. 2011, MNRAS, 413, 101
Haardt, F., & Madau, P. 2012, ApJ, 746, 125
Haiman, Z., Spaans, M., & Quataert, E. 2000, ApJL, 537, 5
Hayes, M., Schaerer, D., Östlin, G., et al. 2011, ApJ, 730, 8
Iye, M., Ota, K., Kashikawa, N., et al. 2006, Natur, 443, 186
Jensen, H., Laursen, P., Mellema, G., et al. 2013, MNRAS, 428, 1366
Jiang, L., Egami, E., Kashikawa, N., et al. 2011, ApJ, 743, 65
Karzas, W. J., & Latter, R. 1961, ApJS, 6, 167
Kashikawa, N., Shimasaku, K., Malkan, M. A., et al. 2006, ApJ, 648, 7
Kennicutt, R. C., Jr. 1998a, ARA&A, 36, 189
Kennicutt, R. C., Jr. 1998b, ApJ, 498, 541
Kennicutt, R. C., Jr., Tamblyn, P., & Congdon, C. E. 1994, ApJ, 435, 22
Komatsu, E., Smith, K. M., Dunkley, J., et al. 2011, ApJS, 192, 18
Larson, D., Dunkley, J., Hinshaw, G., et al. 2011, ApJS, 192, 16
Latif, M. A., Schleicher, D. R. G., Spaans, M., & Zaroubi, S. 2011, MNRAS, 413, L33
Lehnert, M. D., Nesvadba, N. P. H., Cuby, J.-G., et al. 2010, Natur, 467, 940
Lidz, A., Furlanetto, S. R., Oh, S. P., et al. 2011, ApJ, 741, 70
Madau, P., & Pozzetti, L. 2000, MNRAS, 312, L9
Maraston, C. 2005, MNRAS, 362, 799
Martin, P. G. 1988, ApJS, 66, 125
Mesinger, A., & Furlanetto, S. 2007, ApJ, 669, 663
Mesinger, A., & Haiman, Z. 2007, ApJ, 660, 923
Mitra, S., Choudhury, T. R., & Ferrara, A. 2012, MNRAS, 419, 1480
Oesch, P. A., Bouwens, R. J., Illingworth, G. D., et al. 2012, ApJ, 745, 110
Ota, K., Iye, M., Kashikawa, N., et al. 2008, ApJ, 677, 12
Ota, K., Iye, M., Kashikawa, N., et al. 2010, ApJ, 722, 803
Ouchi, M., Shimasaku, K., Akiyama, M., et al. 2008, ApJS, 176, 301
Ouchi, M., Shimasaku, K., Furusawa, H., et al. 2010, ApJ, 723, 869
Pawlik, A. H., Schaye, J., & van Scherpenzeel, E. 2010, in ASP Conf. Ser. 432, New Horizons in Astronomy: Frank N. Bash Symposium 2009, ed. L. M. Stanford, J. D. Green, L. Hao, & Y. Mao (San Francisco, CA: ASP), 230
Pengelly, R. M. 1964, MNRAS, 127, 145
Popesso, P., Biviano, A., Rodighiero, G., et al. 2012, A&A, 537, A58
Razoumov, A. O., & Sommer-Larsen, J. 2010, ApJ, 710, 1239
Salvaterra, R., Della Valle, M., Campana, S., et al. 2009, Natur, 461, 1258
Santos, M. G., Ferramacho, L., Silva, M. B., Amblard, A., & Cooray, A. 2010, MNRAS, 406, 2421
Santos, M. G., Silva, M. B., Pritchard, J. R., Cen, R., & Cooray, A. 2011, A&A, 527, A93
Santos, M. R. 2004, MNRAS, 349, 1137
Schaerer, D. 2002, A&A, 382, 28
Sheth, R. K., & Tormen, G. 1999, MNRAS, 308, 119
Shibuya, T., Kashikawa, N., Ota, K., et al. 2012, ApJ, 752, 114
Shimasaku, K., Kashikawa, N., Doi, M., et al. 2006, PASJ, 58, 313
Shull, J. M., & van Steenberg, M. E. 1985, ApJ, 298, 268
Shull, M., Harness, A., Trenti, M., & Smith, B. 2012, ApJ, 747, 100
Siana, B., Teplitz, H. I., Colbert, J., et al. 2007, ApJ, 668, 62
Smith, B. D., Hallman, E. J., Shull, J. M., & O'Shea, B. W. 2011, ApJ, 731, 6
Springel, V., White, S. D. M., Jenkins, A., et al. 2005, Natur, 435, 629
Steidel, C. C., Bogosavljević, M., Shapley, A. E., et al. 2011, ApJ, 736, 160
Taniguchi, Y., Ajiki, M., Nagao, T., et al. 2005, PASJ, 57, 165
Visbal, E., & Loeb, A. 2010, JCAP, 11, 16
Wang, X., Tegmark, M., Santos, M. G., & Knox, L. 2006, ApJ, 650, 529
Wise, J. H., & Cen, R. 2009, ApJ, 693, 984
Wyithe, S., Loeb, A., & Schmidt, B. 2007, arXiv:0705.1825
Yajima, H., Choi, J.-H., & Nagamine, K. 2011, MNRAS, 412, 411
Zahn, O., Reichardt, C. L., Shaw, L., et al. 2012, ApJ, 756, 65
Zaldarriaga, M., Colombo, L., Komatsu, E., et al. 2008, arXiv:0811.3918
Zheng, Z., Cen, R., Trac, H., & Miralda-Escudé, J. 2010, ApJ, 716, 574
Zheng, Z., Cen, R., Weinberg, D., Trac, H., & Miralda-Escudé, J. 2011, ApJ, 739, 62

A.5 Paper V

Foreground contamination in Lyman alpha intensity mapping during the Epoch of Reionization

Gong Y., **Silva M. B.**, Cooray A. and Santos M. G.
The Astrophysical Journal, 785:1, 72 (2012)
arXiv:1312.2035

Draft version March 3, 2014
Preprint typeset using LaTeX style emulateapj v. 5/2/11

FOREGROUND CONTAMINATION IN LYα INTENSITY MAPPING DURING THE EPOCH OF REIONIZATION

Yan Gong[1], Marta Silva[2,3], Asantha Cooray[1], and Mario G. Santos[2,3,4]
[1]Department of Physics & Astronomy, University of California, Irvine, CA 92697
[2]CENTRA, Instituto Superior Tecnico, Technical University of Lisbon, Lisboa 1049-001, Portugal
[3]Department of Physics, University of Western Cape, Cape Town 7535, South Africa and
[4]SKA SA, 3rd Floor, The Park, Park Road, Pinelands, 7405, South Africa

Draft version March 3, 2014

ABSTRACT

The intensity mapping of Lyα emission during the epoch of reionization (EoR) will be contaminated by foreground emission lines from lower redshifts. We calculate the mean intensity and the power spectrum of Lyα emission at $z \sim 7$, and estimate the uncertainties according to the relevant astrophysical processes. We find that the low-redshift emission lines from 6563 Å Hα, 5007 Å [OIII] and 3727 Å [OII] will be strong contaminants on the observed Lyα power spectrum. We make use of both the star formation rate (SFR) and luminosity functions (LF) to estimate the mean intensity and power spectra of the three foreground lines at $z \sim 0.5$ for Hα, $z \sim 0.9$ for [OIII] and $z \sim 1.6$ for [OII], as they will contaminate the Lyα emission at $z \sim 7$. The [OII] line is found to be the strongest. We analyze the masking of the bright survey pixels with a foreground line above some line intensity threshold as a way to reduce the contamination in an intensity mapping survey. We find that the foreground contamination can be neglected if we remove pixels with fluxes above 1.4×10^{-20} W/m^2.

Subject headings: cosmology: theory - diffuse radiation - intergalactic medium - large-scale structure of universe

1. INTRODUCTION

The epoch of reionization (EoR) is an important and largely unconstrained stage in the evolution of our universe (Barkana & Loeb 2001). The first stars and galaxies can start ionization of the neutral intergalactic medium (IGM) as early as $z \sim 20$ or even before while completion of the ionization process should end much later, at a redshift as low as $z \sim 6$. This is suggested by the observations of the absorption of the Lyα emission from quasars by the neutral hydrogen in the IGM (Fan et al. 2006), i.e. the Gunn-Peterson effect (Gunn & Peterson 1965). Most of the fundamental stones of this era are still poorly known, such as the history, the formation and evolution of the stars and galaxies, and the formation of large scale structure (LSS).

One method to study the EoR is through 21-cm emission of neutral hydrogen in the IGM (Furlanetto et al. 2006), which provides a direct method to study the ionization history of the IGM. However, the 21-cm measurement can not directly trace the galaxy distribution or reflect the star formation. It also suffers from foreground contamination at several orders of magnitude higher than the cosmological 21-cm signal. These disadvantages restrict the 21-cm measurements to explore the LSS and the processes of the formation and evolution for stars and galaxies during the EoR.

A complementary measurement to 21-cm observations is the intensity mapping of the emission lines. This approach is more closely connected to the galaxy properties. The emission lines generated from the stars and molecular or atomic gas in galaxies are more sensible probes of the metallicity and star formation of galaxies. They trace the galaxy distribution at large scales, providing information about the LSS. Several emission lines from galaxies have been proposed to study the EoR (Visbal & Loeb 2010), e.g. CO rotational lines (Righi et al. 2008; Gong et al. 2011; Carilli 2011; Lidz et al. 2011), [CII] fine structure line (Gong et al. 2012), and the Lyα line (Silva et al. 2013; Pullen et al. 2013). Even molecular hydrogen H_2 in the pre-reionization era can be used to study the formation of first stars and galaxies (Gong et al. 2013).

The intensity mapping technique is a powerful tool to explore large areas at poor spatial or angular resolution. It does not attempt to resolve individual sources, but measures the cumulative emission from all sources. Thus, intensity mapping of emission lines from galaxies provides a suitable way to study the statistical properties of galaxies during the EoR in an acceptable survey timescale. However, intensity maps are easily contaminated by other emission lines from lower redshifts in the same observed frequency range. Since intensity mapping cannot resolve individual sources, it is important to independently identify and eliminate the contamination from the foreground lines.

In this work, we study the foreground contamination on Lyα intensity maps of the EoR. We first compute the Lyα emission from both galaxies and the IGM due to recombination and collision processes. We calculate the Lyα mean intensity and power spectrum at $z \sim 7$. We find the 6563 Å Hα, 5007 Å [OIII] and 3727 Å [OII] are the strongest contamination on the Lyα observations. We estimate the mean intensities of these three lines using the star formation rate (SFR) derived from observations and simulations. Also, for comparison, we make use of luminosity functions (LFs) from different observations to calculate the mean intensities and derive their anisotropy power spectra. We then discuss ways to remove contamination by masking the bright pixels of the intensity maps.

The paper is organized as follows: in the next Section, we estimate the Lyα emission from both galaxies and the IGM, and calculate the mean intensity and power spectrum during the EoR. In Section 3, we explore the intensity and power spectra of the foreground emission lines of the Hα, [OII] and [OIII] around $z = 0.5$, 0.9 and 1.6 that can contaminate the Lyα emission at $z \sim 7$, and derive their mean intensity and power spectra. In Section 4, we discuss the projection effect of the foreground power spectra and investigate the methods of removing the foreground contamination from low-redshift emission lines. We summarize our results in Section 5. We assume the flat ΛCDM with $\Omega_{\rm M} = 0.27$, $\Omega_{\rm b} = 0.046$, and $h = 0.71$ for the calculation throughout the paper (Komatsu et al. 2011).

2. THE LYα INTENSITY AND ANISOTROPY POWER SPECTRUM DURING THE EOR

In this Section, we estimate the mean intensity and power spectrum of the Lyα emission during the EoR. The processes that originate Lyα in galaxies and in the IGM are mainly recombinations and collisions. The other processes, e.g. gas cooling by the falling of the IGM gas into the potential wells of the dark matter, and continuum emission by stellar, free-free, free-bound and two-photon emission, can be safely neglected according to previous studies (Cooray et al. 2012; Silva et al. 2013).

2.1. *The Lyα mean intensity*

Following Silva et al. (2013), we estimate the luminosity of the Lyα emission from galaxies by the recombination and collision processes as

$$L^{\rm gal}_{\rm rec}(M,z) = 1.55\times10^{42}\ f_{{\rm Ly}\alpha}(z)\ [1-f^{\rm ion}_{\rm esc}(M,z)] \times\ \frac{{\rm SFR}(M,z)}{M_\odot\ {\rm yr}^{-1}}\ ({\rm erg\ s}^{-1}), \quad (1)$$

$$L^{\rm gal}_{\rm coll}(M,z) = 4.03\times10^{41}\ f_{{\rm Ly}\alpha}(z)\ [1-f^{\rm ion}_{\rm esc}(M,z)] \times\ \frac{{\rm SFR}(M,z)}{M_\odot\ {\rm yr}^{-1}}\ ({\rm erg\ s}^{-1}), \quad (2)$$

respectively [1]. Here the $f_{{\rm Ly}\alpha} = 10^{-3}\times C_{\rm dust}(1+z)^\xi$ is the fraction of the Lyα photons which are not absorbed by the dust in the galaxy, where $C_{\rm dust} = 3.34$ and $\xi = 2.57$ (Hayes et al. 2011). Note that this fitting formula is mainly derived from low-redshift sources and extrapolated to high redshifts ($z > 6$). The $f_{{\rm Ly}\alpha}$ can be much lower at $z \sim 7$ (e.g. Stark et al. 2010, 2011). The $f^{\rm ion}_{\rm esc} = \exp[-\alpha(z)M^{\beta(z)}]$ is the escape fraction of the ionizing photons, where M is the halo mass, and $\alpha = 5.18\times10^{-3}$ and $\beta = 0.244$ (Razoumov & Sommer-Larsen 2010; Silva et al. 2013). The ${\rm SFR}(M,z)$ is the star formation rate, which is parameterized as

$${\rm SFR}(M,z=7) = 1.6\times10^{-26}\ M^a\left(1+\frac{M}{c_1}\right)^b \times\left(1+\frac{M}{c_2}\right)^d\left(1+\frac{M}{c_3}\right)^e, \quad (3)$$

[1] Note that the ratio $L^{\rm gal}_{\rm coll}/L^{\rm gal}_{\rm rec} = 0.26$ can be larger at high redshifts due to strong galaxy forming process (Laursen et al. 2013). This ratio is still observationally unconstrained, and also has large uncertainty suggesting by simulations.

where $a = 2.59$, $b = -0.62$, $c_1 = 8\times10^8\ M_\odot$, $c_2 = 7\times10^9\ M_\odot$, $c_3 = 10^{11}\ M_\odot$, $d = 0.4$ and $e = -2.25$. This SFR parameterization was derived to fit the properties of the simulated galaxies catalogs from De Lucia et al. (2007) and Guo et al. (2011),and is available at $z = 7$ in (Silva et al. 2013). Then the integrate Lyα mean intensity from individual galaxies is given by

$$\bar{I}_{\rm gal}(z) = \int_{M_{\rm min}}^{M_{\rm max}} dM\frac{dn}{dM}\frac{L_{\rm gal}(M,z)}{4\pi D_{\rm L}^2}y(z)D_{\rm A}^2, \quad (4)$$

where $L^{\rm gal} = L^{\rm gal}_{\rm rec} + L^{\rm gal}_{\rm coll}$ is the total luminosity of Lyα emission from galaxies, dn/dM is the halo mass function (Sheth & Tormen 1999), and $D_{\rm L}$ and $D_{\rm A}$ are the luminosity and comoving angular diameter distance respectively. The factor $y(z) = dr/d\nu = \lambda_{{\rm Ly}\alpha}(1+z)^2/H(z)$, where $r(z)$ is the comoving distance at z, $\lambda_{{\rm Ly}\alpha} = 1216$ Å is the Lyα wavelength in the rest frame, and $H(z)$ is the Hubble parameter. We take $M_{\rm min} = 10^8\ h^{-1}M_\odot$ and $M_{\rm min} = 10^{13}\ h^{-1}M_\odot$, which denote the mass range of the halos that host the galaxies with the Lyα emission in this work.

For the Lyα emission from the IGM, we use the luminosity density to estimate the mean intensity

$$\bar{I}_{\rm IGM} = \frac{l^{\rm IGM}(z)}{4\pi D_{\rm L}^2}\ y(z)D_{\rm A}^2, \quad (5)$$

where $l^{\rm IGM} = l^{\rm IGM}_{\rm rec} + l^{\rm IGM}_{\rm coll}$ is the Lyα luminosity density for the IGM in erg s^{-1}cm^{-3}. The $l^{\rm IGM}_{\rm rec}$ and $l^{\rm IGM}_{\rm coll}$ are the luminosity densities from recombination and collision processes, respectively. The $l^{\rm IGM}_{\rm rec}$ can be estimated by $l^{\rm IGM}_{\rm rec} = \epsilon^{\rm rec}_{{\rm Ly}\alpha}h\nu_{{\rm Ly}\alpha}$, where $\epsilon^{\rm rec}_{{\rm Ly}\alpha}$ is the Lyα recombination emission rate per cm^3, which is given by

$$\epsilon^{\rm rec}_{{\rm Ly}\alpha} = f^{\rm rec}_{{\rm Ly}\alpha}n_e n_{\rm HII}\alpha^{\rm rec}_{\rm B}. \quad (6)$$

The n_e and $n_{\rm HII}$ are the number density of the electron and HII. Here we have $n_e n_{\rm HII} = C_{\rm IGM}(z)\bar{n}_e(z)\bar{n}_{\rm HII}(z)$, where $\bar{n}_e(z)$ and $\bar{n}_{\rm HII}(z)$ are the mean number density of the electron and HII at z, which are dependent on the reionization fraction $x_{\rm i}$ during the EoR. The $C_{\rm IGM}(z) = \langle n^2\rangle/\langle n\rangle^2$ is the clumping factor of the IGM at z which can be set by $C_{\rm IGM} = 6$ at z=7 (Pawlik et al. 2009; Silva et al. 2013). The $\alpha^{\rm rec}_{\rm B}$ is the hydrogen case B recombination coefficient which can be fitted by (Hummer 1994; Seager et al. 1999)

$$\alpha^{\rm rec}_{\rm B}(T) = 10^{-13}\frac{aT_4^b}{1+cT_4^d}\ ({\rm cm}^3/{\rm s}), \quad (7)$$

where $a = 4.309$, $b = -0.6166$, $c = 0.6703$, $d = 0.5300$, and $T_4 = T/10^4$ K. The $f^{\rm rec}_{{\rm Ly}\alpha}$ is the the fraction of the Lyα photons produced in the case B recombination, and we use the fitting formula from Cantalupo et al. (2008) to evaluate it as

$$f^{\rm rec}_{{\rm Ly}\alpha}(T) = 0.686 - 0.106\log_{10}(T_4) - 0.009T_4^{-0.44}. \quad (8)$$

This formula is accurate to 0.1% for $100 < T < 10^5$K. We assume the mean gas temperature of the IGM to be 1.5×10^4 K in this work, which is in a good agreement with the results from simulations and the current measurements from quasars (Theuns et al. 2002;

Tittley et al. 2007; Trac et al. 2008; Bolton et al. 2010, 2012).

The Lyα collisional emission in the IGM involves free electrons that collide with the neutral hydrogen atoms (HI) and transfer their kinetic energy by exciting the HI to high energy levels. The hydrogen atoms then decay by emitting photons, including Lyα photons. During the EoR, this process mainly occurs in the ionizing fronts of the reionization bubbles, since this emission will be the strongest when $n_e \sim n_{\rm HI}$. Similar to the recombination emission, the luminosity density of the collisional emission in the IGM can be calculated by $l_{\rm coll}^{\rm IGM} = \epsilon_{\rm Ly\alpha}^{\rm coll} h\nu_{\rm Ly\alpha}$. The $\epsilon_{\rm Ly\alpha}^{\rm coll}$ is the collisional emission rate per cm^3

$$\epsilon_{\rm Ly\alpha}^{\rm coll} = C_{\rm Ly\alpha}^{\rm eff} n_e n_{\rm HI}, \tag{9}$$

where $n_{\rm HI}$ is the number density of the neutral hydrogen atoms. We assume $n_e n_{\rm HI} = f_{\rm front}^{\rm ion} C_{\rm IGM}(z)\bar{n}_e(z)\bar{n}_{\rm HI}(z)$, where $\bar{n}_{\rm HI}(z)$ is the mean number density of neutral hydrogen at z. The $f_{\rm front}^{\rm ion}$ is the volume fraction of the bubble ionizing fronts. Because the ionizing front just takes a very small part of the whole ionizing bubble, as a good approximation, the volume fraction of the ionizing front can be estimated as $f_{\rm front}^{\rm ion} = \frac{4}{3}\pi(r_2^3 - r_1^3)$, where $r_1 = [(3/4\pi)x_{\rm i}]^{1/3}$, and $r_2 = r_1 + d$ and $d = \frac{1}{6}[n_{\rm H}\sigma_{\rm H}(\langle\nu\rangle)]^{-1}$ is the thickness of the bubble ionizing front. The factor 1/6 is derived from the integration of $x_{\rm HI}(1 - x_{\rm HI})$ over the ionizing front where $x_{\rm HI}(r)$ is the fraction of the HI in the front at radius r (Cantalupo et al. 2008). Here $\sigma_{\rm H}$ denotes the cross section of the hydrogen ionization, where $\langle\nu\rangle$ is the mean frequency of the ionizing photons, and it is given by (Osterbrock 1989)

$$\sigma_{\rm H}(\nu) = \frac{\sigma_0}{1 - \exp(-2\pi/\epsilon)} \left[\frac{\nu_0}{\nu}\exp\left(1 - \frac{\tan^{-1}\epsilon}{\epsilon}\right)\right]^4. \tag{10}$$

Here ν_0 is the Lyman limit frequency, $\sigma_0 = 6.3 \times 10^{-18}$ cm^2 and $\epsilon \equiv (\nu/\nu_0 - 1)^{1/2}$. Here we take $\langle\nu\rangle = 2.4\nu_0$ in our calculation (Gould & Weinberg 1996). Note that we set $f_{\rm front}^{\rm ion} = 0$ when $x_{\rm i} \geq 1$, which means there is no collisional emission in the IGM when the universe is totally ionized.

In Eq. (9), the $C_{\rm Ly\alpha}^{\rm eff}$ is the effective collisional excitation coefficient, which can be estimated by (Cantalupo et al. 2008)

$$C_{\rm Ly\alpha}^{\rm eff} = C_{1,2p} + C_{1,3s} + C_{1,3d}\,. \tag{11}$$

Here we take into account the excitation up to $n = 3$ energy level to decay and produce Lyα photons. The contribution of emission from higher energy levels can be neglected at $z \approx 7$ given that the gas temperature and density of the IGM are on average too low to excite these levels. The collisional excitation rate $C_{\rm l,u}$, in cm^3 per second, is given by

$$C_{\rm l,u} = \frac{8.629 \times 10^{-6}}{g_{\rm l}\sqrt{T}}\gamma_{\rm l,u}(T)\exp\left(\frac{-\Delta E_{\rm l,u}}{kT}\right)\ ({\rm cm}^3/{\rm s}), \tag{12}$$

where T is the gas temperature that we assume $T = 1.5 \times 10^4$ K, $\Delta E_{\rm l,u}$ is the energy difference between lower level and higher level, $g_{\rm l}$ is the statistic weight for lower level, and $\gamma_{\rm l,u}(T)$ is the effective collision strength calculated by the fitting formulae from Giovanardi et al. (1987).

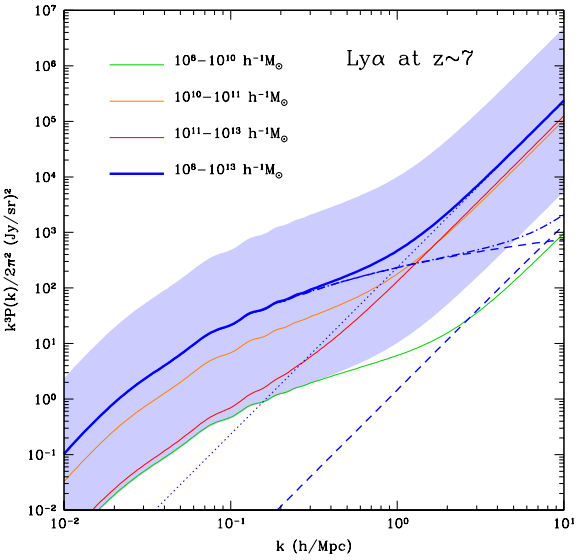

FIG. 1.— The power spectrum of the Lyα emission at $z = 7$. The dash-dotted line is the clustering power spectrum which consists of 1-halo and 2-halo components in dashed lines, the dotted line denotes the shot-noise power spectrum, and the total power spectrum is shown in solid line. The uncertainty of the power spectrum is shown in shaded region which is estimated by the uncertainties of the $f_{\rm esc}^{\rm ion}$, $f_{\rm Ly\alpha}$, SFR and IGM clumping factor. The contributions of different halo mass scales to the total power spectrum are also shown. We find 10^{10}-10^{11} $h^{-1}M_\odot$ dominates the clustering power spectrum.

Then we estimate the total mean intensity of the Lyα emission $\bar{I}_{\rm Ly\alpha} = \bar{I}_{\rm gal} + \bar{I}_{\rm IGM}$ using Eq. (4) and Eq. (5). At $z \sim 7$, we get $\bar{I}_{\rm gal} = 9.2$ Jy/sr and $\bar{I}_{\rm IGM} = 1.2$ Jy/sr if assuming $\bar{x}_{\rm i} = 0.85$. Thus, according to the assumptions we have made, Lyα emission from galaxies is larger than that from the IGM around $z = 7$. Note that the collisional emission in the IGM is much smaller than the recombination emission with $\bar{I}_{\rm coll}^{\rm IGM} \simeq 0.1$ Jy/sr and $\bar{I}_{\rm rec}^{\rm IGM} \simeq 1.1$ Jy/sr,respectively, assuming $T = 1.5 \times 10^4$ K for the gas temperature of the IGM.

There are large uncertainties for the parameters in the estimation of the Lyα intensity. According to the current measurements (Razoumov & Sommer-Larsen 2010; Hayes et al. 2011; Blanc et al. 2011), we find the $f_{\rm esc}^{\rm ion}$ and $f_{\rm Ly\alpha}$ [2] in Eq. (1) and (2) have an uncertainty of a factor of 2 each. Besides, we take into account of the uncertainties in the SFR and the clumping fator, which can be factors of 3 and 5 at $z \sim 7$ respectively (Silva et al. 2013). Eventually, we find $\bar{I}_{\rm Ly\alpha} = 10.4^{+39.3}_{-9.0}$ Jy/sr around

[2] This $f_{\rm Ly\alpha}$ is Lyα "effective" escape fraction instead of real escape fraction which should include the scattered Lyα emission from the diffuse halos surrounding galaxies (Dijkstra & Jeeson-Daniel 2013). The Lyα emission from the diffuse halos has low surface brightness, but the total flux can exceed the direct emission from galaxies by a significant factor (e.g. Zheng et al. 2010; Steidel et al. 2010; Matsuda et al. 2012). Thus the real Lyα escape fraction can be much larger than the effective escape fraction. This diffused emission could contribute to the intensity mapping. We find our fiducial $f_{\rm Ly\alpha} \simeq 0.7$ at $z = 7$ which is close to one, and we also add an uncertainty of a factor of 2 on it. So the effect of the diffused Lyα emission is safely covered in our calculation.

$z = 7$. Our results are well consistent with other works when allowing for uncertainty (e.g. Silva et al. 2013; Pullen et al. 2013). Besides, we note that the estimated Lyα emission of high-z metal-poor galaxies with standard case-B assumption can be underestimated by a factor of $\sim 2-3$ compared to accurate prediction (Raiter et al. 2010). This possible departure can be covered by the intensity uncertainty we consider.

2.2. *The Lyα power spectrum*

According to the calculations above, the absolute value of the Lyα intensity background during the EoR is small and hard to measure directly in an absolute intensity experiment. Instead, we can try to measure the fluctuations of the Lyα intensity and estimate the anisotropy power spectrum. Since the Lyα emission from galaxies and IGM in the ionization bubbles surrounding the galaxies trace the underlying matter density field, we can calculate the Lyα intensity fluctuations by

$$\delta I_{\rm Ly\alpha} = \bar{b}_{\rm Ly\alpha}\bar{I}_{\rm Ly\alpha}\delta(\mathbf{x}). \quad (13)$$

Here we set $\bar{I}_{\rm Ly\alpha} \simeq \bar{I}_{\rm gal}$, since the main Ly$\alpha$ emission at $z \sim 7$ comes from galaxies. The $\delta(\mathbf{x})$ is the matter over-density at the position $\mathbf{x}$, and $\bar{b}_{\rm Ly\alpha}(z)$ is the average galaxy bias weighted by the Lyα luminosity

$$\bar{b}_{\rm Ly\alpha}(z) = \frac{\int_{M_{\rm min}}^{M_{\rm max}} dM \frac{dn}{dM} L_{\rm gal}^{\rm Ly\alpha} b(M,z)}{\int_{M_{\rm min}}^{M_{\rm max}} dM \frac{dn}{dM} L_{\rm gal}^{\rm Ly\alpha}}, \quad (14)$$

where $L_{\rm gal}^{\rm Ly\alpha}(M,z)$ is the Lyα luminosity of the galaxy, and $b(M,z)$ is the halo bias (Sheth & Tormen 1999). Then we can calculate the Lyα clustering power spectrum due to galaxy clustering as

$$P_{\rm Ly\alpha}^{\rm clus}(k,z) = \bar{b}_{\rm Ly\alpha}^2 \bar{I}_{\rm Ly\alpha}^2 P_{\delta\delta}(k,z), \quad (15)$$

where $P_{\delta\delta}(k,z)$ is the matter power spectrum which can be estimated from the halo model (Cooray & Sheth 2002). The clustering power spectrum dominates the fluctuations at large scales. At small scales the Poisson noise caused by the discrete distribution of galaxies becomes important. This Poisson or shot-noise power spectrum takes the form (e.g. Visbal & Loeb 2010; Gong et al. 2011):

$$P_{\rm Ly\alpha}^{\rm shot}(z) = \int_{M_{\rm min}}^{M_{\rm max}} dM \frac{dn}{dM} \left[\frac{L_{\rm gal}^{\rm Ly\alpha}}{4\pi D_{\rm L}^2} y(z) D_{\rm A}^2\right]^2. \quad (16)$$

Therefore, the total power spectrum can be written by $P_{\rm Ly\alpha}^{\rm tot}(k,z) = P_{\rm Ly\alpha}^{\rm clus}(k,z) + P_{\rm Ly\alpha}^{\rm shot}(z)$. In Figure 1, we show the Lyα power spectrum at $z = 7$. We show the total, clustering and shot-noise power spectrum in solid, dash-dotted and dotted line, respectively. The dashed lines denote the 1-halo and 2-halo terms of the clustering power spectrum. The uncertainty of the total power spectrum is also shown in shaded region, which is derived from the uncertainties of the $f_{\rm esc}^{\rm ion}$, $f_{\rm Ly\alpha}$, SFR and IGM clumping factor. We also show the contributions of different halo mass scales to the total power spectrum in colored solid lines. As can be seen, the halos with mass 10^{10}-10^{11} $h^{-1}M_\odot$ provide the most contribution on the clustering power spectrum, and the halos with higher masses (10^{11}-10^{13} $h^{-1}M_\odot$) have large shot-noise since they are bright and rare. We find $\bar{b}_{\rm Ly\alpha} = 5.0$ and $P_{\rm Ly\alpha}^{\rm shot} = 4.6\times10^3$ (Jy/sr)^2(Mpc/h)$^{-3}$ at $z = 7$, and the shot-noise power spectrum dominates the total power spectrum at $k \gtrsim 1$ Mpc^{-1}h.

3. THE ESTIMATION OF THE FOREGROUND EMISSION LINES

Since we can not resolve individual sources with intensity mapping, the measurements of the Lyα emission during the EoR can be contaminated by emission lines from lower redshifts. Here we consider three low-redshift emission lines, Hα at 6563 Å, [OIII] at 5007 Å and [OII] at 3727 Å. At $z \sim 7$, the frequency of the Lyα line is about 300 THz, which can be then contaminated by Hα at $z \sim 0.5$, [OIII] at $z \sim 0.9$ and [OII] at $z \sim 1.6$, respectively. We will estimate the mean intensity and power spectra of these lines in this Section.

3.1. *The mean intensity from the SFR*

The Hα line at 6563 Å, [OIII] line at 5007 Å and [OII] line at 3727 Å are good tracers of the SFR of galaxies. The luminosity of these lines is related to the SFR as

$$\mathrm{SFR}\,(M_\odot \mathrm{yr}^{-1}) = (7.9\pm2.4)\times10^{-42} L_{\rm H\alpha}, \quad (17)$$

$$\mathrm{SFR}\,(M_\odot \mathrm{yr}^{-1}) = (1.4\pm0.4)\times10^{-41} L_{\rm [OII]}, \quad (18)$$

$$\mathrm{SFR}\,(M_\odot \mathrm{yr}^{-1}) = (7.6\pm3.7)\times10^{-42} L_{\rm [OIII]}. \quad (19)$$

The luminosity here is in erg s^{-1}, and the relations for Hα and [OII] are from Kennicutt (1998), and the [OIII] relation is given in Ly et al. (2007). The SFR-$L_{\rm H\alpha}$ relation assumes the initial mass function from Salpeter (1955), and we add 30% uncertainty to it. These conversions are also in good agreement with other works[3] (e.g. Hopkins et al. 2003; Wijesinghe et al. 2011; Drake et al. 2013). With the help of the relation of the SFR and the halo mass as a function of redshift SFR(M,z), we can use these conversions to derive $L(M,z)$ and compute the mean intensities for these lines using Eq. (4).

To estimate the SFR(M,z), we can make use of the SFRD(z) from the observations and assume the SFR is proportional to the halo mass M. We take the SFRD(z) given by Hopkins & Beacom (2006) with the fitting formula from Cole et al. (2001)

$$\mathrm{SFRD}(z) = \frac{a+bz}{1+(z/c)^d}\ (h\,M_\odot \mathrm{yr}^{-1}\mathrm{Mpc}^{-3}), \quad (20)$$

where $a = 0.0118$, $b = 0.08$, $c = 3.3$ and $d = 5.2$. This fitting formula is consistent with the observational data very well, especially at $z \lesssim 2$, which is good enough for our estimations here. Then assuming

$$\mathrm{SFR}(M,z) = f_*(z)\frac{\Omega_{\rm b}}{\Omega_{\rm M}}\frac{1}{t_{\rm s}}M, \quad (21)$$

where $t_{\rm s} = 10^8$ yr is the typical star formation timescale, and $f_*(z)$ is the normalization factor which can be determined by $\mathrm{SFRD}(z) = \int dM \frac{dn}{dM}\mathrm{SFR}(M,z)$. After obtaining SFR$(M,z)$, we can derive $L(M,z)$ for the Hα, [OII]

[3] The SFR-L$_{\rm [OII]}$ relation has a larger uncertainty, and we will discuss it in Section 3.2.

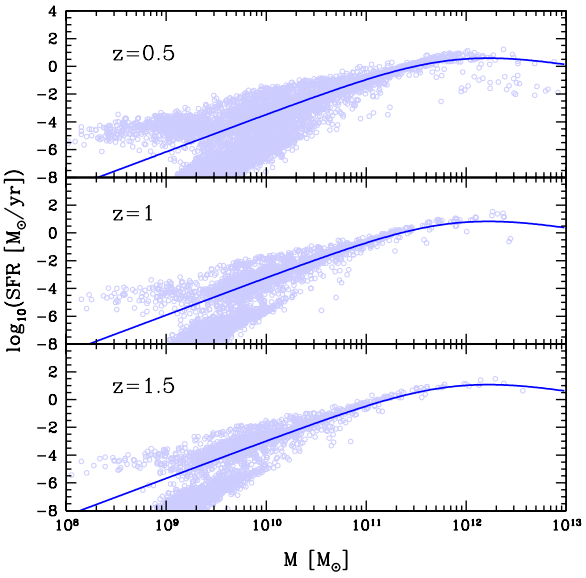

FIG. 2.— The SFR vs. halo mass M at $z = 0.5$, $z = 1$ and $z = 1.5$ from the simulations. The dots are from the galaxy catalog in the simulations of Guo et al. (2011) and the curves are the best fits of the SFR(M).

and [OIII] lines using Eq. (17), (18) and (19) respectively, and then calculate their mean intensities with Eq. (4). We find $\bar{I}_{\rm H\alpha} = 31.2 \pm 9.4$ Jy/sr, $\bar{I}_{\rm [OII]} = 17.5 \pm 5.0$ Jy/sr and $\bar{I}_{\rm [OIII]} = 35.0 \pm 17.0$ Jy/sr. The errors are derived from the uncertainties in the conversions of the SFR and luminosity given by Eq. (17), (18) and (19).

Another way to obtain the SFR(M, z) is with simulations. Here we use the galaxy catalog from Guo et al. (2011), which is obtained by Millennium II simulation with a volume of 100 $({\rm Mpc}/h)^3$ and particle mass resolution $\sim 6.9 \times 10^6\ h^{-1} M_\odot$ (Boylan-Kolchin et al. 2009). We fit the SFR(M, z) derived from this catalog for $z \lesssim 2$ with

$$\mathrm{SFR}(M,z) = 10^{a+bz} \left(\frac{M}{M_1}\right)^c \left(1+\frac{M}{M_2}\right)^d, \qquad (22)$$

where $a = -9.097$, $b = 0.484$, $c = 2.7$, $d = -4.0$, $M_1 = 10^8\ M_\odot$ and $M_2 = 8 \times 10^{11}\ M_\odot$. The simulation results and the best fits of the SFR(M, z) at $z = 0.5$, $z = 1$ and $z = 1.5$ are shown in Figure 2.

We find that the SFR increases quickly with halo mass but becomes flatter for the large halos with $M \gtrsim 10^{12}\ M_\odot$. Also, there is relatively large scattering in the relation at small halo mass with $M \lesssim 10^{10}\ M_\odot$, which could provide additional uncertainty in the intensity calculation. The SFRD derived from this SFR(M, z) are 2.2×10^{-2}, 3.4×10^{-2} and $6.6 \times 10^{-2}\ M_\odot {\rm yr}^{-1}{\rm Mpc}^{-3}$ at $z \sim 0.5$, $z \sim 0.9$ and $z \sim 1.6$, respectively. For comparison, Hopkins & Beacom (2006) based values are 3.7×10^{-2}, 5.9×10^{-2} and $9.7 \times 10^{-2}\ M_\odot {\rm yr}^{-1}{\rm Mpc}^{-3}$ at the corresponding redshifts. Thus the SFRDs from the simulation are lower than the SFRDs from the observations. Then we estimate the $L(M, z)$ and obtain $\bar{I}_{\rm H\alpha} = 16.8 \pm 5.0$ Jy/sr, $\bar{I}_{\rm [OII]} = 9.0 \pm 2.6$ Jy/sr and $\bar{I}_{\rm [OIII]} = 16.6 \pm 8.1$ Jy/sr using Eq. (17), (18), (19) and Eq. (4). These values are lower than what we have from the observational SFRD(z), but they are still consistent within 1σ error.

TABLE 1
THE MEAN INTENSITIES IN JY/SR OF THE Hα, [OIII] AND [OII] AROUND $z = 0.5$, $z = 0.9$ AND $z = 1.6$, DERIVED FROM BOTH OF THE LF AND SFR METHODS.

	$\bar{I}_{\rm H\alpha}(z \sim 0.5)$	$\bar{I}_{\rm [OIII]}(z \sim 0.9)$	$\bar{I}_{\rm [OII]}(z \sim 1.6)$
$\mathrm{SFRD}_{\rm obs}$	31.2 ± 9.4	35.0 ± 17.0	17.5 ± 5.0
$\mathrm{SFR}_{\rm sim}$	16.8 ± 5.0	16.6 ± 8.1	9.0 ± 2.6
$\mathrm{LF}_{\rm L07}$	$12.2^{+17.4}_{-7.1}$	$11.8^{+11.1}_{-5.7}$	$23.5^{+8.3}_{-5.9}$
$\mathrm{LF}^1_{\rm D13}$	8.4	12.7	24.2
$\mathrm{LF}^2_{\rm D13}$	23.0	6.0	50.6
$\mathrm{LF}_{\rm G13}$	17.6	–	–

– L07, D13 and G13 denote Ly et al. (2007), Drake et al. (2013) and Gunawardhana et al. (2013).

3.2. *The mean intensity from the luminosity functions*

A direct way to estimate the mean intensities of the Hα, [OII] and [OIII] lines is to make use of observed LFs. In Figure 3, we show the observed LFs of Hα, [OII] and [OIII] lines around $z = 0.5$, $z = 0.9$ and $z = 1.6$ that can contaminate the Lyα emission from $z \sim 7$. The squares, pentagons, circles and triangles are LFs from Ly et al. (2007)[4], Drake et al. (2013) and Gunawardhana et al. (2013), respectively. The LFs data points shown here are dust extinction-corrected, except for the LFs from Drake et al. (2013) which are lower than the results of the other two works.

The LF is usually fitted by the Schechter function (Schechter 1976)

$$\Phi(L)dL = \phi_* \left(\frac{L}{L_*}\right)^\alpha \exp\left(-\frac{L}{L_*}\right)\frac{dL}{L_*}, \qquad (23)$$

where ϕ_*, L_* and α are free parameters that are obtained by fitting the Schecter function with the data. The LFs from Ly et al. (2007) and Drake et al. (2013) are fitted by this function[5]. Then the mean intensity can be estimated by

$$\bar{I}_\nu(z) = \int_{L_{\rm min}}^{L_{\rm max}} dL \frac{dn}{dL}\frac{L}{4\pi D_{\rm L}^2} y(z) D_{\rm A}^2, \qquad (24)$$

where $dn/dL = \Phi(L)$ is the luminosity function, and $L_{\rm min} = 10^5\ L_\odot$ and $L_{\rm max} = 10^{12}\ L_\odot$ are the lower and upper luminosity limits. We find the result is not changed if choosing smaller $L_{\rm min}$ and larger $L_{\rm max}$ in our calculation. We use the extinction-corrected LFs to calculate the mean intensity for the Hα, [OII] and [OIII] lines. Note that, in Drake et al. (2013), they just correct the L_* for the dust extinction to get the extinction-corrected LFs, and the other two parameters ϕ_* and α are still fixed to the values fitted by the observed LFs.

Using Eq. (24) and the extinction-corrected LFs, we calculate the mean intensities of the Hα, [OIII] and [OII]

[4] We note that the Hα and [OII] LFs from Ly et al. (2007) are well consistent with recent observations with larger survey volumes (e.g. Sobral et al. 2012, 2013). So we just show the LF data from Ly et al. (2007) here.

[5] The Hα LF at $0.24 < z < 0.35$ from Gunawardhana et al. (2013) agrees well with the LF at $z = 0.4$ from Ly et al. (2007) at the faint end, but has flatter slope at the bright end. So it is fitted by an alternative/different function with different form given by Saunders et al. (1990).

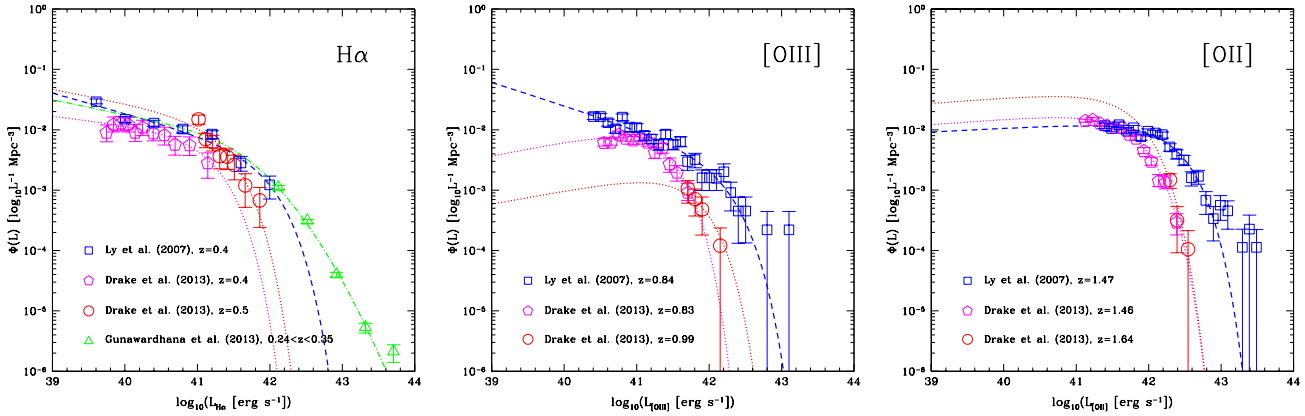

FIG. 3.— The luminosity functions and the best fits for the Hα, [OIII] and [OII] lines around $z = 0.5$, $z = 0.9$ and $z = 1.6$ that could contaminate the Lyα emission at $z \sim 7$. The blue squares, pink pentagons, red circles and green triangles are the observational LFs from Ly et al. (2007), Drake et al. (2013) and Gunawardhana et al. (2013), respectively. The dashed and dotted curves are the best fits of the corresponding LFs. Note that the data points of LFs from Drake et al. (2013) are the observed LFs (without dust extinction correction) which seem lower than the results of the other two works.

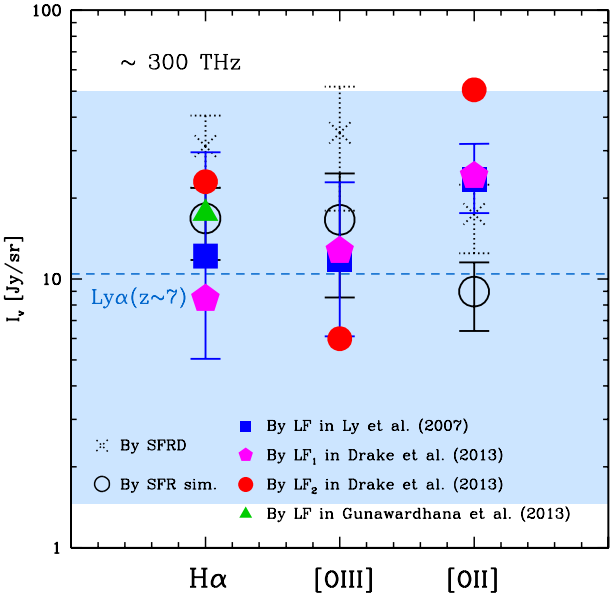

FIG. 4.— The mean intensity of Hα, [OIII] and [OII] using both SFR and LF methods around $z = 0.5$, $z = 0.9$ and $z = 1.6$. The dashed line denotes the mean intensity of Lyα at $z \sim 7$ with uncertainties (shaded region) derived in the last section. The results from these two methods are basically consistent with each other. The mean intensities of the Hα, [OII] and [OIII] are generally higher than the central value of the Lyα mean intensity, which can provide considerable contamination on the Lyα emission.

around $z = 0.5$, $z = 0.9$ and $z = 1.6$. We list and plot the mean intensities from both of the LF and SFR methods in Table 1 and Figure 4 for comparison. We also estimate the errors of the LFs from Ly et al. (2007) based on the errors of the fitted values of the ϕ_*, L_* and α, and then derive the error for the mean intensity. In Table 1, the $\mathrm{SFRD_{obs}}$ and $\mathrm{SFR_{sim}}$ denote the methods of SFRD from observations and SFR from the simulations respectively. The $\mathrm{LF_{L07}}$, $\mathrm{LF_{D13}}$ and $\mathrm{LF_{G13}}$ denote the LF method using the LFs from Ly et al. (2007), Drake et al. (2013) and Gunawardhana et al. (2013) respectively. The $\mathrm{LF^1_{D13}}$ and $\mathrm{LF^2_{D13}}$ denote to use the LFs from Drake et al. (2013) shown in pink pentagons and red circles in Figure 3 respectively. In Figure 4, the dotted crosses and open circles are the values for $\mathrm{SFRD_{obs}}$ and $\mathrm{SFR_{sim}}$, and the blue squares, pink pentagons, red circles and green triangles are the values for $\mathrm{LF_{L07}}$, $\mathrm{LF^1_{D13}}$, $\mathrm{LF^2_{D13}}$ and $\mathrm{LF_{G13}}$ respectively. For comparison, we also shown the mean intensity of the Lyα at $z \sim 7$ (blue dashed line) with uncertainties (shaded region) derived in the last section.

For the mean intensity of the Hα, we find the results from the different LF observations are consistent with each other, and they are safely in the 1σ error of the result from $\mathrm{LF_{L07}}$. Comparing the results from the SFR and LF methods, the mean intensity from $\mathrm{SFR_{sim}}$ is in a good agreement with that from $\mathrm{LF_{L07}}$, $\mathrm{LF^2_{D13}}$ and $\mathrm{LF_{G13}}$ which give an average Hα intensity around 15 Jy/sr. The $\mathrm{SFRD_{obs}}$ and $\mathrm{LF^1_{D13}}$ here give a bit higher and lower results, respectively.

For the [OIII] line, the result of $\mathrm{LF_{L07}}$ agrees with the $\mathrm{LF^1_{D13}}$ result, and they are also consistent with the result from $\mathrm{SFR_{sim}}$ in 1σ error. This gives an average intensity around 13 Jy/sr. The $\mathrm{SFRD_{obs}}$ gives a higher intensity considering its error. The $\mathrm{LF^2_{D13}}$ provides a low [OIII] intensity about 6 Jy/sr, and this can be caused by the poor model fitting of the LF data in Drake et al. (2013) (circles in the middle panel of Figure 3).

For the [OII] emission at $z \sim 1.6$, the results have larger discrepancy compared to the Hα and [OIII] cases. The $\mathrm{LF_{L07}}$ and $\mathrm{LF^1_{D13}}$ still give the same intensity which is around 24 Jy/sr, and their results agree with $\mathrm{SFRD_{obs}}$ in 1σ. But the $\mathrm{SFR_{sim}}$ suggests a low intensity around 9 Jy/sr, while the $\mathrm{LF^2_{D13}}$ gives a much higher value of ~ 50 Jy/sr. It can be the same reason for the $\mathrm{LF^2_{D13}}$ which gives a different result from the others as in the [OIII] case, that there are not enough LF data for the fitting of the LF. In the right panel of Figure 3, we find there are just three data points around 2×10^{42} erg s^{-1} and no data is observed in the faint end (see red circles). For the $\mathrm{SFR_{sim}}$, it actually has large discrepancy between different observations for the SFR-$L_{[\mathrm{OII}]}$ relation. For example, Kewley et al. (2004) proposes anther relation

$$\mathrm{SFR}\,(M_\odot \mathrm{yr}^{-1}) = (6.58 \pm 1.65) \times 10^{-42} L_{[\mathrm{OII}]},$$

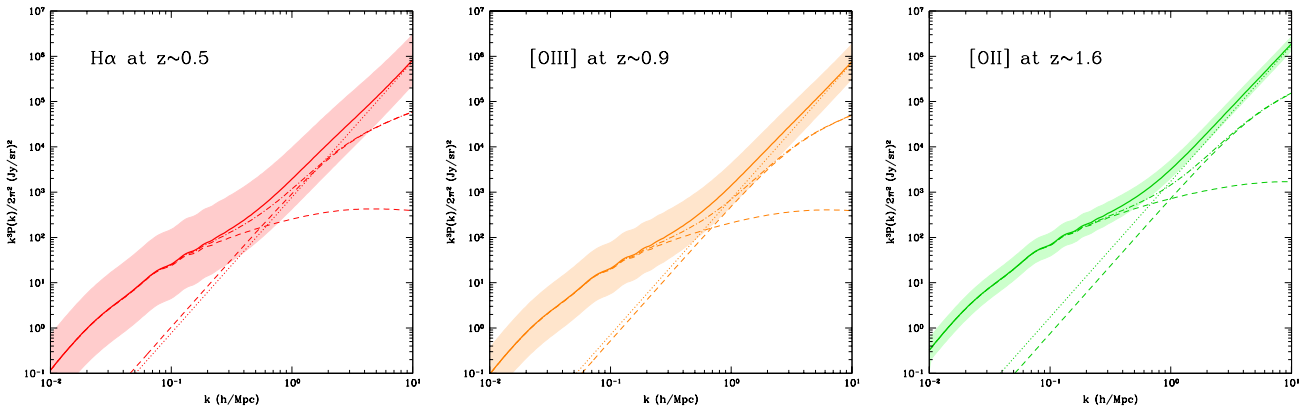

FIG. 5.— The power spectra of the Hα, [OIII] and [OII] lines at $z \sim 0.5$, $z \sim 0.9$ and $z \sim 1.6$, which can contaminate the Lyα emission at $z \sim 7$. The solid, dash-dotted and dotted lines denote the total, clustering and shot-noise power spectrum respectively. The short dashed lines are the 1-halo and 2-halo terms from the halo model (Cooray & Sheth 2002). The uncertainty of the total power spectrum is shown in shaded region, which is estimated by the uncertainty of the mean intensity. Here we adopt the LFs and errors in Ly et al. (2007) to estimate the mean intensity and errors for the three emission lines.

which gives a higher [OII] intensity ~ 17.4 Jy/sr using the $\mathrm{SFR_{sim}}$ method. This substantially reduces the tension between the $\mathrm{SFR_{sim}}$ and the other methods.

Generally, we find that the intensities of the Hα, [OII] and [OIII] around $z = 0.5$, $z = 0.9$ and $z = 1.6$ are larger than that of the Lyα at $z \sim 7$, which provide considerable contamination on the Lyα emission from the EoR. Also, the result derived by the LFs from Ly et al. (2007) is well consistent with the other results from both of the LF and SFR method, hence we would adopt it as the foreground line contamination in our following estimation and discussion.

Next, we calculate the anisotropy power spectra of the Hα, [OII] and [OIII] emissions using their mean intensities. Using Eq. (15) and (16) and replacing the $\bar{b}_{\mathrm{Ly}\alpha}$, $\bar{I}_{\mathrm{Ly}\alpha}$ and $L_{\mathrm{Ly}\alpha}$ to be the bias, mean intensity and line luminosity of the Hα, [OII] and [OIII], we obtain their clustering and shot-noise power spectra. Note that we assume the line luminosity is proportional to the halo mass to get the mean bias of these three lines, i.e. replacing $L_{\mathrm{Ly}\alpha}$ to be M in Eq. (14). This approximation is good enough to estimate the mean bias given the uncertainty in the mean intensity. In Figure 5, we show the power spectrum of the Hα, [OIII] and [OII] lines at $z = 0.5$, $z = 0.9$ and $z = 1.6$, which contaminate the Lyα emission at $z \sim 7$. The total, clustering and shot-noise power spectra are in solid, dash-dotted and dotted lines respectively. The 1-halo and 2-halo terms from the halo model are also shown in short dashed lines (Cooray & Sheth 2002). The uncertainty of the total power spectrum in shaded region is estimated by the uncertainty of the mean intensity. As mentioned, we use the LFs and errors from Ly et al. (2007) to compute the power spectrum and the uncertainty for the three emission lines.

4. THE REMOVAL OF THE FOREGROUND EMISSION LINE CONTAMINATION

4.1. *The observed power spectrum*

So far we have analyzed the expected intensity from contaminating lines. In practice, experiments (at least first generation ones) will try to make a statistical measurement of the 3-d power spectrum. Therefore, this is the quantity that we should compare to in order to access the level of foreground contamination. Because the signal and foregrounds will be emitted at different redshifts there will be an extra factor multiplying the foreground power spectrum. In order to calculate this, we need to take into account the effect of the observed light cone in the 3-D power spectrum.

The intensity that we measure, $I(\Omega, \nu)$ will correspond to a sum of the signal we are interested in, I_s (the Lyα emission from redshift z_s), and the foreground emission, I_f, from lower redshifts z_f, which is contributing to the same frequency:

$$I(\Omega, \nu) = I_s(\Omega, \nu) + I_f(\Omega, \nu). \tag{25}$$

In the flat sky approximation, displacements in angle $\Delta\theta$ and frequency $\Delta\nu$ about a central reference point, can be transformed into a position in 3-D comoving space

$$\begin{aligned} x_1, x_2 &= r(z)\Delta\theta \\ x_3 &= -y(z)\Delta\nu, \end{aligned} \tag{26}$$

where we are already making a translation along the x_3 direction and x_1, x_2 are assumed perpendicular to the line of sight while x_3 is taken to be parallel to it. Note that, besides the flat sky, we are also neglecting cosmic evolution, e.g. assuming that points along the line of sight are all emitted at the same redshift z.

We then write the observed signal as

$$\begin{aligned} I(\Omega, \nu) = &\bar{I}_s(z_s)[1 + b_s(z_s)\delta(z_s, \mathbf{x}_s)] \\ &+ \bar{I}_f(z_f)[1 + b_f(z_f)\delta(z_f, \mathbf{x}_f)] \end{aligned} \tag{27}$$

where $\delta()$ is the dark matter perturbation and $\mathbf{x}_s$, $\mathbf{x}_f$ is the 3-D position of the signal and foreground emission respectively. If we Fourier transform the above signal with respect to $\mathbf{x}_s$, the corresponding foreground Fourier mode will be offset with respect to the true one. The observed power spectrum, P_{obs} will then be:

$$\begin{aligned} P_{\mathrm{obs}}(k_\perp, k_\parallel) = &\bar{I}_s^2(z_s) b_s^2(z_s) P(z_s, k_s) \\ &+ \bar{I}_f^2(z_f) b_f^2(z_f) \left(\frac{r_s}{r_f}\right)^2 \left(\frac{y_s}{y_f}\right) P(z_f, k_f), \end{aligned} \tag{28}$$

where $|\vec{k}_s| = \sqrt{k_\perp^2 + k_\parallel^2}$ is the 3-D k at the redshift of

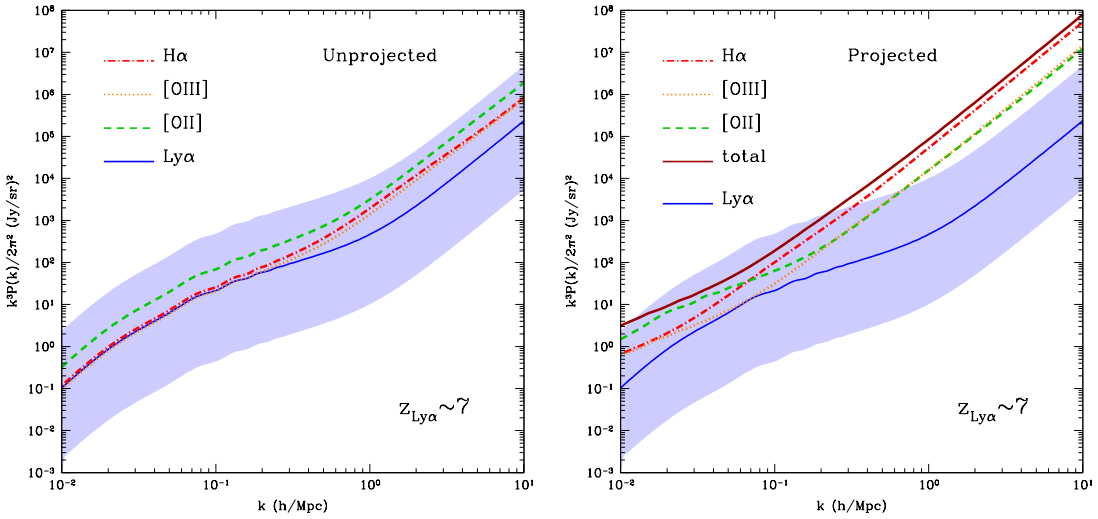

FIG. 6.— *Left* : the comparison of the 3-D total power spectrum of the Lyα at $z \sim 7$ to that of the Hα at $z = 0.5$, [OIII] at $z = 0.9$ and [OII] at $z = 1.6$. The uncertainty of the Lyα power spectrum is shown in shaded region. *Right* : the same as the left panel, but considering the projection effect on the power spectra of the Hα, [OII] and [OIII] lines. The total projected power spectrum is shown in dark red line.

the signal, and $|\vec{k}_f| = \sqrt{(r_s/r_f)^2 k_\perp^2 + (y_s/y_f)^2 k_\parallel^2}$ is the 3-D k at the redshift of the foreground line. The factor $(r_s/r_f)^2(y_s/y_f)$ comes from the distortion of the volume element when Fourier transforming the foreground correlation function to the power spectrum (Visbal & Loeb 2010). This process can be considered to project the foreground power spectrum to the high redshift where the intensity signal comes from. We then see that, even when looking at the spherical averaged power spectrum, e.g. $P_{\rm obs}(k = \sqrt{k_\perp^2 + k_\parallel^2})$, the foreground contribution to the power spectrum will be boosted by this projection. Moreover, there is an anisotropy in the $\mathbf{k}$ space which provides a potential method to distinguish the foregrounds from the signal. We discuss the details of this effect in the Appendix.

In Figure 6, we compare the 3-D power spectrum of Hα, [OII] and [OIII] with and without the projection. In the left panel of Figure 6, we show the total power spectrum of the Hα at $z = 0.5$, [OIII] at $z = 0.9$ and [OII] at $z = 1.6$ without projection. The $P_{\rm Ly\alpha}^{\rm tot}$ and its uncertainty are also shown in blue line and shaded region for comparison. In the right panel of Figure 6, we show the 3-D projected power spectra of the Hα, [OII] and [OIII] lines to the redshift of the Lyα emission ($z \sim 7$). To estimate foreground 3-D projected power spectrum from Eq. (28), we simply assume $k_1 = k_2 = k_\parallel$, where $\mathbf{k} = k_1\hat{\mathbf{i}} + k_2\hat{\mathbf{j}} + k_\parallel\hat{\mathbf{k}}$ and $k_\perp = \sqrt{k_1^2 + k_2^2}$. We also ignore the redshift distortion here. We find the projected power spectra of the three lines become a bit higher than the case where we igore the projection of the foregrounds to the background cosmological signal of intensity during the EoR.

4.2. *Foregrounds masking*

To remove the contamination from these foreground emission lines, we need to mask the bright sources at low redshifts. However, we cannot identify the individual sources and their redshifts in the intensity mapping, and all the signals that lie in the same survey pixel, which is defined by the spectral and angular resolutions, will be mixed together and observed as only one signal.

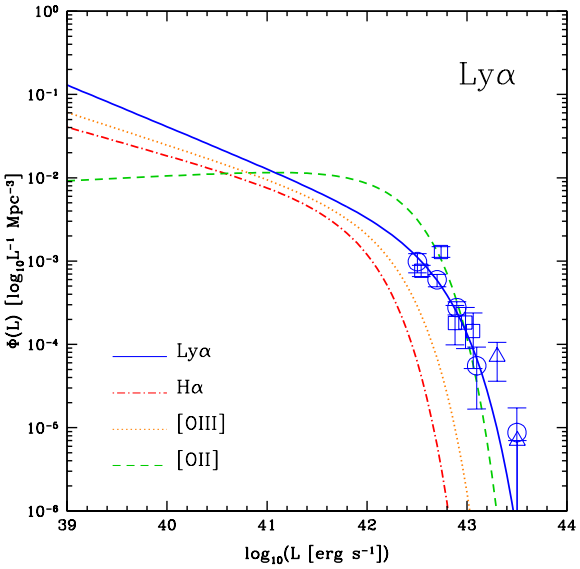

FIG. 7.— The LF of the Lyα at $z \sim 7$ (actually around z=6.6) from the observations of the LAEs. The circles, squares and triangles are the LF data points from Ouchi et al. (2010), Kashikawa et al. (2006) and Hu et al. (2005), respectively. The blue solid curve is the best fit of the LF data using the fitting results given in Ouchi et al. (2010). For comparison, the LFs of the Hα, [OIII] and [OII] around $z = 0.5$, $z = 0.9$ and $z = 1.6$ from Ly et al. (2007) are also shown.

During the EoR, the galaxies are averagely smaller and fainter than the present galaxies, so their LFs should be relatively higher at the faint end than the galaxies at the low redshifts. In Figure 7, we show the Lyα LF at $z \sim 7$ from the observations of the Lyα emitters (LAEs) (Ouchi et al. 2010; Kashikawa et al. 2006;

Hu et al. 2005)[6]. The best fit of the LF is shown in blue solid line using the Schechter function (see Eq. (23)) with fitting values given by Ouchi et al. (2010). The LFs of the Hα, [OIII] and [OII] lines are also shown for comparison. We can see that, the LFs of the Lyα is higher than the others at the faint end, but basically lower than the [OII] LF at the bright end. Therefore, we can mask the whole bright pixels whose fluxes are above some threshold in the intensity mapping to reduce the contamination of low-redshift line emission, and then the remainder pixels should be dominated by the Lyα emission at high redshifts.

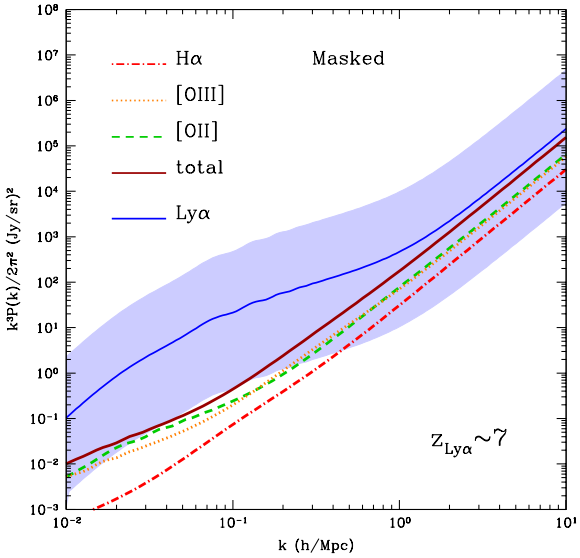

FIG. 8.— The power spectra of the Hα, [OII] and [OIII] with masking and projection. The deep red line denotes the total foreground power spectrum after the masking. We apply a flux cut at 1.4×10^{-20} W/m^2 here, which could make the total foreground power spectrum ~100 times smaller than the Lyα around $k = 0.1$ h Mpc^{-1}.

In Figure 8, the power spectra of the Hα, [OII] and [OIII] lines with masking and projection are shown. Here we try to make the total power spectrum of Hα, [OII] and [OIII] smaller by a factor of $\sim$ 100 around $k = 0.1$ h Mpc^{-1} where the shot-noise is small. We find we need to mask sources with fluxes greater than 1.4×10^{-20} W/m^2. The corresponding line luminosity are $L_{\rm H\alpha} \simeq 3.5 \times 10^6\ L_\odot$, $L_{\rm [OII]} \simeq 6.3 \times 10^7\ L_\odot$ and $L_{\rm [OIII]} \simeq 1.5 \times 10^7\ L_\odot$ respectively. Note that these luminosity cuts are close to the lower luminosity limit ($L_{\rm min} = 10^5\ L_\odot$) we take in Eq. (24), hence our masking results are dependent on the faint-end slopes of the LFs which are not well constrained by observational data.

In Figure 9, we show the number of sources whose flux is greater than some value in a survey volume pixel. Here we assume a survey with $6'' \times 6''$ beam size and $190 - 330$ THz frequency range with R=40 frequency resolution. As can be seen, the Hα sources are dominant at the bright end, but are subdominant in the survey since all of these sources are from low redshifts ($z \sim 0.5$) where the survey volume is small. On the other hand, [OII] sources are the main contamination, and are brighter than 1.4×10^{-20} W/m^2 in approximately 2% of the pixels. In total, we need to mask about 3% survey pixels. Here we should notice the large uncertainty of the Lyα emission. The number of the Lyα sources can be lower by a factor of $\sim$ 10 with the uncertainty, which would lead to a larger masking percentage.

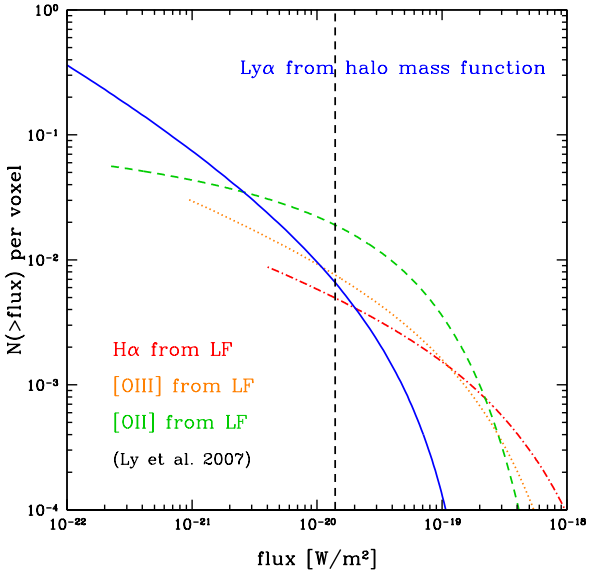

FIG. 9.— The number of sources per volume pixel whose fluxes are greater than the x-axis flux value. The Lyα curve is derived from the halo mass function and the calculation in Section 2, and the curves of Hα, [OII] and [OIII] are computed by the LFs in Ly et al. (2007). The vertical dashed line denotes the flux cut at 1.4×10^{-20} W/m^2. We find this corresponds to remove 3% of the total pixels.

There is a second method that can be used to eliminate the foreground line contamination, which is making use of the cross-correlation between different emission lines at the same redshift. This method is discussed in many previous works and can be used either for the signal (e.g. Visbal & Loeb 2010; Gong et al. 2012; Silva et al. 2013) or the foreground contamination (e.g. Pullen et al. 2013). The idea is that the lines emitted at the same redshift should trace the same underlying matter distribution and hence lead to large cross-correlation on the power spectrum. On the other hand, the emissions at different redshifts, which are far away from each other, would not provide considerable cross power spectrum. Therefore, we can derive the auto power spectrum of one line if we know both the cross power spectrum and the auto power spectrum of the other line. For instance, we can cross-correlate the Lyα line with 21-cm at $z \sim 7$, and then the foreground contamination would be reduced and we can estimate the $P_{\rm Ly\alpha}$ from the $P_{\rm Ly\alpha \times 21cm}$ and $P_{\rm 21cm}$ (Silva et al. 2013). Or we can estimate the auto power spectra of the foreground emission lines by cross-

[6] Using Eq. (24) and the Lyα LF (blue solid curve in Figure 7), we note that the Lyα mean intensity is just ~ 1 Jy/sr around $z = 7$, which is lower than the value of ~ 9 Jy/sr from the galaxy we get in Section 2 (see also Pullen et al. 2013). This can be caused by the absence of the Lyα LF data at the faint end, since only very bright individual sources can be detected at this high redshift. This also means that there could be more faint LAEs around $z = 7$, and the real LF could be higher at the faint end.

correlating with the 21-cm intensity mapping surveys at $z \sim 1$, e.g. the GBT[7], CHIME[8] and Tianlai projects (Chen 2012). However, although we can detect the cross power spectrum, it is still hard to measure the auto power spectrum for the 21-cm or the other lines due to their own foregrounds removal. So this method is indirect and cannot substitute the masking method discussed above. Even if we can only obtain the cross power spectrum, it could still be a good guide and a secondary check for the intensity mapping experiments.

5. SUMMARY

We estimate the Lyα mean intensity and power spectrum during the EoR, and explore the foreground contamination from the low-redshift emission lines. We consider the Lyα emission from both of galaxies and IGM for the recombination and collisional emission processes. We find the Lyα emission of galaxies is dominant over the IGM at $z \sim 7$ with a total mean intensity $\bar{I}_{\rm Ly\alpha} \sim 10$ Jy/sr (about 9 Jy/sr from galaxies and 1 Jy/sr from the IGM). We also evaluate the uncertainty of the mean intensity according to the uncertainties of $f_{\rm esc}^{\rm ion}$, $f_{\rm Ly\alpha}$, SFR and the clumping factor. With the help of halo model, we also calculate the Lyα clustering, shot-noise power spectrum with the uncertainty given by the mean intensity.

Next we investigate the foreground contamination by low-redshift emission lines. We find Hα at 6563 Å, [OIII] at 5007 Å and [OII] at 3727 Å can be the strongest contamination on Lyα emission during the EoR. We estimate the mean intensity of the Hα, [OIII] and [OII] lines at $z \sim 0.5$, $z \sim 0.9$ and $z \sim 1.6$ respectively, which are the redshifts that can contaminate the Lyα emission at $z \sim 7$. We use two methods to do the estimation, i.e. the SFR and LF methods. In the SFR method, both of the SFRD(z) from the observations and the SFR(M, z) derived from the simulations are used to compute the intensity. In the LF method, we adopt the LFs of Hα, [OIII] and [OII] around $z = 0.5$, $z = 0.9$ and $z = 1.6$ respectively from different observations. We find the results from both methods are basically consistent with each other, especially for the Hα and [OIII] lines. The mean intensity of the three lines are $\bar{I}_{\rm H\alpha} \sim 15$ Jy/sr, $\bar{I}_{\rm [OIII]} \sim 13$ Jy/sr and $\bar{I}_{\rm [OII]} \sim 24$ Jy/sr, which are larger than the $\bar{I}_{\rm Ly\alpha} \sim 10$ Jy/sr. The results from the LFs in (Ly et al. 2007) is in good agreements with the others, and we adopt their LFs and the errors to calculate the power spectrum and uncertainty for the three foreground lines.

At last, we discuss the methods to remove the foreground contamination due to low-redshift emission lines. We first compare the power spectrum of the Lyα at $z \sim 7$ to the Hα, [OIII] and [OII] power spectrum at low redshifts, and consider the projection effect in the real survey. The power spectrum of the foreground lines become larger after the projection. We then propose to mask the whole bright pixels with foreground emission above some flux threshold to reduce the contamination of the foreground lines in the intensity mapping. We find the contamination can be neglected when the flux cut is 1.4×10^{-20} W/m^2. The cross-correlation method is helpful to reduce or estimate the contamination, but it is indirect and can not substitute the masking method in the survey of the intensity mapping.

This work was supported by NSF CAREER AST-0645427 and AST-1313319. MBS and MGS acknowledge support by FCT-Portugal under grant PTDC/FIS/100170/2008. MBS acknowledges support by FCT-Portugal under grant SFRH/BD/51373/2011.

REFERENCES

Barkana, R., & Loeb, A. 2001, Phys. Rep., 349, 125
Blanc, G. A., Adams, J. J., Gebhardt, K., et al. 2011, ApJ, 736, 31
Bolton, J. S., Becker, G. D., Wyithe, J. S. B., Haehnelt, M. G., & Sargent, W. L. W. 2010, MNRAS, 406, 612-625
Bolton, J. S., Becker, G. D., Raskutti, S., et al. 2012, MNRAS, 419, 2880-2892
Bouwens, R. J., Illingworth, G. D., Oesch, P. A., et al. 2012, ApJ, 754, 83
Boylan-Kolchin, M., Springel, V., White, S. D. M., et al. 2009, MNRAS, 398, 1150
Cantalupo, S., Porciani, C., & Lilly, S. J. 2008, ApJ, 672, 48
Carilli, C. L. 2011, ApJ, 730, L30
Chen, X. 2013, arXiv:1212.6278
Cole, S., Norberg, P., Baugh, C. M., et al. 2001, MNRAS, 326, 255-273
Cooray, A., & Sheth, R. 2002, Phys. Rep., 372, 1
Cooray, A., Gong, Y., Smidt, J., & Santos, M. 2012, ApJ, 756, 92
De Lucia, G., & Blaizot, J. 2007, MNRAS, 375, 2
Dijkstra, M., & Jeeson-Daniel, A. 2013, MNRAS 435, 3333-3341
Drake, A. B., Simpson, C., Collins, C. A., et al. 2013, MNRAS, 433, 796-811
Fan, X., Carilli, C., & Keating, B. 2006, ARA&A, 44, 415
Furlanetto, S. R., Oh, S. P., & Briggs, F. H. 2006, Phys. Rep., 433, 181
Giovanardi, C., Natta, A., & Palla, F. 1987, A&AS, 70, 269
Gong, Y., Cooray, A., Silva, M. B., Santos, M. G. & Lubin, P. 2011, ApJ, 728, L46
Gong, Y., Cooray, A., Santos, M., et al. 2012, ApJ, 745, 49
Gong, Y., Cooray, A., & Santos, M. 2013, ApJ, 768, 130
Gould, A., & Weinberg, D. H. 1996, ApJ, 468, 462-468
Gunawardhana, M. L. P., Hopkins, A. M., Bland-Hawthorn, J., et al. 2013, MNRAS, 433, 2764
Gunn, J. E., & Peterson, B. A. 1965, ApJ, 142, 1633-1641
Guo, Q., White, S., Boylan-Kolchin, M., et al. 2011, MNRAS, 413, 101
Hayes, M., Schaerer, D., Ostlin, G., et al. 2011, ApJ, 730, 8
Hopkins, A. M., Miller, C. J., Nichol, R. C., et al. 2003, ApJ, 599, 971-991
Hopkins, A. M., & Beacom, J. F. 2006, ApJ, 651, 142
Hu, E. M., Cowie, L. L., Capak, P., & Kakazu, Y. 2005, in IAU Colloq. 199, Probing Galaxies through Quasar Absorption Lines, ed. P. R. Williams, C.-G. Shu, & B. Menard (Cambridge: Cambridge Univ. Press), 363
Hummer D. G. 1994, MNRAS, 268, 109
Kashikawa, N., Shimasaku, K., Malkan, M. A., et al. 2006, ApJ, 648, 7
Kennicutt, R. C. 1998, ARA&A, 36, 189-231
Kewley, L. J., Geller, M., & Jansen, R. A. 2004, ApJ, 127, 2002-2030
Komatsu, E., Smith, K. M., Dunkley, J., et al. 2011, ApJS, 192, 18
Laursen, P., Duval, F., & Ostlin, G. 2013, ApJ, 766, 124
Lidz, A., Furlanetto, S. R., Oh, S. P., et al. 2011, ApJ, 741, 70
Ly, C., Malkan, M. A., Kashikawa, N., et al. 2007, ApJ, 657, 738-759

[7] https://science.nrao.edu/facilities/gbt/
[8] http://chime.phas.ubc.ca/

Matsuda, Y., Yamada, T., Hayashino, T., et al. 2012, MNRAS, 425, 878-883
Osterbrock, D. E. 1989, Astrophysics of Gaseous Nebular and Active Galactic Nuclei (Mill Valley, CA: Univ.Sci.)
Ouchi, M., Shimasaku, K., Furusawa, H., et al. 2010, ApJ, 723, 869-894
Pawlik, A. H., Schaye, J., & van Scherpenzeel, E. 2009, MNRAS, 394, 1812-1824
Pullen, A., Dore, O., & Bock, J. 2013, arXiv:1309:2295
Raiter, A., Schaerer, D., & Fosbury, R. A. E. 2010, A&A, 523, A64
Righi, M., Hernandez-Monteagudo, C., & Sunyaev, R. A. 2008, A&A, 489, 489
Razoumov, A. O., & Sommer-Larsen, J. 2010, ApJ, 710, 1239
Salpeter E. E. 1955, ApJ, 121, 161-67
Saunders, W., Cannon, R., Sutherland, W. 2004, Anglo-Australian Observatory Epping Newslett., 106, 16
Schechter, P. 1976, ApJ, 203, 297
Seager, S., Sasselov, D. D., & Scott, D. 1999, ApJ, 523, L1
Shimasaku, K., Kashikawa, N., Ota, K., et al. 2006, PASJ, 58, 313
Silva, M., Santos, M. G., Gong, Y., Cooray, A., & Bock, J. 2013, ApJ, 763, 132
Sheth, R. K., & Tormen, G. 1999, MNRAS, 308, 119
Sobral, D., Best, P. N., Matsuda, Y., et al. 2012, MNRAS, 420, 1926-1945
Sobral, D., Smail, I., Best, P. N., et al. 2013, MNRAS, 428, 1128-1146
Stark, D. P., Ellis, R. S., Chiu, K., Ouchi, M., & Bunker, A. 2010, MNRAS, 408, 1628-1648
Stark, D. P., Ellis, R. S., & Ouchi, M. 2011, ApJ, 728, L2
Steidel, C. C., Erb, D. K., Shapley, A. E., et al. 2010, ApJ, 717, 289-322
Theuns, T., Schaye, J., Zaroubi, S., et al. 2002, ApJ, 567, L103-L106
Tittley, E. R., & Meiksin, A., et al. 2007, MNRAS, 380, 1369-1386
Trac, H., Cen, R., & Loeb, A. 2008, ApJ, 689, L81-L84
Visbal, E. & Loeb, A. 2010, JCAP, 11, 016
Wijesinghe, D. B., Hopkins, A. M., Sharp, R., et al. 2011, MNRAS, 410, 2291-2301
Wyithe, J. S. B., & Dijkstra, M. 2011, MNRAS, 415, 3929-3950
Zheng, Z., Cen, R., Trac, H., & Miralda-Escude, J. 2010, ApJ, 716, 574
Zheng, Z., Cen, R., Trac, H., & Miralda-Escude, J. 2011, ApJ, 726, 38

APPENDIX

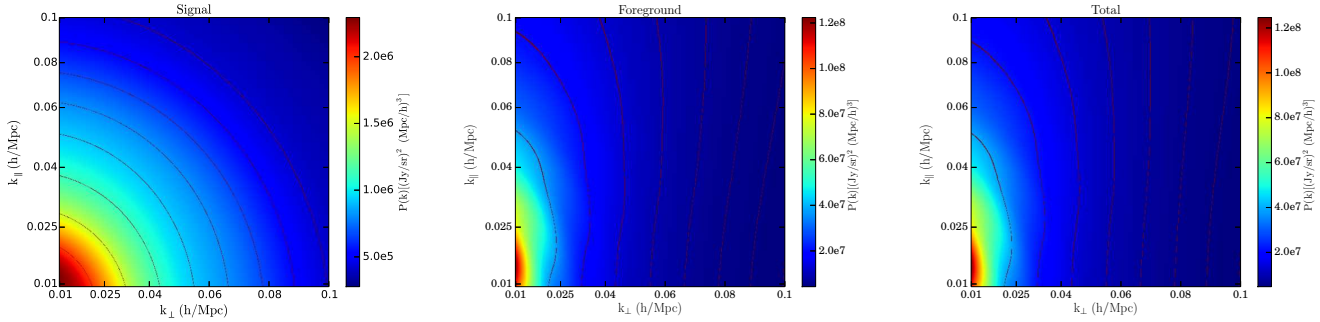

FIG. 10.— The 2-D anisotropic power spectra shown by perpendicular and parallel Fourier modes for the signal (Lyα), foreground (only Hα here) and total observed signal+foreground. We find the 2-D signal power spectrum is almost symmetric for $k_\perp$ and $k_\parallel$, and the redshift distortion effect is relatively small. For the foreground power spectrum at low redshift, because the redshift distortion effect is strong and the shift factor on the foreground $k_\perp$ and $k_\parallel$ are different, the shape of the power spectrum is irregular. This effect provides a way to distinguish the signal and the foreground in principle. The total power spectrum is similar with the foreground power spectrum, since the amplitude of the signal power spectrum is much lower than the foreground.

In Eq. (28) of Section 4.1, we see that the observed foreground power spectrum is actually anisotropic, i.e., not simply a function of $k = \sqrt{k_\perp^2 + k_\parallel^2}$. This can in principle be used in the foreground cleaning process. In particular, after the intensity cut, we can check if there is still any strong contamination by looking at the anisotropy of the total power spectrum. In order to check the strength of these anisotropies caused by the projection effect, we calculate the 2-D anisotropic power spectra for the signal and foregrounds. Here we also take into account of the linear redshift-space distortions. In that case, the bias should be replaced by

$$b_s(z_s) \to b_s(z_s) + \left(\frac{k_\parallel}{\sqrt{k_\perp^2 + k_\parallel^2}}\right)^2 \frac{1}{H(z_s)}\frac{\dot{D}(z_s)}{D(z_s)}$$

$$b_f(z_f) \to b_f(z_f) + \left(\frac{(y_s/y_f)k_\parallel}{\sqrt{(r_s/r_f)^2 k_\perp^2 + (y_s/y_f)^2 k_\parallel^2}}\right)^2 \frac{1}{H(z_f)}\frac{\dot{D}(z_f)}{D(z_f)}.$$

Here, $D(z)$ is the growth factor. The normal expression of the second term of the bias is $f\mu^2$. Here $f = d\ln D/d\ln a$ where a is the scale factor, and $\mu = \cos\theta$ where θ is the angle between the line of sight and the wave-vector $\mathbf{k}$. We also notice that the so-called non-gravitational effects can introduce strong redshift-space distortion effect (Zheng et al. 2011; Wyithe & Dijkstra 2011). According to full Lyα radiative transfer calculations, the Lyα emission is dependent on environment (gas density and velocity) around LAEs. The observed LAE clustering features can be changed by this effect especially at high redshifts. However, this effect relies on "missing" Lyα photons scattering in relatively

close proximity to Lyα emission galaxies, which could be recovered by intensity mapping. Therefore we ignore this effect in our discussion.

In Figure 10, we show the 2-D anisotropic power spectrum decomposed into $k_\perp$ and $k_\parallel$ for the signal, foreground and the total observations. We just show the Hα foreground here, since it has the lowest redshift among the other two foreground lines and has the largest effect of the power spectrum projection. We find the shape of the signal power spectrum is quite symmetric and the redshift distortion effect is relatively small, since the signal comes from high redshifts. However, for the foreground, the shape of the spectrum is irregular due to the redshift distortion and the different factors on the $k_\perp$ and $k_\parallel$ (i.e. r_s/r_f on $k_\perp$ and y_s/y_f on $k_\parallel$) in the projection. This effect provides a potential method to distinguish the signal from the foreground, and could be helpful to remove the foreground in future high sensitive experiments.

A.6 Paper VI

Prospects for detecting CII emission during the Epoch of Reionization

Silva M. B., Santos M. G., Cooray A. and Gong Y.

Draft version September 30, 2014
Preprint typeset using LaTeX style emulateapj v. 12/16/11

PROSPECTS FOR DETECTING CII EMISSION DURING THE EPOCH OF REIONIZATION

Marta Silva[1,2],Mario G. Santos[1,3], Asantha Cooray[2],Yan Gong[2]
[1]CENTRA, Instituto Superior Técnico, Technical University of Lisbon, Lisboa 1049-001, Portugal
[2]Department of Physics & Astronomy, University of California, Irvine, CA 92697 and
[3]Physics Department, University of the Western Cape, Cape Town 7535, South Africa
Draft version September 30, 2014

ABSTRACT

We produce simulations of emission of the atomic CII line in large sky fields in order to determine the current prospects for mapping this line during the high redshift Epoch of Reionization. We estimate the CII line intensity, redshift evolution and spatial fluctuations using observational relations between CII emission and the SFR in a galaxy for the frequency range of 200GHz to 300GHz. The frequency averaged intensity of CII emission obtained is $I_{CII} = 3.36^{+2.64}_{-2.05} \times 10^2 \mathrm{Jysr}^{-1}$. Observations of CII emission in this frequency range will suffer contamination from emission lines at lower redshifts, in particular from the CO rotation lines. For the relevant frequency range we estimated the CO contamination, based in the Obreschkow et al. (2009a) galaxies simulation, to be $I_{CO} \approx 1.13 \times 10^3 \mathrm{Jysr}^{-1}$ and independently confirmed the result based in observational relations. By using detailed simulations of CO and CII emission we found that in order to reduce the foreground contamination we should remove from observations the emission from galaxies with at least a redshift below 2.5 and a CO flux in one of the CO(J:2-1) to CO(J:6-5) lines higher than $5 \times 10^{-22} \mathrm{Wm}^{-2}$ or a AB magnitude lower than $m_K = 22$. We estimate that the additional continuum contamination originated in emission from stars and in dust, free-free, free-bound and two photon emission in the ISM is of the order of $10^{-1} \mathrm{Jysr}^{-1}$ and so a lot lower than the predicted CII signal. It is also considered the possibility of cross correlating foreground lines with galaxies in order to probe the intensity of the foregrounds.

Subject headings: cosmology: theory — diffuse radiation — intergalactic medium — large scale structure of universe

1. INTRODUTION

The Epoch of Reionization (EoR) is a fundamental stage in the history of large scale structure formation. The process of hydrogen reionization is connected with the radiation emitted from the first galaxies which were formed in the more overdense regions and so it depends on a large set of astrophysical and cosmological parameters (Venkatesan 2000).

There are recently in operation or in the planning stage several experiments, such as the Murchison Widefield Arrays (MWA) (Tingay et al. 2013), the Giant Metrewave Radio Telescope (GMRT) (Paciga et al. 2011), the Precision Array for Probing the Epoch of Reionization (PAPER) (Liu & Tegmark 2012), the Low Frequency Array (LOFAR) (Rottgering et al. 2006) and the Square Kilometre Array (SKA) (Carilli et al. 2004), whose main objective is the measurement of the 21 cm signal from neutral hydrogen during the EoR in order to finally constrain the evolution of the ionization field and unveil the characteristics of the sources of radiation responsible for Reionization.

One of the main challenges of probing the EoR with the 21 cm line is that observations will be contaminated by foregrounds several orders of magnitudes higher than the signal we are actually trying to measure (Shaver et al. 1999). Some of these foregrounds can be efficiently removed however others are more complex or poorly known and so the approaches used in order to extract them from the observational data can fail to remove their total emission or can remove part of the 21 cm signal. Independent ways to predict this signal are therefore required to insure the validity of the final data.

In this work we propose to built a CII intensity mapping experiment to probe the EoR during its final stages and so to confirm and complement 21 cm data. The intensity mapping technique has the advantage of not resolving sources but instead of measuring all the emission in a given frequency band originated in a relatively large region and so it also measures radiation from faint sources and from the diffuse IGM which at these high redshifts can not be detected in other ways but whose contribution to the total signal is often important (Gong et al. 2012) (Silva et al. 2012). Compared to other techniques, intensity mapping, has the advantage of providing three dimensional spatial information of the sources of emission that can be used to further understand the processes of structure formation. Intensity maps can also be used as cosmological probes since the fluctuations in the intensity of emission/absorption lines are correlated with the underlying dark matter density fluctuations (Carilli 2011).

We show the potential of intensity mapping of the CII line by simulating mock observational cones of CII emission and its foregrounds at frequencies 200GHz to 300GHz. With the observational cones we were able to realistically estimate the intensity and power spectra of CII emission and of its contaminants. These allowed us to test possible ways to reduce the foregrounds without erasing the signal. The main foregrounds in CII intensity maps from the EoR will be contamination from other infrared emission lines from lower redshifts, in particular emission from CO rotation transitions. CO emission from transitions (2-1) and higher is poorly constrained by observations, therefore, in order to properly estimate

the intensity of these lines and the contamination power spectra relatively to CII observations, we used two independent methods one based in simulations which use a phenomenological model to calculate the luminosities of different CO transitions and other based in observations. The first method for estimating CO emission uses both the simulated galaxies catalog from De Lucia & Blaizot (2007) and the CO fluxes estimated by Obreschkow et al. (2009a) using galaxies physics and the second method uses IR luminosity functions (LFs) and other observational based relations to estimate the relative intensities of the several CO transitions.

We found that CO contamination is dominated by bright sources and so it can be efficiently reduced by erasing the pixels where radiation from these sources is observed. In order to do this CO masking we need a complementary experiment to measure individual CO emission from galaxies above a given flux, in the same angular coordinates in the sky. Such an experiment is in principal possible to be developed with current technology by using one of the existing galaxy surveys or by building an experiment exclusive to measure CO emission from galaxies which would on its own be a potential very powerful astrophysical probe. Alternatively the masking of the contaminant galaxies could be done with a CO tracer, easier to be observed, such as the SFR or the relative magnitude in a given filter.

We also explore the possibility of cross correlating CII and 21 cm maps in order to obtain an independent measure of the two signals which can be used to remove foregrounds from 21 cm observations. This is possible since two lines emitted from the same redshift will be observed at different frequencies and so they will be contaminated mainly by uncorrelated foregrounds (Gong et al. 2012).

This paper is organized as follows: In Section 2 we describe how to theoretically estimate the CII emission, in Section 3 we describe the CII foregrounds. In Sections 4 and 5 we describe how we used simulations to generate the signal and the foregrounds. In the 5th Section we present the parameters of an experiment able to measure the CII signal and the CO signal in the 200GHz to 300GHz band and in Section 6 we discuss how to remove the CII foregrounds. We conclude with a discussion of the results obtained in Section 7.

2. CALCULATING CII EMISSION

CII emission is originated in the interstellar medium (ISM) in Photodissociation regions (PDRs), ionized regions (HII regions), cold atomic gas and CO-dark molecular gas (regions in the boundary of molecular clouds with H_2 but without CO gas). Observations of relative intensity of different emission lines have shown that the main source of CII emission is the dense PDRs located in the boundary of HII regions. PDRs are dense and warm regions of the ISM located between HII regions and molecular clouds which contain mostly neutral gas, but that due to their proximity to radiation sources such as O, B stars or AGNs are affected by a strong far ultraviolet (FUV) field which dominates the physical and chemical properties of the gas. The strong FUV to X-ray radiation that penetrates the PDR is absorbed by dust grains which emit electrons heating the gas, is absorbed by atoms with an energy threshold for ionization below the Lyman alpha limit such as carbon, oxygen and nitrogen and causes transitions from atomic to molecular hydrogen and from ionized carbon to carbon monoxide (Hollenbach & Tielens 1997). CO-dark clouds are envelopes of dense H_2 gas with densities too low for carbon to be converted to CO, but which can be identified by their CII emission. The contribution from CO-dark clouds to the total CII budget is not yet clear but recent studies of our galaxy indicate that it can be high (up to $\sim 28\%$) (Pineda et al. 2013) under certain astrophysical conditions more characteristic of the low redshift Universe. Diffuse cold atomic gas can be characterized by its emission in the hydrogen 21 cm line and in the CII line. The intensity of emission in this gas phase will be proportional to the collisional rate which depends on the gas density and temperature and therefore also on FUV strength.

The carbon ionization energy is only 11.3 eV which is less than the 13.6 eV necessary to ionize hydrogen so at first we could expect, as was done in Gong et al. (2012), that all the carbon in HII regions would be ionized and so there would be a high emission in the CII $157\mu m$ line since its excitation potential is only of 91K. Under this assumption most of the CII emission would come from the highest density locations inside HII regions, however this is not supported by observations. Several observational maps of the spatial distribution of CII emission in galaxies made using relative intensities of CII and other lines indicate that the CII emission originated in HII regions only reaches a few % of the total CII emission which is mainly originated in PDRs (Lebouteiller et al. 2012; Rigopoulou et al. 2014). There are some studies who indicate a contribution from HII regions that can reach up to 30% of the total CII emission (Carral et al. 1994; Stacey et al. 1999; Aannestad & Emery 2003; Rigopoulou et al. 2013) although these studies point out that this CII emission is originated in the low density HII regions component. The more simple explanation for this unexpected result is that the carbon in the more dense places in HII regions is highly shielded from radiation by hydrogen and so almost all of the ionized carbon is located in low density regions. The Hershel telescope and the SOFIA observatory were used to observe typical tracers of PDRs, HII regions and other galactic regions (Kaneda et al. 2013) and these observations showed that CII emission has a much more complex spatial structure than most other lines, which indicates that in order to properly estimate the CII intensity of galaxies we need to observe each galaxy with a high resolution in order to measure the emission from the different galaxy components, which is not possible for most galaxies. Alternatively we can use the intensity mapping technique to measure the total CII emission from several galaxies.

2.1. *Theoretical formulas to estimate CII emission*

The physically based intensity of CII emission is given theoretically (formula taken from Gong et al. (2012)) as:

$$I_\nu = \frac{hc}{4\pi H(z)(1+z)^3} A_{\rm ul}\ f_{\rm CII}^{\rm grd} n_{\rm CII}(z) \times \quad (1)$$
$$\frac{g_{\rm u}}{g_{\rm l}} \exp(-T_{\star,{\rm ul}}/T_{S,{\rm ul}}) \left[1 - \frac{\exp(T_{\star,{\rm ul}}/T_{S,{\rm ul}}) - 1}{(2h\nu^3/c^2 I_\nu)_{\nu_{\rm ul}}}\right],$$

where $f_{\rm CII}^{\rm grd}$ is the fraction of CII ions at the ground level $^2P_{1/2}$, $n_{\rm CII}$ is the number density of once ionized carbon atoms, H(z) is the hubble parameter, T_S is the spin temperature and $T_\star \equiv h\nu_{\rm ul}/k_B$ (where $\nu_{\rm ul}$ is the frequency of the transition). The statistical weights are $g_{\rm u} = 4$ and $g_{\rm l} = 2$ and the Einstein spontaneous emission coefficient is $A_{\rm ul} = 2.36\times10^{-6}$. As many of the parameters in equation 1 are poorly known and cannot be directly obtained with observations we can use an alternative formula to obtain the intensity of a line emitted from several galaxies in a relatively large volume just by assuming that the average luminosity of each of these galaxies is proportional to the mass of the dark matter halo which contains it. The average intensity of a line is then given by:

$$\bar{I}(z) = \int_{\rm M_{min}}^{\rm M_{max}} dM \frac{dn}{dM} \frac{L(M,z)}{4\pi D_{\rm L}^2} y(z) D_A^2 \qquad (2)$$

where dn/dM is the halo mass function (Sheth & Tormen 1999), M is the halo mass, $M_{\rm min} = 10^8{\rm M}_\odot$, $M_{\rm max} = 10^{14}{\rm M}_\odot$, $D_{\rm L}$ is the proper luminosity distance, $D_{\rm A}$ is the comoving angular diameter distance and $y(z) = d\chi/d\nu$, where χ is the comoving distance and ν is the observed frequency. The relation between $L_{\rm CII}$ and the halo mass can also be physically based in the dependence of $L_{\rm CII}$ in the number density of CII atoms which is proportional to the halo mass.

2.2. *Calculating CII emission using observational based relations*

The CII luminosity of a galaxy can be estimated from other observational quantities as long as there is a reasonable correlation between the two. For large volumes since we are considering several galaxies it is even more reliable to use observational relations to estimate the overall luminosity density or intensity from these regions. CII emission is powered by FUV radiation and so there is a relation between these two quantities which can be converted to a relation between CII and FIR luminosities given that the fluxes of a galaxy in different bands are connected. The CII luminosity of a galaxy also depends on other astrophysical properties of the galaxy such as its metallicity, however the average ratio $R = \frac{L_{\rm CII}}{L_{\rm FIR}}$ for nearby, late type galaxies and for $10^8{\rm L}_\odot \leq L_{\rm FIR} \leq 10^{10.5}{\rm L}_\odot$ is approximately constant (Boselli et al. 2002) and given by:

$$L_{\rm CII(M,z)}\,[{\rm L}_\odot] = 0.003 \times L_{\rm FIR}. \qquad (3)$$

This relation is also consistent with recent observations of high redshift galaxies (Stacey et al. 2010) and with observations of ULIRGS ($L_{\rm IR} > 10^{11.5}{\rm L}_\odot$), where a ratio of $(0.8-4)\times10^{-3}$ in the CII to FIR luminosities was found (Rigopoulou et al. 2014). In PDRs the same ratio is inversely proportional to the strength of the ambient radiation field G_0, since $L_{\rm FIR}$ is proportional to G_0 and $L_{\rm CII}$ depends weakly on G_0 (Kaufman et al. 1999). Therefore, this ratio is likely to slightly increase to low mass galaxies (up to 0.01) and to decrease to high mass galaxies. The IR and the FIR luminosities are connected by the following relation:

$$L_{\rm IR}(8-1000\ \mu{\rm m}) = (1.89\pm0.26) L_{\rm FIR}(40-120\ \mu{\rm m}), \qquad (4)$$

taken from (Cardiel et al. 2003). The integrated IR luminosity, $L_{\rm IR} = L(81000\mu{\rm m})$ is related to the galaxies SFR by:

$$L_{\rm IR}(M,z)\,[{\rm L}_\odot] = 5.8\times10^9 SFR(M,z)\,[{\rm M}_\odot/{\rm yr}]\,, \qquad (5)$$

taken from Kennicutt (1998). Using equations 3, 5 and 4 we obtained the following relation between CII luminosity and SFR:

$$\begin{aligned} L_{\rm CII(M,z)}[{\rm L}_\odot] &= 0.003 \times L_{\rm FIR}\,[{\rm L}_\odot] \\ &= 0.003 \times 0.53 \times L_{\rm IR}\,[{\rm L}_\odot] \\ &= 9.22\times10^6 SFR(M,z)\,[{\rm M}_\odot/{\rm yr}]\,. \end{aligned} \qquad (6)$$

The connection between CII luminosity and the SFR can be easily understood in the case of CII emission arising from warm photodissociating regions, since in this case the FUV radiation would ionize the carbon in the outer layers of the photon-dominated molecular clumps which would emit CII with a luminosity proportional to the FUV flux which is linked to the galaxy SFR (de Looze et al. 2011). In HII regions the amount of ionized carbon should increase with the size of the region, which is proportional to the stellar radiation UV intensity. However, given that not all carbon is necessarily once ionized in HII regions and that the CII luminosity of these regions also depends on the astrophysical conditions of the gas than there is expected to be a considerable dispersion in the CII luminosity from HII regions and in the SFR.

Alternative relations between the CII luminosity and the SFR, obtained using different galaxy datasets and using a SFR estimated from the infrared luminosity or from the Hα luminosity, can be taken from for example Boselli et al. (2002), de Looze et al. (2011) and Sargsyan et al. (2012). All of the referred observational studies indicate that the relation between CII and SFR is smaller for very massive galaxies (galaxies with SFRs above $10^{10}M_\odot$).

The studies that led to the referred relations between CII emission and SFR indicate that for the more ultraluminous galaxies the CII luminosity should show a deficit compared to what is predicted by these relations.Very recently there have been published the first five observations of star forming galaxies at $z \simeq 6.5$ detected by the ALMA experiment (see eg. Ota et al. (2014)). These galaxies have upper limits for the CII luminosity below what is predicted by equation 6 however their SFRs are above $10{\rm M}_\odot$ which puts them in the region where a CII deficit was already expected. Also, for intensity calculations according to our model galaxies with SFRs above $10{\rm M}_\odot$ only represent around 20% of the total CII intensity and so when fitting the CII luminosity versus SFR relation in observational data we should take into account that less intense galaxies (which are to faint to be observed especially at high redshifts) have a large weight in the CII intensity and that they are more likely to have a stronger $L_{\rm CII}$/SFR ratio.

In order to obtain upper and lower bounds to our CII intensity estimation we decided to use 4 models for the

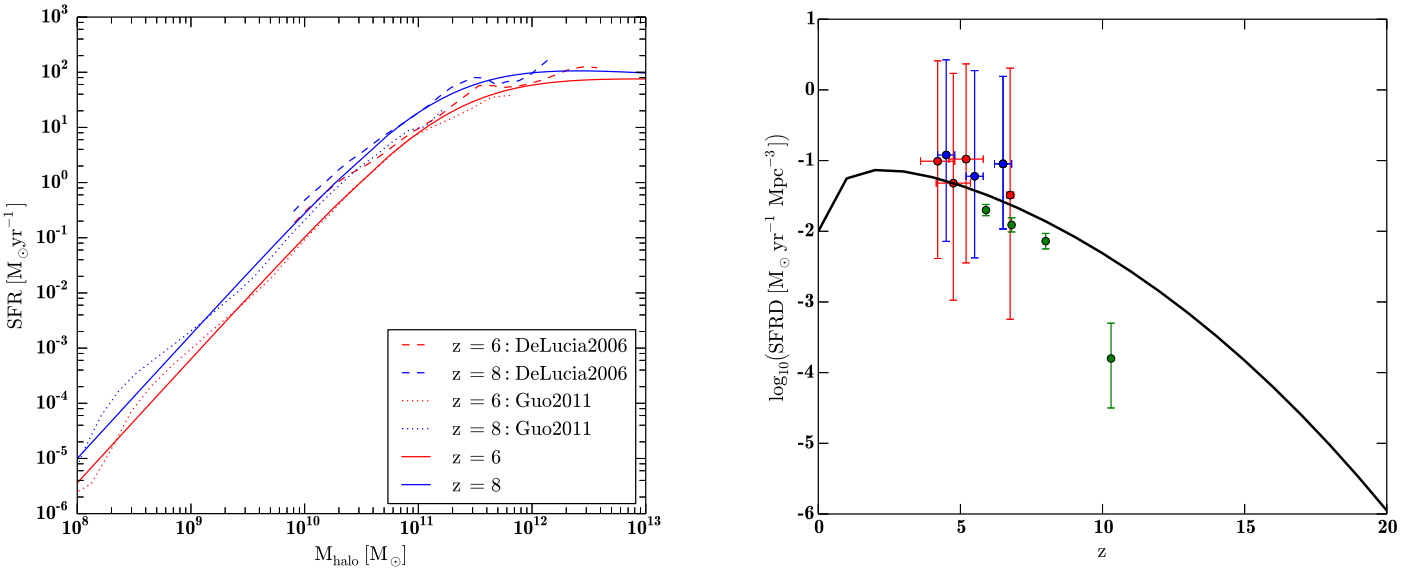

FIG. 1.— Left panel: Star formation rate versus halo mass for redshifts 6 (red upper lines) and 8 (blue upper lines). The dotted lines show the relations taken from the Guo et al. (2011) galaxies catalogue for low halo masses, the dashed lines show the relation taken from the De Lucia & Blaizot (2007) galaxies catalogue for high halo masses at the same redshifts. The solid lines show the parameterizations from equation 8. Right panel: Star formation rate density from the simulations (black solid line), obtained by integrating equation 8 over the halo mass function. The green circles mark the SFRD correspondent to the UV luminosities corrected for dust extinction from Bouwens et al. (2011). The red and blue circles were obtained with measurements of gamma-ray bursts by Kistler et al. (2013) and Robertson & Ellis (2012), respectively.

$L_{\rm CII}$ versus SFR relation referred as $\mathbf{m_1}$, $\mathbf{m_2}$, $\mathbf{m_3}$ and $\mathbf{m_4}$. Where equation 6 corresponds to parameterization $\mathbf{m_2}$, parameterization $\mathbf{m_1}$ corresponds to the recent fit to high redshift galaxies by De Looze et al. (2014) and parameterizations $\mathbf{m_3}$ and $\mathbf{m_4}$ correspond to fits to the galaxies in figure 4. These models can be all parameterized as:

$$\log10(L_{\rm CII}[{\rm L}_\odot]) = a_{\rm LCII} \times \log10(SFR[{\rm M}_\odot]) + b_{\rm LCII}, \quad (7)$$

with the values for $a_{\rm LCII}$ and $b_{\rm LCII}$ presented in table 1.

TABLE 1
PARAMETERS FOR THE $L_{\rm CII}$ VERSUS SFR RELATION

model	$a_{\rm LCII}$	$b_{\rm LCII}$
$\mathbf{m_1}$	0.8475	7.2203
$\mathbf{m_2}$	1.0000	6.9647
$\mathbf{m_3}$	0.8727	6.7250
$\mathbf{m_4}$	0.9231	6.5234

In order to calculate the CII intensity with equation 2 we converted the CII versus SFR relation in equation 7 to a CII versus halo mass relation. Since for low halo masses and high redshifts the SFR versus halo mass relation is poorly constrained observationally we choose to use a parameterization for this relation obtained from simulated galaxy catalogs post processed from the Millennium and Millennium II dark matter simulations (Springel et al. 2005; Boylan-Kolchin et al. 2009). The parameterization is given by:

$$SFR(M,z) = M_0 \times \left(\frac{M}{M_a}\right)^a \left(1+\frac{M}{M_b}\right)^b, \quad (8)$$

where the values for the parameters M_0, M_a, M_b, a and b are available in table 2 for redshifts lower than 20. The evolution of the SFR with mass can be seen in left panel of figure 1 for redshifts 6 and 8.

The use of this formula results in the SFRD evolution shown in right panel of figure 1 assuming a dark matter halo mass range from $10^8{\rm M}_\odot$ to $10^{14}{\rm M}_\odot$. The Millennium and Millennium II simulations only goes till a redshift of 20 however unless we want to consider unusual stars the relation for z=20 should be a good approximation for $z > 20$.

2.3. *Calculating CII emission using gas physics*

The maximum possible upper value for the CII emission can be obtained assuming that all the carbon in the hot gas (typical of HII regions) in a galaxy is ionized and therefore emitting in the CII line such as was done in Gong et al. (2012). Here, we do a similar calculation but with an improved parameterization of the metallicity in the galaxies hot gas obtained using the Guo et al. (2011) galaxies catalog for low mass halos and the De Lucia & Blaizot (2007) galaxies catalog for high halo masses. The resulting halo mass versus metallicity of the hot gas relation is shown in figure 2. By analysing this figure we found that the metallicity in the lower mass halos of the De Lucia & Blaizot (2007) simulation is lower than the one found in the halos from the Guo et al. (2011) simulation although these simulations used very similar prescriptions to determinate the galaxies metallicity. Since the Guo et al. (2011) simulation has a much higher mass resolution we believe that their results are more reliable for the low luminosity halos since the halos in the De Lucia & Blaizot (2007) galaxies catalog are only well resolved for masses above $3 \times 10^{10} M_\odot$.

The average relation between M_Z and halo mass M

TABLE 2
SFR PARAMETERS BASED IN THE AVERAGE RELATIONS FROM THE SIMULATED GALAXY CATALOGS

Redshift range	M_0	M_a	M_b	a	b
0.00-00.50	$10^{-8.855}$	1.0×10^8	8.0×10^{11}	2.7	-4.0
0.00-02.75	$10^{-9.097+0.484\times z}$	1.0×10^8	8.0×10^{11}	2.7	-4.0
2.75-03.25	3.3×10^{-8}	1.0×10^8	4.0×10^{11}	2.7	-3.4
3.50-04.50	1.5×10^{-7}	1.0×10^8	3.0×10^{11}	2.6	-3.1
4.50-05.50	9.0×10^{-7}	1.0×10^8	3.0×10^{11}	2.4	-2.3
5.50-06.50	3.6×10^{-6}	1.0×10^8	2.0×10^{11}	2.25	-2.3
6.50-07.50	6.6×10^{-6}	1.0×10^8	1.6×10^{11}	2.25	-2.3
7.50-09.00	1.0×10^{-5}	1.0×10^8	1.7×10^{11}	2.25	-2.4
9.00-11.00	3.7×10^{-5}	1.0×10^8	1.7×10^{11}	2.1	-2.2
11.00-13.00	5.0×10^{-5}	1.0×10^8	1.5×10^{11}	2.1	-2.2
13.00-20.00	$[5.0 + (z - 13.0)] \times 10^{-5}$	1.0×10^8	$[1.5 + (z - 13) \times 0.015] \times 10^{11}$	2.1	$-2.2 - (z - 13) \times 0.03$

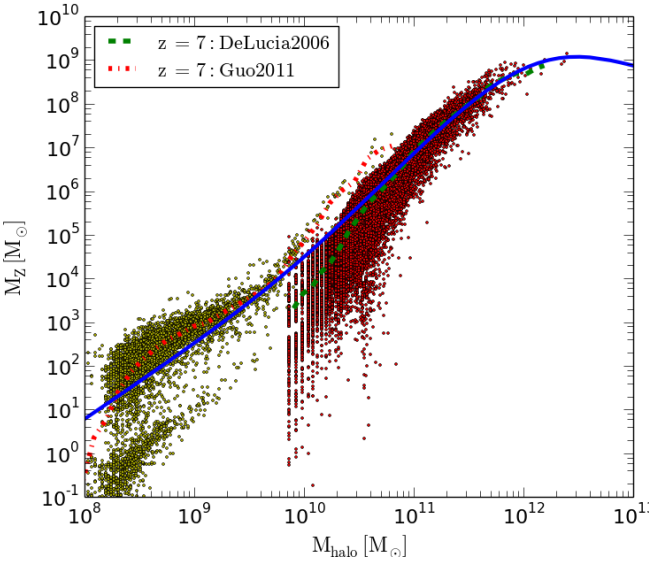

FIG. 2.— Mass in metals in the hot gas component M_Z as a function of the halo mass M at $z \approx 7$. The dahed dotted line shows the mean relation from the (Guo et al. 2011) galaxy catalog, the dashed line shows the mean relation from the (De Lucia & Blaizot 2007) galaxy catalog and the solid line shows our fits to the mean values. The dots show the dark matter halos in the two catalogs.

can therefore, be parameterized in the form:

$$M_Z(M) = M_0 \, (M/M_{\rm a})^{\rm a} \, (1 + M/M_{\rm b})^{\rm b} \times (1 + M/M_{\rm c})^{\rm c} \times (1 + M/M_{\rm d})^{\rm d}, \quad (9)$$

where at the redshift range 5.0 to 8.5 these parameters take the values: $M_0 = z - 1$, $M_a = 1.0 \times 10^8 {\rm M}_\odot$, $M_b = 9.0 \times 10^9 {\rm M}_\odot$, $M_c = 2.0 \times 10^{12} {\rm M}_\odot$, $M_d = 2.0 \times 10^{13} {\rm M}_\odot$, $a = 1.7$, $b = 1.0$, $c = -5.0$ and $d = 2.5$.

Assuming that all the carbon in the hot gas is ionized and that the carbon mass corresponds to a fraction of 0.21% of the total mass in metals (this is the same percentage of carbon found in the sun) we obtain $M_{\rm CII} = 0.21 M_{\rm Z}$. In reality only a fraction of the carbon in HII regions is ionized which can be easily included in these calculations. Therefore, at large enough volumes the number density of CII atoms can be estimated from the halos mass using the formula:

$$n^{\rm sim}_{\rm CII}(z) = \int_{M_{\rm min}}^{M_{\rm max}} dM \frac{dn}{dM} \frac{M_{\rm CII}(M, z)}{m_{\rm c}}, \quad (10)$$

where $m_{\rm c}$ is the atomic carbon mass, M is the halo mass and dn/dM is the halo mass function (Sheth & Tormen 1999).

Using equation 1 with the CII number density obtained from equation 10 and assuming that HII regions have an electronic temperature of 10^4 K and an electronic density of $10^4 {\rm cm}^{-3}$ we can obtain an upper value for the CII intensity in these regions (the T^e_K and n_e values used correspond to saturation values as obtained in Gong et al. (2012)).

In figure 3 we show the CII intensity estimated assuming several models. The average intensity of CII emission in the redshift range shown is between $\bar{I}_{\rm CII} \approx 6 \times 10^2 {\rm Jy\ sr}^{-1}$ for model $\mathbf{m_1}$ and $\bar{I}_{\rm CII} \approx 9 \times 10^1 {\rm Jy\ sr}^{-1}$ for model $\mathbf{m_4}$.

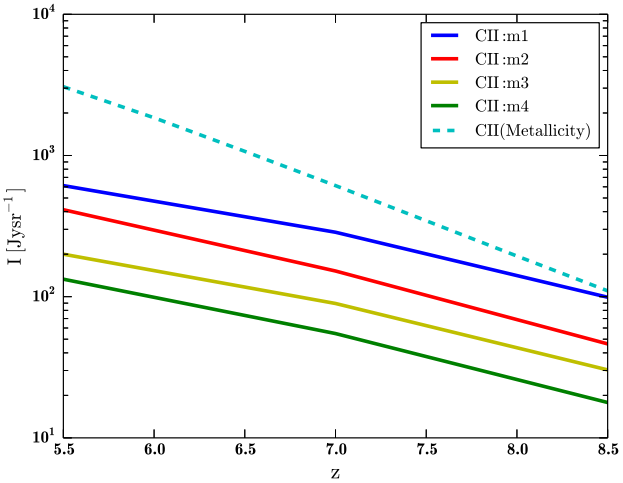

FIG. 3.— CII intensity as a function of redshift according to models **m1**, **m2**, **m3** and **m4** and estimated from the metallicity (see eq. 1).

In figure 4 the CII luminosity as a function of the SFR calculated with the different methods described is shown together with observational points of normal local galaxies from Malhotra et al. (2001) and with observational upper limits for high redshift galaxies. The high redshift galaxies shown in figure 4 have high SFRs which indicates that they are very massive and rare or that they have extreme SFRs/Mass ratios and in either case these galaxies will have little effect in the overall CII intensity. The CII luminosities estimated from the metallicity, pre-

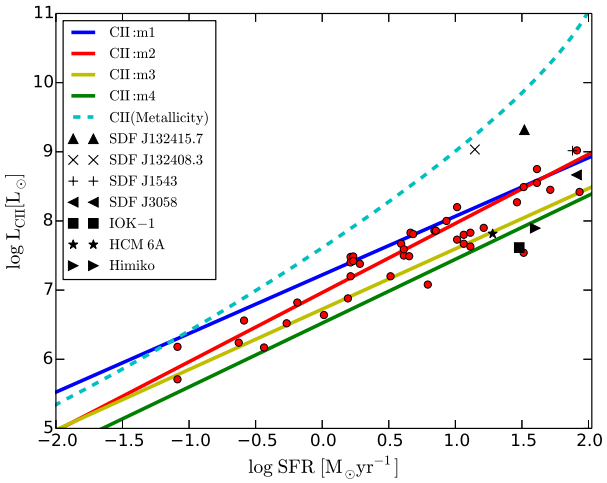

FIG. 4.— CII luminosity as a function of the SFR. The cyan dashed line corresponds to the CII luminosity from HII regions (assuming that all the carbon is ionized) and the solid lines corresponds to the CII luminosity obtained from equation the SFR using relations **m1**, **m2**, **m3** and **m4**. The red dots are local universe galaxies from the ISO Key Program (Malhotra et al. 2001) and the other symbols are upper limits from galaxies at $z > 6.5$ (taken from: (González-López et al. 2014) and (Kanekar et al. 2013) and (Ota et al. 2014)).

sented in figure 4, were obtained by assuming that $L_{\rm CII}$ was linearly proportional to the halo mass and by determining the constant of proportionality between these two quantities by setting equation 2 to the CII intensities obtained using equation 1. The correspondence between mass and SFR was assumed to follow equation 4.

3. CII FOREGROUNDS

The CII line emitted in the redshift range z ≈ 8.51-5.35 is observed at frequencies $200 - 300$GHz. CII is emitted in the infrared band and so CII intensity maps will be contaminated by other infrared lines and by infrared continuum emission from galaxies and from the IGM. In this section we show estimations for the contamination from all of these sources in the relevant observing frequency band. In addition we also consider contamination from emission from our galaxy.

3.1. *Contamination from line emission*

The main contaminants in CII intensity maps will be emission lines from lower redshifts namely the [OI]145μm, the [NII]122μm, the [NII]205μm and the CO rotation lines from transitions CO(2-1) and higher.
The [OI]145μm and the [NII]205μm lines are typical of PDRs while the [NII]122μm line is typical of HII regions and so the SFR is a good tracer of their emission such as in the CII case (see: section 3.3).
The CO lines are emitted from molecular gas and their luminosities depend on several characteristics of the gas and so we carefully estimate their intensity of emission separately in Section 3.2.

3.2. *Contamination from line emission* - CO transitions

As we will show in this Section the CO rotation lines will be the main contaminants of CII intensity maps observed at frequencies 200-300GHz. Since the luminosities of the several relevant CO transitions are poorly constrained observationally we estimated their intensity using the CO fluxes in the simulated galaxies catalog from Obreschkow et al. (2009a) and confirmed our results with a CO intensity calculated using only observational relations. The Obreschkow et al. (2009a) catalog is available for halo masses above $10^{10} M_{\rm odot}$ and has the galaxies positions in a mock observational cone and additional astrophysical properties such as CO fluxes for rotational transitions (1-0) to (10-9). These CO fluxes were estimated from the galaxies molecular gas content and the ISM temperature using physically based prescriptions and assuming thermal equilibrium.

Each CO rotation line that is observed in the frequency range 200-300GHz will come from the redshift range shown in table 3. Note that for the CO(2-1), as is shown in table 3, the minimum relevant redshift for this study is zero which corresponds to the line rest frequency.

TABLE 3
EMISSION REDSHIFTS FOR THE CO ROTATIONAL TRANSITIONS IN THE FREQUENCY RANGE 200-300GHZ

transition (J)	$\nu^{\rm J}_{\rm CO}$(GHz)	z($\nu_o \approx 300$GHz)	z($\nu_o \approx 200$GHz)
2-1	230.542	0	0.150
3-2	345.813	0.150	0.730
4-3	461.084	0.535	1.305
5-4	576.355	0.920	1.881
6-5	691.626	1.305	2.458
7-6	806.897	1.690	3.035
8-7	922.168	2.074	3.610
9-8	1037.439	2.458	4.186
10-9	1152.71	2.842	4.762

The CO intensity can be estimated from its luminosity as:

$$\bar{I}_{\rm CO}(\nu) = \sum_J \int_{M_{\rm min}}^{\infty} dM \frac{dn}{dM}(z,M) \frac{L^{\rm J}_{\rm CO}(z,M)}{4\pi D_{\rm L}^2} y^J(z) D_{\rm A}^2, \tag{11}$$

where the sum in J (angular momentum) is a sum over the luminosities of the different rotation lines from CO(2-1) to CO(6-5) and $z = \nu^J_{\rm CO}/\nu_{\rm o} - 1$.
We do not account for higher CO transitions since according to this CO model the CO contamination in CII intensity maps is highly dominated by the lower transitions. We also justifie our choice by arguing that the contamination from transitions (7-6) and higher would be originated from high redshifts ($4.8 > z > 1.7$) and so the lower metallicity of these galaxies would result in considerably lower CO emission. Using the simulated fluxes we parameterized the CO luminosity of galaxies as a function of halo mass for transitions CO(2-1) to CO(6-5) as:

$$L^{\rm J}_{\rm CO}(M)[L_\odot] = L_0 \times M^{\rm d0} \times \left(1 + \frac{M}{M_{\rm c1}}\right)^{\rm d1} \times \left(1 + \frac{M}{M_{\rm c2}}\right)^{\rm d2} \left(1 + \frac{M}{M_{\rm c3}}\right)^{\rm d3} \left(1 + \frac{M}{M_{\rm c4}}\right)^{\rm d4}, \tag{12}$$

where the parameters for each transition can be found in table 4. Note that this parameters were obtained for

TABLE 4
CO TRANSITIONS LUMINOSITY PARAMETERS

Trans	L_0	M_{c1}	M_{c2}	M_{c3}	M_{c4}	$d0$	$d1$	$d2$	$d3$	$d4$
2-1	4.70×10^{-29}	1.0×10^{11}	6.0×10^{11}	5.0×10^{12}	5.0×10^{14}	3.05	−2.0	−2.3	1.9	5.0
3-2	3.00×10^{-24}	6.0×10^{11}	5.0×10^{12}	4.0×10^{13}	0.0	2.6	−3.5	0.2	2.2	0.0
4-3	8.00×10^{-18}	9.0×10^{11}	5.0×10^{12}	3.0×10^{13}	0.0	2.05	−1.7	−1.8	2.3	0.0
5-4	3.50×10^{-18}	2.0×10^{12}	4.0×10^{12}	1.0×10^{13}	0.0	2.05	−2.0	−3.9	4.5	0.0
6-5	4.00×10^{-18}	9.0×10^{10}	6.0×10^{11}	0.0	0.0	2.0	1.5	−3.75	0.0	0.0

each transition by averaging the CO luminosity in the redshift range shown in table 3.

Figure 5 shows the luminosity of the CO(2-1) transition as a function of halo mass, in the redshift range 0 to 0.15, obtained from the simulation.

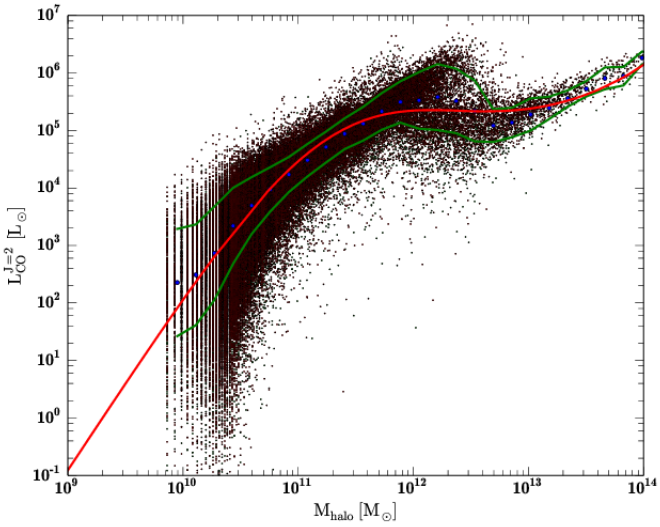

FIG. 5.— Luminosity of the CO(2-1) transition as a function of halo mass for the band $z \sim 0 - 1.5$. The black dots correspond to halos in the Obreschkow et al. (2009a) simulation. The blue dots show the mean of the scatter when binned in 30 logarithmic intervals in mass. The solid green lines show the $\pm 1\sigma$ relation. The red solid line corresponds to the parameterization given by equation 13 with the parameters from table 4.

Given that the used galaxies simulation only goes down till masses of $M = 1.0 \times 10^{10} M_\odot$ we extrapolated the average CO luminosity for lower halo masses assuming that it decayed at approximately the same rate as the SFR. The CO luminosities were parameterized as a function of dark matter halo masses and not as a function of galaxy masses and therefore for high halo masses they include the contribution from a main galaxy and several satellite galaxies. This parameterization could also have been made as a function of IR luminosity or SFR, however galaxies powered by active galactic nuclei have relatively small IR luminosities, small SFRs and high CO fluxes and so this population would have to be taken into account separately.

The theoretical average power spectra of CO contamination presented in figure 7 for transitions CO(2-1) to CO(6-5) indicates that the dominant contamination will be originated in the low CO transitions however the ratios of different CO lines were obtained by assuming a simple model with a single gas component in local thermodynamic equilibrium which does not necessary have to represent well the molecular gas conditions in all types of galaxies. A more recent work described in Lagos et al. (2011) and Lagos et al. (2012) attempted to estimate the luminosity of the several CO transitions using an improved method to estimate the molecular gas content in galaxies and using a more detailed model of the gas properties to estimate the relation between CO emission and molecular gas content compared to the Lagos et al. (2012) model. The main difference in the results from these two models is that the new model predicts a smaller molecular content in galaxies for $z > 2$ and higher ratios between the CO luminosities of higher transitions. These two corrections practically compensate themselves in terms of contamination in CII maps at the relevant frequencies for these study and so they should not have a significant affect in the validity of our predictions for intensity mapping. Even though there are limitations to the CO luminosities calculation made by Obreschkow et al. (2009a), observationally only the CO(1-0) line is well constrain at small redshifts ($z \leq 1$) and in that case the LFs derived from the properties in the simulated galaxies catalog are compatible with observations.

An observational only based model to estimate the CO(1-0) luminosity is presented in Sargent et al. (2013) and so to support our conclusions we used this completely independent model to estimate the CO contamination. The Sargent model estimates CO emission from a recent IR luminosity function at $z = 1$ presented in Sargent et al. (2012) and with the observational relations between IR and CO luminosities presented in Sargent et al. (2013).

A luminosity function consists in the evolution of the number density of galaxies per luminosity interval as a function of luminosity. The LF is commonly plotted in units of number density per decade in luminosity ($\Phi[\mathrm{Mpc}^{-3}\mathrm{dex}^{-1}]$, where dex accounts for the logarithmic variation of the luminosity for the bin used ($\log_{10} L_\mathrm{f} - \log_{10} L_\mathrm{i}$) as a function of luminosity. his function is an useful way to put constraints on the overall luminosity of observed galaxies above a given luminosity limit characteristic of each survey. The Sargent IR LF for $z \neq 1$ can be scaled with redshift using the factor $(1+z)^{2.8}$ in the galaxies number density and scaling the density as $\Phi \propto (1+z)^{-2.4}$ for $z > 1.0$ (for lower redshifts the density is fixed).

The CO luminosities can be obtain from the IR LF using:

$$log\left(\frac{L'_{\mathrm{CO(J=1\rightarrow 0)}}}{\mathrm{K\ km\ s^{-1}\ pc^2}}\right) = \alpha_1 + \beta_1 log\left(\frac{L_\mathrm{IR}}{\mathrm{L_\odot}}\right) \qquad (13)$$

where $(\alpha_1, \beta_1) = (0.18 \pm 0.02; 0.84 \pm 0.03)$ for normal galaxies and $(\alpha_1, \beta_1) = (-0.28^{+0.15}_{-0.09}; 0.84 \pm 0.03)$ for star-

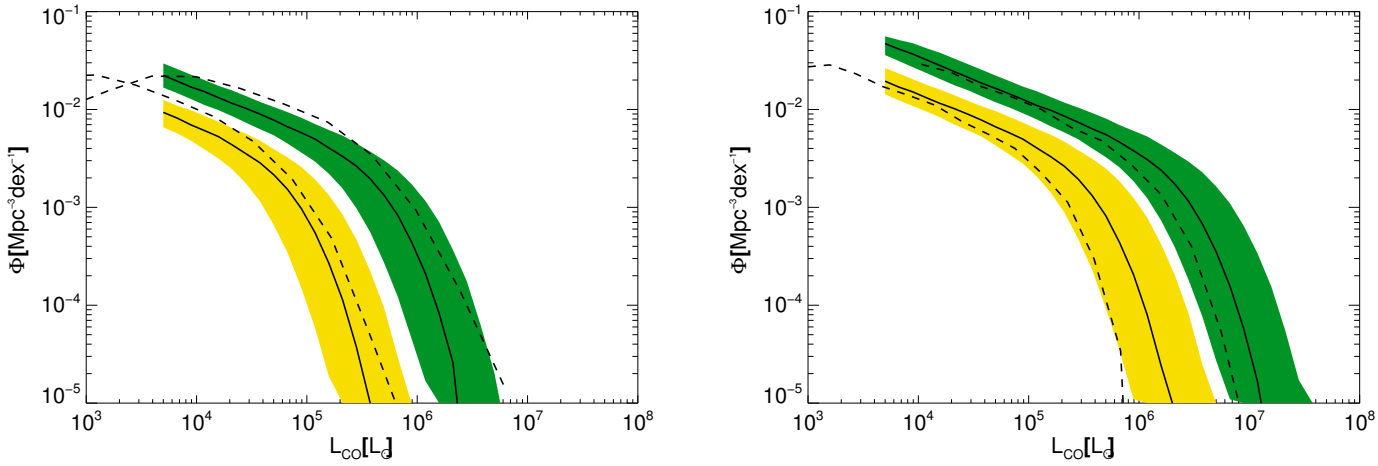

FIG. 6.— CO luminosity functions based on the galaxies catalog from the Obreschkow et al. (dashed lines) and on the Sargent CO model plus the Carilli et al. relation between the CO(2-1) and CO(1-0) transitions (solid lines) at redshifts 0 (left panel) and 1 (right panel). The yellow and green regions show the uncertainty in the Sargent luminosity functions take into account only the uncertainty in the passage from IR luminosity to CO(1-0) luminosity. The upper curves correspond to the transition CO(2-1) and the lower curves correspond to transition CO(1-0)

bursts (Sargent et al. 2013). In figure 6 the CO LF based in the Obreschkow et al. (2009b) galaxies catalog was theoretically obtained using a halo mass function and the CO luminosity parameterization in equation 13. In figure 6 the predictions from the Obreschkow and the Sargent CO models agree taking into account the uncertainty in the passage from IR luminosity to CO(1-0) luminosity in the Sargent method showed in the shaded regions. The uncertainties in the Sargent CO LFs are even higher if we take into account the error in the IR luminosity function, or the uncertainty in the passage from the CO(1-0) line to higher transitions. Ratios between the luminosities of the CO(1-0) line and higher CO transitions (in units proportional to the surface brightness $L'_{\rm CO}$ [K km s^{-1} pc^2]) for different types of galaxies are available in Carilli & Walter (2013). In order to obtain observationally only based estimations for the LFs of the relevant CO transitions we used the Sargent CO(1-0) model plus the Carilli et al. observational ratios: $r_{21} = 0.85$, $r_{31} = 0.66$, $r_{41} = 0.46$ and $r_{51} = 0.39$ which are appropriate for submillimiter galaxies. For the transition CO(6-5) since there are no available observational relations for the luminosities ratio r_{61} we assumed a ratio $r_{61} = r_{51}$. For each transition the CO luminosity in [L$_\odot$] ($L_{\rm CO}$) can be obtained using:

$$L_{\rm CO} = 3 \times 10^{-11} \nu^3 L'_{\rm CO}. \qquad (14)$$

We will from now on refer to the observational CO luminosities predicted using the Sargent CO(1-0) LF plus the Carilli et al. ratios for CO transitions as the observational CO model. The main differences between the two CO models lies in the conversion ratios between the luminosity of the several transitions since the average ration in the Obreschkow simulation are $r_{21} = 0.93$, $r_{31} = 0.70$, $r_{41} = 0.38$, $r_{51} = 0.12$ and $r_{61} = 0.02$ at a redshift close to zero and slightly increase for higher redshifts. The flux ratios in the Obreschkow simulation are appropriate for regular galaxies, while for star bursts and quasars the ratios between fluxes of high transitions are much higher.

Given the lack of observations of CO fluxes of high transitions in normal galaxies, with masses below 10^{12}M$_\odot$, the CO transition ratios and LFs are poorly constrained and this work can serve as motivation to plan an experiment especially designed to measure CO emission from several rotational transitions and their redshift evolution.

We will now show theoretical estimates for the intensity and the power spectra of CO contamination using the LFs obtained with the two CO methods. The CO intensity can be obtained by integrating over the CO LF for the luminosity range available for each line. Following Gong et al. (2012) the CO intensity formula is given by:

$$I^J_{\rm CO}(\nu) = \int_{L^{\rm J}_{\rm max}}^{L^{\rm J}_{\rm min}} dL \frac{dn}{dL} \frac{L^{\rm J}_{\rm CO}}{4\pi D_L^2} y\left(z(\nu, J)\right) D_{\rm A}^2, \qquad (15)$$

where $dn/dL = \Phi(L)$.

Since the contamination by CO in CII maps will be analysed as if CO was emitted at the CII redshifts than the CO contamination power spectra for each transition has to be scaled from the original CO power spectra. Following Gong et al. (2014) the contamination CO power spectra is given by:

$$P_{\rm obs}(k_\perp, k_\parallel) = \left[P^{\rm clus}_{\rm CO}(z_f, J, k_f) + P^{\rm shot}_{\rm CO}(z_f, J, k_f)\right] \times \left(\left[\frac{\chi(z_{\rm s})}{\chi(z_f)}\right]^2 \left[\frac{y(z_{\rm s})}{y(z_f)}\right]\right), \qquad (16)$$

where the clustering power spectra is given by:

$$P^{\rm clus}_{\rm CO}(z_f, J, k_f) = \bar{I}^2_{\rm f}(z_f) b^2_{\rm f}(z_f) P_{\delta\delta}(z_f, k_f), \qquad (17)$$

the indexes s or f indicate whether we are referring to respectively the source (CII) or the foreground (CO) redshifts, χ is the comoving distance, $|\vec{k_f}| = \left[(r_s/r_f)^2 k_\perp^2 + (y_s/y_f)^2 k_\parallel^2\right]^{1/2}$ is the three dimensional k vector at the redshift of the foreground line, $P_{\delta\delta}$ is the matter power spectra and $b^{\rm J}_{\rm CO}$ is the average bias between

the luminosity of the CO($J \rightarrow J-1$) transition and the matter power spectra. The shot noise power spectra due to the discrete nature of galaxies is given by:

$$P_{\rm CO}^{\rm shot}(z,J) = \int_{M_{\rm min}}^{M_{\rm max}} dM \frac{dn}{dM} \left[\frac{L_{\rm CO}^{J}(M,z)}{4\pi D_L^2} y(z,J) D_A^2 \right]^2 . \quad (18)$$

There are distortions in the observed power spectra in different directions due to redshift evolution of the signal. In theory these distortions could be used to differentiate between the signal and the foregrounds or to confirm if the foregrounds where effectively removed since in that case there should be observed no distortions. However, in practice this would require an experiment with an extremely high resolution and so in this study we will only consider the spherical average power spectra. The foreground lines will contaminate the spherical average CII power spectra at $|\vec{k}_s| = \left[k_\parallel^2 + k_\perp^2\right]^{1/2}$.

If we assume that there is a correlation between CO luminosity and mass of the dark matter halo which contains the galaxies than for large enough volumes the bias between the overall CO emission and the underlying dark matter density field can be estimated from the halo bias ($b(z,M)$) as:

$$b_{\rm CO}^{J} = \frac{\int_{M_{\rm min}}^{M_{\rm max}} dM \frac{dn}{dM} L_{\rm CO}^{J}(M,z) b(z,M)}{\int_{M_{\rm min}}^{M_{\rm max}} dM \frac{dn}{dM} L_{\rm CO}^{J}(M,z)} \quad (19)$$

where $M_{\rm min} = M(L_{\rm min}^{\rm J})$, $M_{\rm max} = M(L_{\rm max}^{\rm J})$ and $L_{\rm CO}^{\rm J}(M,z) \propto M^{\alpha_{\rm CO}}$. The correct value for $\alpha_{\rm CO}$ changes with the galaxy mass, assuming the values from the galaxies in the Obreschkow simulation we have $\alpha_{\rm CO} = 1.5 \pm 0.5$ for halos with $M < 10^{12} {\rm M}_\odot$ and $\alpha_{\rm CO} < 1$ for higher mass halos. For the observationally based CO contamination power spectra we will assume $\alpha_{\rm CO} = 1$ in our calculations. The theoretically estimated contamination power spectra of CO emission in CII maps observed in the frequency range 200GHz to 300GHz is shown in figures 7 and 8 for the Obreschkow CO model and the observational CO model.

3.3. *Contamination from atomic emission lines*

The [OI]145μm, the [NII]121.9μm and the [NII]205.2μm atomic emission lines are emitted from PDRs or from HII regions and so the luminosity of these lines is powered by stellar emission and therefore it is expected to be correlated with the galaxies SFRs. The luminosity of these lines depends highly on the galaxies gas density and FUV flux (Kaufman et al. 1999), however for a large number of galaxies their luminosity densities scales with the FIR luminosity and so we used the observational ratios, presented in table 5 (where $[x]/[FIR]$ stands for the average fraction of FIR emission of each line), taken from (Graciá-Carpio et al. 2011), (Brauher et al. 2008), (Ferkinhoff et al. 2011) and (Zhao et al. 2013) to estimate the lines luminosities. The luminosity of these lines as a function of halo mass was than obtained using equations 4, 5 and 8. The intensity of each line in the relevant range of 200 to 300GHz can be estimated using equation 2. The resulting intensities are shown in table 5.

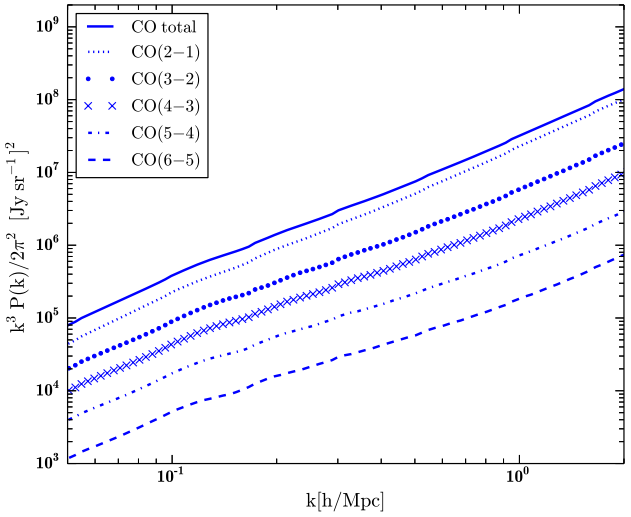

FIG. 7.— Power spectra of CO line emission made using the parameterization from equation 13 in the frequency range 200GHz to 300GHz projected to the redshift of the CII line. The top solid line shows the total CO power spectra and the lower lines show the CO(2-1) to CO(6-5) transitions.

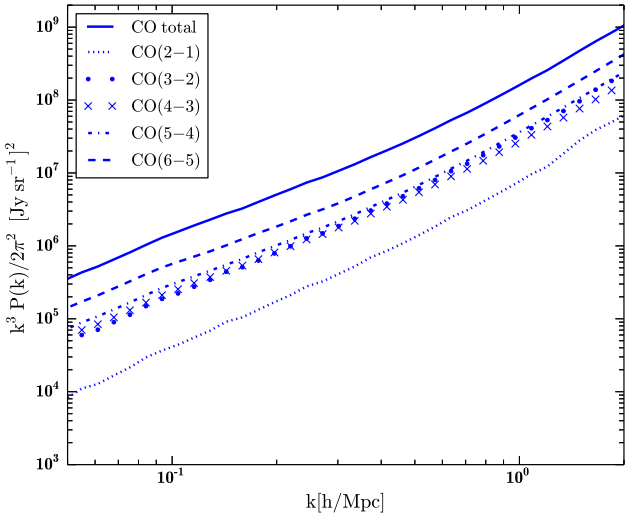

FIG. 8.— Power spectra of CO line emission made using the observational CO model in the frequency range 200GHz to 300GHz projected to the redshift of the CII line. The top solid line shows the total CO power spectra and the lower lines show the CO(2-1) to CO(6-5) transitions.

TABLE 5
AVERAGE INTENSITY OF SEVERAL EMISSION LINES IN THE OBSERVED FREQUENCY RANGE 200-300GHZ IN UNITS OF [Jy sr^{-1}].

line	$[x]/[FIR]$	$z[200GHz]$	$z[300GHz]$	*Intensity*
[OI]145μm	0.05%	9.3	5.9	5.1
[NII]122μm	0.01%	11.3	7.2	5.5
[NII]205μm	0.03%	6.3	3.9	58

The average contamination from these lines is consid-

erably below the CII intensity.

3.4. *Contamination from continuum emission*

The continuum emission that contaminates observations can be estimated from the galaxies SFR and gas properties. Stellar continuum emission can directly contaminate observations but it can also be absorbed by the dust in the galaxy and be re-emitted at lower frequency bands .0.4. Interactions between free electrons and ions in the galaxies gas also produces free-free and free-bound continuum emission. During a recombination there is the possibility of emission of two photons which also contributes to the continuum infrared luminosity. Since continuum radiation (with the exception of stellar radiation) observed in the frequency range 200-300GHz will be emitted in the infrared band, it will not be absorbed by any of the main hydrogen lines or by dust and so we can assume that this radiation is not affected during its path towards us.

The intensity of contamination from all of the referred continuum sources of infrared emission is shown in table 6 and the detailed calculations are presented in the appendix.

TABLE 6
Intensity of continuum emission observed at frequencies of 300GHz and 200GHz in units of [Jy sr^{-1}]

Source of emission	I(300GHz)	I(200GHz)
dust	2.2×10^{-5}	1.8×10^{-7}
stellar	4.1×10^{-3}	8.5×10^{-1}
free-free+free-bound	2.4×10^{-12}	1.6×10^{-12}
2-photon	3.4×10^{-12}	2.8×10^{-12}

It is also expected to be some contamination from the Milky Way which can be estimated from temperature maps of our galaxy for the relevant frequencies. Using temperature maps from Planck at frequencies 143GHz, 217GHz and 353GHz we estimated that unless we were in the center of the Milky Way where the brightness temperature can reach 0.2-0.3K the average brightness temperature is well below 0.1K which corresponds to an observed intensity of 2.44×10^{-32}Jy sr^{-1} to 1.18×10^{-32}Jy sr^{-1} for 200GHz and 300GHz respectively.

The intensities in table 6 show that the continuum contamination is below the CII signal and so in principle it is not necessary to remove this contamination from observational CII intensity maps.

4. SIGNAL GENERATION

The CII mock observational cone was made using the following steps:

1. A dark matter density field with a size of $L_{\rm box} = 634\ {\rm h}^{-1}$Mpc and a number of cells of $N_{\rm box}^3 = 1800^3$ was generated using the Simfast21 code (Santos et al. 2010; Silva et al. 2012).

2. The same code was used to generate dark matter halo catalogs from the previously generated density field using the excursion set formalism and by sampling the halos directly from the density field. These catalogs were made for redshifts 5.3 to 8.5 with a redshift step of 0.1 and a halo mass range of $10^8 {\rm M}_\odot$ to $10^{15} {\rm M}_\odot$. At this point the halo properties contained in the catalogs included only the halo mass and position in a three dimensional box with the size and resolution of the density field.

3. We randomly assigned astrophysical properties, such as SFR, from the De Lucia & Blaizot (2007) galaxies catalog, to the generated halos according only to the halos mass and redshift.

4. We added CII luminosities to the halo properties using the halos SFR versus CII luminosity relations shown in section 2.2, which resulted in four CII luminosity values for each halo, one for each of the $\mathbf{m_1}$, $\mathbf{m_2}$, $\mathbf{m_3}$ and $\mathbf{m_4}$ models.

5. In order to build the observational cones we made a box with 50 by 256^2 cells which covers de frequency range 200 to 300 GHz and the 1.3deg $\times$ 1.3deg field of view with steps of respectively $df_{\rm o}$ =2GHz and $d_{\rm ang} = 8 \times 10^{-3}$deg. The angular coordinates correspond to positions in right ascension (RA) and declination (DECL), where the center of the box (cone rotation axis) is at RA=0 and DECL=0.

6. We filled the box with the halos by assuming that the halos z direction corresponded to the direction of the line of sight and that moving in this direction was equivalent to moving in redshift. Since the size of the halo catalogs in the z direction is smaller than the comoving distance from redshift 5.3 to 8.5 we piled the catalogs in order to cover all the needed distance range but we rotated the upper catalogs in order to not repeat structures in the line of sight direction. The position z=0 of the halos was assumed to be at the comoving distance at which emitted CII photons are observed at a frequency of 300GHz ($d_{\rm f300}$). The position $({\rm x_i}, {\rm y_i}, {\rm z_i})$ of the halos was assumed to be at a distance ($d_{\rm x} = {\rm x_i} \times d_{\rm r} - L_{\rm box}/2$, $d_{\rm y} = {\rm y_i} \times d_{\rm r} - L_{\rm box}/2, dist_{\rm z} = d_{\rm f200} + {\rm z_i} \times d_{\rm r}$), where $d_{\rm r} = L_{\rm box}/N_{\rm box}$, which corresponds to a comoving distance $dist_c = (d_x^2 + d_y^2 + d_z^2)^{1/2}$ and to an angular position in right ascension and declination of respectively:

$$\text{RA}= \arctan\left(\frac{d_{\rm x}}{d_{\rm com}}\right), \tag{20}$$

and

$$\text{DEC}= \arctan\left(\frac{d_{\rm y}}{d_{\rm com}}\right). \tag{21}$$

Each comoving position was converted first to a redshift and then to an observed frequency using $\nu_{\rm obs} = \nu_{\rm CII}/(1+z)$. The halos were than distributed in the cone according to their angular position and observed frequency. For each halo catalog at a redshift z we only used the halos with a redshift lower than $z + dz$.

7. In each cell of the mock observing cone the intensity was assumed to be given by a sum over the contribution from each galaxy as:

$$I_{\rm CII} = \sum_i \frac{1}{df_{\rm o}} \frac{L_{\rm CII}(M,z)}{4\pi D_L^2}, \quad (22)$$

with $v_{\rm cell} = df_{\rm o} \times dr_{\rm com}^2$, where $dr_{\rm com} = {\rm tang}(d_{\rm ang}) \times d_{\rm com}$.

8. In order to estimate the effect of the masking technique we also made mock observing cones with CII where we put to 0 the cells where the CO cones had been masked.

5. CO FOREGROUNDS GENERATION

The CO mock observational cones were made using the following steps:

1. A dark matter density field with a size of $L_{\rm halos}^3 = 296^3$ h^{-3}Mpc^3 and a number of cells of $N_{\rm halos} = 1200^3$ was generated using the Simfast21 code.

2. The same code was then used to generate dark matter halo catalogs from the previously generated density field using the excursion set formalism and by sampling the halos directly from the density field. These catalogs were made for redshifts 0 to 2.5 with a redshift step of 0.1 and a halo mass range of 10^8M$_\odot$ to 10^{15}M$_\odot$. The halo properties contained in the catalogs included only the halo mass and position in a three dimensional box with the size and resolution of the density field.

3. We randomly assigned astrophysical properties, such as SFR, CO fluxes and visual absolute magnitudes, from the De Lucia & Blaizot (2007) and the Obreschkow et al. (2009a) galaxy catalogs, to the generated halos according only to the halos mass and redshift.

4. We added CO luminosities to the halo properties using the halos CO fluxes.

5. We repeated steps 5 and 6 of the CII signal generation assuming that the position z=0 of the halos corresponded to a comoving distance of zero and that the redshift could be converted to an observed frequency using $\nu_{\rm obs} = \nu_{\rm CO}^{\rm J}/(1+z)$.

6. For each CO transition we built mock observing cones with intensities estimated as in the CII case and than we added the cones to obtain the total CO intensity.

7. In order to simulate the effect of the masking technique we made a mock observing cone with only the galaxies with CO fluxes above a given threshold. The pixels with at least one galaxy correspond to pixels that should be masked in order to decrease the CO contamination in CII observational maps and so we put to zero the corresponding pixels in the initial CO box and in the CII box. We also used the same technique with a limit in magnitudes in the AB system K filter ($m_{\rm K}$) instead of a limit in CO flux.

One of the advantages of simulating mock observational cones is that we can directly add the signal and its contaminants to obtain a more realistic version of an observational intensity map. This is useful because it gives as better predictions of what an observational experiment will actually measure and how to relate the observed signal to the intrinsic signal which is where the scientific information really lies.

The analysis of the information contained in these cones is mainly made using the power spectra of the signal and so we used slices in frequency (these slices correspond to the signal emission around a given redshift) from these cones to construct intensity maps in Cartesian coordinates, from which we calculated the signal power spectra. With this method we directly mapped the contaminants intensity spatial fluctuations into Cartesian coordinates at the signal redshift. This allowed us to directly obtain a contamination power spectra which is very useful to determine the real degree of foreground contamination and to plan ways to clean observational maps.

A slice of a mock observational CII cone is shown in figure 9. This figure shows that CII emission is not randomly distributed but that it follows the underlying density fluctuations.

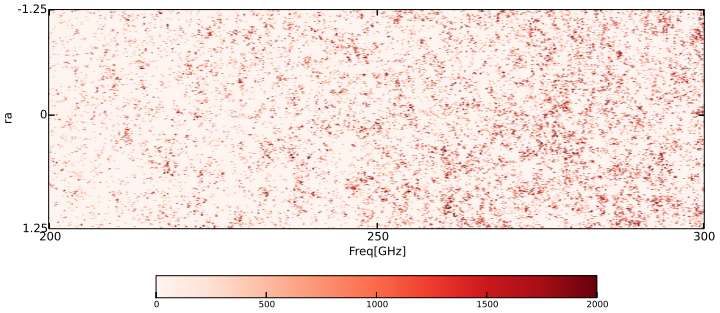

FIG. 9.— Slice of a CII mock observing cone with 2.5 square degrees from frequencies 200GHz to 300GHz.

The CII intensities obtained with these observing cones is shown in table 7 together with the overall CO intensity from transitions (2-1) to (6-5) at the same observed frequencies. The results show that CO contamination will dominate observations especially for low frequencies.

TABLE 7
INTENSITY OF CII EMISSION FROM GALAXIES AS A FUNCTION OF REDSHIFT CALCULATED USING THE SFR, THE MEDIUM, MAXIMUM AND MINIMUM VALUES OF THE CII INTENSITY CORRESPOND TO THE LCII VERSUS SFR PARAMETERIZATIONS $\mathbf{m_2}$, $\mathbf{m_1}$ AND $\mathbf{m_4}$ RESPECTIVELY. ALSO SHOWN ARE THE CO INTENSITIES ESTIMATED USING THE OBRESCHKOW CO MODEL. THE INTENSITIES HAVE UNITS OF [Jy sr^{-1}].

$z_{\rm CII}$	$\bar{I}_{\rm CII}$	$I_{\rm CII}^{\rm max}$	$I_{\rm CII}^{\rm min}$	$I_{\rm CO}$
8.5	47.0×10^1	9.50×10^1	1.80×10^1	1.05×10^3
7.5	1.00×10^2	2.00×10^2	3.70×10^1	1.25×10^3
6.5	1.90×10^2	3.50×10^2	7.50×10^2	1.12×10^3
5.5	3.36×10^2	6.00×10^2	1.33×10^2	1.06×10^3

TABLE 8
PARAMETERS FOR A CII EXPERIMENT

Instrument	CII-Stage I	CII-Stage II
Dish size (m)	10	10
Survey area A_s (arcmin^2)	78×0.5	78×1.0
Instantaneous FOV (arcmin^2)	13.6×0.5	13.6×0.5
Freq. range (GHz)	200-300	200-300
Frequency resolution (GHz)	2	0.4
Number of Spectrometers	32	64
Total number of bolometers	864	1728
On-sky integration time (hr)	1000	1000
NEFD on sky (mJy$\sqrt{\text{sec}}$)	65	65

6. INSTRUMENT PARAMETERS

The characteristics of an experiment able to measure the CII intensity and spatial fluctuations will now be briefly discussed.

We propose to use one of two similar setups, the first one CII-Stage I is appropriate for optimistic CII models (models with a high CII luminosity density) and the second one CII-Stage II has the minimum requirements to insure a CII power spectra detection in the case of a more pessimistic CII model. The choice of a setup for the CII experiment is mainly dependent on the evolution of the CII luminosity for high redshifts and so it can be updated when more high redshift CII observations are available.

The basic experiment proposed here (CII-Stage I) consists in using one stack of independent single beam, single polarization spectrometers, one stack for each polarization. Each of this spectrometers would contain several bolometers and each of the stacks would cover a line on the sky via a polarizing grid. The details of the proposed experimental setups are shown in table 8.

7. CLEANING CONTAMINATION FROM LOWER REDSHIFT EMISSION LINES

7.1. *Pixel masking*

As was shown in previous sections the main line contaminants for the planned observations are CO rotation lines from low redshifts. Since the contamination from CO emission lines in the CII power spectra is high we made CO flux cuts to study which galaxies are dominating the contamination and if they can be removed from the observational data by masking the pixels with the stronger contaminants.

Given that detecting all galaxies with low CO fluxes can be very challenging we also consider using a CO tracer easier to detect such as the SFR or the relative magnitude in a broad band filter such as the K filter (measured as magnitudes in the AB system in the K filter m_K) which is centered at 2190 nm and covers around 390 nm. The SFR can only be used as a CO tracer in star forming galaxies and since there is also an intense CO emission in galaxies powered by active galactic nuclei if we want to use SFR or infrared emission as a CO tracer we should use an additional tracer like observations in the visible band to target the active galactic nuclei.

In figure 10 we can see that galaxies with a high CO flux also have relatively low magnitudes in the K band and so we estimated the m_K cut necessary to reduce the power spectra of CO contamination.

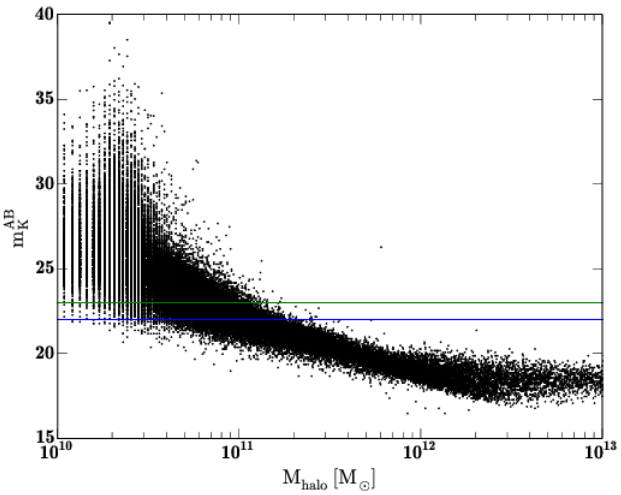

FIG. 10.— AB magnitude in the K filter versus halo mass relation at redshift z=0.06. The relation showed has a small evolution with redshift. The horizontal lines show what galaxies are being masked according to the m_K cuts showed in figure 11.

We show in the bottom panels of figure 11 that for most optimistic CII models the power spectra of CO contamination can be efficiently reduced by removing from the observations contamination by galaxies with CO fluxes in one of the CO rotation lines higher than 5×10^{-22}Wm^{-2} and that this can be done by masking less than 10% of the pixels in the planned observations. In alternative the top panels of this figure show that masking in m_K magnitudes is also possible and the necessary masking would requier a cut of m_K =22 in order to sufficiently decrease the power spectra of CO contamination for a CII model like $\mathbf{m_2}$. For CII models which yield lower intensities the m_K cut would have to be of m_K =23 or even higher which would not be realistic for masking.

The CO masking can be done with cuts in quantities like CO flux, SFR, IR luminosity, magnitude in a given band or a combination of probes depending of the CO tracer experiments available. The masking cuts considered in this study are presented in table 9 for a CII experiment with a observational pixel defined by an angular resolution of 8.4×10^{-3}deg^2 and a frequency resolution of 2GHz.

TABLE 9
MASKING PERCENTAGES FOR AN OBSERVATION IN A FREQUENCY RANGE OF 200 TO 300GHZ MADE WITH A PIXEL RESOLUTION OF 8.4×10^{-3}deg^2 TIMES 0.4GHZ OR 2GHZ FOR CII-STAGE I AND CII-STAGE II RESPECTIVELY

Flux/m_K cuts	CII-Stage I Masking %	CII-Stage II Masking %
$F_{CO} > 1 \times 10^{-21}$[Wm^{-2}]	7.70	1.59
$F_{CO} > 5 \times 10^{-22}$[Wm^{-2}]	12.99	9.30
$F_{CO} > 2 \times 10^{-22}$[Wm^{-2}]	23.31	9.31
$m_K < 22$	6.23	1.28
$m_K < 23$	13.76	2.92

In the case that the CO luminosities of some galaxies at low redshifts can be measured to a high precision it is also possible to remove their intensity from the observational pixel instead of masking it however the intensity of the

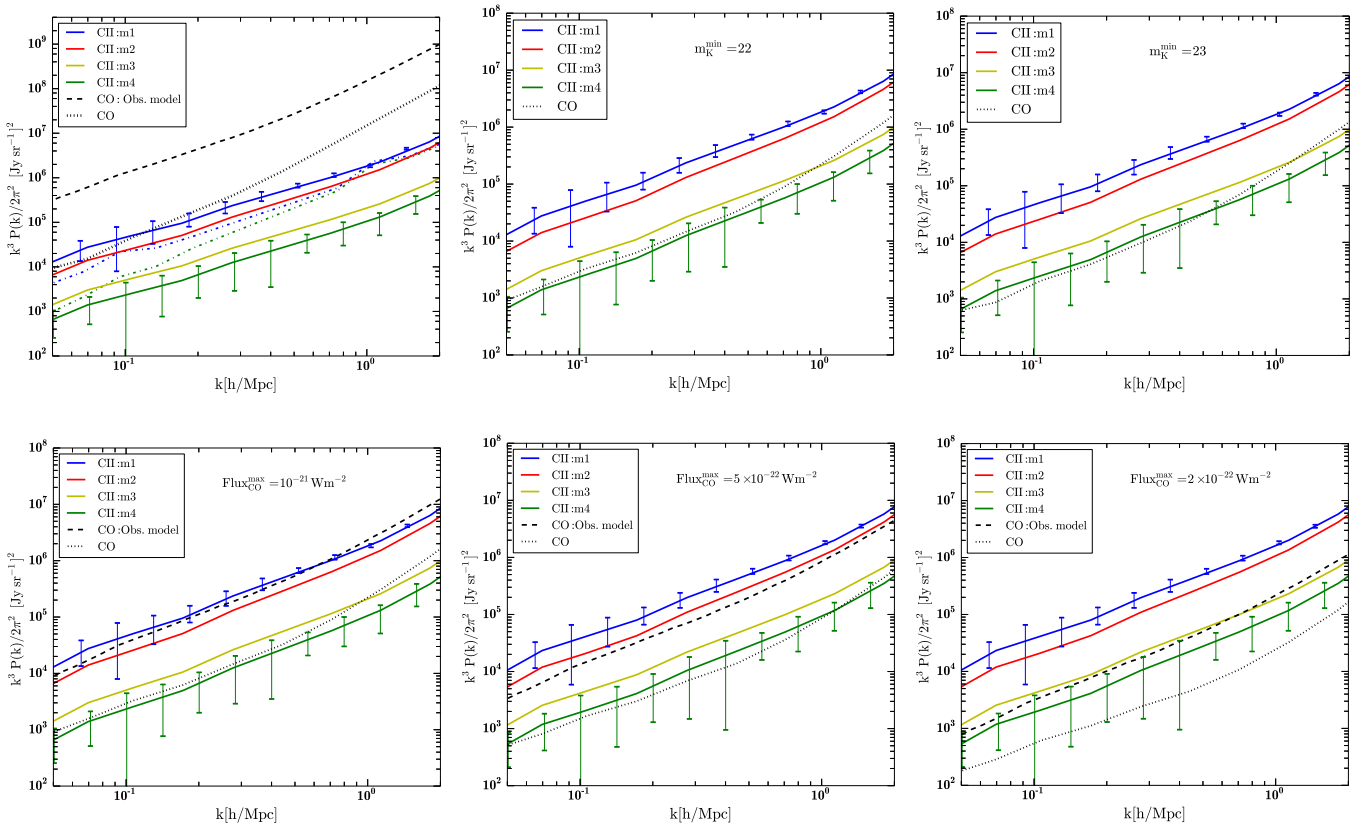

FIG. 11.— Power spectra of CII emission for four parameterizations of LCII vs SFR (solid lines) and power spectra of CO contamination (dotted lines) observed in a frequency range of 37GHz centered at $F_{obs} \approx 250$GHz. Upper Left panel corresponds to the total CII power spectra and CO contamination power spectra. The middle and right upper panels assume only CO sources with AB relative magnitudes in the K band above $m_K = 22$ and $m_K = 23$ respectively. Lower panels assume only CO sources with Fluxes below 10^{-21}Wm^{-2} (left panel), 5×10^{-22}Wm^{-2} (middle panel) and 2×10^{-22}Wm^{-2} (right panel). Also shown in the upper left and in the lower panels are dashed lines of the theoretical CO emission, with the same flux cuts, estimated using the CO observationaly based model which is based in the Sargent et al. (2013) CO(1-0) model plus observational based relations to obtain the luminosities of higher CO transition lines. The error bars in the CII models m1 and m2 are based in the experimental setup of the CII-StageII experiment described in table 8.

contamination would have to be above the "noise" in that pixel and so this would only be possible to do with very bright galaxies and the CII signal from this pixels would have a greater error than the signal from other pixels.

7.2. *Cross correlation as a foreground cleaning method*

In intensity mapping experiments where the degree of contamination is high and the masking technique is not successful in cleaning observational maps either because its not possible to detect all of the contaminant galaxies which need to be masked or because the masking percentages are too high and we do not want to erase the signal during the foregrounds cleaning it is useful to have an additional method to remove the foregrounds and/or to confirm if the masking procedure was successful.

In this section I will discuss the possibility to use cross correlation as a method to help removing CO foregrounds from CII maps and as a way to probe the degree of CO contamination remaining in CII maps after the masking technique has been applied.

7.2.1. *Cross correlating foregrounds*

As is shown in figure 12 the intensity of CO emission in one line is strongly correlated with the galaxies number density at the same redshift since they both trace the underlying density fluctuations. Therefore, if we use

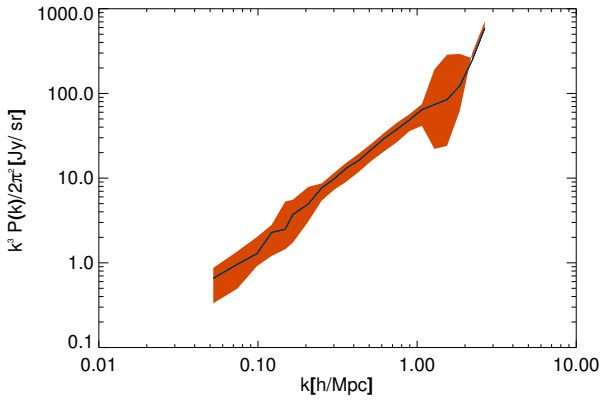

FIG. 12.— Cross correlation power spectra between number of galaxies and intensity of the CO(5-4) line at redshift z=1.4 obtained from our simulations. The 1σ uncertainty shown in orange was obtained by cross correlating these two quantities in different regions of the space.

galaxy surveys to map the number density of galaxies at a redshift such as 1.4 and cross correlate it with an observational intensity map of the CO(5-4) line centered at the same redshift (obtained from the 200-300GHz observing cone) the result will be proportional to the intensity fluc-

tuations of the CO(5-4) line even it the intensity maps also contains CII and other CO lines. This can be done for several foreground lines and redshifts to probe the intensity of contamination of these lines.

7.2.2. *Cross correlation between CO lines at different redshifts*

As can be observed in table 3, in some cases there are two CO lines originated from the same redshift contaminating the observational maps at two different frequencies. For example, the CO(3-2) and the CO(4-3) emitted at a redshift of $z = 0.6$ will be observed at frequencies of 288.2GHz and 216.1GHz respectively and so they will contaminate CII intensity maps at redshifts 7.8 and 5.6. As is shown in figure 13 the cross correlation between observational maps with CII plus CO will be more strongly correlated than maps with just CII and so by cross correlating intensity maps before and after masking the CO contamination we can confirm if the cleaning procedure was successful or if there are still strong foregrounds. Also, the existence of contamination from two lines emitted from the same redshift can in principle be used to develop algorithms to help removing the CO contamination, although that task is out of the objectives of this study.

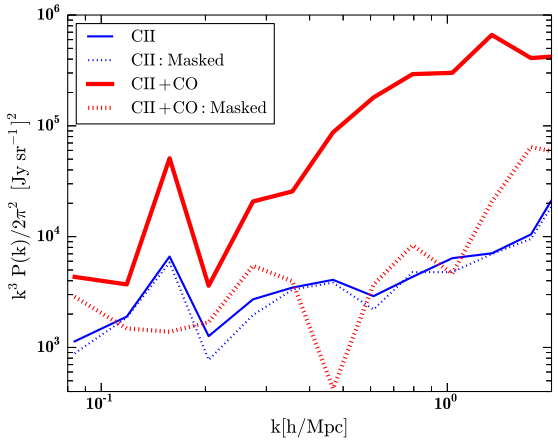

FIG. 13.— Cross correlation power spectra between observational maps with 70Mpc centered at frequencies 288.2GHz and 216.1GHz which correspond to CII emission from redshift 7.8 and 5.6. The blue thin lines shows the cross correlation obtained from maps with only CII emission. The red thick lines shows the cross correlation obtained from maps with CII plus CO. Solid line denote the full signal while dotted lines denote the signals masked till a CO flux of $2 \times 10^{-22}\mathrm{Wm}^{-2}$. The masking was done assuming the CII-Stage II experimental setup.

8. CROSS CORRELATION BETWEEN HI AND CII

Both fluctuation in HI and in CII intensity maps are correlated with fluctuations in the underlying density field and so the cross correlation power spectra from these lines gives an independent measure of their intensity. Since CII is emitted from galaxies and HI is emitted from the IGM these two quantities are mostly negatively correlated at large scales. At small scales the correlation disappears given that different processes of radiative emission have different bias with the underlying density fluctuations. In figure 14 we show that the

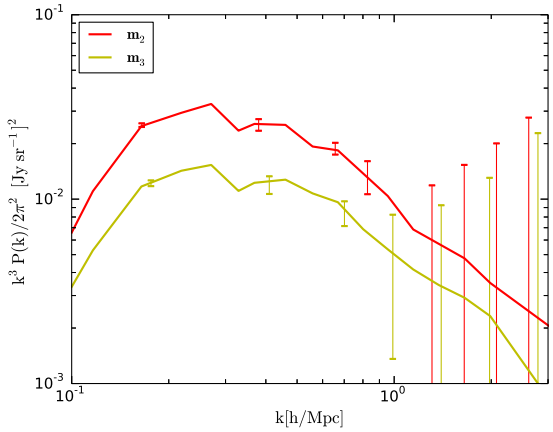

FIG. 14.— Module of the correlation power spectra between CII emission (models $\mathbf{m_2}$ and $\mathbf{m_3}$) and the neutral hydrogen 21 cm line at redshift z=7.0. The error bars were estimated assuming the CII-Stage II experimental setup. Note that these two lines are negatively correlated at the shown scales.

cross power spectra between HI emission and two models for CII emission. The Error bars shown in this figure were obtained with the HI 21 cm line experiment described in table 10 and with the CII-Stage II instrument previously described.

TABLE 10
PARAMETERS FOR SKA1-LOW

	SKA1-low(z=7)	unit
ant. diameter D_{ant}	35	m
survey area A_{s}	6.55	deg^2
FoV per ant.	10.9	deg^2
effective area per ant. A_e	355.04	m^2
freq. resolution $d\nu$	3.9	kHz
bandwidth (z=8±0.5) BW	18	MHz
tot. int. time t_{int}	200	hr
min. baseline D_{min}	35	m
max. baseline D_{max}	1	km
collecting area A_{coll}	307466	m^2
$\mathrm{uv}_{\mathrm{min}}$	21	
$\mathrm{uv}_{\mathrm{max}}$	596	
$\mathrm{T}_{\mathrm{sys}}$	291	K
effective num. ant.	866	

9. CONCLUSIONS

Intensity mapping of the CII line during the end of the EoR is in the reach of today's technology.
The intensity of the CII signal from $z \sim 8.5$ to $z \sim 5.5$ is likely to be between $10^2 - 10^3 \mathrm{Jysr}^{-1}$ although higher values would be possible if the SFRD is higher than the current predictions.

The CII emission of a galaxy is a good probe of its SFR and so intensity mapping of this line should provide good independent constraints in the SFRD and its evolution. This line is also dependent in the ISM metallicity and although CII intensity maps cannot give strong constraints to this quantity they will provide a lower limit which will be on its own an improvement over current constraints of the gas metallicity at high redshifts. Note

that redshift evolution of the metallicity can tell us about the characteristics of POP II and POP III stars which is also particularly important for Reionization studies.
Emission from CO rotation lines is going to be the main contaminant in CII observations and although the CO and CII intensities have a large uncertainty it is reasonably confirmed that some of the CO signal has to be removed from observations in order to recover the correct CII fluctuations.
We estimated the CO intensity using two independent methods, one based in detailed simulations of gas conditions in galaxies and physical relations between CO transitions and other which uses only observational quantities and observational based relations between these quantities. Both these methods predict similar CO intensities. The current constraints in CO and CII emission indicate that the CO power spectra will be up to one order of magnitude higher than the CII power spectra however we showed that the CO signal can be reduced at least as much by masking the pixels contaminated by the galaxies with the brighter CO emission. We described an experiment which is in the reach of current technology and is able to measure the CII power spectra with enough resolution so that we can mask most of the CO contamination without erasing the CII signal. In order to identify the most luminous CO galaxies we propose to use a galaxy survey able to measure CO luminosities or a more modest survey able to detect the galaxies AB magnitudes in the K band, since this is a good tracer of CO luminosity.

A galaxy survey able to measure CO luminosities of several transitions till a redshift of at least 2.5 would also provide the first LFs for CO transitions higher than the first CO rotational transition which would by it self be a valuable contribution to the study of gas conditions of galaxies.

If the CO contamination is to high and the masking technique is not enough to successfully clean the images or in order to confirm if the contamination was well removed we can use cross correlations between different CO lines to estimate the intensity of their contamination.

Finally the CII line and the 21 cm line are expected to be strongly anticorrelated. By cross correlating CII and 21 cm maps we will have a statistical estimate of the intensity of these signals independent of most foregrounds which can be a valuable asset in constraining Reionization.

REFERENCES

Aannestad, P. A., & Emery, R. J. 2003, A&A, 406, 155
Amblard, A., Cooray, A., Serra, P., et al. 2010, A&A, 518, L9
Boselli, A., Gavazzi, G., Lequeux, J., & Pierini, D. 2002, A&A, 385, 454
Bouwens, R. J., Illingworth, G. D., Oesch, P. A., et al. 2011, ArXiv e-prints
Boylan-Kolchin, M., Springel, V., White, S. D. M., Jenkins, A., & Lemson, G. 2009, MNRAS, 398, 1150
Brauher, J. R., Dale, D. A., & Helou, G. 2008, ApJS, 178, 280
Brown, R. L., & Mathews, W. G. 1970, ApJ, 160, 939
Cardiel, N., Elbaz, D., Schiavon, R. P., et al. 2003, ApJ, 584, 76
Carilli, C. L. 2011, ApJ, 730, L30
Carilli, C. L., Furlanetto, S., Briggs, F., et al. 2004, NAR, 48, 1029
Carilli, C. L., & Walter, F. 2013, ARA&A, 51, 105
Carral, P., Hollenbach, D. J., Lord, S. D., et al. 1994, ApJ, 423, 223
Cooray, A., Gong, Y., Smidt, J., & Santos, M. G. 2012, ApJ, 756, 92
de Looze, I., Baes, M., Bendo, G. J., Cortese, L., & Fritz, J. 2011, MNRAS, 416, 2712
De Looze, I., Cormier, D., Lebouteiller, V., et al. 2014, ArXiv e-prints
De Lucia, G., & Blaizot, J. 2007, MNRAS, 375, 2
Dopita, M. A., & Sutherland, R. S. 2003, Astrophysics of the diffuse universe
Ferkinhoff, C., Brisbin, D., Nikola, T., et al. 2011, ApJ, 740, L29
Fernandez, E. R., & Komatsu, E. 2006, ApJ, 646, 703
Fernandez, E. R., & Zaroubi, S. 2013, ArXiv e-prints
Furlanetto, S. R., Oh, S. P., & Briggs, F. H. 2006, Phys. Rep., 433, 181
Gong, Y., Cooray, A., Silva, M., et al. 2012, ApJ, 745, 49
Gong, Y., Silva, M., Cooray, A., & Santos, M. G. 2014, ApJ, 785, 72
González-López, J., Riechers, D. A., Decarli, R., et al. 2014, ArXiv e-prints
Graciá-Carpio, J., Sturm, E., Hailey-Dunsheath, S., et al. 2011, ApJ, 728, L7
Guo, Q., White, S., Boylan-Kolchin, M., et al. 2011, MNRAS, 413, 101
Hollenbach, D. J., & Tielens, A. G. G. M. 1997, ARA&A, 35, 179
Kaneda, H., Nakagawa, T., Ghosh, S. K., et al. 2013, A&A, 556, A92
Kanekar, N., Wagg, J., Ram Chary, R., & Carilli, C. L. 2013, ApJ, 771, L20
Karzas, W. J., & Latter, R. 1961, ApJS, 6, 167
Kaufman, M. J., Wolfire, M. G., Hollenbach, D. J., & Luhman, M. L. 1999, ApJ, 527, 795
Kennicutt, Jr., R. C. 1998, ApJ, 498, 541
Kistler, M. D., Yuksel, H., & Hopkins, A. M. 2013, ArXiv e-prints
Lagos, C. D. P., Baugh, C. M., Lacey, C. G., et al. 2011, MNRAS, 418, 1649
Lagos, C. d. P., Bayet, E., Baugh, C. M., et al. 2012, MNRAS, 426, 2142
Larson, R. B. 1998, MNRAS, 301, 569
Lebouteiller, V., Cormier, D., Madden, S. C., et al. 2012, A&A, 548, A91
Liu, A., & Tegmark, M. 2012, MNRAS, 419, 3491
Malhotra, S., Kaufman, M. J., Hollenbach, D., et al. 2001, ApJ, 561, 766
Obreschkow, D., Heywood, I., Klöckner, H.-R., & Rawlings, S. 2009a, ApJ, 702, 1321
Obreschkow, D., Klöckner, H.-R., Heywood, I., Levrier, F., & Rawlings, S. 2009b, ApJ, 703, 1890
Ota, K., Walter, F., Ohta, K., et al. 2014, ArXiv e-prints
Paciga, G., Chang, T.-C., Gupta, Y., et al. 2011, MNRAS, 413, 1174
Pineda, J. L., Langer, W. D., Velusamy, T., & Goldsmith, P. F. 2013, A&A, 554, A103
Razoumov, A. O., & Sommer-Larsen, J. 2010, ApJ, 710, 1239
Rigopoulou, D., Hurley, P. D., Swinyard, B. M., et al. 2013, MNRAS, 434, 2051
Rigopoulou, D., Hopwood, R., Magdis, G. E., et al. 2014, ApJ, 781, L15
Robertson, B. E., & Ellis, R. S. 2012, ApJ, 744, 95
Rottgering, H. J. A., Braun, R., Barthel, P. D., et al. 2006, ArXiv Astrophysics e-prints
Salpeter, E. E. 1955, ApJ, 121, 161
Santos, M. G., Ferramacho, L., Silva, M. B., Amblard, A., & Cooray, A. 2010, MNRAS, 406, 2421
Sargent, M. T., Béthermin, M., Daddi, E., & Elbaz, D. 2012, ApJ, 747, L31
Sargent, M. T., Daddi, E., Béthermin, M., et al. 2013, ArXiv e-prints
Sargsyan, L., Lebouteiller, V., Weedman, D., et al. 2012, ApJ, 755, 171
Shaver, P. A., Windhorst, R. A., Madau, P., & de Bruyn, A. G. 1999, A&A, 345, 380
Sheth, R. K., & Tormen, G. 1999, MNRAS, 308, 119
Silva, M., Santos, M. G., Gong, Y., & Cooray, A. 2012, ArXiv e-prints

Springel, V., White, S. D. M., Jenkins, A., et al. 2005, Nature, 435, 629
Stacey, G. J., Hailey-Dunsheath, S., Ferkinhoff, C., et al. 2010, ApJ, 724, 957
Stacey, G. J., Swain, M. R., Bradford, C. M., et al. 1999, in ESA Special Publication, Vol. 427, The Universe as Seen by ISO, ed. P. Cox & M. Kessler, 973
Tingay, S. J., Goeke, R., Bowman, J. D., et al. 2013, PASA, 30, 7
Venkatesan, A. 2000, ApJ, 537, 55
Zhao, Y., Lu, N., Xu, C. K., et al. 2013, ApJ, 765, L13

APPENDIX

In this appendix we summarize the key steps necessary to obtain the continuum foregrounds which will contaminate CII intensity maps in the frequency range 200-300GHz. This study includes contamination by stellar emission, dust emission, free-free and free-bound emission and finally two photon emission.

Stellar emission

The stellar luminosity density can be estimated as a function of redshift and frequency using the SFR versus halo mass relation parameterization shown in equation 8 and the relations for stellar emission from Cooray et al. (2012). The stellar luminosity at frequency ν is approximately given by the emissivity of a black body (B_ν) integrated over the solid angle and the area of the stellar surface ($4\pi R_*^2$):

$$L_\nu^\star = \pi\ 4\pi R_*^2 B_\nu(T_*^{eff}). \tag{1}$$

For estimating the stellar radius (R_*) and for the star effective temperature (T_{eff}) we used the formulas in (Cooray et al. 2012) for POP II stars and POP III stars. We calculated separately the emission from POP II and POP III stars assuming that the POP III stellar population evolution could be described using the error function. The error function is given by:

$$fp(z') = \frac{1}{2}\left[1 + erf\left(\frac{z - zt}{\sigma_p}\right)\right], \tag{2}$$

where we imposed that the POP III population ended at z=6, that POP III stars are the dominant population for $z_{\rm t} \geq 10$ and that the POP III transition width is $\sigma_{\rm P} = 0.5$. A discussion for the choice of these values can be found at (Fernandez & Zaroubi 2013).

The observed stellar luminosity density is the sum of the luminosity density of POP II stars ($l^{\rm POPII}$) and of POP III stars ($l^{\rm POPIII}$) given respectively by:

$$l^{\rm POP_{II}}(\nu, z) = \int_z^{\rm z_{max}} \int_{\rm M_*^{min}}^{\rm M_*^{cut(z,z')}} K(z') M_*^{-2.35} \times L_\nu^\star dM'_* \frac{dt}{dz'} dz', \tag{3}$$

and

$$l^{\rm POP_{III}}(\nu, z) = \int_z^{\rm z_{max}} \int_{\rm M_*^{min}}^{\rm M_*^{cut(z')}} K(z') M_*^{-1} \times \left(1 + \frac{M_*}{M_*^c}\right)^{-1.35} L_\nu^* dM_* \frac{dt}{dz'} dz'. \tag{4}$$

The integration in stellar mass was made using a (Salpeter 1955) IMF (Initial Mass Function) with a mass range from 0.1 to 100 $\rm M_\odot$ for POP II stars and a (Larson 1998) IMF with a mass range from 0.1 to 500 $\rm M_\odot$, and $M_*^c = 250 \rm M_\odot$ for POP III stars. In equations 3 and 4, $M^{\rm cut}(z, z')$, corresponds to the maximum stellar mass of a star created at redshift z' which is still alive at z and $K(z')$ is the normalization of the mass function in units of [$\rm Mpc^{-3} s^{-1}$] so that the total stellar mass coincides with the value that can be obtain with the SFRD(z'). For POP II and POP III stars $K(z')$ is given by:

$$K(z') = \frac{SFRD(z') fp(z')}{\int_{\rm M_*^{min}}^{\rm M_*^{max}} M_*^{-2.35} M_* dM'_*} \tag{5}$$

and

$$K(z') = \frac{SFRD(z')[1 - fp(z')]}{\int_{\rm M_*^{min}}^{\rm M_*^{max}} M_*^{-1} \left(1 + \frac{M_*}{M_*^c}\right)^{-1.35} M_* dM'_*} \tag{6}$$

where the SFRD is in units of $M_\odot Mpc^{-3}s^{-1}$. The stellar emission contamination to the observed frequency ν_o is given by:

$$I_{\nu_o} = \int_{z=0}^{z_{max}} y(z') \frac{l^{POP_{II}}(\nu, z') + l^{POP_{III}}(\nu, z')}{4\pi(1+z')^2} dz', \tag{7}$$

where ν is the emitted frequency which is related to the observed frequency by $\nu = \nu_o(1+z)$. The resulting intensity in the 200GHz to 300GHz frequency range is of $I_\nu \approx 2.5 \times 10^{-4} Jysr^{-1}$.

Dust emission

UV emission from stars between 13.6eV and 6eV is absorbed by the dust in the galaxy and is re-emitted as continuum infrared radiation. The dust spectral emission is the result of emission by dust particles with different sizes emitting at a temperature proportionally to the particle size. Each particle emits approximately as a black body and so the overall emission spectra is well described by a black body spectra at temperature Td, modified by the emissivity function $\epsilon_\nu \propto \nu^\beta$ in order to account for the different dust temperatures. Using the data from the Herschel-Astrophysical Terahertz Large Area Survey and from the Sloan Digital Sky Survey Amblard et al. (2010) estimated that $\beta \approx 1.5$ and that the dust temperature as a function of the Infrared (IR) luminosity can be approximated by:

$$T_d = T_0 + \alpha log(L_{IR}/L_\odot), \tag{8}$$

with $T_0 = -20.5$K and $\alpha = 4.4$. The data set used for this fit contains galaxies with $L_{FIR} > 10^8 L_\odot$ and is not accurate for lower luminosity galaxies. So for lower luminosity galaxies we assumed that $T_d = T_d(L_{IR} = 10^8 L_\odot) \approx 10$K. We set the amplitude of the dust emission (A_{dust}) by imposing that:

$$A_{dust} = \frac{L_{FIR}(40 - 120\mu m)}{\int_{40\mu m}^{120\mu m} \nu^\beta \frac{\nu^3}{e^{(h\nu/kT_d)}-1}}, \tag{9}$$

where L_{IR} and L_{FIR} can be obtained from the galaxy mass using equations 5, 4 and 8. The observed intensity originated from dust emission will therefore be:

$$I_\nu = \int_{z_{min}}^{z_{max}} \int_{M_{min}}^{M_{max}} \frac{dn}{dm} \frac{A_{dust}\nu_e^\beta \frac{\nu_e^3}{e^{(h\nu_e/kT_d)}-1}}{4\pi D_L^2} D_A^2 y(\nu_e) dM dz \tag{10}$$

where $\nu_e = \nu(1+z)$. The resulting intensity is of the order of 10^{-5}Jy sr^{-1} with un upper limit of the order of 10^{-1}Jy sr^{-1} in the unlikely case of the dust temperature for galaxies with $L_{IR} < 10^8 L_\odot$ to be 5K. Therefore, the contamination from dust emission will be several orders of magnitude below the CII intensity in the 200-300GHz observing frequency range.

Free-free and free-bound emission

Free electrons scatter off ions without being captured giving origin to free-free continuum emission. If during this interaction the electrons are captured by the ions then there is emission of free-bound radiation. Both free-free and free-bound photons contribute to the continuum infrared background. Following the approach of (Fernandez & Komatsu 2006), the free-free and free-bound continuum luminosities can be obtained using:

$$L_\nu(M, z) = V_{sphere}(M, z)\varepsilon_\nu \tag{11}$$

where V_{sphere} is the volume of the Strömgren sphere (the emitting volume) which can be roughly estimated using the ratio between the number of ionizing photons emitted by a halo and the number density of recombinations in the ionized volume:

$$V_{sphere}(M, z) = \frac{Q_{ion} SFR(M, z)(1 - f_{esc})}{n_e n_p \alpha_B}, \tag{12}$$

where ε_ν is the total volume emissivity of free-free and free-bound emission, Q_{ion} is the average number of ionizing photons per solar mass in star formation, n_e is the number density of free electrons, n_p is the number density of protons (ionized atoms) and α_B is the case B recombination coefficient (taken from Furlanetto et al. (2006)) given by:

$$\alpha_B \approx 2.6 \times 10^{-13} (T_K/10^4 K)^{-0.7} (1+z)^3 cm^3 s^{-1}, \tag{13}$$

and f_{esc} is the ionizing photon escape fraction. In our calculations we used the redshift and halo mass dependent escape fraction of ionizing radiation from Razoumov & Sommer-Larsen (2010) and we used $Q_{ion} = 5.38 \times 10^{60} M_\odot^{-1}$ appropriate for POP II stars (Silva et al. 2012).

The volume emissivity estimated by (Dopita & Sutherland 2003) is given by:

$$\varepsilon_\nu = 4\pi n_e n_p \gamma_c \frac{e^{-h\nu/kT_K}}{T_K^{1/2}} J\mathrm{cm}^{-3}\mathrm{s}^{-1}\mathrm{Hz}^{-1}, \tag{14}$$

where γ_c is the continuum emission coefficient including free-free and free-bound emission given in SI units by:

$$\gamma_c = 5.44 \times 10^{-46} \left[\bar{g}_{ff} + \Sigma_{n=n'}^{\infty} \frac{x_n e^{x_n}}{n} g_{fb}(n) \right], \tag{15}$$

where $x_n = Ry/(k_B T_K n^2)$ (n is the level to which the electron recombines to and $Ry = 13.6$eV is the Rydberg unit of energy), $\bar{g}_{ff} \approx 1.1 - 1.2$ and $g_{fb}(n) \approx 1.05 - 1.09$ are the thermally average Gaunt factors for free-free and free-bound emission (values from Karzas & Latter (1961)). The initial level n' is determined by the emitted photon frequency and satisfies the condition $cR_\infty/n'^2 < \nu < cR_\infty/(n'-1)^2$ where $R_\infty = 1.1 \times 10^7 m^{-1}$ is the Rydberg constant. We then obtained the free-free plus free bound luminosity formula given by:

$$L_\nu(M,z) = 9.26 \times 10^7 \alpha_B^{-1}(\mathrm{T_K}, z) \left[\frac{Q_{ion}}{5.38 \times 10^{60}} \right] \tag{16}$$
$$\left[1.15 + \Sigma_{n=n'}^{\infty} \frac{x_n e^{x_n}}{n} 1.07 \right] \frac{e^{-h\nu/k_B T_K}}{T_K^{1/2}} SFR(M,z).$$

Assuming a gas temperature of $(1-4) \times 10^4$K we estimated the intensity of emission in the frequency range 200-300GHz to be of $I_{\mathrm{free}} \approx 1 - 2 \times 10^{-12}$Jy sr^{-1}.

Two photon emission

The infrared luminosity from two photon emission during recombination is given by:

$$L_\nu^{2\gamma}(M) = \frac{2h\nu}{\nu_{Ly\alpha}} (1 - f_{Ly\alpha}) P(\nu/\nu_{Ly\alpha}) Q_{\mathrm{ion}} SFR(M,z), \tag{17}$$

where P(y)dy is the normalized probability that in a two photon decay one of them is the range $dy = d\nu/\nu_{Ly\alpha}$ and $1 - f_{Ly\alpha} \approx 1/3$ is the probability of 2 photon emission during an hydrogen n=2→1 transition. The probability of two photon decay was fitted by Fernandez & Komatsu (2006) using Table 4 of Brown & Mathews (1970) as:

$$P(y) = 1.307 - 2.627(y-0.5)^2 + 2.563(y-0.5)^4 - 51.69(y-0.5)^6. \tag{18}$$

The intensity from continuum emission is given by:

$$\bar{I}_{\mathrm{cont}}(\nu) = \int_{z=0}^{z_{\mathrm{max}}} dz \frac{l_{\mathrm{cont}}(\nu_e, z)}{4\pi D_{\mathrm{L}}^2} y D_{\mathrm{A}}^2, \tag{19}$$

where $l_{\mathrm{cont}} = [L_\nu^{2\gamma}/SFR(M,z) + L_\nu/SFR(M,z)] \times SFRD(z)$.

The continuum intensity at frequencies 200-300GHz is of $\bar{I}_{\mathrm{cont}} \approx 3 \times 10^{-12}$Jy sr^{-1}, which is well below the expected CII signal.